

PREMIO FIRENZE UNIVERSITY PRESS  
TESI DI DOTTORATO

- 4 -



Matteo Mannini

**Molecular Magnetic Materials  
on Solid Surfaces**

Firenze University Press  
2008

Molecular Magnetic Materials on Solid Surfaces / Matteo Mannini. – Firenze : Firenze University Press, 2008.  
(Premio FUP. Tesi di dottorato ; 4)

<http://digital.casalini.it/9788884539014>

ISBN 978-88-8453-900-7 (print)

ISBN 978-88-8453-901-4 (online)

Progetto grafico di Alberto Pizarro Fernández

© 2008 Firenze University Press  
Università degli Studi di Firenze  
Firenze University Press  
Borgo Albizi, 28  
50122 Firenze, Italy  
<http://www.fupress.com/>

*Printed in Italy*

*A Maura e Varesco*

*«...So many objects and machines these days are stuffed full of intellect – and most of the time it's just turned of.*

*We're surrounded by unused intelligence, and for once it's not our own. For every fridge which tells you what's fresh and what's not, there'll be fifty which have been told just shut the fuck up. [...]*

*We created things which are clever and then told them to be stupid instead, because we realized we didn't need clever toasters or vehicles which insisted on driving you the quickest route when you had all the afternoon to kill and noth-ing to do once you got there....»*

*“Spares” (Michael Marshall Smith)*



# Contents

<b>Chapter 1</b>	
<b>Nano-Science and Nano-Magnetism</b>	1
<b>Chapter 2</b>	
<b>The surface analysis techniques</b>	5
1. X-ray Photoelectron Spectroscopy	6
2. Time-of-Flight Secondary - Secondary Ion Mass Spectrometry	7
3. Scanning Probe Microscopies	10
3.1 Scanning Tunneling microscopy	14
3.2 Atomic Force Microscopy	19
<b>Chapter 3</b>	
<b>Deposition processes</b>	23
1. Evaporation techniques	23
2. Drop-casting method	26
3. Self-Assembling of Monolayer technique	26
4. Micro-contact printing technique	31
<b>Chapter 4</b>	
<b>Syntheses of Single Molecule Magnets for deposition on gold surfaces</b>	33
1. The Mn <sub>12</sub> - <i>acetate</i> cluster and the general scheme of derivation	33
2. Mn <sub>12</sub> sulphur-based derivatives	40
2.1 Aliphatic acetyl-thio-derivative of Mn <sub>12</sub>	41
2.1 Aromatic acetyl-thio-derivative of Mn <sub>12</sub>	44
2.3 Aromatic methyl sulphide-derivative of Mn <sub>12</sub>	46
2.4 Aliphatic disulphide-derivative of Mn <sub>12</sub>	48
2.5 Toward the iso-orientation of Mn <sub>12</sub> molecules on surface	49
3. Bulk magnetic characterization of Mn <sub>12</sub> -sulphur derivatives	51

<b>Chapter 5</b>	
<b>Syntheses of Nitronyl Nitroxide radicals for deposition on gold surfaces</b>	57
1. Nitronyl Nitroxide radicals	57
1.1 General synthesis of Nitronyl Nitroxides	57
1.2 The first sulphur derivative of Nitronyl Nitroxides	59
1.3 The bi-phenyl derivative of Nitronyl Nitroxides	60
1.4 The benzylic derivative of Nitronyl Nitroxides	62
1.5 Aliphatic disulphide derivative of Nitronyl Nitroxides	65
<b>Chapter 6</b>	
<b>Deposition of magnetic molecules on gold surfaces</b>	67
1. Deposition and characterization of SMMs on surface	67
1.1 Homogeneous monolayers	68
1.2 Isolated (and organized?) molecules	76
1.3 Isolated and oriented molecules	83
1.4 Patterned molecules	84
2. Deposition and characterization on surface of organic radicals	88
2.1 From disordered to ordered monolayers	88
2.2 Patterned molecules	95
<b>Chapter 7</b>	
<b>Attempts in detecting the magnetism of one layer of molecules on surfaces</b>	99
1. Traditional measurement of Mn12 functionalized surfaces	99
2. Surface measurement of Mn12 functionalized surfaces	100
2.1 Magneto-optical characterization of functionalized surfaces	101
2.2 XAS and XMCD characterization of functionalized surfaces	102
3. Measurement of Nitronyl Nitroxide functionalized surfaces	113
<b>Chapter 8</b>	
<b>Magnetism of single molecules</b>	119
1. Magnetism of a single molecule magnet	119
2. Detection of a single spin of organic radicals through the ESN-STM	121
2.1 ESN-STM instrumentation description	122
2.2 Testing of the ESN-STM with standards	125
2.3 ESN-STM investigation of Nitronyl Nitroxide molecules.	131
<b>Chapter 9</b>	
<b>Conclusions</b>	133
<b>Bibliographic references</b>	135

# Chapter 1

## Nano-Science and Nano-Magnetism

The prefix *nano-* denotes a factor of  $10^{-9}$  and has its origin in the Greek *νανός*, meaning dwarf. Nanoscience is a new discipline which investigates systems which are of the size of a few nanometres in one- two- or three-dimensions. One of the starting points of Nanoscience can be considered the famous seminal talk of R. P. Feynman talk called *There's Plenty of Room at the Bottom* (Feynman R. P. 1959). Another fundamental event for the development of Nanoscience has been the implementation of Scanning Probe Microscopies which allow to observe, to handle, to modify nano-objects with an unprecedented resolution. These techniques have prompted to use a bottom up approach, which is one of the distinctive features of Nanoscience. Finally one of the key features of Nanoscience is that of going beyond the borders of classical disciplines, like Physics, Chemistry, Biology providing a unified approach.

The *bottom-up approach* can be achieved by using molecules as building blocks and innovative *nano-materials* are currently produced by exploiting the properties of single molecules (Aviram A. and Ratner M. A. 1974).

One of the important areas of Nanoscience is *Nanomagnetism*, meaning with this the investigation of the magnetic properties of nano-objects of different nature. In this thesis chemical as well as physical tools have been used to investigate the nanomagnetic properties of objects obtained through the organization of molecular building blocks.

Before starting the description of the experience exploited in this field within this thesis a small overview of the state of the art in Nanomagnetism is needed, first of all shortly introducing the characteristics of the employed building blocks, then describing with a critical approach the real objectives of these studies.

Not all the phenomena are scalable toward miniaturization, this is well known in magnetism where, for instance, hysteresis loop in magnetization is observable for systems with different sizes but origins from different physical phenomena (Wernsdorfer W. 2001) as summarized in Figure 1.1.

In fact, starting from a bulk magnetic material, ideally working in a *top-down approach* decreasing the size of a magnetic object, a breakdown of the expected multi-domain model occurs when the radius of particle is comparable with the size of the domain walls (Morrish A. H. 1966). At this point a single-domain model must be used to describe the magnetization curve of the system. The rotation of the magnetization of the particles occurs with a concerted movement of all the spins. Generally the magnetization has a preferred orientation which can be reversed by overcoming a barrier depending on the magnetic anisotropy. Decreasing further the size of the

particles also the single domain model breaks down (Néel L. 1949) when the energy of the barrier within the two magnetization states become comparable to thermal energy, as evidenced by the free fluctuation of the magnetization, analogously to that observed in a paramagnet. This is called the *superparamagnetic regime* which is achieved for particles of size of a few nanometres. It marks the starting point for innovative applications for instance in bioscience (Pankhurst Q. A. et al. 2003) but it represents also the dead point for data storage applications (Moore G. E. 1965). A technological escape to overcome this problem has been suggested and applied recently (Bertram H.N. and Williams M. 2000).

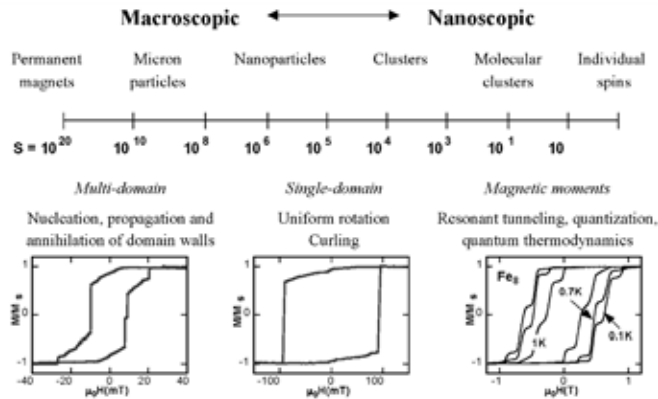


Figure 1.1. The transition from macroscopic to microscopic magnetism. The hysteresis loops observed origin from different phenomena. Picture courtesy of Wolfgang Wernsdorfer

An alternative approach is that of using a bottom up strategy. The idea (Gatteschi D. et al. 2006) is that it should be possible to employ single molecules which are large enough to behave as bulk magnets. These molecules were discovered in the '90s (Caneschi A. et al. 1991) and named *Single Molecule Magnets* (SMMs) (Eppley H. J. et al. 1997). In this case the origin of the magnetism is again completely different; in fact it is bound to the slow relaxation of the magnetization of individual molecules, in other words it is due to the inner chemical structure of each molecular unit without any cooperative effects.

The SMMs approach stimulated a strong activity in finding the perfect candidate allowing the production of molecular based data storage devices. However no real progress was done in this sense, after the discover of the archetypal of the SMMs, the dodecamanganese, Mn<sub>12</sub> cluster (Lis T. 1980; Caneschi A. et al. 1991; Sessoli R. et al. 1993a). In fact the use of this cluster for potential applications was made difficult by the very low temperature needed to observe these properties and a decade of scientific efforts in increasing the operational temperature seem to be resulted useless. However, from a scientific point of view their discovery and the strong efforts devoted to the rationalization of the SMMs features improved enormously the knowledge concerning the dynamics of magnetization as well as the coexistence of classical and quantum effects in mesoscopic magnets (Gatteschi D. and Sessoli R. 2003). Moreover different technological interests are now stimulating the interest in SMM

systems as well as simpler paramagnetic molecules like stable organic radicals. In fact the ability to manipulate electron and nuclear spins in molecular materials should offer an attractive route towards molecular spintronics applications (Rocha A. R. et al. 2005). This renewed interest in SMMs and in simpler molecules opens new exciting perspectives. Phenomena like the electronic transport through this kind of material in presence of a magnetic field are now stimulating a wide class of theoreticians (Kim G.H. and Kim T.S. 2004; Romeike C. et al. 2006) as well as experimentalists (Heersche H. B. et al. 2006; Jo M.-H. et al. 2006; Ni C. et al. 2006). From the chemical point of view it prompts the design of new classes of molecules and challenges to synthesize them providing new building blocks for these *Molelectronics* (Tour J. M. et al. 1998) purposes. In this sense also slight variations of the characteristics of *molecule* used for these *spintronics* applications can tune the fine physics involved in it; thus, again, a strong multidisciplinary work and continuous feedback between physical and chemical approaches are required. This last aspect is well evidenced in this thesis work: slight chemical modification of molecules strongly influence physical aspects and fine physical characterizations are required to characterize appropriately the produced nano-materials.

During this work we explored the deposition of magnetic entities on surfaces. We focused our effort in this new area for Molecular Magnetism in order to achieve a direct addressing of isolated magnetic molecules on a surface, studying directly single molecule properties instead of extrapolating them from bulk analysis. The complete achievement of such purposes is one of the needed steps toward the production of prototypes of molecular based magnetic devices.

In summary, in this manuscript we will describe the experimental work of three years, that has been focused on depositing *Single Molecules Magnets* as well as simpler paramagnetic radicals, the *Nitronyl Nitroxides*, on metallic surfaces. First in Chapter 2 the physical tools allowing a preliminary characterization of functionalized surfaces will be described, then in Chapter 3 a survey of the chemical tools employed to obtain these nanostructured materials to be investigated, will be provided. In the following two Chapters (4 and 5) we will describe the two class of compound taken in to account in this work, the Mn12 family, as it represents the widest studied series of Single Molecule Magnets, and the nitronyl nitroxides family as one of the more promising class of stable organic radicals respectively. Different steps, going from the synthesis of the simplest derivative to the species suitable to a deposition to the surface, will be described.

Obviously the efforts on the deposition of these kinds of substances on surfaces are strongly related to the possibility to study, to manipulate, and to use single spins as well as more complicated magnetic structure in data-storage and spintronics devices. For this reason all the suggested procedures for depositing these molecules on surfaces will be analyzed in Chapter 6 not only in terms of the quality of the achieved nano-organization but also taking into account the reproducibility of their preparation as established by morphological and physico-chemical investigations.

Finally in Chapter 7 we will provide direct information about magnetism of the deposited monolayer of magnetic materials obtained with the higher sensitivity techniques available and compatible with these systems. In Chapter 8 some insights toward a real single molecule magnetism detection based on evolutions of scanning

probe techniques will be provided in order to rekindle some hope in the feasibility of single molecule based data storage devices as well as to approach the theoretically suggested potentiality of spintronics based devices.

## Chapter 2

### The surface analysis techniques

The surface analysis techniques provide qualitative and quantitative chemical information as well as local morphological and structural indications of ultrathin films (Riviere J. C. 1990). The analytical objective of the different techniques depends on the used probe. Surface analysis techniques can be considered as scattering experiments: a particle is incident on the sample, and another particle (not necessarily the same) is detected after an interaction with the sample. The probe will be formed by a particular type of particle, and a well defined series of parameters like its energy. The response may be either the same or a different particle and, depending on the detection system, its energy or other attributes, may be measured. By understanding the nature and the physics of the scattering we can interpret the experiment and deduce the corresponding characteristics of the sample.

It is easy to see from the following Table 2.1 how the number of techniques can be very large, especially once one realises that each probe particle can give rise to all other particles as a response.

Table 2.1 Classification of surface analysis techniques as particle scattering techniques.

Probe		Response
Electrons Photons Atoms Ions	} Sample	{ Electrons Photons Atoms Ions

We are interested in techniques providing evidences of the presence of molecules deposited on metallic surfaces and then in this Chapter we describe some of these powerful techniques that we adopted in order to characterize ultrathin films functionalized with magnetic molecules. The goal was that of obtaining some indications of the presence of the molecules on the surface both from a topographic and a chemical point of view: in this work we noticed that it is of fundamental importance to maintain a strong correlation between what is nicely observed with imaging techniques and what is indeed chemically present after deposition. For this reason in this chapter we will couple imaging techniques, that attracted our interest for their enormous potentiality, and surface chemical characterization techniques, which in parallel to the first ones permit to check if the obtained images correspond to the expected deposited molecules.

## 1. X-ray Photoelectron Spectroscopy

The *X-ray Photoelectron Spectroscopy* (XPS) (Grant J. T. and Briggs D. 2003) is a powerful qualitative and quantitative analysis instrumentation for surface investigation of solid samples. It provides information about the presence of a given element and on its chemical bonds, allowing the identification of the different chemical species present on surfaces.

Briefly, XPS is based on the photoelectric effect (Einstein A. 1905) consisting in the emission of electrons from a material when exposed to an electromagnetic radiation with a frequency higher than a threshold value. Electrons obtained in this process (Figure 2.1) are called photoelectrons and, in a mono-electronic approximation the process can be described by the formula:

$$h\nu = BE + KE + \Phi \quad (\text{Eq. 2.1})$$

where  $\nu$  is the frequency of the radiation,  $BE$  is the *Binding Energy* of the electron defined respect to the vacuum level,  $KE$  represents the kinetic energy of the extracted photon and  $\Phi$  the work function of the investigated solid.

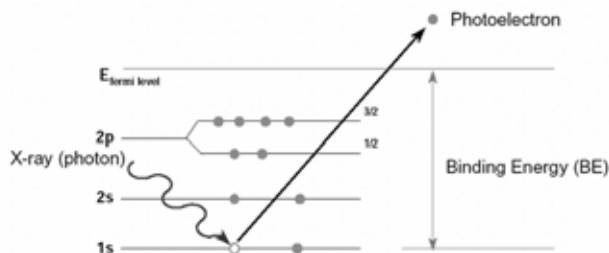


Figure 2.1. Representation of the photoemission process occurring in XPS measurements.

In the instrumental apparatus (Fig 2.2) X-rays are produced by accelerating electrons (obtained by a thermoionic effect) from a filament to a metallic anode. The obtained radiation is composed by a continuum background (*bremstrahlung*) and monochromatic intense components characteristic of the material constituting the anode (typically *Mg* or *Al*). Photoelectrons ejected from the sample invested by this radiation are collected and dispersed by an electrostatic analyzer: this analyzer is formed by two concentric hemispheres. By varying the difference of potential between the two hemispheres, the energy of electrons that can go over the trajectory toward the detector is changed. In this way electrons with different  $KE$  are selected, each  $KE$  corresponds to a  $BE$  (in function of the experimental setup) and plotting the intensity of the detected signal respect to the  $BE$  it is possible to obtain an XPS spectrum.

This  $BE$  will depend on the kind of atom from which the electron is extracted and from the specific orbital but also from the specific chemical surrounding of the considered atom. In fact specific chemical shifts will be observed by studying the signal coming from atoms with different oxidation states.

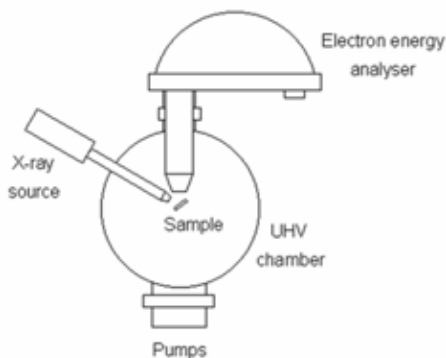


Figure 2.2. Scheme of an XPS apparatus.

In conclusion the XPS technique allows to determine the type, the concentration and the chemical state of the surface atoms. Thus, XPS has been utilised as a powerful diagnostic tool to analyse ultrathin films. For instance studies of SAMs using XPS showed that a covalent bond exists between the sulphur headgroup and the gold substrate (Bourg M.-C. et al. 2000). In addition, through angular dependent sputtering experiments in which the X-rays are focused to etch the SAM down to the underlying substrate, the thickness of the SAM can be calculated based on the variation of the substrate signal intensity before and after the etching process (Laibinis P.E. et al. 1991).

## 2. Time-of-Flight Secondary Ion Mass Spectrometry

By sending accelerated ions instead of electrons to the sample, a different sputtering process is obtained. The impact of a *primary* ion determines an emission process of *secondary* ions.

This process is exploited in *Secondary Ion Mass Spectrometry* (SIMS) technique (Benninghoven A. 1973) where the investigated sample is bombarded with primary ions (generally  $Ga^+$  and  $Cs^+$ , but recently also with  $Au^+$  (Davies N. et al. 2003) and  $C_{60}^+$  (Wong S. C. C. 2003) in order to increase high mass resolution), pulsed with energy in the range of 10-25 keV. Direct collisions between primary ions and atoms in the sample as well as indirect phenomena, like collisions of atoms in the sample already in motion with other atoms in the sample (*knock-on effects*), produce an extensive fragmentation and bond breaking near the collision site, obtaining essentially only the emission of atomic particles. As the collision cascade moves away from the collision site, the collisions become less energetic and thus less efficient in fragmentation and bond breaking, producing the emission of molecular fragments (Fig. 2.3). These sputtered particles are ejected as neutral atoms and molecules, electrons, and ions. Only these ions are subsequently analyzed and revealed through a mass spectrometer in function of their  $m/z$  ratio.

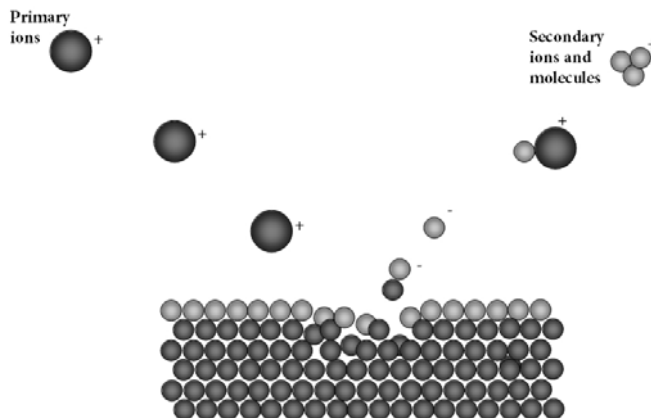


Figure 2.3. Simulation of the impact of primary ion on sample surface and consequent emission of secondary ions.

Particles produced with this process come from the top 2–3 monolayers of the sample; only these molecules in fact have sufficient energy to overcome the surface binding energy and can leave the sample. For this reason SIMS detects really only the composition of the surface and consequently the number of particles produced in this process of sputtering is so low that high sensitivity detectors are required.

Different solutions have been suggested (Reed N.M. and Vickerman J. C. 1993) for detectors but the most improved one is based on the *Time-of-Flight* (ToF) detection (Fig. 2.4) that permits an exhaustive investigation of surfaces with an excellent mass resolution (often exceeding  $10,000 m/\Delta m$ ).

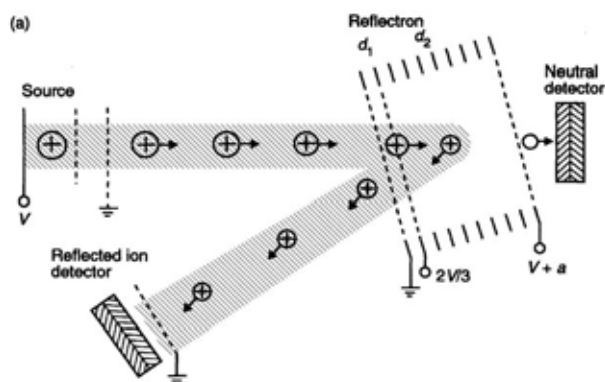


Figure 2.4. A simplified scheme of a ToF detector.

A Time-of-Flight mass spectrometer operates on the principle that ions are accelerated from the ion-source region into a field-free drift region where they move towards the instrument detector with a velocity that is determined by their  $m/z$  value. Ions of lower  $m/z$  values will have higher velocities than those of higher  $m/z$  values

and will reach the detector first. More in details, the mass,  $m$ , of the ions is determined according to the time it takes them to travel through the length,  $L$  of the field-free flight tube, after they have been accelerated in an extraction field to a common energy,  $E$  (Belu A. M. et al. 2003). The relationship between  $E$  and flight time,  $t$ , is straightforward (where  $v$  is velocity):

$$E = mv^2/2 = mL^2/2zt^2 \quad (\text{Eq. 2.2})$$

Since flight time is proportional to the square root of the mass of the secondary ion, the lighter ions travel at a faster velocity and arrive at the detector earlier than the heavier ions:

$$t = L(m/2zE)^{1/2} \quad (\text{Eq. 2.3})$$

As evident from the last formula, to obtain the best separation of ions the energy of the ion must be constant and this is achieved by pulsing the primary ion source with short pulse widths (sub-nanosecond) in order to yield secondary ions with minimal time dispersion, and thus with minimal energy spread. A fixed voltage then accelerates the secondary ions into the ToF analyzer, with its polarity determining whether positive or negative secondary ions, are analyzed. The energy and angular dispersion of the secondary ions that originate with the emission process can be compensated using focusing elements such as an ion mirror or reflector.

After separation in the ToF analyzer, the secondary ions are focused onto the detector by an ion lens. A post-acceleration voltage of up to 15 kV is applied to the ions to improve the detection efficiency of the high-mass ions because they travel at slower velocities. The ions strike the detection unit, which is typically composed of a photo-converter electrode, channel plate, scintillator, photomultiplier and a counter, all in series. The complete setup of the used ToF-SIMS apparatus is sketched in Figure 2.5.

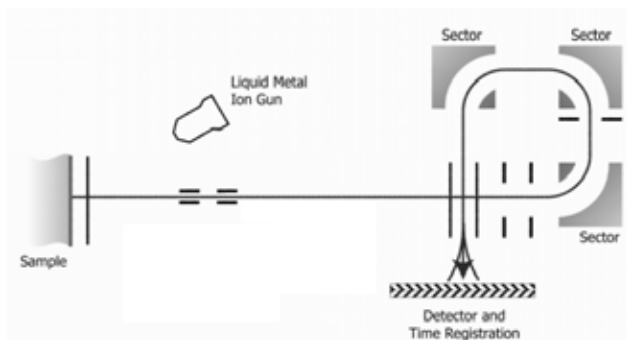


Figure 2.5. TRIFT III (ToF) spectrometer simplified scheme.

The advantages of this instrumentation are not limited to average chemical information about the sample. In fact, by focusing the primary beam to a narrow diameter (down to  $\sim 100$  nm), exploiting the time dependent measurement capability and describing a raster movement with this beam (see next paragraph) it is possible to map the local composition of the sample. In this way a complete mass spectrum is

obtained at each point of the scanned surface. After data acquisition a specific ion signal or a combination of them can be mapped in order to establish interesting relationship between these signals and the morphology of the surface extrapolated from the *total ion map* (the count of the total ions detected in each point of the map).

In conclusion, for our viewpoint, ToF-SIMS technique must be considered as one of the most powerful techniques to investigate ultrathin films of molecules. In particular this technique has been widely applied to SAM as well as patterned films investigation providing the chemical fingerprint of the expected molecules on surface as well as permitting a real chemical mapping of patterned surfaces made by monolayers of molecules (Graham D. J. and Ratner B.D. 2002).

### 3. Scanning Probe Microscopies

In the last part of this chapter we are going to describe a series of instrumentation which corresponds to the eyes, and in some cases to the hands, of the nanotechnologist. These techniques allow the observation of surfaces down to the limit of the atom size, and, in some cases, behind the limit between classical and quantum physics. We are going to describe the *Scanning Probe Microscopies* (SPMs) techniques by following their recent history. We will start from the discovery of the principle of the measurement, then continuing with the extension to different interaction forces and completing this panorama with a small summary of derived techniques. In Chapter 8 this subject will be extended by describing in details how scanning can be used to detect single molecule magnetism.

SPMs seems to be as an outsider in the general model of scattering used for introducing surface analysis techniques but this is not completely true. In fact we can consider SPMs as “near-field” scattering experiments: while previous experiments are based on far-field effects, here near-field effects such as tunnelling currents, van der Waals forces, local fields are detected at localized points on the surface.

Before starting a specific description of the different techniques we consider as quite important to introduce the general functioning of SPMs with a trivial simplification and then, starting from this, we will describe the core of the functioning of these machines.

To understand how SPMs work it is useful to introduce an example: the gramophone. The gramophone is constituted by a *driving system*, which allows turning the disk, a *probe*, which investigates the surface of the disk following the tracks containing music records, a *damping system*, which avoids failures in the motion of the tip or it damaging, and, eventually, the apparatus of the *transduction and output* of the music record.

In SPM techniques a probe, exploiting a particular kind of interaction that defines the kind of microscopy, locally investigates the sample; to map the surface of the sample the tip is moved using a driving system based on a piezo-electric system; punctual interactions are memorized in function of the position and represented by an output system that usually is constituted by the electronics of the microscope, a computer and, obviously, a monitor with which the operator can observe the result of the analysis. The following part of this paragraph will be devoted to describe these components starting from the motor of the scanning, the piezoelectric devices.

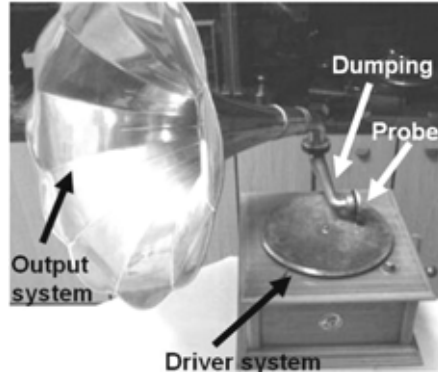


Figure 2.6. Photo of a gramophone.

The word "*piezo*" is derived from the Greek word for "pressure". The piezoelectric effect was discovered by Pierre and Jacques Curie in 1883. It is the property of certain crystals to exhibit electrical charges under mechanical loading. Later they also verified that an electrical field applied to the crystal could lead to a deformation of the material. This effect is referred to as the *inverse piezo effect* and is the effect exploited in piezo-electrodes that are at the basis of piezo-scanners used in SPMs. Generally they are made by *synthetic piezoelectric materials*, in particular ferroelectric ceramics like  $\text{BaTiO}_3$  and  $\text{PbZrTiO}_3$  (known as its acronym *PZT*: Lead Zirconate Titanate) with a perovskite-like structure.

A treatment, named *poling*, is necessary to obtain "piezoelectric" features: an electric field ( $> 2000 \text{ V/mm}$ ) is applied to the (heated) piezo ceramics. For instance the elementary cell of PZT is centro-symmetric cubic (isotropic) before poling while after poling exhibits tetragonal symmetry (anisotropic structure) below the Curie temperature (see Fig 2.7).

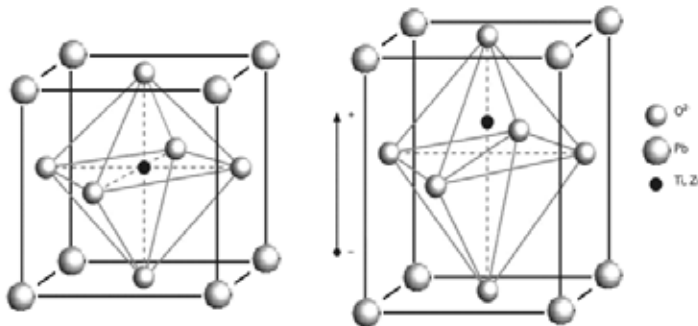


Figure 2.7. PZT unit cell: (left) Perovskite-type lead zirconate titanate (PZT) unit cell in the symmetric cubic state above the Curie temperature. (right) Tetragonally distorted unit cell below the Curie temperature. From PI 2005, copyright (2005) Physik Instrumente (PI) GmbH & Co. KG.

In a macroscopic point of view this phenomenon can be described with a simple electric dipole domains structure (Fig. 2.8).

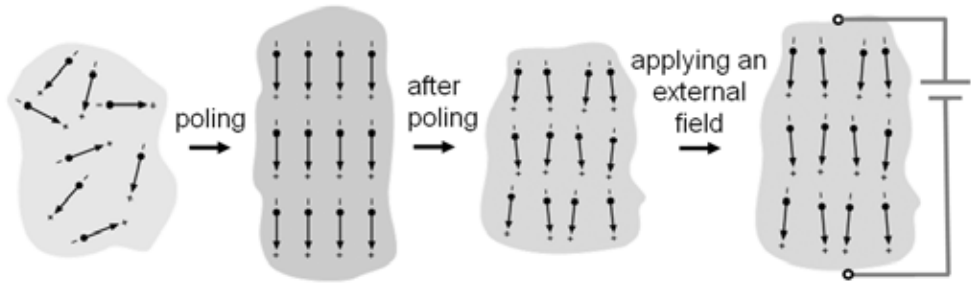


Figure 2.8. Electric dipoles in domains. From left to right: (1) unpoled ferroelectric ceramic, (2) during and (3) after poling piezoelectric ceramic, (4) applying an external electric field. From PI 2005, copyright (2005) Physik Instrumente (PI) GmbH & Co. KG.

Before the poling procedure dipoles are isotropically oriented while during poling, due to the strong electric field, a complete reorientation of dipoles is achieved. After poling the material presents a remnant polarization with Weiss domains. When small electric voltages are applied to a poled piezoelectric material, the Weiss domains increase their alignment proportional to the voltage with the result of a change of the dimensions (expansion, contraction) of the Piezo material ( $10^{-4}$ ~ $10^{-7}$  % length change per V). This process then permits a positioning accuracy of less than one angstrom and this accuracy is at the basis of the functioning of SPMs.

To obtain a 3D movement a single PZT crystal is not enough and in fact three-dimensional movements are obtained by combining orthogonally three piezo obtaining a tripod scanner (Figure 2.9a) or using a tube scanner (Figure 2.9b) in which 3D movements are controlled by a system of electrodes placed inside the scanner for the  $z$  direction and outside for  $x$  and  $y$  directions.

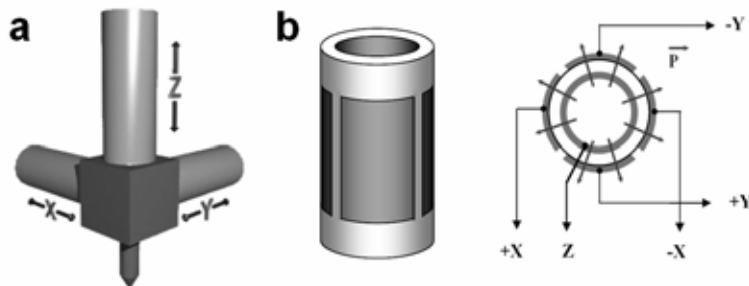


Figure 2.9. (a) Tripod Scanner scheme. (b) Tube scanner scheme and electrodes connections. From Mironov V. L. 2004. Copyright (2004) NT-MDT.

Using this scanners is possible to examine all the surface. The scan is usually performed by a *raster movement* (Howland R. and Benatar L. 2000) in which a fast scanning direction and a slow scanning direction are defined, as described in Figure 2.10.

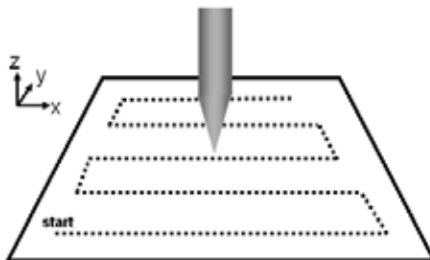


Figure 2.10. Raster movement scheme of displacement of the tip in respect of the sample.

This relative displacements of the tip in respect of the sample can be achieved either by moving the tip or the sample but it has been found that the displacement of the sample induces a lower distortion from condition of linearity versus the applied voltage (Mironov V.L. 2004). An image is obtained pixel by pixel. Each pixel has an  $(x, y)$  position derived from the voltage applied to the piezos through ramp generators. While each measurement of the interaction between the tip and the sample is converted to a  $z$  value proportional to the signal or to the variation of the tip-to-sample distance that permits to keep constant this interaction. In this condition, most widely used than the previous one, the control of the interaction value is achieved via a *feedback* circuit, that keeps the strength of this interaction close to the *set-point* value by imposing a  $z$  displacement. Using these  $(x, y, z)$  coordinates the computer reconstructs an image representing the investigated area.

Obviously the distance between the tip and the sample must be controlled in a rigorous way and any external influence must be avoided. For this reason a strong attention is devoted to vibration insulation via active or passive dumping systems isolating the sample from external noise. Temperature variation must also be avoided because they induce drift effects on the scanning and a distortion of the imaging due to dilatation or contraction of both the tip and the sample.

Finally we conclude this general overview of SPMs by summarizing tips characteristics. This is equivalent to introduce the different SPMs. In fact changing the probe we change microscopy: using a conductive probe and detecting tunneling current, we are employing a *Scanning Tunneling Microscopy* (STM) setup; using an elastic probe we measure forces and we perform an *Atomic Force Microscopy* (AFM). These are the two main and original techniques from which all the other SPMs derive. In table 2.2 are summarized the most employed SPMs techniques.

Table 2.2. Some of the most used SPMs techniques, the exploited interaction and their applications.

Microscope	Interaction	Information
STM	Tunneling current	3-D topography: size, shape and periodicity of features, surface roughness. Electronic structure, and possible elemental identity (Binnig G. and Rohrer H. 1982; Binnig G. et al. 1982).
Contact and Intermittent contact AFM	Interatomic and intermolecular forces	3-D topography: size and shape and periodicity of features, surface roughness (Binnig G. et al. 1986).
Force-Modulated AFM	Interatomic and intermolecular forces	Hardness and surface elasticity at various locations (Maivald P. et al. 1991).
LFM	Frictional forces	Differences of adhesiveness and friction at various locations (Colchero J. et al. 1992).
MFM	Magnetic forces	Size and shape of magnetic features. Strength and polarity of magnetic fields at different locations Martin Y. et al. (1987).
SThM	Heat transfer	Thermal conductivity differences between surface features (Williams and C. C. and Wickramasinghe H. K. 1987).
EFM	Electrostatic forces	Electrostatic field gradients on the sample surface due to doping concentrations (Martin Y. and Wickramasinghe H. K. 1987).
KPM	Kelvin Probe	Contact potential difference between the probe and the sample (Nonnenmacheri M. et al. 1991).
SNOM	Reflection, absorption and Fluorescence of light	Optical properties of surface features (Pohl D. W. et al. 1984).

### 3.1 Scanning Tunneling microscopy

The *Scanning Tunneling microscopy* was introduced in the 1982 by G. Binnig and H. Rohrer (Binnig G. and Rohrer H. 1982; Binnig G. et al. 1982; Binnig G. and Rohrer H. 1986). This discovery represents for many points of view the beginning of the new era of Nanoscience and was celebrated in 1986 when these two researchers at the IBM Laboratory in Zurich (Switzerland) were awarded with the Nobel prize. However the starting point of this technology can be found earlier. In fact in 1972 R. Young et al. presented a nice instrument, the Topografiner, that included almost the same innovations re-introduced ten years later but didn't reach the atomic resolution due to problems related to dumping (Young R. et al. 1972).

In any case the evolution imposed by the STM introduction is unquestionable. In the technique of STM a sharp metal tip is brought very close ( $< 10\text{\AA}$ ) to a conducting surface. When a bias voltage is placed across the tip – sample junction, electrons quantum mechanically tunnel across the gap and produce a measurable tunneling current

(typically from 10 fA to about 10 nA). This current has an exponential dependence on the tip – sample separation, resulting in atomic resolution of surface features.

A theory explaining in detail all the STM physics has been proposed ( Tersoff J. and Hamann D. R. 1985; Gottlieb A. D. and Wesoloski L. 2006) but this is out of the main subject of this thesis work. In order to describe in a nutshell the scanning tunneling microscopy theory (Chen C.J. 1993) we can start considering a metal border as a rectangular barrier. In the classical physics an electron cannot pass though this potential barrier  $E$  if its energy is smaller than the potential  $\Phi$  within the barrier. However a quantum mechanic treatment predicts an exponential decay solution for the electron wave function in the barrier. This can be expressed as the solution of the Schrödinger equation inside  $\Psi(0)$  and outside  $\Psi(d)$  a solid with non-infinite walls:

$$\Psi(d) = \Psi(0)e^{-kd} \tag{Eq. 2.4}$$

Where  $k$ , the minimum inverse decay length for the way function near the barrier, corresponds to:

$$k = \sqrt{2m(\Phi - E)} / \hbar \tag{Eq. 2.5}$$

On these basis the probability of finding an electron behind the barrier of the width  $d$  will be expressed by the relationship:

$$W(d) = |\Psi(d)|^2 = |\Psi(0)|^2 e^{-2kd} \tag{Eq. 2.6}$$

Then, as sketched in Figure 2.11, electron density decays exponentially away from surface.

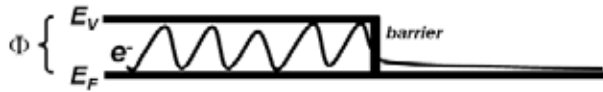


Figure 2.11. Scheme of a potential barrier.

If two identical metals are brought in close proximity ( $\Phi_1 = \Phi_2$ ) current will flow equally in both directions. But applying a potential  $V$  to one metal electron, will be driven in one way (see Figure 2.12).

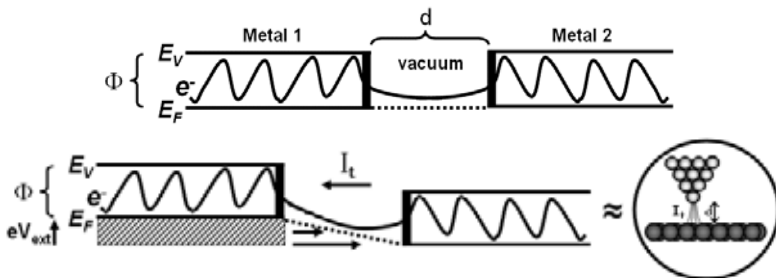


Figure 2.12. Scheme of a two metallic surfaces keep in quasi-contact at the same energy (up) and applying an external potential (down).

With metal 1 negative with respect to metal 2 (as above) tunneling occurs from filled states within  $V(\text{ext})$  of EF in metal 1 to empty states at EF in metal 2, while with metal 1 positive with respect to metal 2 tunneling occurs from filled states within  $V(\text{ext})$  of EF in metal 2 to empty states at EF in metal 1. This simple model permits, in a first approximation, to describe tunneling within the metallic tip of the microscope and the investigated metallic surface. In STM, the barrier can be approximated by the average workfunction of sample and tip:

$$\Phi' \approx (\Phi_{\text{sample}} + \Phi_{\text{tip}}) / 2 \quad (\text{Eq. 2.7})$$

Moreover we can consider  $eV \ll \Phi'$  then:

$$k \approx \sqrt{2m(\Phi')} / \hbar \quad (\text{Eq. 2.8})$$

The final expression for the tunneling current is given by:

$$I_t \propto \sum_{E_N = E_F - eV}^{E_F} |\Psi(0)|^2 e^{-2kd} \quad (\text{Eq. 2.9})$$

This relation evidences the well known exponential dependence of the current on the tip-sample distance in STM that is at the basis of the high vertical resolution of STM. Combined with the high accuracy of the positioning of the tip parallel to the surface, images with a corrugation amplitude smaller than  $0.01 \text{ \AA}$  can be obtained reaching without any kind of problem the atomic resolution on metallic surfaces.

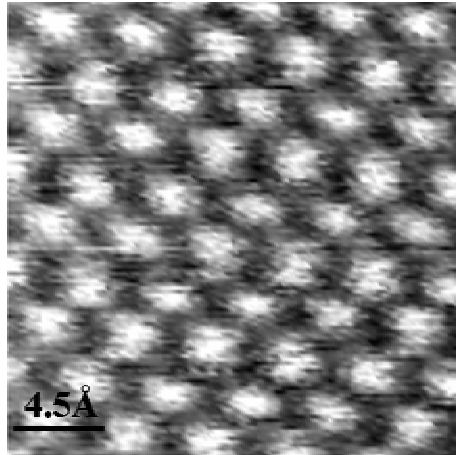


Figure 2.13. Room temperature STM image of High Ordered Pyrolytic Graphite with atomic resolution.

In Figure 2.13 for instance High Ordered Pyrolytic Graphite (HOPG) atomic resolution imaging is shown. This sample is considered as one of the easiest surfaces to be scanned and in fact it is used for short range calibration of the scanner in  $x$ - $y$  direction while  $z$  direction is usually calibrated using a step of evaporated gold that will be described in the following Chapter.

The so-called HOPG atomic resolution however does not correspond to the real surface atomic structure of the graphite since every second atom in the hexagonal surface unit cell remains hidden, and STM images show only a single atom in the unit cell (Hembacher S. et al. 2003). This is due to the fact that actually the STM contrast origins from the electronic structure of both the surface and the tip. In fact tunnelling is sensitive to a convolution of filled (empty) density of State of the tip and empty (filled) density of states of the surface depending on the applied bias voltage (Chen C.J. 1993).

For this reason only examining uncontaminated metallic surfaces we can build a direct relationship between topography and electronic structure of the investigated surfaces. Considering semiconductor as well as metallic surfaces “contaminated” by different atoms or by molecules, this direct relationship and obviously the linear dependence within applied voltage and tunneling current is lost. For this reason the interpretation of STM images on such surfaces must be carried out with care. However this increase of difficulties permits to achieve more information concerning, for instance, molecules deposited on surface. By exploring the dependencies of the tunneling current on the applied bias voltage it is possible to observe different features of the surface. In the case of deposited molecules on surface (Gimzewski J. K. et al. 1987) this corresponds to a tunneling process in which different molecular orbitals of the molecules are involved Grobis M. et al. (2002); Lu X. et al. 2003.

Obviously this kind of investigation requires an absolute control of the purity of the surface as well as the absence of contaminants in the tunneling junction. For this reason this kind of studies and the characterisation of the behaviour of the tunneling current dependence on the applied voltage (Scanning Tunneling Spectroscopy, STS technique; Wiesendanger R. 1994) must be carried out under ultra high vacuum conditions, at very low temperature and usually with evaporated molecules. On the contrary, by investigating samples obtained ex-situ on air, all these effects increase the difficulties and hamper the extraction of complete information. Nevertheless they provide partial information and can evidence interesting effects that require UHV set-up to be completely characterized.

During this thesis work a commercial standard room temperature STM apparatus has been used. The mainly used STM is a P47-Pro system (NT-MDT, Zelenograd, Moscow, Russia) that allows to investigate conductive samples also under nitrogen saturated environment. This apparatus is equipped with two STM heads, a standard one, characterised by one amplification configuration for tunneling currents of the order of nA and a customised head for lower tunneling current (up to 3pA). This last set-up is essential for imaging of molecules adsorbed on surfaces that in some cases can be moved or destroyed by higher tunneling currents employed during the scanning (Kim J. et al. 2003).

Tips used in this thesis work have been mainly prepared by mechanically cutting of a Pt/Ir 90:10 wire. This procedure allows to easily prepare nice atomically sharpen probes without problems of oxidation of their surface. Cutting is made at an angle of

about  $45^\circ$  with simultaneous tension of the wire to tear it apart. The applied stretching force produces a plastic deformation of the wire (Figure 2.14a). Another preparation technique we tried to use was the electrochemical etching, which we successfully employed with both Pt/Ir (Figure 2.14b) and W wires following indications retrieved in the literature (Knapp H. F. and Guckenberger R. 1998). Etching is made by feeding a current through the wire and an electrolytic solution that is selected on the basis of the material of the wire.

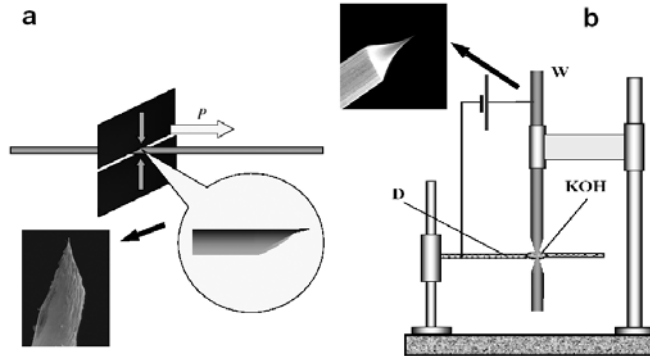


Figure 2.14. Preparation of the tips using mechanical cutting (a) and electrochemical etching (b). From Mironov V. L. 2004, copyright (2004) NT-MDT. On the inset are presented SEM images of prepared tips.

In both cases the goal is to achieve a sharpening of the tip. Advantages of the second method are the reproducibility of the preparation as well as the high aspect ratio achievable that reduces the problems connected to the mechanical stability of the tip. We have however preferred to use the mechanical method due to its rapidity as well as the higher quality of the results obtained.

Scanning conditions are usually defined depending on sample characteristics. For samples with high roughness the feedback circuitry is fundamental. The image in this case will be obtained keeping the value of tunneling current constant by varying the distance between the tip and the sample (*constant current mode*, Figure 2.15a). If the samples is really flat it is possible to open the feedback loop and perform a faster scan directly monitoring the variation in the tunneling current (*constant height mode*, Figure 2.15b). In this case a better resolution is easily achieved.

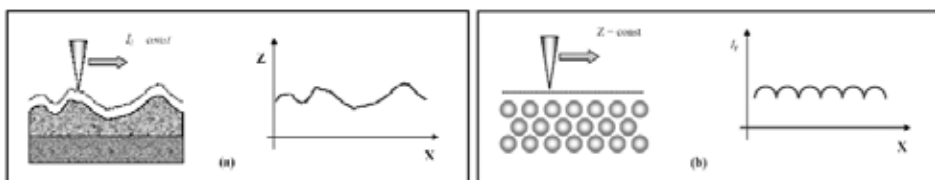


Figure 2.15. STM scanning modes: constant current mode (a) and constant height mode (b). From Mironov V. L. 2004, copyright (2004) NT-MDT.

In this thesis work both modes have been employed: the former in order to achieve the higher statistics of explored areas with height mode and then, while the latter to obtain at a second stage a higher spatial resolution. However we observed that, in our experimental setup, the most important parameter for scanning molecules was the use of the lower current detection head that represented, as we will explain in next chapters, the key point in the imaging of adsorbed molecules on surface.

### 3.2 Atomic Force Microscopy

The introduction of the Atomic Force Microscopy (Binnig G. et al. 1986) followed in a short time the invention of STM. This newer set-up permitted to investigate non conductive surfaces achieving in some case the atomic resolution too (Hembacher S. et al. 2003).

In this case the measured physical properties are the interaction forces between a sharp tip and the sample surface; this allows investigations on insulators and semi-conductors as well as on electrical conductors (Howland R. and Benatar L. 2000; Giessibl F. J. 2003).

The AFM probes the surface of a sample with a sharp tip, a couple of microns long and characterised by a curvature radius of 10-50 nm. Preparation of these tips is a quite complex process involving photolithography, ion implantation, chemical and plasma etching phases (Mironov V. L. 2004). Usually these probes are made by silicon or silicon nitride and can be coated with different metals (Pt, Co, W, Au etc.) as well as with molecules (usually a sort of self assembled monolayer of thiols on a Au pre-coated tip). This large variability has strongly influenced the evolution of this technique permitting to access special kind of interactions or different properties. In the most common configuration, the tip is located at the free end of a cantilever that is 100 to 200  $\mu\text{m}$  long (see Figure 2.16) and acts as a spring that bends when the tip interact with the surface.

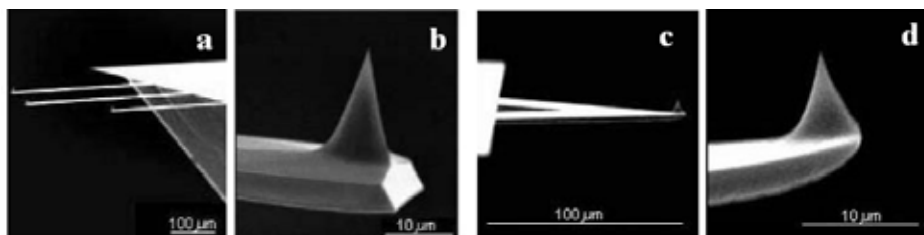


Figure 2.16. SEM images of silicon AFM tips: rectangular tips (a,b), and triangular tips (c,d).

Detected forces between the tip and the sample surface are in the range of 1 pN to 1 nN and induce a bending in the range 1-100  $\text{\AA}$ . In order to detect the deflection of the cantilever different approaches have been used: the first one was based on the use of an STM tip by exploiting the exponential dependence of tunneling current with the distance (Figure 2.17a); another way is based on the interferometry effect obtained by the reflection of a laser beam transmitted from (and to) the tip through an optical fiber (Figure 2.17b). However the most commonly used technique is based on the use of the optical lever principle (Figure 2.17c).

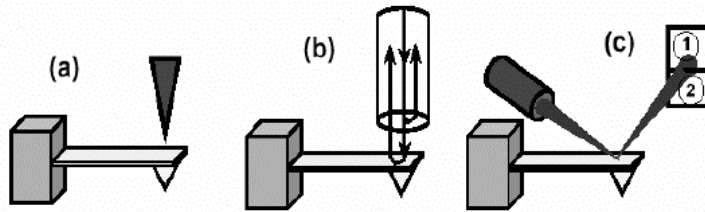


Figure 2.17. Detection of tip deflection via: (a) STM tip; (b) Laser interferometry (c) Beam deflection. From Mironov V. L. 2004. Copyright (2004) NT-MDT.

In the laser deflection set-up, a laser beam bounces off the back of the cantilever onto a position-sensitive photodetector: as the cantilever bends, the position of the laser beam on the detector shifts. The detector measures the cantilever deflection as the tip is scanned over the sample or the sample is scanned under the tip. The measured cantilever deflection allows to generate a map of surface topography.

The interaction forces in the AFM are often quite complex due to several factors. In contrast with STM where the tunneling current originates essentially from the first atom of the tip, with AFM several atoms contribute to the interaction, even if the tip apex is monoatomic, due to long-range forces. Moreover forces are strongly dependent on the medium surrounding the tip, which can be a gas, a liquid or vacuum. Finally, the tip can deform the sample.

Typically several forces contribute to the deflection of an AFM cantilever. The force most commonly associated with atomic force microscopy arises from Van der Waals interactions (Mironov V. L. 2004). The dependence of the Van der Waals force upon the distance between the tip and the sample is shown in Fig.2.18.

Different regimes depending on the distance can be encountered. In the contact regime, the cantilever is held less than a few angstroms from the sample surface, and the interatomic forces between the cantilever and the sample are repulsive. In the non-contact regime, the cantilever is held tens or hundreds of angstroms from the sample surface and the interatomic forces between the cantilever and the sample are attractive (largely a result of long-range Van der Waals interactions).

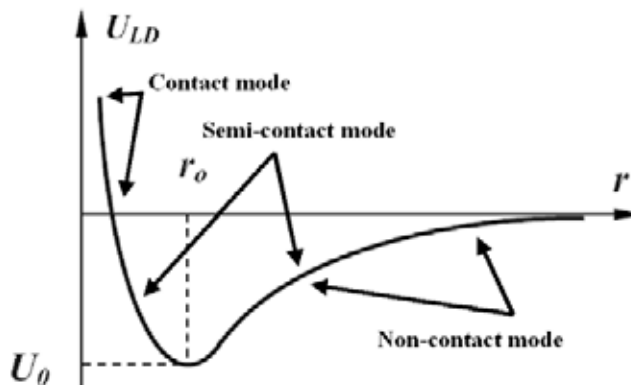


Figure 2.18. Interatomic potential versus distance curve. From Mironov V. L. 2004. Copyright (2004) NT-MDT.

In contact-AFM mode, also known as repulsive mode, an AFM tip makes soft “physical contact” with the sample. As the scanner gently traces the tip across the sample (or the sample under the tip), the contact force causes the cantilever to bend to accommodate changes in topography. Once the AFM has detected the cantilever deflection, topographic data are generated, similarly to the STM, in two modes: the *constant height* or the *constant force* mode. In constant-height mode, the spatial variation of the cantilever deflection is used directly to generate the topographic data set. In constant-force mode, the deflection of the cantilever is used as an input to the feedback circuit keeping the cantilever deflection constant.

Non-contact AFM (NC-AFM) is the first of several vibrating cantilever techniques in which an AFM cantilever is vibrated near the surface of a sample (Giessibl F. J. 2003; Garcia R. and Perez R. 2002). NC-AFM provides a means for measuring sample topography with little or no contact between the tip and the sample and very low interactions (the total force between the tip and the sample in the non-contact regime is about  $10^{-12}$ N). This low force is advantageous for studying soft or elastic samples. In this mode, the system vibrates a stiff cantilever near its resonant frequency (typically from 100 to 400 kHz) with an amplitude from a few tens to hundreds of Angstroms. Then changes in the resonant frequency or vibration amplitude are detected as the tip comes near the sample surface. The system monitors the resonant frequency or vibrational amplitude of the cantilever and keeps it constant with the aid of the feedback thus maintaining the same tip-sample average distance.

If a few monolayers of condensed water are lying on the surface of a sample, for instance, an AFM operating in contact mode will penetrate the liquid layer to image the underlying surface but with strong friction problems, whereas in non-contact mode an AFM will image the surface of the liquid layer without exploring the real sample surface.

Intermittent-contact (or Semi-contact) mode solves the problem of water layer: this mode is similar to non contact, but in this case the tip is brought closer to the sample so that at the bottom of its travel it just barely hits, or “taps”, the sample. With this mode lateral forces (friction) between the tip and the sample are eliminated reducing problems compared to the contact mode.

Recently another operation mode has been presented. In this mode a topography of the surface is recorded first with one of the previous techniques, then the tip is lifted far away from the surface and following the already investigated profile is kept in oscillation. In this way long range interaction (magnetic and electrostatic for instance) contributions are isolated and detected. This has led to the evolution of the AFM technique into magnetic force microscopy (MFM) as well as into electrostatic force microscopy EFM set-up that can be realized by simply replacing the tip (Martin Y. et al. 1987).

In this thesis we have mainly used again the P47-Pro apparatus equipped with an AFM head that permits to work in all the modes described above. Investigation of ultrathin films has been carried out principally in intermitted contact mode due to the lower damaging of the samples.



## Chapter 3

### Deposition processes

The potentiality of scanning probe microscopies enabled a revival in the interest on surface passivation phenomena. The molecular “dirt” present on a metallic surface can finally be “seen” and, as previously described, the more traditional surface techniques can usefully complement the information obtained by SPM.

The adsorption of molecules on surfaces is a complex phenomenon; a simplified classification distinguishes between *physisorption*, where the adsorbate preserves its electronic structure, and *chemisorption* where some modification of electronic levels of the adsorbate occurs due to a strong interaction with the surface. In the former the enthalpies of interactions are significantly lower ( $\Delta H < 10 \text{ kcal/mol}$ ) than in the chemisorption process ( $\Delta H > 10 \text{ kcal/mol}$ ) (Zangwill A. 1988).

Here we are mainly interested in the capabilities of chemisorption. Selective interactions within some kind of molecule and a specific surface can be exploited with a wet chemical approach to *functionalize* surfaces with one layer of molecules. If these molecules are characterized by a specific property then it is ideally “transmitted” to the nanostructure providing a functionalized material.

In this Chapter we will briefly describe the method used to deposit molecules on surfaces to obtain ultrathin films with monolayer thickness control. Before describing these basic techniques an overview of the methods of preparation of metallic surfaces on which these films are grown is provided.

#### 1. Evaporation techniques

The first step in the investigation of a layer of molecules is that of acquiring a full control of the “cleanness” of the surface. Moreover this surface should be sufficiently flat over a large area, not easily degradable and preferably a good conductor to allow the use of scanning tunneling microscopy (STM).

The easiest and cheapest way to obtain a clean surface is the evaporation in high vacuum conditions of metallic gold on a different surface (*substrate*) that act as support.

The exploited procedure is a *thermal evaporation*, a physical vapour deposition (PVD) process for depositing a thin film of metal on the surface of a substrate (Fig. 3.1). This process works by heating a metal in a vacuum chamber ( $< 10^{-6} \text{ mbar}$ ) to a temperature high enough for the vapour pressure of the metal to become significant. The substrates for coating are placed inside the chamber, above the evaporation source. Once enough metal has evaporated, it will begin to condense on the surface and form a layer. The metal to be evaporated is placed in a crucible (usually made by

W) and a current is passed through it. The current heats the crucible and subsequently the metal forms a gas and fills the chamber.

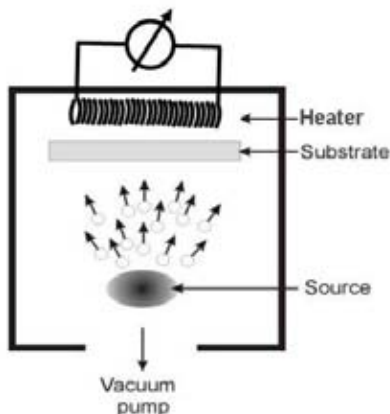


Figure 3.1. Scheme of a metal evaporator.

In the specific home-made setup we have used, in collaboration with Dr. G. D. Aloisi of the University of Florence, the growing gold film has been monitored with a quartz crystal microbalance (QCM) by measuring the change in frequency of oscillation that has been correlated to the increasing thickness of the growing layer. Moreover in this setup a back-heating of the substrate is carried out in order to promote the diffusion of gold thus achieving big terraces of deposits instead of small islands.

Freshly cleaved surfaces of muscovite mica, a yellowish, light-coloured, silicate (phyllosilicates) mineral with approximate composition  $K_2Al_4Si_6Al_2O_{20}(OH,F)_4$ , are usually employed as a substrate for this evaporation. Mica is stable and inert to water, acids (except hydrofluoric and concentrated sulphuric acids), alkalis, conventional solvents and oil. It is a hard and crystalline (monoclinic) material that has a layered structure of aluminum-silicate sheets weakly bonded together by layers of potassium ions. The potassium ions occupy large holes between 12 oxygen atoms, 6 from the layer above and 6 from the layer below; the resulting K-O ionic bonds are rather weak and easily broken (Fig 3.2). The cleavage sheets are fairly flexible and elastic, hydrophilic, and negatively charged in water. Muscovite Mica has low iron content and is a good electrical and thermal insulator.

During the evaporation of gold the back-heating of the mica must be carried out also to achieve the desorption of water molecules from its surface; in this way, peeling-off problems occurring when the gold on mica slide are immersed in solution are avoided.

In figure 3.4(a) an STM investigation of the gold surface obtained in these conditions is shown.

Different substrates are also used. In particular during this thesis work we have employed silicon wafer and glass slides as solid supports. In both cases, an adhesive *underlayer* of Cr or Ti or Al must be added to the surface before the deposition of gold.

In general, further treatments are then required in order to improve the cleanliness as well as the quality (in terms of flatness) of the deposited gold layer. Usually these treatments are ruled out by a *flame annealing* procedure (Dishner M. H. et al. 1998).

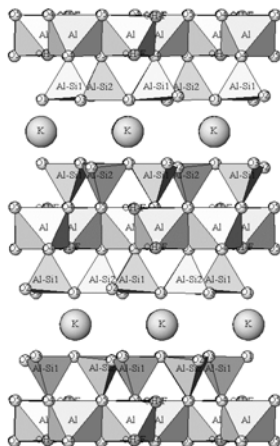


Figure 3.2. Structure of muscovite mica. Courtesy of K. Nomura (2002).

In this procedure a hydrogen flame is used to heat evaporated gold to obtain, in a clean environment, the annealing of the surface. This corresponds to a superficial melting that induces the reconstruction of the surface: flattening of the surface as well as the formation of triangular features are thus observed. The latter structures have their origin in the fact that with this procedure the Au(111) face is reconstructed starting from the original face epitaxially grown on the mica surface; the misfit between gold and mica induces the formation of triangular dislocations.

Flame annealing is most effective when performed with a “reducing flame” and permits the removal of moderate amounts of contaminants from the surface of gold films. Usually a subsequent cleaning with pure ethanol follows this annealing. The results obtained using this procedure are apparent by comparing the gold surface morphology before and after this treatment presented in Figure 3.4.

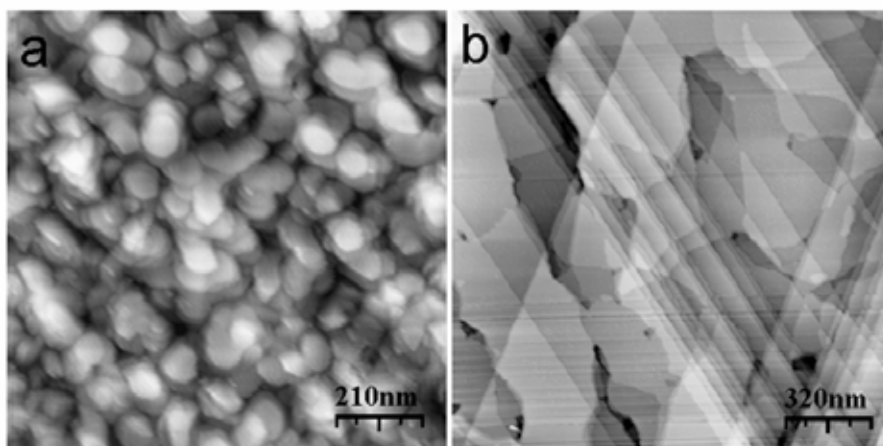


Figure 3.4. STM images of gold deposits evaporated on mica before (a) and after (b) hydrogen flame annealing.

We have experimented also different cleaning procedures, like chemical etching methods (Guiseppi-Elise A. 2000) as well as flame annealing with butane and with ethanol. Chemical etching has been employed with success with gold evaporated on silicon and glass with a Ti underlayer. In fact during the fame annealing procedure atoms of the Ti underlayer migrate contaminating the surface. Different flame annealing has been used when a hydrogen source was not available. However comparing different results we found that the flame annealing with hydrogen provides the highest quality surface and therefore we employed this procedure in most parts of this thesis work.

Evaporation techniques are also used to deposit molecular films on surfaces. This procedure provides good samples to be observed for instance with STM, however it is completely incompatible with our materials and therefore we will skip their description.

## 2. Drop-casting method

The easiest wet chemical method to produce thin layers of molecules is the *drop casting* method that trivially consists in dissolving a molecule in a volatile solvent, in dropping a specific amount of this solution on the surface and letting the solvent to evaporate. If the solvent has been selected (considering its polarity) by taking into account the hydrophobic nature of the surface a complete wetting of the surface is achieved. If very dilute solutions have been used, it is statistically possible to achieve a homogeneous deposition. Obviously the interaction between the surface and molecules must be larger than intermolecular interaction in order to avoid clustering problems. Generally these interactions are non specific and no real chemical bonding occurs between surface and molecules and correspond to the earlier described physisorption process.

It's important to underline that using this method only average control is possible and local images by STM become definitively unrepresentative of the effective characteristics of the deposited film. We used this method to produce thick film layers of molecules in order to obtain useful standards for comparison with monolayer deposits prepared using different procedures that will be described in the following paragraphs.

## 3. Self-Assembling of Monolayer technique

A chemisorption process allows a higher control of the deposition: molecules chemically linked to a surface can selectively form a monolayer. This fact is exhaustively exploited in *Self-Assembling of Monolayers* (SAMs) technique (Schreiber F. 2000; Ulman A. 1991; Ulman A. 1996; Bigelow W. C. 1946). This technique permits to deposit ordered monolayers of molecules on the surface. The structure of the employed molecule is at the basis of this process: the spontaneously occurring interaction between the surface and an *headgroup* (chemical functionality with a strong affinity for a specific substrate) is strong enough to form either polar covalent or ionic bonds with the surface, while lateral interactions (obtained by a *spacer unit*) between

adjacent molecules permit a real assembly of these molecules in a bidimensional structure. The terminal functional group (*end-group*) of a SAMs plays a critical role in the assembling and influences interfacial properties of the surface as for instance the hydrophobic/hydrophilic character, the adhesive characteristics and reactivity. In Figure 3.5 we summarize the characteristic moieties of molecules suitable for self assembling from solution while in the inset the most typical combinations between linking groups and surfaces are presented.

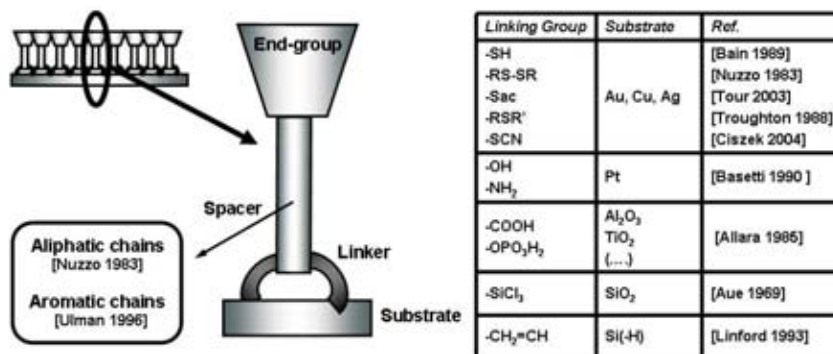


Figure 3.5. Typical scheme of molecules for SAMs.

Generally, self-assembling occurs in a two step reaction (Ulman A. 1996): when the selected substrate is soaked in a solution (usually  $10^{-3}$ M) containing molecules functionalized with a specific linker group, an interaction with surface rapidly occurs; then a slower organization that permits the bidimensional ordering is achieved. After the formation of this deposit the functionalized slide can be extracted from the solution and cleaned with pure solvents that remove the physisorbed material like contaminants and excess of depositing molecules.

From the previous scheme it is evident the versatility of this approach that allows to use different substrates, linkers and spacer groups in function of the desired active head that we would like to deposit on a specific support. In particular, the use of pre-functionalized complex molecules is very appealing as well as the ability to perform chemical reactions on surface using the pendant functional groups. This is the key to introduce on surface any kind of active groups and is at the basis of the continuing interest in the development of this technique.

We focus our description on a particular class of SAMs, the one based on sulphur derivatives as linker group and gold as substrate for the assembling that we have employed during this thesis work.

Sulphur compounds have a very strong affinity for transition metal surfaces. The number of reported organo-sulphur compounds that forms monolayers on gold has increased in recent years. These include, among others, di-n-alkyl sulphide (Troughton E. B. et al. 1988; Katz E. et al. 1992), di-n-alkyl disulphide (Nuzzo R. G. and Allara D. L. 1983), alkylmercaptanes (Bain C. D. et al. 1989), arylmercaptanes (Jin Q. et al. 1999), poliphenylmercaptanes (Ulman A. 2001), thiophenols (Sabatani E. et al. 1993; Bryant M. A. et al. 1992), mercaptopyridines (Bryant M. A. et al. 1992), mer-

captoanilines (Hill W. and Wehling B 1993), thiophenes (Li T. T.-T. et al. 1984), xanthates (Ihs A. et al. 1993), thiocarbaminates (Arndt Th. et al. 1989), thiocarbamates (Mielczarski J. A. and Yoon R. H. 1991), thioureas (Edwards T. R. G. et al. 1989), mercaptoimidazoles (Arduengo A. J. et al. 1990).

Organo-sulphur compounds coordinate very strongly also to silver (Ulman A. 1989), copper (Walczak M. W. et al. 1991), platinum (Shimazu K. et al. 1994), and other surfaces. However, the most studied, and probably best understood SAMs are those of n-alkanethiolates and related molecules on Au(111) substrate, the most used substrate that represents a testing ground for studying deposition of functionalized surfaces.

The surface structures formed by the adsorption of n-alkanethiols on gold substrates are generally well ordered and crystalline (Fig. 3.6). Upon exposure of a gold substrate to such a thiol either in relatively dilute solution (generally  $\sim 10^{-3}$  M) (Ulman A. 1992) or in the gas phase (Poirier G.E. 1997), a bond between gold and sulphur ( $\sim 60$  kcal/mol) rapidly forms, typically within seconds to minutes, by the end of which the thickness of the layer is about 80-90% of its maximum. In the next few hours is the close-packing of the hydrocarbon tails into a primarily all-trans configuration follows, thus contributing to a significant amount of order of the assembly. At the end of this slow step the thickness of the layer reaches its final value (Tripp C. P. and Hair M. L. 1995). The film growth is blocked when the surface is completely passivated by adsorbed molecules achieving a monomolecular thickness. The initial step, described by a diffusion-controlled adsorption process, was found to strongly depend on thiol concentration. At 1 mM solution the first step was over after  $\sim 1$  min, while it can require over 100 min at  $1\mu\text{M}$  concentration (Bain C. D. et al. 1989). The second step can be described as a surface crystallization process, where alkyl chains get out of the disordered state forming a two dimensional crystal. Therefore, the kinetics of the first step is governed by the surface - head group reaction, and the activation energy may depend on the electron density of the adsorbing sulphur. On the other hand, the kinetics of the second step is related to chain disorder, chain interaction and the surface mobility of chains. It was also found that the kinetics is faster for longer alkyl chains, probably due to the increased Van der Waals (VDW) interactions (Bain C. D. et al. 1989). Studies also showed pronounced differences between short ( $n < 9$ ) and long ( $n > 9$ ) chains. This is probably due to a decreased rate of the second step resulting from the decrease of the interchain VDW attraction energy.

The mechanism (Ulman A. 1996) leading to the formation of SAMs from alkanethiols may be considered as an oxidative addition of the S-H bond to the gold surface, followed by a reductive elimination of the hydrogen:



X-ray Photoelectron Spectroscopy (XPS) (Porter M. D. 1987), Fourier Transform Infrared (FTIR) spectroscopy (Nuzzo R. G. et al. 1987), electrochemistry (Li Y. et al. 1992), ToF-SIMS (Graham D. J. and Ratner B.D. 2002) and Raman Spectroscopy (Widrig C. A. et al. 1991) demonstrated that the adsorbing species is the thiolate (RS-) group.

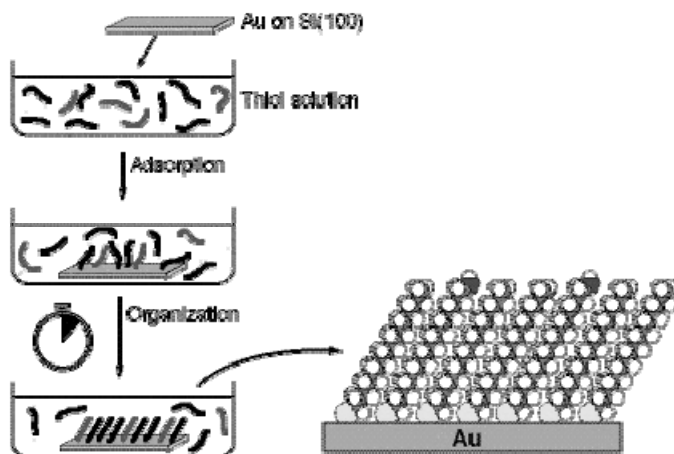


Figure 3.6. Scheme of an *n*-dodecanethiolate monolayer self-assembling process on an atomically flat gold substrate. Courtesy of P. Tengvall (2000).

The physical structures and chemical properties of *n*-alkanethiolate SAMs adsorbed on gold surfaces have been studied by many techniques to determine the macroscopic characteristics of the monolayer; complementary local probe techniques yield a comprehensive picture of the SAM. From the early 1990s, Scanning Tunnelling Microscopy (STM) studies of *n*-alkanethiolate SAMs on gold have shown their organization at the nanometre scale (Poirier G.E. 1997). But also earlier experiments (Strong L. and Whitesides G. M. 1988) demonstrated that usually the symmetry of sulphur atoms is hexagonal with an S-S spacing of  $4.97\text{\AA}$  and calculated area per molecule of  $2.14\text{\AA}^2$ , thus confirming that the structure formed by alkanethiolates on Au(111) is commensurate with the underlying gold lattice (Fig. 3.7) and described as  $(\sqrt{3}\times\sqrt{3})R30^\circ$ .

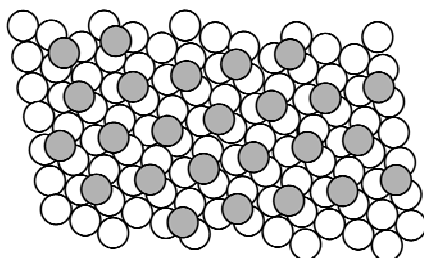


Figure 3.7. Hexagonal coverage scheme for alkanethiolates on Au(111). The open circles are gold atoms and the gray circles are sulphur atoms.

Different phases have been also noted and correspond to sub-saturation coverages (Poirier G. E. 1999); these different phases are observable (Larsen N. B. et al.

1997) also in films obtained with the micro-contact printing technique that will be discussed in the following paragraph.

A first, even if approximate, investigation of a SAM with STM usually provides evidence of the presence of a film on gold surface by evidencing a variety of local defects. Such defects, named “pinholes”, correspond to a one layer deeper portion of the gold surface that has been formed during the adsorption process by the etching of Au in the alkanethiol solution (Bucher J. P. et al. 1994; Edinger K. et al. 1997). The presence of these defects however can be ascribed also to different phenomena related to defects of the molecular lattice (Poirier G.E. 1997) including vacancies within the crystalline lattice and domain boundaries of the SAM, like tilt boundaries, stacking faults, rotational boundaries and antiphase boundaries. Figure 3.8 shows typical STM image of a SAM of n-alkanethiolates on Au(111).

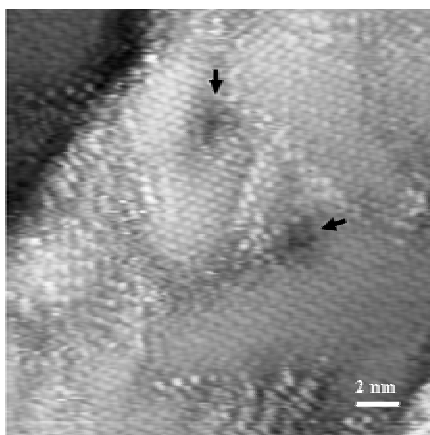


Figure 3.8. STM image of an n-decanethiolate self-assembled monolayer on Au(111) showing two pinholes defects (marked by the black arrows) and multi-domain features.

Alkanethiolate SAMs have been studied in extensive detail by a variety of methods and the ability to control the types, densities and distributions of defects in the final monolayer has continuously increased. The overall quality of the films allowed the possibility for further patterning, manipulation and post-adsorption processing, including the backfilling of defects with new adsorbates as well as their inclusion in the monolayer, these approaches paves the way to the characterization and manipulation of single molecules with STM.

In special case however the direct use of thiolates is undesirable due to chemical incompatibility with different functionalities present in the molecule that we plan to anchor to the surface. In these cases, as well as in the case a tuning of the interaction with gold surface is required, the thiol linker group can be replaced with different group exploiting the previous knowledge on thiols as a standard for these preparations. Sulphides has been widely used in this thesis work as alternative linker group due to their higher redox stability as well as to their smaller interaction with gold surface. Details concerning the grafting of this class of molecules are not summarized here but they will be provided in Chapter 6.

#### 4. Micro-contact printing technique

There is a way to couple the experienced local molecular ordering of SAMs with patterning features typical of lithographical techniques. This method is very inexpensive, simple, and permits to achieve patterned deposits of one layer of molecules chemically anchored to the surface. This technique is the *micro-contact printing* ( $\mu$ CP) technique, introduced by Whitesides group several years ago (Kumar A. and Whitesides G.M. 1993) as the earliest example of “soft lithography”, the family of techniques for constructing molecular architectures at the nanometre scales (Xia Y. and Whitesides G. M. 1998). These techniques consist on the use of soft elastomeric polymers to transfer and fabricate features onto surfaces without the assistance of energetic beams.

In particular  $\mu$ CP has grown in popularity due to the easiness of fabricating the printing tools, the relatively high spatial resolution of the produced features, and the large printing capacity. Patterning by  $\mu$ CP makes use of a *stamp* to transfer molecular ink to a hard substrate. The most commonly used material for the stamp is poly(dimethylsiloxane) (PDMS). A stamp is usually made by curing an elastomeric PDMS mixed with a specific amount of a curing agent and poured on a *master*, which usually consists of a silicon patterned surface obtained by photolithography or e-beam lithography that provide the desired final patterning structure. This stamp is warmed up to 60°C to facilitate the curing and then removed from the master. The stamp is ‘inked’ with a dilute solution of the adsorbates and brought into contact with a substrate. Transfer of ink occurs only in the contact areas between the stamp and the surface. The most commonly used *inks* for  $\mu$ CP are long chain alkanethiols which, when printed on gold, form a sort of self assembled monolayers directly in the contact areas. Moreover this method allows to deposit single layers of molecules (Wu X. C. et al. 2004), biomolecules (Thibault C. et al. 2005) and nanoparticles (Bae S.-S. et al. 2004) on a variety of substrates. In the case of the use of chemisorbed materials it is possible to clean the prepared sample by washing with pure solvents that remove contamination due to excess of material and different contaminating agents. After a drying phase with an inert gas the patterned surface has thus been obtained in a procedure that has been carried out in less then five minutes (if we consider that stamps can be used at least hundreds of times).

The complete procedure followed in preparation of the stamps as well as their use for  $\mu$ CP is sketched in Figure 3.9.

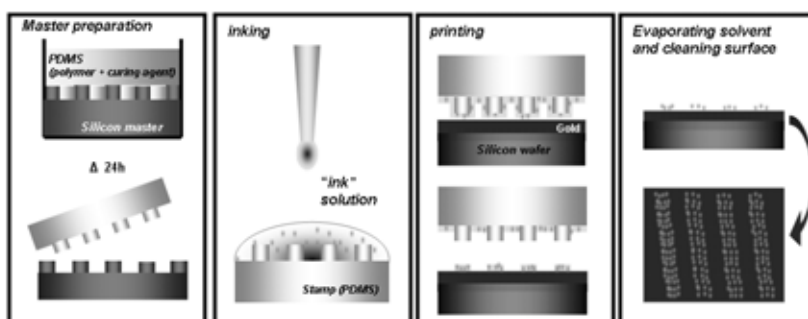


Figure 3.9.  $\mu$ CP technique schematic summary. (From left to right). Stamp preparation from a pre-patterned silicon master. Inking phase. Printing step. Evaporation and cleaning phases.

In the original preparation moreover an etching process followed the printing, in order to remove gold only on bare areas while protected by thiols areas conserved gold. Obviously this step is neglected with damageable printed materials, where the printed material become more interesting than the patterning itself.

A further widening of the  $\mu$ CP technique is achievable by the back-filling  $\mu$ CP technique, also known as a “molecular ruler” approach that consist in pre-patterning the surface with sample molecule and allowing a second kind of molecule to adsorb only on the bare areas (*back-filling procedure*) (Levi S. A. et al. 2001).

The  $\mu$ CP technique is attractive because it is generally cost-effective and inherently rapid, can be performed printing simultaneously many features with one stamp application and can be applied to many substrates and desired patterns. However, the quality and the resolution of the resulting patterns are dependent on a number of factors. The best lateral resolution of printed thiols depends on the pattern definition of the stamp, the amount of ink loaded onto the stamp, the pressure applied during printing, the printing time and the shape of the structures. Among these factors, ink diffusion plays a significant role in getting high-resolution patterns. Ink transfer to the non contacted areas is mainly due to vapour phase deposition and to ink diffusion along the surface from the areas of contact. When feature sizes are smaller than 400 nm, the ink diffusion is already significant enough to compromise the final resolution when using long chain alkanethiols as the ink. The width of the diffusion zone scales with the mobility of the molecules: use of linear alkanethiols with molecular weight increasing from dodecanethiol to hexadecanethiol, and up to eicosanethiol decreases both the vapour-phase transport and the surface diffusion of the ink during printing. Longer alkanethiols tend to form more disordered monolayers on gold and, in addition to their limited solubility, tend to crystallize at the surface of PDMS stamps.

Typical features that have been constructed are of the order of hundreds of nanometres to micrometers, although structures with dimension as low as 30 nm have been reported (Odom T.W. et al. 2002). Different ways of improving the resolution of the micro-contact printed patterns have been investigated, including the employment of stamps with increased stiffness, able to support smaller features (Schmid H. and Michel B. 2000), as well as the use of heavier inks like for instance dendrimers (Wu X. C. et al. 2004) to reduce the diffusion process of the transferred patterns.

## Chapter 4

### Syntheses of Single Molecule Magnets for deposition on gold surfaces

The research in depositing molecules that are interesting from a “magnetic” point of view has been the main purpose of this thesis. The deposition through wet chemistry has been selected as a powerful technique to explore the behaviour of series of compounds. Due to the selected deposition procedures many efforts have been devoted to optimize the synthetic process in order to introduce linkers to surfaces.

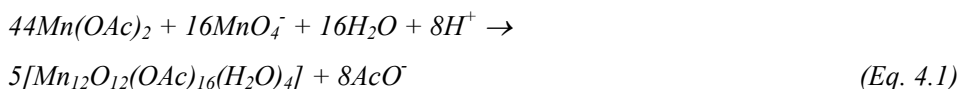
Our interest has been attracted by Single Molecule Magnets (SMMs) deposition for their unique behaviour, and the first attempts has been carried out on the class of compounds corresponding to the best known SMMs, the dodecamanganese (Mn<sub>12</sub>) clusters.

Before describing the synthesis of the final compounds used during this thesis we describe here briefly the synthesis of the earliest SMM focusing on its molecular structure, which is at the origin of its peculiar magnetic properties. We present also how it is possible to modify its external organic shell in order to introduce different functionalities (like anchoring capability) without changing its unique magnetic behaviour.

#### 1. The Mn<sub>12</sub>-acetate cluster and the general scheme of derivation

The first SMM,  $[Mn_{12}O_{12}(O_2CCH_3)_{16}(H_2O)_4] \cdot 2CH_3CO_2H \cdot 4H_2O$  (Mn<sub>12</sub>-acetate, 1) was obtained as an unexpected product by T. Lis in 1980 (Lis T. 1980). The magnetic properties of this compound started to be investigated only ten years later (Caneschi A. et al. 1991; Sessoli R. et al. 1993a).

At present the synthesis has been optimized and affords high yields of crystalline material (80%). It consists in a comproportionation reaction (Aromi G. et al. 1998; Brechin E. K. 2005) between a Mn<sup>VII</sup> source and a Mn<sup>II</sup> one in a 60% v/v AcOH-water mixture, as described by the equation:



The preparative method used by Lis is similar to that routinely employed in the synthesis of  $Mn(O_2CCH_3)_3 \cdot 2H_2O$  (Bush J. B. Jr. et al. 1968), but increasing the  $MnO_4^- / Mn(O_2CCH_3)_2$  ratio to a value appropriate for the average Mn oxidation state in Mn12 clusters.

The resulting cluster contains eight manganese(III) and four manganese(IV) ions connected by oxygen bridging atoms obtaining a disk-like structure. This structure is schematically depicted in Figure 4.1, and shows the crystallographic  $S_4$  symmetry of the molecule; the four manganese(IV) ions are located in the central cubane unit, which is surrounded by the ring of eight manganese(III) ions. The resulting core is held together by twelve  $\mu_3-O^{2-}$  ions and sixteen  $\mu$ -acetates, while the four water molecules provide terminal ligation to every second manganese(III) ion. The acetate bridges are partitioned into three chemically distinct sets, labelled with A, B and C in Figure 4.1. A-type and B-type acetates provide axial ligation to  $Mn^{IV}$ - $Mn^{III}$  and  $Mn^{III}$ - $Mn^{III}$  pairs, respectively, whereas C-type acetates bridge  $Mn^{III}$ - $Mn^{III}$  pairs equatorially, where axial and equatorial refer to the disk-like shape of the cluster. Notice that C-type acetates comprise two crystallographically-independent subsets, labelled with C' and C'' in Figure 4.1. All the constituent ions reside in distorted octahedral environments, the eight manganese(III) centres displaying a pronounced Jahn-Teller (JT) distortion by tetragonal elongation. The elongated Mn-O bonds involve exclusively axial acetate (A,B) and water ligands, so that the JT axes are essentially collinear with the unique  $S_4$  molecular axis. Such peculiar arrangement of the JT axes has important consequences on the magnetic properties.

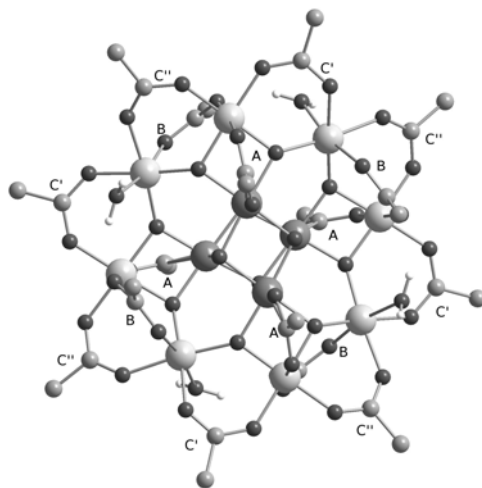


Figure 4.1. Structure of the  $[Mn_{12}O_{12}(OAc)_{16}(H_2O)_4]$  cluster in Mn12-acetate (1) viewed along the  $S_4$  axis, with the labelling scheme for acetate ligands. Atom code (size/grayscale):  $Mn^{III}$  = large/light-gray;  $Mn^{IV}$  = large/gray; O = medium/black; C = medium/light-gray; H = small/gray. Methyl hydrogen atoms omitted for clarity.

The crystal lattice of 1 also comprises non-coordinated water and acetic acid molecules, which are hydrogen bonded to the dodecamanganese unit. The acetic acid

molecules, in particular, are disordered over two equally-populated positions and determine a local symmetry lowering (Cornia A. et al. 2002a; Cornia A. et al. 2002b), as confirmed also by detailed spectroscopic investigations (Takahashi S. et al. 2004).

Mn12-*acetate* is soluble and perfectly stable in organic solvents such as acetonitrile and toluene. The  $^1\text{H-NMR}$  spectrum in acetonitrile, for instance, shows three resonances at 48.2, 41.8 and 13.9 ppm (vs tetramethylsilane) with integrated intensities in a 1:2:1 ratio. The signals arise from the  $\text{CH}_3$  groups of B-, C- and A-type acetates, respectively, and demonstrate that the solid-state structure is preserved in solution (Eppley H. J. et al. 1995).

The distinctive property of SMMs is the occurrence of magnetic hysteresis at low temperature (Caneschi A. et al. 1991; Sessoli R. et al. 1993a; Friedman J. R. et al. 1996; Thomas L. et al. 1996). When the magnetization of a single crystal of Mn12-*acetate* is measured at 2 K by applying the magnetic field along the tetragonal Z axis, the zero-field magnetization depends on the previous history of the sample (Figure 4.2). If the sample is first magnetically saturated in a 3 T magnetic field [1] and the field is subsequently reduced to zero, the magnetization is maintained essentially unaltered [2]. In order to bring the magnetization back to zero, a magnetic field exceeding 1 T (coercive field) has to be applied in the opposite direction [3]. By further increasing the applied field to 3 T, saturation is achieved again [4]. Switching off the field the magnetization largely persists [5], but now lies in the opposite direction as compared with [2]. Again, demagnetizing the system requires the application of a substantial field [6]. The resulting hysteresis loop [1]  $\rightarrow$  [2]  $\rightarrow$  [3]  $\rightarrow$  [4]  $\rightarrow$  [5]  $\rightarrow$  [6]  $\rightarrow$  [1] recalls the magnetic behaviour of bulk ferromagnetic materials, but the underlying physics is completely different. In fact, no long-range order is established in the crystal lattice due to the efficient magnetic shielding provided by the organic ligands which surround the cluster core.

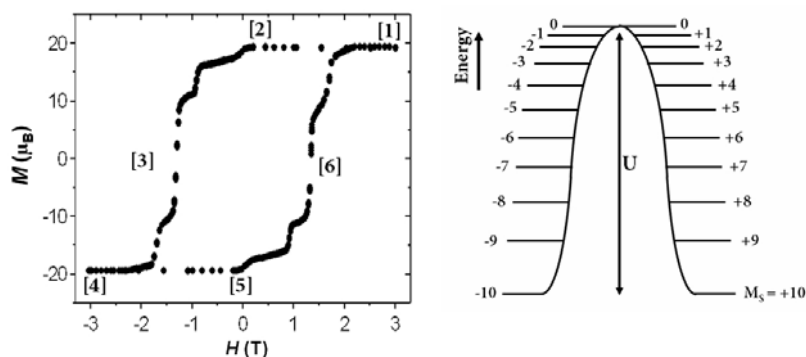


Figure 4.2. (Left) Hysteresis loop recorded at 2.1 K on a single crystal of Mn12-*acetate* (1), with the magnetic field directed along the tetragonal axis. (Right) Splitting of the  $S = 10$  ground spin state in Mn12-*acetate*.  $M_S$  is the quantum number. The arrows indicate the successive spin transitions required to overcome the anisotropy barrier  $U$ .

Rather, magnetic bistability originates purely from intramolecular magnetic interactions, as firmly established by dilution experiments (McInnes E. J. L. et al.

2002; Cheesman M. R. et al. 1997; Domingo N. et al. 2004). In essence, SMM behaviour arises from the association of a high-spin ground state with an easy-axis (i.e. Ising-type) magnetic anisotropy. In the vast majority of Mn12 complexes, superexchange interactions transmitted by the bridging oxide ligands result in a  $S = 10$  ground state, which can be pictorially (but not rigorously) described by arranging the  $\text{Mn}^{\text{III}} S = 2$  spins antiparallel to the  $\text{Mn}^{\text{IV}} S = 3/2$  spins (Robinson R.A et al. 2000).

The second ingredient required for SMM behaviour is an easy-axis anisotropy, which in Mn12 complexes is brought about by the manganese(III) ions. HF-EPR investigations on simple model complexes (Barra, A.-L. et al. 1997) have established that the JT elongation axis of manganese(III) corresponds to an easy magnetic direction for the  $S = 2$  spin. Since the eight JT axes in Mn12-*acetate* are roughly collinear, the local anisotropies sum up and determine a huge Ising-type anisotropy in the  $S = 10$  ground state of the molecule. The magnetic moment then preferably lies along the tetragonal axis and much less favourably perpendicular to it. In other terms, the energy of the  $2S + 1 = 21$  substates pertaining to the  $S = 10$  multiplet decreases with increasing  $|M_S|$  in a way most simply described by Equation 4.2:

$$E(M_S) = DM_S^2 \quad \text{and} \quad M_S = -S, -S+1, \dots, S-1, S \quad (\text{Eq. 4.2})$$

where  $D < 0$  is called the axial zero-field splitting parameter. Evidently, the total splitting of the multiplet is  $U = |D|S^2$  for integer  $S$  and  $|D|(S^2 - 1/4)$  for half-integer  $S$  (Figure 4.2).

Experimentally, at temperatures such that  $k_B T \ll U$  the magnetization relaxes with a characteristic time which follows the Arrhenius law:

$$\tau = \tau_0 \exp(U_{\text{eff}} / k_B T) \quad (\text{Eq. 4.3})$$

where  $U_{\text{eff}} \leq U$  is the effective anisotropy barrier. The value of  $\tau$  can be measured either in DC mode, i.e. by following the time dependence of the magnetization as the field is switched off, or more commonly in AC mode, i.e. by applying a small, oscillating magnetic field with frequency. When the condition:

$$\tau = (2\pi\nu)^{-1} \quad (\text{Eq. 4.4})$$

is fulfilled, the out-of-phase component of magnetic susceptibility,  $\chi''$ , reaches a maximum. Though equation 4.4 can be satisfied by varying  $\nu$  at constant  $T$ , in practice the temperature dependence of  $\chi''$  is measured for a set of different frequencies and the relaxation time  $\tau$  at the temperature of the maximum in  $\chi''$  extracted. When the results are plotted in the form of  $\ln \tau$  vs  $T^{-1}$ , the slope and intercept of the best straight line through experimental data points directly provide  $U_{\text{eff}}$  and  $\tau_0$  (62 K and  $2.1 \cdot 10^{-7}$  s in Mn12-*acetate*, Sessoli R. et al. 1993a). The activation parameters, and in particular the height of the anisotropy barrier, are distinctive features of Mn12 complexes and have been often used to probe their structural integrity in a variety of organic or inorganic matrices (Clemente-Leon M. et al. 2003; Schubert U. and Hüsing N. 2005; Gómez-Romero P. and Sanchez C. 2004).

From equation 4.3, it is clear that the relaxation time increases exponentially upon cooling. At sufficiently low temperatures, the relaxation of the magnetization becomes so slow that hysteresis appears (Figure 4.2). More generally, a characteristic temperature  $T_B$  exists for each investigation technique, below which the magnetization is blocked on the timescale of the experiment ( $T_B = 3$  K in SQUID measurements).

The temperature dependence of  $\tau$  in SMMs has been theoretically explained by Villain et al., who described thermally-activated magnetization reversal as step-by-step process driven by spin-phonon interactions (Villain J. et al. 1994). By successive exchange of phonons, the system undergoes the transition from  $M_S = -S$  to  $-S+1$ , to  $M_S = -S+2$ , etc. climbing up the ladder of states and then descending to  $M_S = S$  (Figure 4.2). Quite simply, the total splitting of the multiplet,  $U$ , can be perceived as an energy barrier which must be overcome for spin reversal to occur. For integer  $S$ , the pre-exponential factor  $\tau_0$  is given by the formula:

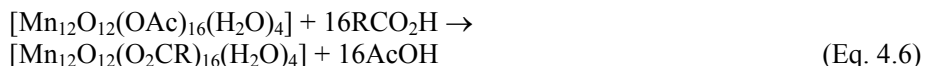
$$\tau_0^{-1} \approx \frac{1}{\hbar^4 c_s^5 \rho} \left| \langle \pm 1 | \widehat{\mathbf{V}}_{sp} | 0 \rangle \right|^2 (E_0 - E_{\pm 1})^3 \quad (\text{Eq. 4.5})$$

where  $c_s$  is the speed of sound in the material, whose density is  $\rho$ , and  $\widehat{\mathbf{V}}_{sp}$  is the Hamiltonian describing spin-phonon interaction. Due to the phonon distribution and to equation 4.2, the transitions between  $M_S = 0$  and  $M_S = \pm 1$  states at the top of the anisotropy barrier are the slowest ones and thus represent the rate-determining step of the whole relaxation process. For this reason,  $\tau_0$  depends exclusively on the energy separation between the  $M_S = 0$  and  $M_S = \pm 1$  states ( $E_0 - E_{\pm 1}$ ) and on the corresponding spin-phonon matrix element.

What makes SMMs unique magnetic systems, however, is the coexistence of classical and quantum mechanical mechanisms for spin reversal. In fact, beside the above-described thermally-activated process, spin reversal in SMMs may also occur by quantum tunneling of the magnetization (Friedman J. R. et al. 1996; Thomas L. et al. 1996; Gatteschi D. and Sessoli R. 2003). Whenever two states lying on opposite sides of the barrier have the same energy and are quantum-mechanically admixed, a direct under-barrier transition is in principle permitted. Quantum tunneling effects are indeed responsible for the stepped hysteresis loops of Mn12-acetate (Figure 4.2) and explain why the effective anisotropy barrier probed by relaxation measurements ( $U_{\text{eff}}$ ) is usually lower than  $U$ . Clearly, quantum tunneling effects are of paramount importance for an accurate description of SMM behaviour and their origin is among the most actively investigated topics in molecular nanomagnetism (Gatteschi D. and Sessoli R. 2003).

The investigation of subtle changes in the magnetic properties on small chemical and structural variations, as well as the introduction of new functions to graft these molecules on surfaces has required the modification of the external organic shells made of acetate groups in 1. The Mn12-acetate cluster easily undergoes ligand exchange reactions when treated with suitable carboxylate or other bidentate ligands. The total replacement of  $\text{AcO}^-$  groups has been widely exploited to access new homocarboxylate derivatives, like  $[\text{Mn}_{12}\text{O}_{12}(\text{O}_2\text{CPh})_{16}(\text{H}_2\text{O})_4]$  (Mn12-benzoate) (Ses-

solis R. et al. 1993b), the second member of the Mn12 family to be reported after Mn12-acetate:



In order to drive the equilibrium to the right, it is advisable to use a large excess of incoming ligand and to remove the produced acetic acid by azeotropic distillation with toluene that form a negative azeotrope which contains 28 wt% of the acid and boils at 100.6 °C at 1 atm vs 110.7 and 118.1 °C for pure toluene and acetic acid, respectively.  $\text{CH}_3\text{CO}_2^-$  can be substituted by  $\text{RCO}_2^-$  when the conjugate acid  $\text{RCO}_2\text{H}$  has a comparable or even smaller pKa than the acetic acid. It has been proven that a large variability of ligands can substitute the original acetate ones as shown in Table 4.1.

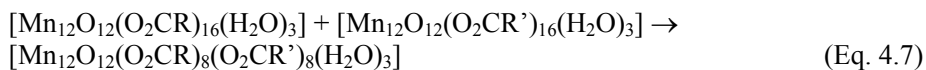
Table 4.1. Some Mn12 derivatives with reported structures. General formula  $[\text{Mn}_{12}\text{O}_{12}(\text{RCOO})_{16}(\text{H}_2\text{O})_x]$

R group / L <sup>a</sup>	x	Space group	Solvent. Molecules of crystallization	Water coord.	References
CH <sub>3</sub>	4	I $\bar{4}$	2CH <sub>3</sub> COOH ·4H <sub>2</sub> O	1:1:1:1	Lis T. 1980
CH <sub>2</sub> CH <sub>3</sub>	3	P $\bar{1}$	4H <sub>2</sub> O	1:1:1	Eppley H. J. et al. 1995
CH <sub>2</sub> CH <sub>3</sub>	3	P2 <sub>1</sub> /c		1:1:1	Aubin S. M. J. et al. 2001
CH <sub>3</sub> ; CH <sub>2</sub> CH <sub>3</sub>	4	I $\bar{4}$	2H <sub>2</sub> O ·4EtCOOH	1:1:1:1	Wei Y.-G. et al. (1997)
CH <sub>2</sub> C(CH <sub>3</sub> ) <sub>3</sub>	4	P $\bar{1}$	CH <sub>2</sub> Cl <sub>2</sub> ·CH <sub>3</sub> NO <sub>2</sub>	1:2:1	Sun Z. M. et al. 1998
CH <sub>2</sub> C(CH <sub>3</sub> ) <sub>3</sub>	4	P $\bar{1}$	CH <sub>2</sub> Cl <sub>2</sub> ·CH <sub>3</sub> CN	1:2:1	Soler M. et al. 2003
C <sub>6</sub> H <sub>5</sub>	4	P $\bar{1}$		2:0:2	Sessoli R. et al. 1993b; Boyd P. D. et al. 1988
C <sub>6</sub> H <sub>5</sub>	4	Fdd2	2C <sub>6</sub> H <sub>5</sub> COOH	2:0:2	Takeda K. et al. 1997
C <sub>6</sub> H <sub>4</sub> -p-CH <sub>3</sub>	4	C2/c	HO <sub>2</sub> C- C <sub>6</sub> H <sub>4</sub> -p-CH <sub>3</sub>	1:2:1	Aubin S. M. J. et al. 2001
C <sub>6</sub> H <sub>4</sub> -p-CH <sub>3</sub>	4	I2/a	3H <sub>2</sub> O	1:1:2	Aubin S. M. J. et al. 2001
C <sub>6</sub> H <sub>4</sub> -p-Cl	4	C2/c	8CH <sub>2</sub> Cl <sub>2</sub>	2:0:2	Aubin S. M. J. et al. 2001
C <sub>6</sub> H <sub>4</sub> -m-Cl	3	P $\bar{1}$	HO <sub>2</sub> C- C <sub>6</sub> H <sub>4</sub> -m-Cl	1:1:2	An J. et al. 2000
C <sub>6</sub> H <sub>4</sub> -o-Cl	4	Pnn2	CH <sub>2</sub> Cl <sub>2</sub> ·5H <sub>2</sub> O	1:1:2	Ruiz D. 1998
CH <sub>2</sub> -C <sub>6</sub> H <sub>5</sub>	4	P $\bar{1}$		1:2:1	Sun Z. M. et al. 1999
CHCHCH <sub>3</sub>	4	Ibca	H <sub>2</sub> O	2:0:2	Ruiz-Molina D. et al. 2002
CF <sub>3</sub>	4	P $\bar{1}$	2.5H <sub>2</sub> O	1:1:2	Gomez-Segura J. et al. 2005
CF <sub>3</sub>	4	I $\bar{4}$	2CF <sub>3</sub> COOH ·4H <sub>2</sub> O	1:1:1:1	Zhao H. H. et al. 2004
CF <sub>3</sub>	4	P2 <sub>1</sub> /n	CF <sub>3</sub> COOH ·7H <sub>2</sub> O	2:0:2	Zhao H. H. et al. 2004

R group / L <sup>a</sup>	x	Space group	Solvent. Molecules of crystallization	Water coord.	References
$CH_2Cl;CH_2C(CH_3)_3$	3	$P\bar{1}$	$CH_2Cl_2 \cdot H_2O$	2:0:1	Soler M. et al. 2001
$CH_2Cl;CH_2CH_3$	3	$P\bar{1}$	$CH_2Cl_2$	2:0:1	Soler M. et al. 2001
$CH_2Br$	4	I42d	$4CH_2Cl_2$	1:1:1:1	Tsai H. et al. 2001
$CH_2C(CH_3)_3/NO_3$	4	C2/c	$CH_3NO_2$	2:0:2	Artus P. et al. 2001
$CH_3/Ph_2PO_2$	4	$P4_2/n$	$12CH_2Cl_2$	1.1:1:1	Boskovic C. et al. 2001
$CH_3/PhSO_3$	4	$P\bar{1}$	$4CH_2Cl_2$	2:0:2	Chakov N. E. et al. 2003
$CH_3/CH_3SO_3$	3	Pbca	$3CH_3CNl_2 \cdot 4H_2O$	1:1:1	Kuroda-Sowa T. et al. 2004
$CH_3/Ph_2PO_2$	-	$P2_1/n$	$6.1 CH_2Cl_2 \cdot 0.4H_2O$	-	Bian G. Q. 2004
$C_6H_4-p-SCH_3$	4	$I\bar{4}$	$8CHCl_3$	1 : 1 : 1 : 1	Zobbi et al. 2005
$C_6H_5 / adc^b$	4	$I4_1/am$ d	$8CH_2Cl_2$	1 : 1 : 1 : 1	Pacchioni M et al. 2004

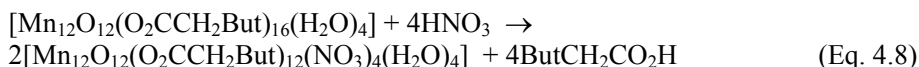
Notes: a) when appropriate L indicates the non carboxylate ligand. b) adc=10-(4-acetylsulphanylmethyl-phenyl)anthracene-1,8 dicarboxylic acid.

It is possible to exchange the acetate ligands of 1 using different procedures obtaining different derivatives with different chemical properties compared to the original Mn12-*acetate*. This provides, for instance, an increased solubility of these clusters in organic solvents and can also alter their redox potentials, significantly expanding the chemistry of this family of molecules. A whole family of Mn12 clusters featuring different carboxylate ligands has been synthesized and characterized, including mixed-carboxylate species. Heterocarboxylate species have been synthesized by ligand redistribution as for instance:



with (R = Et or CH<sub>2</sub>But and R' = CH<sub>2</sub>Cl) (Soler M. et al. 2001).

However, the simplest route to mixed-ligand Mn12 complexes involves treatment of a homocarboxylate with a stoichiometric amount of the proper incoming ligand by playing with the *pKa* of the ligand. This strategy proved to be successful for the introduction, among the others, of nitrates, sulphonates, phosphates and phosphinates as for instance:



Interestingly, the exchange reaction is usually site selective, i.e. the different ligands are located at specific sites rather than being disordered, thus allowing the preparation of derivatives with selective substitution of the original ligands. (Artus P. et al. 2001; Soler

M. et al. 2001; Chakov N. E. et al. 2003) This feature is due to the different reactivity of different ligand sites as a function of the strength of the carboxylate base. The weaker bases (lower  $pK_a$  for the conjugated acid) are most often found in B-type axial sites of Fig. 4.1, i.e. those bridging a pair of  $Mn^{III}$  ions, whereas stronger bases usually occupy A-type axial or C-type equatorial positions. The observed trend is ascribed to the strength of the ligand-to-metal interaction, which is minimal for B-sites due to the larger Mn–O distances along the  $Mn^{III}$  JT elongation axes.

Another important aspect of the reactivity of Mn12 complexes is their capability to be isolated in one- and two- electrons reduced forms (Eppley H. J. et al. 1995; Aubin S. M. J. et al. 1999; Kuroda-Sowa T. et al. 2001; Takeda K. and Awaga K. 1997).

The feasibility of chemically reduction of a Mn12 cluster was established by the observation of a reversible one-electron reduction process in the cyclic voltammogram. When the neutral Mn12 molecule with a  $S = 10$  ground state is reduced by one electron the reduced species exhibits SMM properties, the spin of the ground state of the anionic complex being a half-integer value of  $S = 19/2$  (Eppley H. J. et al. 1995).

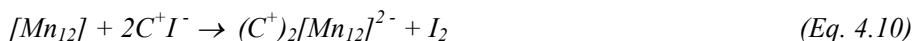
The chosen reducing agent was  $I^-$  because of its sufficient, mild reducing strength, its ready availability as a variety of salts of organic cations, and the high solubility of many of the latter in organic solvents. Indeed, chemical reduction of the Mn12 clusters with  $C^+I^-$  ( $C^+$  is  $NPr_4^+$ ,  $PPh_4^+$ , or  $PPN^+$ ) was found to provide a convenient route to the corresponding salts of the anions  $[Mn_{12}]^-$  in good yield:



The shape and volume of the inner  $[Mn_4O_4]$  cube remains essentially constant for all the complexes, including the one-electron reduced clusters. In fact the reduction yields valence-localized species with one of the external  $Mn^{III}$  ions being reduced to manganese(II). The identification of the reduced ion is easily made on the basis of the disappearance of the Jahn-Teller elongation.

Reduced complexes are thus a very unusual example of a complex with three different valence-trapped  $Mn^{II}$ ,  $Mn^{III}$ , and  $Mn^{IV}$  ions in the same molecule.

Moreover, using two equivalent of reducing agent it is possible to obtain two-electron (Soler M. et al. 2000) reduced Mn12 complexes that retain both a high ground state value ( $S = 10$ ) and the SMM properties of the  $[Mn_{12}]^{0-}$  species.



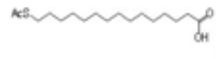
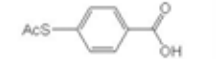
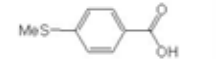
## 2. Mn12 sulphur-based derivatives

Recently these functionalizations techniques have been used to produce Mn12-derivatives suitable for binding to a suitable surface in order to obtain SMMs based materials (Cornia et al. 2006).

In this thesis we have mainly focused our interest on gold substrates and therefore we have proceeded through the synthesis of derivatives (Table 4.2) carrying a function able to covalently interact with the gold surface. In the remaining of this

chapter the synthesis and characterization of the Mn<sub>12</sub> derivatives employed in this thesis will be discussed.

Table 4.2. Mn<sub>12</sub>-sulphur based derivatives used in this work.

Ligand	Acronym of Mn <sub>12</sub> derivative	Reference
	Mn <sub>12</sub> LC15 (2)	Cornia A. et al. 2003
	Mn <sub>12</sub> PhSAc (3)	Heersche H. B. et al. 2006
	Mn <sub>12</sub> PhSMe (4)	Zobbi L. et al. 2005
	Mn <sub>12</sub> C10SC10 (5)	Mannini M. et al. unpublished data
	Mn <sub>12</sub> ADCSMe (6)	Pacchioni M. et al. 2004

## 2.1 Aliphatic acetyl-thio-derivative of Mn<sub>12</sub>

The first attempt of depositing a single layer of a molecular magnet on a conductive surface was performed in our research group before the start of this work (Cornia A. et al. 2003). In that work it was suggested to use the functionalizations of the Mn<sub>12</sub> with a protected mercapto-alkylic acid combined with the self assembling technique procedure. The same derivative compound has been used in this thesis for the preparation of patterned SMMs based surfaces by the use of a micro-contact printing technique (Mannini M. et al. 2005).

As the most investigated SAMs are based on the use of thiols for their strong interaction with the gold surface, the first attempts for anchoring SMMs on the Au(111) were based on a similar approach.

Theoretically the use of thiolic derivatives of carboxylic acids, in order to replace acetates in the Mn<sub>12</sub>, would permit the realization of clusters able to interact with the surfaces. Unfortunately the redox instability of the Mn<sub>12</sub> core in the presence of free thiols prevents this substitution reaction. Actually the formation of an insoluble residual (probably some manganese oxides) is evident after the addition of small amount of thiols to Mn<sub>12</sub> solutions.

To circumvent this problem we found in literature that it is possible to protect the thiol function through the formation of an acetyl thioester, and to promote an in-situ deprotection through a catalytic amount of ammonia. The deprotected thiols react with gold providing a covalently binding to metallic surface (Tour J. M. et al. 1995).

The first step of this preparation procedure thus consisted in the preparation of the alkylic carboxylate ligand functionalized with the protected thiol.<sup>1</sup>

Subsequently a ligand exchange reaction is used to obtain the thiol-protected functionalized clusters. The exchange reaction consists in treating a slurry of freshly-prepared 1 in toluene with 16 equivalents of HLC15SAc and removing the acetic acid via distillation of the azeotrope mixture with toluene. The details of the synthesis to obtain the Mn<sub>12</sub>LC15 derivative procedure are given in the footnote.<sup>2</sup>

The obtained cluster can be schematized as in Figure 4.3 but the presence of the long alkylic chains prevents their crystallization and thus a determination of the molecular structure through X-ray diffraction. Different investigation techniques have therefore been employed to confirm the ligand replacement.

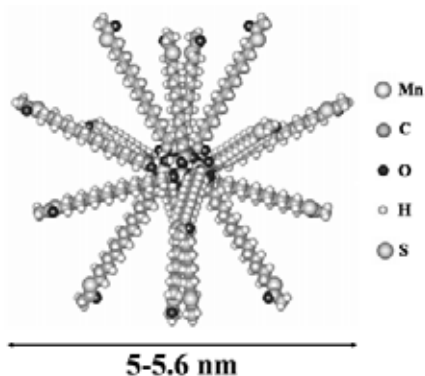


Figure 4.3. Structure simulation of 2.

<sup>1</sup> The 16-Mercaptohexadecanoic acid (HLC15SAc)(250 mg, 0.87 mmol) was dissolved in CH<sub>2</sub>Cl<sub>2</sub> (3 mL) and acetic acid (3 mL). Zinc powder (0.5 g) was added, and after 15 min (when di-sulphide was no longer detected by TLC), the now clear reaction mixture was cooled to 0 °C prior to addition of acetyl chloride (1.2 mL, 17 mmol). When the evolution of hydrogen gas ceased (5 min), the reaction mixture was allowed to attain room temperature. After 10 min, zinc was removed by filtration through celite, and the filtered organic solution was washed twice with aqueous HCl (0.1 M, 25 mL) mixed with ice. The solvent was evaporated, and the crude product was purified by flash chromatography (toluene/EtOAc 100:1 to 10:1) to give 245 mg (86%) of HLC15SAc as a white solid. <sup>1</sup>H-NMR (CDCl<sub>3</sub>): 2.86 (2 H, t), 2.34 (2 H, t), 2.32 (3 H, s), 1.7-1.4 (4 H, m), 1.3-1.2 (14 H, m); <sup>13</sup>C-NMR (CDCl<sub>3</sub>): 196.17, 180.03, 34.05, 30.67, 29.7-29.0, 28.82, 24.70.

<sup>2</sup> A slurry of freshly-prepared 1 (304 mg, 0.147 mmol) in anhydrous toluene (10 mL) was treated with HLC15SAc (819 mg, 2.478 mmol) and the solvent was distilled off under reduced pressure (50 mmHg). Additional azeotropic distillations were performed with toluene (10 mL, 80 mmHg; 2 x 10 mL, 100 mmHg). The residue was dissolved in CH<sub>2</sub>Cl<sub>2</sub>, the solution was centrifuged, and the solvent was evaporated to give 2 as a black lustrous solid (765 mg, yield 84%). Elemental analysis (%) calc. for Mn<sub>12</sub>O<sub>64</sub>C<sub>288</sub>H<sub>536</sub>S<sub>16</sub>: C 55.83, H 8.72, S 8.28; found: C 55.72, H 8.72, S 7.98. <sup>1</sup>H-NMR (toluene-*d*<sub>8</sub>): 47.5 [8 H; CH<sub>2</sub> (α, axial, Mn<sup>III</sup>-Mn<sup>III</sup>)], 46.2 [8 H; CH<sub>2</sub> (α, equatorial, Mn<sup>III</sup>-Mn<sup>III</sup>)], 43.1 [8 H; CH<sub>2</sub> (α, equatorial, Mn<sup>III</sup>-Mn<sup>III</sup>)], 13.9 [8 H; CH<sub>2</sub> (α, axial, Mn<sup>III</sup>-Mn<sup>IV</sup>)], 8.8 [8 H; CH<sub>2</sub> (β, axial, Mn<sup>III</sup>-Mn<sup>III</sup>)], 5.1 [8 H; CH<sub>2</sub> (β, axial, Mn<sup>III</sup>-Mn<sup>IV</sup>)], 2.8 [32 H; CH<sub>2</sub>S], 2.0 [48 H; CH<sub>3</sub>], 1.3 [384 H; CH<sub>2</sub>], -3.9 [8 H; CH<sub>2</sub> (β, equatorial, Mn<sup>III</sup>-Mn<sup>III</sup>)], -4.7 ppm [8 H; CH<sub>2</sub> (β, equatorial, Mn<sup>III</sup>-Mn<sup>III</sup>)] (Eppley H. J. et al. 1995).

The composition of **2** has been established by elemental analysis,  $^1\text{H-NMR}$  spectroscopy, and MALDI-ToF mass spectrometry.

Among the various mass spectrometric techniques that can be used, matrix-assisted laser desorption/ionization time-of-flight mass spectrometry (MALDI-ToF MS) has emerged as a particularly useful and efficient tool for the characterization of molecular clusters in a non-crystalline form (Coronado E. 2001; Ruiz-Molina D. et al. 2002).

Mass spectra collected<sup>3</sup> in positive and negative mode show isolated molecular peaks at  $m/z = 6125$  and  $6123$ , which correspond to  $[\text{M}+\text{H}]^+$  and  $[\text{M}-\text{H}]^-$  respectively, for the species  $[\text{Mn}_{12}\text{O}_{12}(\text{LC15SAC})_{16}]$  ( $M = 6124$ ). Neither the positive nor the negative mode spectra exhibit peaks that correspond to a cluster with  $\text{H}_2\text{O}$  ligands; these ligands are presumably lost under the measurement process. Satellite peaks for the partially substituted species  $[\text{Mn}_{12}\text{O}_{12}(\text{O}_2\text{CCH}_3)_n(\text{LC15SAC})_{16-n}]$  with molecular weight  $M' = M - 270n$  are not observed (Figure 4.4) confirming that the acetate ligands have been completely replaced.

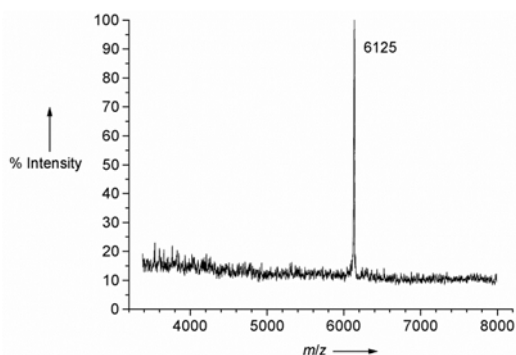


Figure 4.4. Positive-mode MALDI-TOF spectrum of **2**.

The protons of the alkylic chains in alpha to the carboxylic groups undergo a paramagnetic shift, in the  $^1\text{H-NMR}$  spectra of a toluene solution of **2** (Figure 4.5), similar to the methylenic protons of **1**. The only proton signal indicative of the substitution is the one in the region of negative chemical shift. Analogously to what reported in the literature for **1** where the acetates have been replaced by propionates (Eppley H. J. et al. 1995), this signal has been assigned to protons in  $\beta$  position of the carboxylic groups in ligands bridging  $\text{Mn}^{\text{III}}$  atoms in equatorial position (C and C' of Fig. 4.5).

<sup>3</sup> Mass spectra were collected using a Voyager-DE-RP MALDI-TOF mass spectrometer (Applied Biosystems/PerSeptive Biosystems, Inc., Framingham, MA, USA) equipped with delayed extraction. 337-nm UV nitrogen laser was used and the mass spectra were obtained in both linear and reflection modes. Samples were prepared by mixing a solution of the sample in  $\text{CH}_2\text{Cl}_2$  (10  $\mu\text{L}$ ) with a solution of the matrix (dihydroxybenzoic acid in  $\text{CH}_2\text{Cl}_2$ , 30  $\mu\text{L}$ , 1  $\text{mg L}^{-1}$ ). 1  $\mu\text{L}$  of the solution was loaded on to a gold-sample plate, the solvent was removed in warm air, and the sample transferred to the mass spectrometer for analysis.

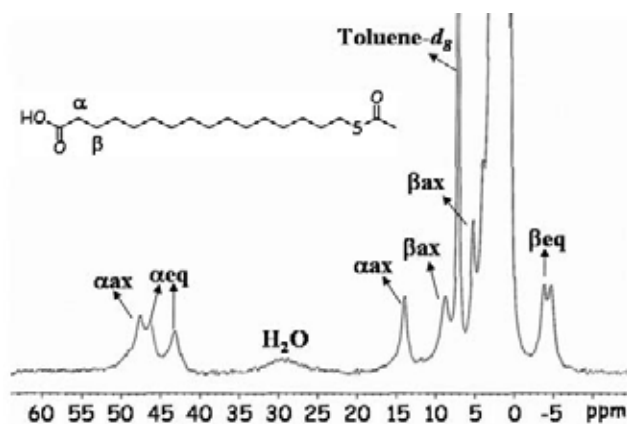


Figure 4.5. <sup>1</sup>H-NMR spectrum of 2.

## 2.1 Aromatic acetyl-thio-derivative of Mn12

The second Mn12 derivative functionalized with an acetyl thioester that has been investigated contains an aromatic ring and has been obtained by a ligand exchange reaction from 1 and the 4-(acetylthio)benzoic acid (Heersche H. B. et al. 2006).<sup>4</sup>

The MALDI-ToF analysis has been performed in order to confirm the structure of the obtained Mn12 derivative in the absence of X-ray diffraction data. Unlike compound 2, mass spectra for compound 3 (Fig. 4.6) reveal no peaks for the corresponding molecular ion, but show the presence of a peak at  $m/z = 3821.75$  corresponding to the  $[Mn_{12}O_{12}(L')_{15}(O_2C)]$  species. This peak may arise from the loss of a  $C_6H_4SAc$  unit ( $m/z = 151$ ) from the fully substituted species  $[Mn_{12}O_{12}(L')_{16}]$  with molecular weight  $M = 3972$ , or from the loss of a  $CH_3$  unit ( $m/z = 15$ ) from the partially substituted  $[Mn_{12}O_{12}(L')_{15}(OAc)]$  species with molecular weight  $M^* = 3836$ .

<sup>4</sup> 4-(acetylthio)benzoic acid was obtained by reacting 4-mercaptobenzoic acid with acetic anhydride, as described elsewhere (Okuno H et al. 1990). Compound 3 was synthesised by adding an excess of 4-(acetylthio)benzoic acid (403mg, 2.054mmol) to a slurry of 1·4H<sub>2</sub>O·2AcOH (206mg, 0.1mmol) in anhydrous toluene and the resulting mixture was stirred to give a dark brown solution. Then the solution was concentrated at reduced pressure to remove acetic acid as the toluene azeotrope. To fully substitute the acetate ligands several treatments with 10mL portions of toluene and additional azeotropic distillations were performed. The residue was dissolved in CH<sub>2</sub>Cl<sub>2</sub> and the solution layered with *n*-hexane and stored at room temperature. In spite of repeated efforts, the crystals obtained were not suitable for X-ray structural determination. The overall yield of 3 was ~ 60%. Elemental analysis. Found: C, 42,87; H, 2,63; S, 12,59; Calc. for  $[Mn_{12}O_{12}(O_2CC_6H_4SAc)_{16}(H_2O)_4]$ : C, 42,74; H, 2,99; S, 12,68; X-EDS: S/Mn atomic ratio= 1.41(13).

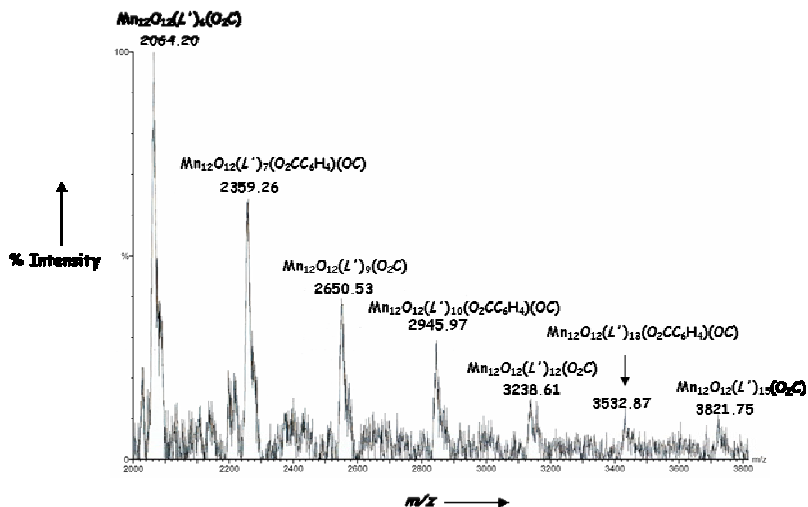


Figure 4.6. Positive-mode MALDI-TOF spectrum of 3.

In addition mass spectra show a fragmentation pattern that can be assigned to the stepwise loss of several ligand units. Mass data for compound 3 demonstrate the successful replacement of acetate ligands in 1 but do not prove the formation of a fully substituted derivative. However elemental analysis of 3 is in good agreement with the expected values for the  $[Mn_{12}O_{12}(L')_{16}(H_2O)_4]$  species,  $C_{144}H_{120}Mn_{12}O_{64}S_{16}$ .

$^1H$ -NMR (200MHz) spectrum for  $CD_2Cl_2$  solution of 3 (Fig. 4.7) has been assigned by comparison with the  $^1H$ -NMR spectrum of  $[Mn_{12}O_{12}(O_2CC_6H_4-p-Me)_{16}(H_2O)_3]$  complex described elsewhere (Aubin S. M. J. et al. 2001) and completely analyzed by a combination of relaxation times measurements and 2-D NMR studies.

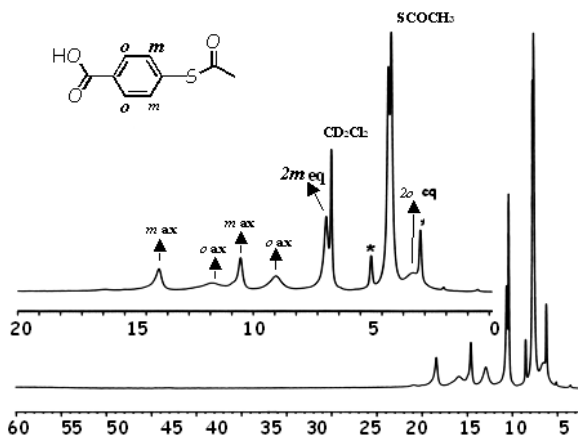


Figure 4.7.  $^1H$ -NMR spectrum of a  $CD_2Cl_2$  solution of 3. The asterisks are used to mark residual  $Et_2O$ .

The spectra show six peaks attributed to aromatic protons and additional peaks corresponding to the *para*-CH<sub>3</sub> groups. All the peaks from both complexes are found within a relatively narrow chemical shift window (from 14 to 0 ppm), as might be expected from a complex with all protons significantly far away from the paramagnetic centre. The peak width varies greatly, and is largest for ortho-protons, which are the closest to the paramagnetic metal centre. In addition, on the basis of peak integration, we can differentiate protons of equatorial ligands from axial ones. The eight equatorial carboxylate ligands bridging Mn<sup>III</sup>-Mn<sup>III</sup> ions show doubly intense peaks in the spectrum with respect to the four axial ones bridging Mn<sup>III</sup>-Mn<sup>III</sup> ions and the four axial ones bridging Mn<sup>III</sup>-Mn<sup>IV</sup> ions. Also in this case, a comparison with spectra recorded in CDCl<sub>3</sub> and toluene-*d*<sub>8</sub> was useful for a correct assignment of the peaks.

### 2.3 Aromatic methyl sulphide-derivative of Mn12

It is well known that also methyl-thio derivatives can be covalently grafted to gold. In addition, they afford a more coordinative grafting, the Au-S bond energy being ca. 60 kJ mol<sup>-1</sup> as compared to ca. 120 kJ mol<sup>-1</sup> for thiolates (Lavrich D.J. et al. 1998). This allows, as described in the next chapter, to isolate Mn12 molecules on the surfaces.

We have demonstrated that the methyl-thio function is redox compatible with the Mn<sup>III</sup>/Mn<sup>IV</sup> oxidation states of Mn12 (Zobbi et al. 2005). As thioether groups interact directly with the Au substrate, protection/deprotection procedure for derivative 2 and 3 is therefore unnecessary.

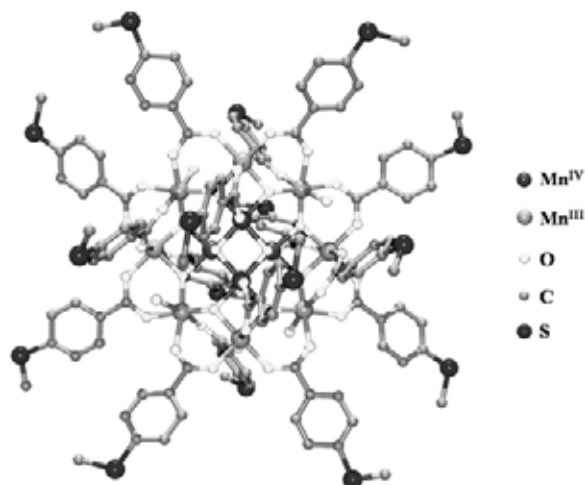
In the following we describe how this derivative, based on the use of the commercially available 4-(methylthio)benzoic (HPhSMe) acid has been obtained following a procedure similar to that described for complex 3.<sup>5</sup>

Suitable single crystals for the XRD analysis<sup>6</sup> were obtained by slow evaporation of a chloroform solution of the needle shaped crystals. A representation of the cluster, [Mn<sub>12</sub>O<sub>12</sub>(PhSMe)<sub>16</sub>(H<sub>2</sub>O)<sub>4</sub>]·8CHCl<sub>3</sub> (4·8CHCl<sub>3</sub>), is provided in Figure 4.8 while crystallographic data is listed in Table 4.3. Complex 4 crystallizes in tetragonal space group  $I\bar{4}$ , X-ray structure investigation at 193 K revealed that the core has the same overall structure as 1 complex, comprising a central Mn<sub>4</sub><sup>IV</sup>O<sub>4</sub> cubane unit and an outer ring of eight Mn<sup>III</sup> ions.

The molecular structure exhibits crystallographic S<sub>4</sub> symmetry, which is comparatively rare in Mn12 derivatives. The periphery of the cluster features sixteen sulphur atoms which provide as many surface-binding sites.

<sup>5</sup> A slurry of complex 1 (204 mg, 0.0990 mmol) in anhydrous toluene (10 mL) was treated with 4-(methylthio)benzoic acid (333 mg, 1.98 mmol). The mixture was concentrated at reduced pressure to remove acetic acid as the toluene azeotrope. Several treatments with 10 mL portions of toluene and a final recrystallization from n-hexane/CHCl<sub>3</sub> afforded black needle shaped crystals of 4·8CHCl<sub>3</sub> (yield 62%). Elemental analysis (%) on a vacuum-dried sample calculated for C<sub>128</sub>H<sub>120</sub>Mn<sub>12</sub>O<sub>48</sub>S<sub>16</sub> (4) C 42.72, H 3.36, S 14.23; found: C 42.58, H 3.14, S 13.78. X-EDS (single cryst.): S/Mn atomic ratio= 1.35(3).

<sup>6</sup> Data were collected on a Siemens P4-RA diffractometer and corrected for absorption (Psi-scan); all nonhydrogen atoms treated anisotropically; hydrogen atoms added in idealised positions; merohedral-twinning (twinning matrix: 1 0 0 0 -1 0 0 0 -1). The structures were solved by direct methods (SIR 92) and subsequent Fourier syntheses and refined by full-matrix least-squares on F<sup>2</sup> (SHELXL-97).

Figure 4.8. X-ray determined crystallographic structure of  $[\text{Mn}_{12}\text{O}_{12}(\text{PhSMe})_{16}(\text{H}_2\text{O})_4]$  (4)Table 4.3. Crystallographic data for  $4 \cdot 8\text{CHCl}_3$ .

Empirical formula	$\text{C}_{136}\text{H}_{128}\text{Cl}_{24}\text{Mn}_{12}\text{O}_{48}\text{S}_{16}$	
Formula weight	4553.42	
Temperature	193(2) K	
Wavelength	0.71073 Å	
Crystal system	Tetragonal	
Space group	$I\bar{4}$	
Unit cell dimensions	$a = 19.9340(10)$ Å $\alpha = 90^\circ$	$\beta = 90^\circ$
	$b = 19.9340(10)$ Å	$\gamma = 90^\circ$
	$c = 25.343(3)$ Å	
Volume	$10070.4(14)$ Å <sup>3</sup>	
Z	2	
Density (calculated)	1.502 g/cm <sup>3</sup>	
Absorption coefficient	1.276 mm <sup>-1</sup>	
F(000)	4584	
Crystal size	0.58 x 0.46 x 0.36 mm <sup>3</sup>	
$\theta$ range for data collection	2.16 to 25.99°	
Index ranger	$-24 \leq h \leq 8, -22 \leq k \leq 24, -20 \leq l \leq 31$	
Reflections collected	6172	
Independent reflections	5988 [R(int) = 0.0193]	
Completeness to $\theta = 25.99^\circ$	98.4 %	
Absorption correction	Psi-scan	
Max. and min. transmission	0.511 and 0.465	
Refinement method	Full-matrix Least-squares on $F^2$	
Data / restraints / parameters	5988 / 37 / 563	
Goodness-of-fit on $F^2$	1.060	
Final R indices [ $I > 2\sigma(I)$ ]	$R_1 = 0.0499, wR_2 = 0.1323$	
R indices (all data)	$R_1 = 0.0509, wR_2 = 0.1339$	
Largest diff. peak and hole	1.014 and -0.432 eÅ <sup>-3</sup>	

## 2.4 Aliphatic disulphide-derivative of Mn12

We have further explored the synthesis of derivatives to be anchored on gold by combining the presence of aliphatic chains and of sulphide linker groups in a dialkyl-sulphide carboxylic acid. This new ligand has been designed in order to confirm the previous indications concerning the isolation of single molecules by the use of the coordinative linking of the sulphide instead the thiol-protected as well as for exploring with a different cluster the patterned depositions via micro-contact printing method as evidenced for 2. This last part is not already done and it will be the subject of future investigations. The structure of these clusters is shown in Figure 4.9.

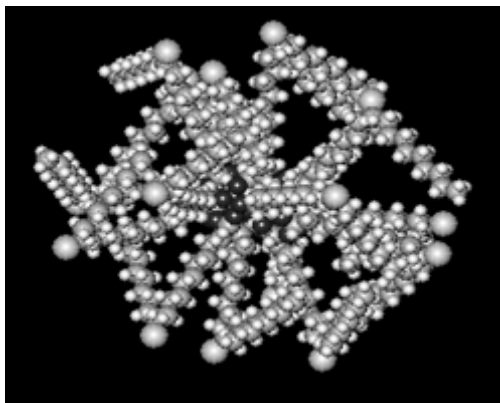


Figure 4.9. Structure simulation of compound 5.

The decylthioundecanoic acid (HC10SC10) has been prepared by coupling 1-undecanthiol and 11-Br-undecanoic acid as described elsewhere (Liebau M. et al. 2002).<sup>7</sup>

Then the ligand exchange reaction has exploited following a similar procedure to that described for complex 2.<sup>8</sup> Again, the impossibility to obtain a crystalline mate-

<sup>7</sup> 1-Decanthiol (10.7 g; 61.5 mmol), 11-bromoundecanoic acid (12.8 g; 48.3 mmol), powdered KOH (6.7 g; 119.6 mmol) and 125 mL EtOH were stirred and heated at reflux overnight. The mixture was allowed to cool down to room temperature, water was added and the aqueous solution was extracted twice with hexane to remove apolar contaminants. Thereafter, the water layers was acidified with HCl-solution and extracted twice with ether. The combined ether layers were washed with NaCl-solution and dried with MgSO<sub>4</sub>. Evaporation and recrystallization from hexane gave 13.7g pure decylthioundecanoic acid. <sup>1</sup>H-NMR (CDCl<sub>3</sub>): 0.85 (3 H, t), 1.45-1.15 (26 H, m), 1.7-1.5 (6 H, m), 2.35 (2 H, t), 2.50 (4 H, t), 11.8-11.0 (1H, bs); <sup>13</sup>C-NMR (CDCl<sub>3</sub>): 180.03, 34.0, 32.1, 31.8-29.67, 29.52, 29.50, 29.39, 29.30, 29.27, 29.22, 29.16, 28.99, 28.91, 24.6, 22.6, 14.0.

<sup>8</sup> A slurry of complex 1 (302 mg, 0.146 mmol) in anhydrous toluene (10 mL) was treated with decylthioundecanoic acid (895 mg, 2.5 mmol). The mixture was concentrated at reduced pressure to remove acetic acid as the toluene azeotrope. Several treatments with 10 mL portions of toluene and a final recrystallization from CH<sub>3</sub>CN /CH<sub>2</sub>Cl<sub>2</sub> result in a black powder of 5 (yield 54%). Elemental analysis (%) on a vacuum-dried sample calculated for C<sub>336</sub>H<sub>664</sub>Mn<sub>12</sub>O<sub>48</sub>S<sub>16</sub> (5) C 60.72, H 10.07, S 7.70; found: C

rial required a confirmation of the formation of this cluster by means of alternative techniques, first of all by elemental analysis, then by the use of MALDI-ToF. Also in this case mass spectra (Fig. 4.10) reveal no peaks for the corresponding molecular ion ( $m/z=6645$ ), but show the presence of a peak at  $m/z = 3216$  corresponding to the bi-charged  $[Mn_{12}O_{12}(C_{10}H_{21}-S-C_{10}H_{20}COO)_{15}-S-C_{10}H_{20}COO]^{2+}$  species attributed to the loss of water molecules and a  $C_{10}H_{21}$  fragments. Moreover we find signals at 2972, 2657, 2342, 2027, 1712  $m/z$  due to the loss of a  $C_{10}H_{21}S$  fragment and to the gradual loss of  $C_{10}H_{21}SC_{10}H_{21}$  ligand fragments.

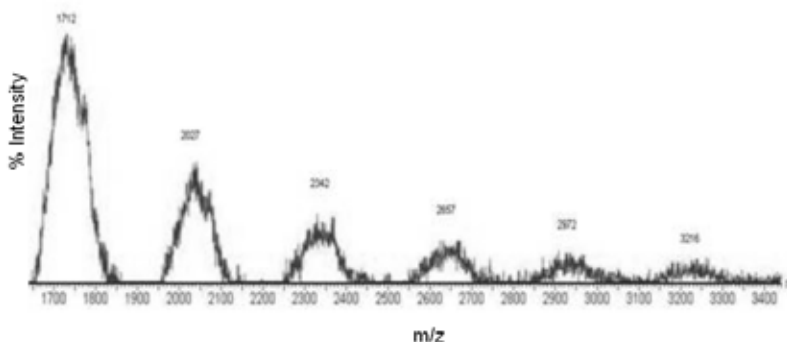


Figure 4.10 Positive-mode MALDI-ToF spectrum of 5.

Concluding also in this case the combination of MALDI-ToF and elemental analysis data demonstrate the successful replacement of acetate ligands in 1 with a fully C10SC10 substituted derivative.

## 2.5 Toward the iso-orientation of Mn12 molecules on surface

The last Mn12 derivative that we describe here is the outcome of strong efforts focused on a site-specific ligand replacement on the Mn12 clusters. This is aimed to the control of the orientation of SMMs on the surface, a parameter of paramount importance as all the interesting magnetic features of SMMs are originated by their magnetic anisotropy. The synthesis of selectively substituted Mn12 cluster has been the main goal of a previous PhD thesis of our group (Pacchioni M. et al. 2004; Pacchioni M. 2005), and we refer to this work for the complete synthesis steps to achieve the used ligand. Here we describe briefly only the synthesis of the final compound, the Mn12ADCSMe and, in Chapter 6, their deposition on gold surface.

vacuum-dried sample calculated for  $C_{336}H_{664}Mn_{12}O_{48}S_{16}$  (5) C 60.72, H 10.07, S 7.70; found: C 60.86, H 10.55, S 7.43

$^1H$ -NMR (toluene- $d_8$ ): 49.5 [8 H;  $CH_2$  ( $\alpha$ , axial,  $Mn^{III}$ - $Mn^{III}$ )], 48.2 [8 H;  $CH_2$  ( $\alpha$ , equatorial,  $Mn^{III}$ - $Mn^{III}$ )], 45.1 [8 H;  $CH_2$  ( $\alpha$ , equatorial,  $Mn^{III}$ - $Mn^{III}$ )], 14.2 [8 H;  $CH_2$  ( $\alpha$ , axial,  $Mn^{III}$ - $Mn^{IV}$ )], 9.2 (8 H;  $CH_2$  ( $\beta$ , axial,  $Mn^{III}$ - $Mn^{III}$ )), 5.5 (8 H;  $CH_2$  ( $\beta$ , axial,  $Mn^{III}$ - $Mn^{IV}$ )), -3.8 (8 H;  $CH_2$  [ $\beta$ , equatorial,  $Mn^{III}$ - $Mn^{III}$ )], -4.7 ppm [8 H;  $CH_2$  ( $\beta$ , equatorial,  $Mn^{III}$ - $Mn^{III}$ )].

This compound has been obtained from Mn12-*benzoate* using for site-selective ligand replacement a conformationally-rigid dicarboxylate ligand derived from anthracene-1,8-dicarboxylic acid (H<sub>2</sub>ADC). The two carboxylic groups are at a distance of 5.2 Å, calculated on the C atoms, which nicely fit the distance observed between the two carboxylic groups that bridge Mn<sup>III</sup> and Mn<sup>IV</sup>, i.e. the A mode of Fig. 4.1 The results is that the ADC ligand acts in a bis-bidentate fashion and occupies axial sites only.

Moreover, the anthracene moiety can be easily functionalized in the 10-position, for instance with a phenyl-methyl-thio fragment in order to achieve the deposition on gold in analogy to the other derivatives discussed in this chapter. Details of the synthetic procedure are given in the footnote.<sup>9</sup>

The crystal structure of this compound has not been obtained yet, due to the weak diffracting power and the small size of the crystals that prevents a complete crystallographic analysis of the cluster. The elementary cell has been however determined and it results to be comparable (Table 4.4) to a similar anthracene derivative of Mn12, the Mn12ADCCH<sub>2</sub>Sac with the thio-acetyl substituent in 10-position (Pacchioni M. 2005), whose structure has been fully determined and here reproduced in Figure 4.11.

Table 4.4. Comparison between elementary cell of Mn12ADCSMe (6) and Mn12ADCCH<sub>2</sub>Sac. The cell of 6 has been obtained at room temperature, crystal with other liquid in a  $\varnothing = 0.3$  mm capillary.

	Mn12ADCSMe	Mn12ADCCH <sub>2</sub> Sac
Empirical formula	Mn <sub>12</sub> O <sub>48</sub> C <sub>148</sub> H <sub>104</sub> S <sub>4</sub>	Mn <sub>12</sub> O <sub>52</sub> C <sub>164</sub> H <sub>128</sub> S <sub>4</sub> Cl <sub>16</sub>
Formula weight	3437.90 dalton	4285.38 dalton
Temperature	298 K	100(2)K
Wavelength	0.71073 Å	0.71073 Å
Crystal system	Tetragonal <i>I</i>	Tetragonal <i>I</i>
Unit cell dimensions	a = 27.003(5) Å	a = 26.2604(12) Å
	b = 27.003(5) Å	b = 26.2604(12) Å
	c = 28.08(2) Å	c = 27.4733(13) Å
Volume	20476.9(192) Å <sup>3</sup>	18945.8(15) Å <sup>3</sup>

<sup>9</sup> To a solution of  $[Mn_{12}O_{12}(O_2CC_6H_5)_{16}(H_2O)_4]$  (117.3 mg, 0.039 mmol) in CH<sub>2</sub>Cl<sub>2</sub> (9.7 mL) was added H<sub>2</sub>ADC-PhSMe (60.7 mg, 0.156 mmol) and the resulting solution was stirred for 24 hours. Recrystallization was achieved by slow diffusion of *n*-hexane into this solution. The resulting crystals of 6 were collected, washed with *n*-hexane and dried on the frit (97.5 mg, 73%). Elemental analysis calculated for Mn<sub>12</sub>O<sub>48</sub>C<sub>148</sub>H<sub>104</sub>S<sub>4</sub>: C, 51.71; H, 3.05; S, 3.73. Found (vacuum dried sample: 0.1-0.2 mmHg, 75 min.): C 51.37; H 3.31; S 3.69.

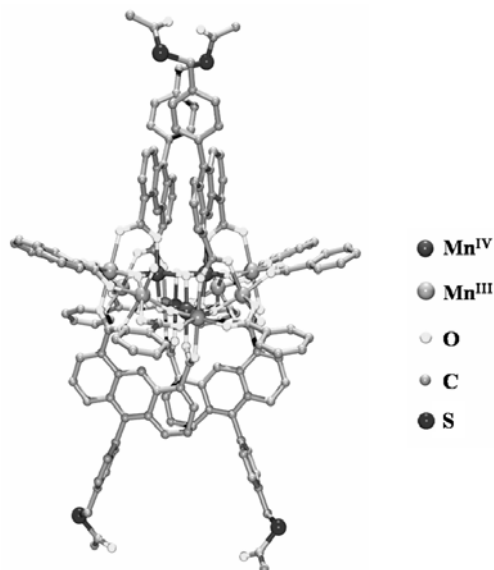


Figure 4.11. Crystallographic structure of  $[\text{Mn}_{12}\text{O}_{12}(\text{O}_2\text{CC}_6\text{H}_5)_8(\text{ADC-PhCH}_2\text{SAC})_4(\text{H}_2\text{O})_4]$  (Mn12ADCCH<sub>2</sub>SAC). (Pacchioni M. et al. 2004).

### 3. Bulk magnetic characterization of Mn12-sulphur derivatives

A necessary step in the characterization of the bulk materials to be grafted on gold is the investigation of their magnetic properties in order to confirm that the typical SMM behaviour is preserved after the inclusion of a sulphur-based function on the ligands. All the above described compounds have been investigated and in all cases the slow relaxation of the magnetization is preserved, even if in some cases slight differences are found.

The magnetization dynamics studied by variable-frequency AC susceptibility measurements<sup>10</sup> on a polycrystalline sample of Mn12LC15 (2) exhibits the distinctive features of Mn12 derivatives, i. e. the imaginary component  $\chi''$ , goes through a maximum on lowering the temperature and the temperature of the maxima is frequency dependent, as shown in Figure 4.12.

<sup>10</sup> Magnetic measurements were performed on a Cryogenic S600 SQUID magnetometer, a Vibrating Sample Magnetometer (VSM) and a home-made AC probe.

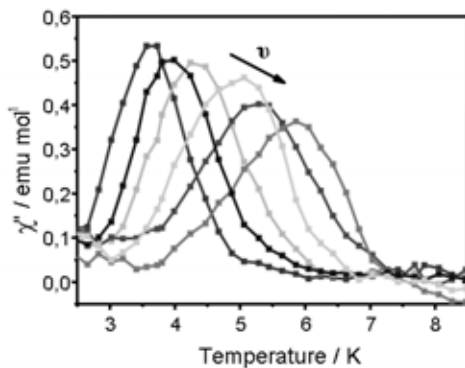


Figure 4.12. AC out-of-phase signals ( $\chi''$ ) at different frequencies (between 1.61 and 510 Hz) for complex 2.

The relaxation rate of the magnetization ( $1/\tau=2\pi\nu$ ) is plotted in Figure 4.13 as a function of the inverse blocking temperature  $1/T_{max}$  (that is the temperature at which the out-of phase susceptibility reaches a maximum at each frequency). An Arrhenius-type behaviour is observed, with  $\tau_0 = 2.4 \times 10^{-8}$  s and  $U_{eff} = 55.2$  K, which suggests a thermally activated mechanism for magnetization reversal. The energy barrier is close to that found for 1 (60.5 K),<sup>35</sup> which confirms that the Mn12 core remains intact during the ligand-exchange reaction.

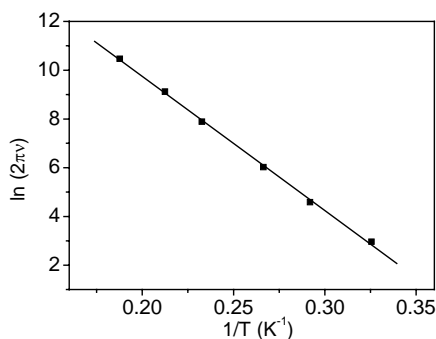


Figure 4.13. Relaxation rate of the magnetization of 2 plotted as a function of inverse blocking temperature.

A similar characterization has been done for Mn12PhSAc (3) and Mn12PhSMe (4); noticeable is the observation that two frequency dependent peaks in the temperature range 2 - 3.5 K and 4 - 8 K, respectively, are observed.

This behaviour, which points to the presence of at least two different relaxation processes, has been previously observed for other Mn12 complexes. The origin has been attributed to the presence of different isomers in the same crystal (Aubin S. M. J. et al. 2001; Sun Z. M. et al. 1999). Isomeric forms of a given complex can indeed be obtained and differ for instance in the placement of the H<sub>2</sub>O ligands, in the degree

of solvation or in the arrangement of JT axes (*JT isomerism*). Jahn-Teller isomers of Mn12 complexes differ in the orientation of one JT axis that, always referring to the disc like structure of the cluster, is equatorial rather than axial. As the magnetic anisotropy of the cluster results from a vectorial combination of the single ion contributions, the tilting of the easy axis of magnetization of one or more MnIII sites results in a decreased magnetic anisotropy and thus in an increased relaxation rate, as revealed by the occurrence of the  $\chi''$  peaks in the low temperature region.

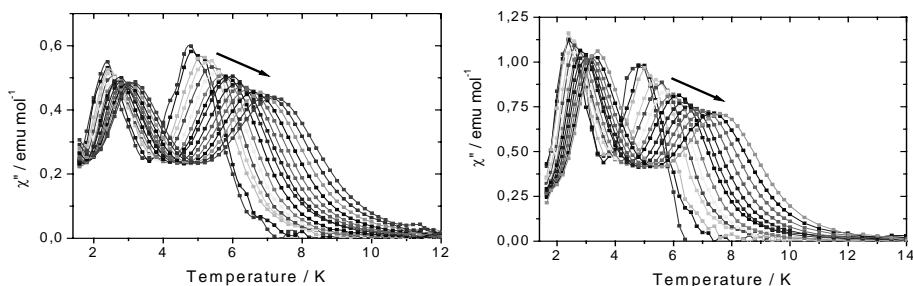


Figure 4.14 Ac out-of-phase signals ( $\chi''$ ) at different frequencies (between  $\nu=10$  and 6580 Hz) for complex 3 (left) and 4 (right).

In particular the second relaxation process for complex 4 may be ascribed to the partial desolvation of the single-crystal samples used for the measurements rather than to JT isomerism, since the structural investigation provides no evidence for equatorially oriented JT axes.

Deconvolution of  $\chi''$  vs. temperature curves with Gaussian functions allows to plot the relaxation rate ( $1/\tau = 2\pi\nu$ ) as a function of the inverse blocking temperature  $1/T_{max}$ . The obtained Arrhenius plots provide the dynamic parameters, are shown in Figure 4.15 and confirm a thermally activated mechanism for magnetization reversal that is distinctive of the SMM behaviour (Gatteschi D. and Sessoli R. 2003). In addition, the two values of the energy barriers ( $\Delta E/k$ ) are close to that found in  $1\cdot4\text{H}_2\text{O}\cdot 2\text{AcOH}$  (62 K), confirming again that the Mn12 core remains intact during the ligand exchange reaction.

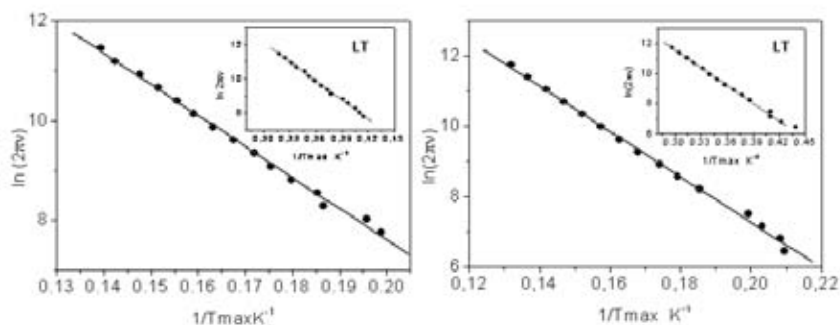


Figure 4.15. Plots of the natural logarithm of relaxation rate versus inverse temperature for 3 (left) and 4 (right). The solid lines are the fits to the Arrhenius equation. In the insets the plots for low temperature relaxations are presented.

Since complex 4 has been obtained in well defined crystals, it was of interest to investigate the magnetization response to a changing applied field of an aligned single-crystal sample. The field dependence of the magnetization has been recorded at different applied temperatures on a single-crystal of 4 oriented with its easy axis parallel to the applied field. At 4 K, a saturation value of  $20\mu_B$  is reached, which is the value expected for an  $S = 10$  ground spin state. Below 4K, a stepped hysteresis appears (Fig. 4.16) indicating the occurrence of thermally assisted quantum tunnelling of the magnetization, a phenomenon typical of Mn12 derivatives, further confirming retention of SMM behaviour.

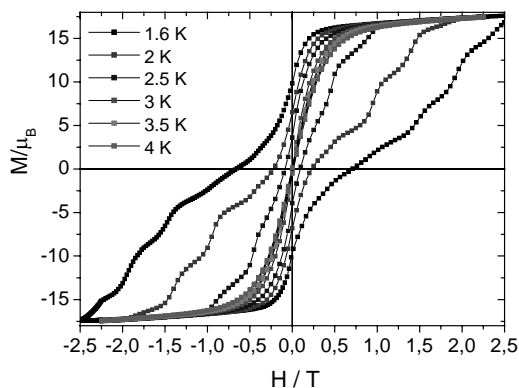


Figure 4.16. Magnetization hysteresis loops at different temperatures recorded on a single crystal of 4 with the magnetic field along the tetragonal axis.

As described above complex 5 cannot be obtained in crystalline form, however a hysteresis loop has been observed for the amorphous powder, as shown in Figure 4.17.

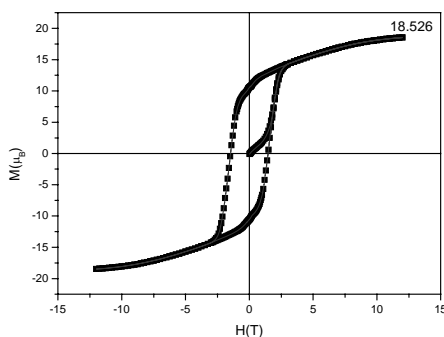


Figure 4.17 Magnetization hysteresis loops at 1.8 K recorded on an amorphous powder of 5 pressed in a pellet.

In this case the stepped loop is not observed because the easy axes of the grains are randomly oriented, being them pressed in a pellet to prevent partial alignment in the magnetic field.

We have performed also variable-frequency AC susceptibility measurements on compound 5. The results, reported in Figure 4.18, show the typical frequency de-

pendent maxima in  $\chi''$ , this time with a very small hint of a second peak at lower temperature. The Arrhenius plot of the relaxation time provides the following parameters,  $\tau_0=1.59*10^{-9}$  s and  $U_{eff}= 72$  K, which indicate a significant decrease of the pre-exponential factor compared to 1.

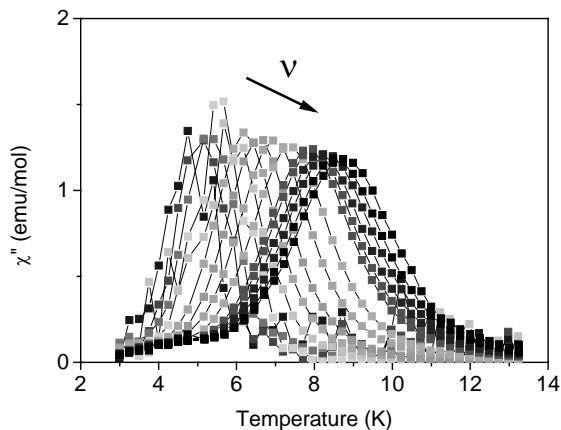


Figure 4.18 Ac out-of-phase signals ( $\chi''$ ) at different frequencies (between 30 and 25000Hz) for complex 5.

AC magnetic susceptibility data were collected also for complex 6. Plots of the in-phase component ( $\chi'_M$ , plotted as  $\chi'_M T$ ) and the out-of-phase component ( $\chi''_M$ ) versus T at the different frequencies are shown in Figure 4.19.

The  $\chi'_M T$  value remains relatively constant at a value of 55 emu K mol<sup>-1</sup> between 15 K and 8 K, in agreement with what expected for an  $S = 10$  spin ground state. Below this temperature, the value of  $\chi'_M T$  decreases rapidly, simultaneously with the sharp decrease in  $\chi'_M T$ , the appearance of an out-of-phase signal is observed.

Also in this case two components are observed and the low temperature one represents around 25 % of the whole behaviour, estimated from the  $\chi' T$  curve.

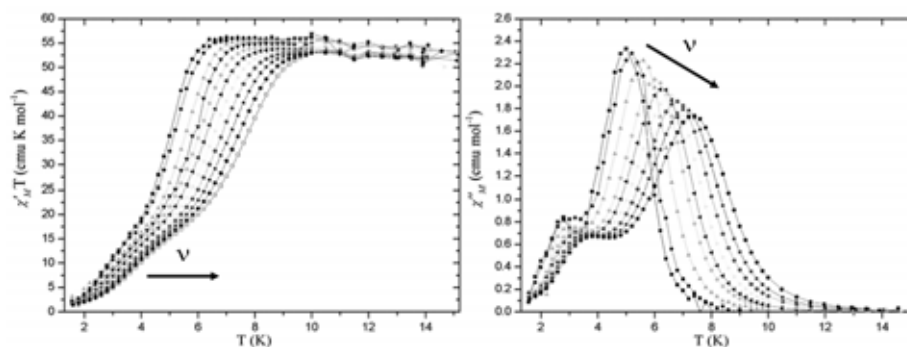


Figure 4.19 Plot of the in-phase, as  $\chi'_M T$ , and out-of-phase,  $\chi''_M$ , ac susceptibility signals vs. temperature for complex 6 at different oscillation frequencies between 100 and 6580Hz.

The relaxation times for both processes were determined by deconvolution of the curves with two Gaussians. The Arrhenius plots obtained plotting the relaxation times as function of the inverse blocking temperature  $1/T_{max}$  lead to the dynamic parameters of the system (Fig. 4.20). For the high temperature dynamic  $\tau_0 = 1.8 \times 10^{-9}$  s and  $U_{eff} = 69.5$  K, for the low temperature dynamic  $\tau_0 = 2.7 \times 10^{-10}$  s and  $U_{eff} = 42.1$  K.

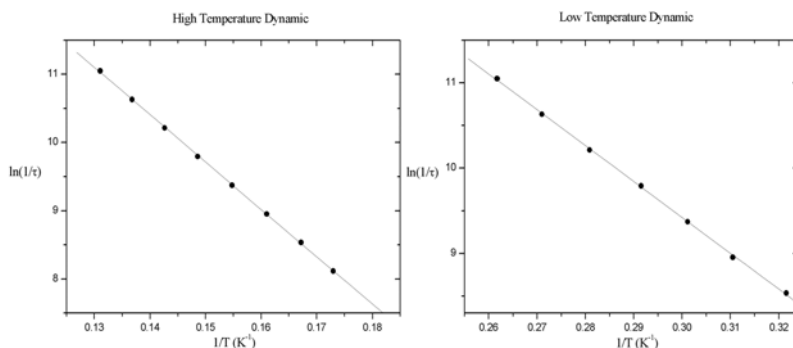


Figure 4.20. Plots of the natural logarithm of the magnetization relaxation rate,  $\ln(1/\tau)$ , versus  $1/T$  for complex 6. The solid line is a fit to the Arrhenius equation as described in the text.

All the dynamical parameters of the sulphur derivatives are summarized in Table 4.5 for an easy comparison.

Table 4.4. Comparison between all the dynamic parameters obtained for the Mn12-acetate and the Mn12-sulphur derivatives.

Mn12 derivative	$U_{eff}(LT)$ [K]	$U_{eff}(HT)$ [K]	$\tau_0(LT)$ [s]	$\tau_0(HT)$ [s]
Mn12LC15 (2)	/	55.2	/	$2.4 \cdot 10^{-8}$
Mn12PhSAc (3)	37.0	65.0	$0.7 \cdot 10^{-10}$	$2.3 \cdot 10^{-9}$
Mn12PhSMe (4)	39.4	65.9	$0.7 \cdot 10^{-10}$	$1.42 \cdot 10^{-9}$
Mn12C10SC10 (5)	/	72.0	/	$1.6 \cdot 10^{-9}$
Mn12ADCSMe (6)	42.1	69.5	$2.7 \cdot 10^{-10}$	$1.8 \cdot 10^{-9}$

## Chapter 5

### Syntheses of Nitronyl Nitroxide radicals for deposition on gold surfaces

#### 1. Nitronyl Nitroxide radicals

The second class of compounds studied during this thesis is a simpler one, namely purely organic paramagnetic radicals widely investigated both for their intrinsically interesting magnetic properties (Tamura M. et al. 1991; Chiarelli R. et al. 1993) and as building blocks for assembling complex magnetic structures in which they act as chemical and magnetic linkers between transition metal ions (Caneschi A. et al. 1989), to yield magnetic polymers including Single Chain Magnets (SCMs) (Caneschi A. et al. 2001). In this thesis the goal was again to deposit these molecules on suitable surfaces and to investigate their properties after their deposition. In order to do this, the first steps, in analogy to the Mn12 case, have been the modification of their chemical structure in order to introduce the linking groups able to bind the surfaces without affecting the paramagnetic behaviour of these molecules as well as their redox stability. Therefore the “methyl-thio” functionalization has been employed also in this case.

#### 1.1 General synthesis of Nitronyl Nitroxides

This class of organic radical was introduced by Ullman in 1968 (Osiecki J. H. and Ullman E. F. 1968); Ullman E. F. et al. 1970; Ullman E. F. et al. 1972) and their synthesis procedure are described hereafter and sketched in the following scheme (Figure 5.1).

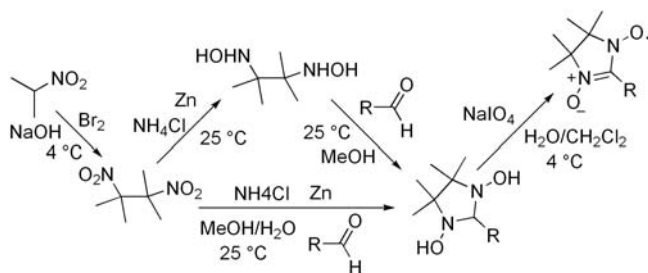


Figure 5.1. Reaction scheme for the synthesis of NIT(R) radicals (Bogani L. 2005). Two possible pathways for the condensation of the aldehyde are represented. See text for details on each step.

As the commercially available sources of the starting reagent, 2,3-dimethyl-2,3-dinitrobutane are not pure enough for our purposes, and the purification procedure is as time-consuming as the synthesis of the compound from scratch, we found it convenient to synthesize it too.<sup>11</sup>

The condensation of the aldehyde is generally achieved using directly N,N'-dihydroxy-2,3-diamino-2,3-dimethylbutane (obtained from the reduction of 2,3-dimethyl-2,3-dinitrobutane) or their sulphate salt that is more stable and can be stored for a long time. These two precursors are obtained as described in footnotes.<sup>12</sup> In both cases the obtained N,N'-dihydroxy-2,3-diamino-2,3-dimethylbutane shall subsequently be condensed with the aldehyde.<sup>13</sup> Once the condensation has been carried out, the 1,3-dihydroxy-(2-R)-4,4,5,5-tetramethylimidazoline can be oxidized to the corresponding Nitronyl Nitroxide (NIT) radical.<sup>14</sup> These general guidelines for the production of NIT radicals have been followed preparing the radical that we used for the deposition.

<sup>11</sup> This is accomplished in the following way: 0.5 mol of 2-nitropropane (0.5 g) are dissolved in 86 ml of a water solution 6 M of NaOH. Over the period of 1 hr 0.25 mol of bromine (40 g) are then added dropwise under stirring and at 4 °C. 165 ml of ethanol are then added and the mixture is left to reflux for about 3 hrs. When the product starts to crystallize 500 ml of ice-cold water are added and the product is then filtrated.

<sup>12</sup> i) A solution with 1 Eq. of 2,3-dimethyl-2,3-dinitrobutane and 2 Eq. of NH<sub>4</sub>Cl in 100 ml of H<sub>2</sub>O and 100 ml of THF is cooled in an ice bath. Zinc powder (4 Eq.) is then added progressively during a 2-3 hours period. The product is then left to stir overnight at 25°C and is then filtrated. The cake of zinc oxide is washed several times with a 1:1 mixture of H<sub>2</sub>O and THF. The filtrate is then acidified to pH = 2 with HCl and the solvent is evaporated under reduced pressure. The residual oil is then cooled with an ice bath and mixed with 0.6 mol of anhydrous K<sub>2</sub>CO<sub>3</sub>. the resulting solid is then continuously extracted with 500 ml of CH<sub>2</sub>Cl<sub>2</sub> in a Soxhlet apparatus for about 12 hours and the extracted liquid is then evaporated under reduced pressure and recrystallized in petroleum ether, giving N,N'-dihydroxy-2,3-diamino-2,3-dimethylbutane with a mean yield of 65%.

ii) 1 Eq. of 2,3-dimethyl-2,3-dinitrobutane is dissolved in THF (300 ml for 0.11 mol) and 4 Eq. of NH<sub>4</sub>Cl are added to the solution, together with 30 ml of water. The mixture is then cooled with an ice bath and 5.4 Eq. of Zn are added in about 1 hr under constant stirring. The solution is then left to stir for about 12-14 hours at 10-20°C, gradually acquiring a bluish hue, which turns grey at the end of the reaction. The mixture is then filtered and the precipitate is washed with THF. The residual THF is then eliminated under reduced pressure from the obtained pale-yellow filtrate. This is redissolved in EtOH and the solution is filtered to remove the non reacted 2,3-dimethyl-2,3-dinitrobutane. To obtain the salt a 10% mixture of H<sub>2</sub>SO<sub>4</sub> in ethanol is added dropwise to the filtrate after cooling to about 0°C. When pH 3 is reached the precipitated monosulphate salt is filtered off, washed with ethanol and dried. The obtained compound, obtained usually with a 60% yield, can then be stored and, when the condensation is needed, 2 Eq. of solid NaOH can be added during a 1 hour period to a suspension of the monosulphate salt in MeOH kept at 0°C under stirring. The precipitate is then separated by centrifugation and discarded, while the solvent is evaporated under reduced pressure. The residue is then redissolved in dry THF and the solution is filtered to remove residual NaSO<sub>4</sub>. Evaporation under vacuum affords crystalline N,N'-dihydroxy-2,3-diamino-2,3-dimethylbutane.

<sup>13</sup> The condensation is obtained with the following a general procedure. N,N'-dihydroxy-2,3-diamino-2,3-dimethylbutane is dissolved in methanol (15 ml for 12 mmol) and 1.3 equivalents of the appropriate aldehyde R-CHO are then added. The solution is then let to stir at room temperature for about 12 hours. The precipitate so obtained is then filtered, washed with methanol and dried.

<sup>14</sup> The reaction is carried out by dissolving 1 equivalent of 1,3-dihydroxy-(2-R)-4,4,5,5-tetramethylimidazoline in CH<sub>2</sub>Cl<sub>2</sub> (usually about 25 ml) and then adding drop-wise, over a five minutes period, 1.5 equivalents of NaIO<sub>4</sub> in water. The temperature must be kept at around 4 °C, and vigorous stirring is required, to avoid the production of superoxidized species. During the reaction the colour of

## 1.2 The first sulphur derivative of Nitronyl Nitroxides

This compound was first synthesized several years ago (Caneschi A. et al. 1995) without exploring the possibility of its deposition on metallic surfaces. Here this molecule has been synthesized by following previous indications and taking into account the degree of purity of the final product. The starting building block to produce these compounds is the 4-(methylthio)benzaldehyde and is commercially available, then the synthesis consists only in the condensation with *N,N'*-dihydroxy-2,3-dimethylbutane and in the consequent oxidization and isolation of the final product. This synthesis exactly reproduces the general procedure described earlier and is summarized in the scheme sketched in Fig. 5.2.

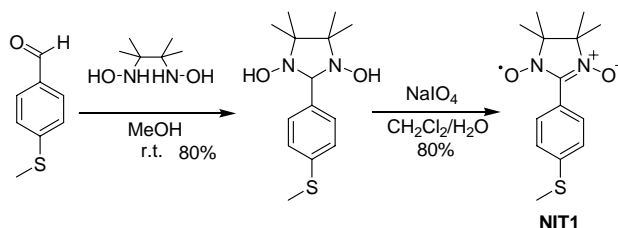


Figure 5.2. Scheme of the preparation of NIT1.

In order to exclude the presence of over-oxidized species in the final product we characterized it by Electron Spin Resonance. The spectrum and its temperature dependence were recorded on the same solution used for the deposition on gold. (Fig. 5.3).<sup>15</sup>

The fluid solution (room temperature) ESR spectrum is composed of 5 lines with relative intensity 1:2:3:2:1 arising from the coupling of the electron spin  $S=1/2$  with the two equivalent  $^{14}\text{N}$  ( $I=1$ ) nuclei. On cooling the isotropic hyperfine structure is smeared out due to slow motion and disappears at lower temperature.

Bulk magnetic properties of this radical have been widely investigated in past years, in particular it has been shown by neutron diffraction studies on crystalline samples (Pontillon Y. et al. 1999) that the spin density is shared between nitrogen

the solution usually turns to dark blue or red for an aromatic and an aliphatic residue, respectively. Being the superoxidized species yellow or orange, the observation of a greenish tonality indicates that the reaction has already proceeded too far. The workup usually consists of a filtration to eliminate solid residues, and washing (4-5 times) with water to remove the remnant oxidizing agent. The solution is then dried over  $\text{MgSO}_4$  and evaporated under reduced pressure to give a coloured, crystalline product. When further purification is needed it is performed on a  $\text{SiO}_2$  chromatographic column, using  $\text{Et}_2\text{O}$  as eluent.

<sup>15</sup> ESR measurements were carried out on an X-band Bruker Elexsys E500 spectrometer equipped with a ER 4131VT liquid nitrogen cryostat for variable temperature studies and a ER4122SHQE cavity to enhance the sensitivity of the instruments.

and oxygen atoms and a non-negligible spin density has also been found on the methylenic tail as sketched in the following figure.

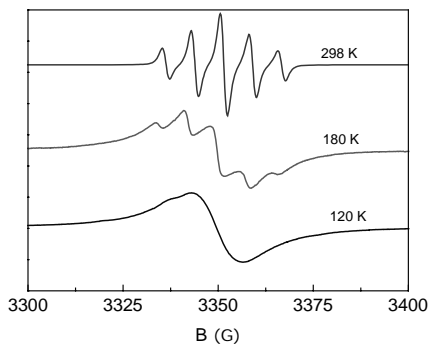


Figure 5.3. X-band ESR spectra of NitPhSMe in  $\text{CH}_2\text{Cl}_2$  in function of the temperature of the solution.

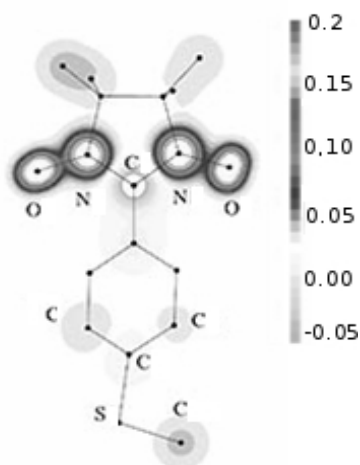


Figure 5.3. Experimental spin probability density obtained from polarized neutron diffraction data on the NIT1 radical. Image courtesy of A. Caneschi. Original data extracted from Pontillon Y. et al. 1999.

### 1.3 The bi-phenyl derivative of Nitronyl Nitroxides

As it will be described in Chapter 6, in order to improve the ordering of the monolayer of these molecules, the NIT1 radical has been modified by including a second phenyl ring with the objective of increasing the  $\pi$ - $\pi$  stacking lateral interactions in the assem-

bly on the surface. In this case the synthesis is more complex, due to the non-availability of the corresponding aldehyde obtained with a Suzuki coupling reaction.<sup>16</sup> The NitPhPhSMe (NIT2) radical was obtained by the standard condensation<sup>17</sup> followed by their oxidation that has been carried out following a new procedure based on the use of TPAP-NMO oxidizing reactant<sup>18</sup> (Gorini L. et al. 2006).

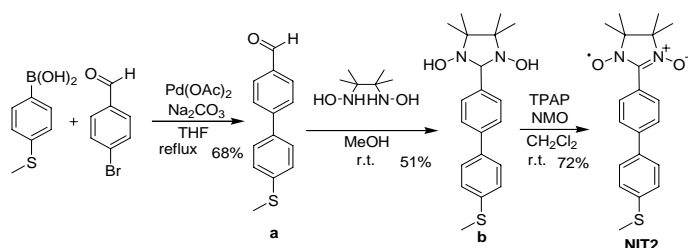


Figure 5.4 Scheme of the preparation of NIT2

The complete synthesis process is described in the above sketched scheme (Fig. 5.4). Also the purity of this product has been verified through ESR spectroscopy of a  $\text{CH}_2\text{Cl}_2$  solution. As shown in Figure 5.5 the room temperature spectrum evidences the same features observed for NIT1. On the other hand lower temperature spectra show different details, probably due to the lower concentration of the solution, resulting in a more resolved structure.

<sup>16</sup> To a solution of 4-methylthioboronic acid (1 eq, 4.5 mmol, 759 mg) in 18 mL of dry tetrahydrofuran, 4-bromobenzaldehyde (1.1 eq, 4.98 mmol, 924 mg),  $\text{Na}_2\text{CO}_3$  (2 eq, 9 mmol, 954 mg),  $\text{Pd}(\text{OAc})_2$  (0.1 eq, 0.45 mmol, 101 mg) were added. The mixture was heated to reflux under nitrogen. After 16 h  $\text{Pd}(\text{OAc})_2$  (0.05 eq, 0.225 mmol, 50 mg) was added. The reaction was followed by TLC. After 24 h the reaction mixture was cooled and the solid phase was filtered. The solution was diluted with dichloromethane, washed with water (3x) and brine (1x), dried on  $\text{Na}_2\text{SO}_4$ . The crude material was further purified on a silica gel column using petroleum benzene: diethyl ether = 10:1 as an eluent to give the intermediate a (697 mg, 68%).  $^1\text{H-NMR}$  (300MHz,  $\text{CDCl}_3$ )  $\delta$ (ppm) = 10.04 (s, 1H, CHO), 7.94 (m, 2H, Ar), 7.73 (m, 2H, Ar), 7.57 (m, 2H, Ar), 7.34 (m, 2H, Ar), 2.56 (s, 3H,  $\text{CH}_3$ ).

<sup>17</sup> 4,4,5,5-Tetramethyl-2-(4'-methylsulphonyl-biphenyl-4-yl)-imidazolidine-1,3-diol (b). To a solution of aldehyde a (1 eq, 0.96 mmol, 220 mg) in 5 mL of methanol:dichloromethane=3:2, 2,3-di(hydroxyamino)-2,3-dimethylbutane (2 eq, 1.92 mmol, 284 mg) was added. The solution was stirred at room temperature overnight. The white solid material was filtered, washed with methanol and dried to give the intermediate b as white solid (175 mg, 51%).  $^1\text{H-NMR}$  (300MHz,  $\text{DMSO-d}_6$ )  $\delta$ (ppm) = 7.78 (s, 2H, 2OH), 7.63-7.59 (m, 2H, Ar), 7.56-7.53 (m, 1H, Ar), 7.35 (m, 1H, Ar), 4.55 (s, 1H, NCHN), 2.51 (s, 3H,  $\text{SCH}_3$ ), 1.09 (s, 6H, 2 $\text{CH}_3$ ), 1.07 (s, 6H, 2 $\text{CH}_3$ ).

<sup>18</sup> 4,4,5,5-Tetramethyl-2-(4'-methylsulphonyl-biphenyl-4-yl)-imidazolidine-1,3-diol (b, 1 eq, 0.47 mmol, 170 mg) was dissolved in 5 mL of dichloromethane. *N*-tetrapropylammonium peruthenate (0.05 eq, 0.023 mmol, 8 mg) and *N*-methylmorpholine *N*-oxide (1 eq, 0.47 mmol, 55 mg) were added in sequence and the reaction mixture left at room temperature under stirring until the complete disappearance of the starting material monitored by TLC. After 1.5 h the crude is purified on a silica-gel column using diethyl ether as eluent. The product NIT2 was obtained as a blue powder (83 mg, 72%).

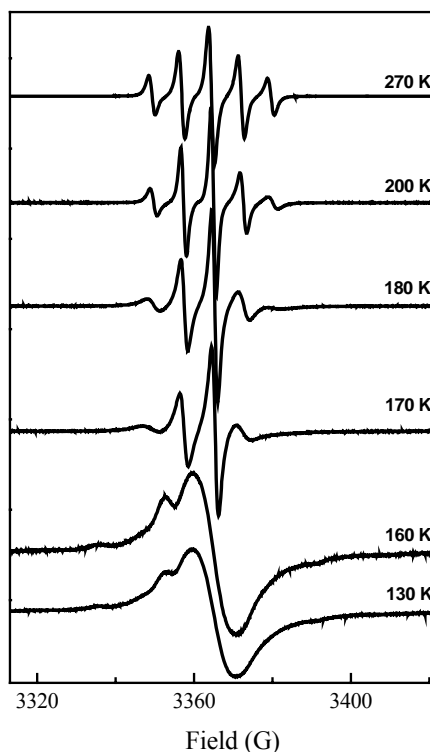


Figure 5.5. X-band ESR spectra of NIT2 in  $\text{CH}_2\text{Cl}_2$  in function of the temperature of the solution.

#### 1.4 The benzylic derivative of Nitronyl Nitroxides

The last component of this series of radicals has been obtained introducing a methylenic moiety instead of a second phenyl ring. This apparent slight modification as well as the previous one has however required a fine chemistry work as resumed in the following paragraph and described more in details in another PhD Thesis (Gorini L. 2007). In any case these synthetic efforts allowed us to obtain interesting results in deposition described in Chapter 6. In particular in this last case, the introduction of a  $\text{CH}_2$  spacer group between the sulphur atom and the aromatic ring improved the ordering of the monolayer, as we expected from the suggestions found in the literature (Tao Y.-T. et al. 1997). The steps occurred to prepare the third radical are here summarized and sketched in Figure 5.6.

First of all a five-step reaction<sup>19</sup> has been needed to produce the non commercial aldehyde (m).

<sup>19</sup> i) 4-Bromomethyl benzonitrile (1 eq, 26 mmol, 5 g) was dissolved at 40°C in 45 mL of ethanol. A solution of sodium methanethiolate (1 eq, 26 mmol, 1.8 mg) in 10 mL of ethanol was added. The suspension was

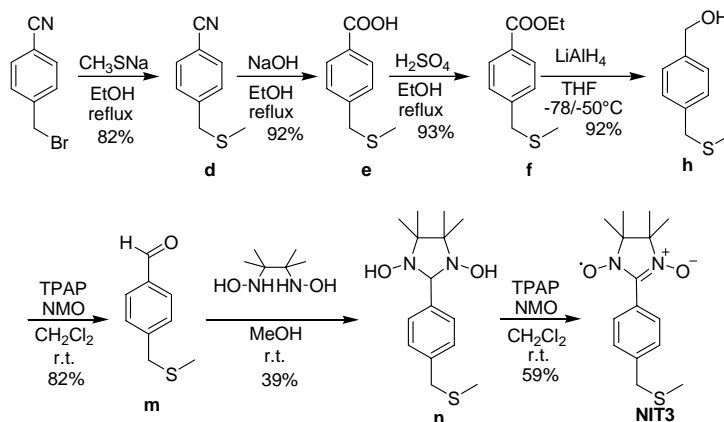


Figure 5.6. Scheme of the preparation of NIT3.

stirred at reflux for 1 h. The reaction mixture was then cooled at room temperature and the solid phase filtered. Water was added to the solution and after extraction with diethyl ether the solvent was evaporated to give the pure product **d** (4-Methylsulphanylmethyl benzonitrile) as a white solid (3.5 g, 82%).  $^1\text{H-NMR}$  (300MHz,  $\text{CDCl}_3$ )  $\delta$  (ppm)= 7.62 (m, 2H, Ar), 7.42 (m, 2H, Ar), 3.70 (s, 2H,  $\text{CH}_2$ ), 1.99 (s, 3H,  $\text{CH}_3$ ).

ii) Nitrile **d**, (1 eq, 21 mmol, 3500 mg) was added to 30 mL of NaOH 10%. The solution was heated to reflux for 4 h and then cooled to room temperature. The yellow solution was washed with diethyl ether (2x) and acidified with HCl 10% to give the crude as a yellow solid. The solid was filtered, dried on  $\text{P}_2\text{O}_5$  overnight and purified on a silica-gel column using diethyl ether:petroleum benzene=2:1 as eluent to give the intermediate **e** (4-Methylsulphanylmethyl benzoic acid) as a white solid (3.5 g, 92%).  $^1\text{H-NMR}$  (300MHz,  $\text{DMSO-d}_6$ )  $\delta$  (ppm)= 12.9 (bs, 1H,  $\text{COOH}$ ), 7.93 (m, 2H, Ar), 7.46 (m, 2H, Ar), 3.79 (s, 2H,  $\text{CH}_2$ ), 1.99 (s, 3H,  $\text{CH}_3$ ).

iii) A solution of 4-methylsulphanylmethyl benzoic acid (**e**, 9 mmol, 1.64 g) in 15 mL of ethanol and  $\text{H}_2\text{SO}_4$  conc. (1 mL) was stirred at reflux for 4 h. After cooling dichloromethane was added and the solution washed with water (2x), a solution of  $\text{NaHCO}_3$  sat (2x) and brine. The solvent was evaporated and the product **f** (4-Methylsulphanylmethyl benzoic acid ethyl ester) obtained as a colourless oil (1.75 g, 93%).  $^1\text{H-NMR}$  (300MHz,  $\text{CDCl}_3$ )  $\delta$  (ppm)= 7.99 (m, 2H, Ar), 7.36 (m, 2H, Ar), 4.36 (q,  $J=8.1$  Hz, 2H,  $\text{CH}_2\text{CH}_3$ ), 3.69 (s, 2H,  $\text{CH}_2\text{SCH}_3$ ), 1.97 (s, 3H,  $\text{SCH}_3$ ), 1.38 (t,  $J=8.1$  Hz, 3H,  $\text{CH}_2\text{CH}_3$ ).

iv) 4-Methylsulphanylmethyl benzoic acid ethyl ester (**f**, 1 eq, 8.4 mmol, 1.75 g) was dissolved in 30 mL of dry tetrahydrofuran under nitrogen. The solution was cooled at  $-78^\circ\text{C}$  and  $\text{LiAlH}_4$  (1.5 eq, 12.6 mmol, 479 mg) was added. The reaction mixture was stirred for 2 h at  $-78/-50^\circ\text{C}$ , under nitrogen. A solution of HCl 10M was added drop to drop until pH=2 was reached. The product was extracted with diethyl ether (3x), the organic phase was washed with water, a solution of  $\text{NaHCO}_3$  sat (2x), brine and dried on  $\text{Na}_2\text{SO}_4$ . The solvent was evaporated to give the product **h** ((4-Methylsulphanylmethyl-phenyl) methanol) as a colourless oil (1.3 g, 92%).  $^1\text{H-NMR}$  (300MHz,  $\text{DMSO-d}_6$ )  $\delta$  (ppm)= 7.29 (m, 4H, Ar), 5.18 (t,  $J=6.5$  Hz, 1H,  $\text{OH}$ ), 4.52 (d,  $J=6.5$  Hz, 2H,  $\text{CH}_2\text{OH}$ ), 3.70 (s, 2H,  $\text{CH}_2\text{SCH}_3$ ), 1.98 (s, 3H,  $\text{SCH}_3$ ). v) (4-Methylsulphanylmethyl-phenyl) methanol (**h**, 1 eq, 7.73 mmol, 1.3 g) was dissolved in 70 mL of dichloromethane. *N*-tetrapropylammonium perruthenate (0.05 eq, 0.386 mmol, 135 mg) and *N*-methylmorpholine *N*-oxide (1 eq, 7.73 mmol, 904 mg) were added in sequence and the reaction mixture left at room temperature under stirring for 1.5 h. The brown solid was filtered off on silica, the solution was washed with water (2x), brine (1x) and dried on  $\text{Na}_2\text{SO}_4$ . After evaporating the solvent, the aldehyde **m** (4-Methylsulphanylmethyl benzaldehyde) was obtained as a yellow oil (1.18 g, 82%).  $^1\text{H-NMR}$  (300MHz,  $\text{CDCl}_3$ )  $\delta$  (ppm)= 10.00 (s, 1H,  $\text{CHO}$ ), 7.85 (m, 2H, Ar), 7.47 (m, 2H, Ar), 3.73 (s, 2H,  $\text{CH}_2$ ), 2.00 (s, 3H,  $\text{CH}_3$ ).

The standard condensation permitted to produce the radical precursor *n* that has been oxidized again using the new oxidizing procedure<sup>20</sup> (Gorini L. et al. 2006).

Following the procedure used for previous derivatives also the purity of this compound has been checked by measuring solution ESR spectra as a function of temperature (Fig. 5.7).

In addition to this, we measured a very diluted solution ( $10^{-9}$  M) of this radical (Fig. 5.8), in order to use experimental conditions comparable to those necessary to obtain a spectrum of a monolayer deposit.

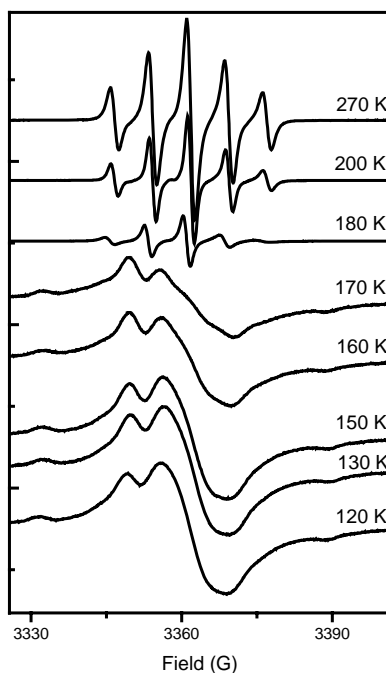


Figure 5.7. X-band ESR spectra of NitPhCH<sub>2</sub>SMe in CH<sub>2</sub>Cl<sub>2</sub> in function of the temperature of the solution.

<sup>20</sup> i) To a solution of aldehyde *m* (1 eq, 4.2 mmol, 700 mg) in 25 mL of methanol, 2,3-di(hydroxyamino)-2,3-dimethylbutane (1.5 eq, 6.3 mmol, 932 mg) was added. The solution was stirred at room temperature overnight. The white solid material was filtered, washed with methanol and dried to give the intermediate *n* (4,4,5,5-Tetramethyl-2-(4-methylsulphanyl-methyl-phenyl)-imidazolidine-1,3-diol) as a white solid (480 mg, 39%). <sup>1</sup>H-NMR (300MHz, DMSO-*d*<sub>6</sub>) δ (ppm)= 7.60 (s, 2H, 2OH), 7.27 (m, 2H, Ar), 7.10 (m, 2H, Ar), 4.34 (s, 1H, NCHN), 3.53 (s, 2H, CH<sub>2</sub>SCH<sub>3</sub>), 1.82 (s, 3H, SCH<sub>3</sub>), 0.92 (s, 6H, 2CH<sub>3</sub>), 0.89 (s, 6H, 2CH<sub>3</sub>).

ii) 4,4,5,5-Tetramethyl-2-(4-methylsulphanyl-methyl-phenyl)-imidazolidine-1,3-diol (*n*, 1 eq, 1.62 mmol, 480 mg) was dissolved in 13 mL of dichloromethane. *N*-tetrapropylammonium perruthenate (0.05 eq, 0.081 mmol, 28 mg) and *N*-methylmorpholine *N*-oxide (1 eq, 1.62 mmol, 189 mg) were added in sequence and the reaction mixture left at room temperature under stirring until the complete disappearance of the starting material monitored by TLC. After 1.5 h the crude is purified on a silica-gel column using diethyl ether as eluent. The product NIT3 was obtained as a blue powder (281 mg, 59%).

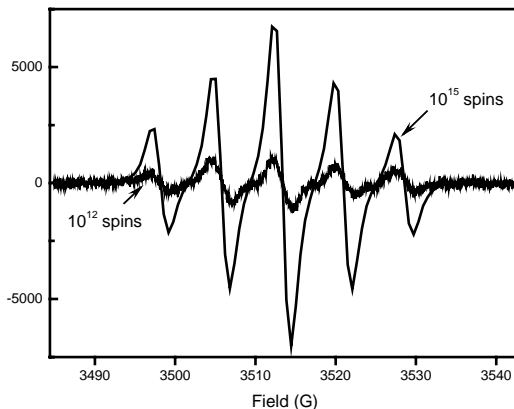


Figure 5.8. Room temperature X-band ESR spectra of NIT3 in  $\text{CH}_2\text{Cl}_2$  in function of the quantity of spins contained in the examined solutions.

### 1.5 Aliphatic disulphide derivative of Nitronyl Nitroxides

Besides the series of aromatic derivatives, we investigated also a different Nitronyl Nitroxide molecule based on a di-alkyl sulphide linker group. This molecule has been used to prepare patterned surfaces as it will be described in Chapter 6; its synthesis required also in this case to prepare the aldehyde because it is not commercially available and in this case we followed the procedure described here based on the direct reduction of the earlier described decylthioundecanoic acid (p) to the corresponding 11-(decylthio)undecanal (r) through the use of the hexyl(bromo)borane-dimethyl sulphide that allows the quantitative reduction of aliphatic carboxylic acids without damaging the dialkyl sulphide moiety (Cha J. S. et al. 1987a; Cha J. S. et al. 1987b). This reaction is due to the substitution of the bromine group of the reagent by a carboxylate to form a hexyl(acyloxy)borane; the acyloxy group is then easily reduced to aldehyde by another equivalent of the reagent probably via a cyclic intermediate.

The aldehyde has been recovered by exploiting the Bertagnini reaction (a bisulphide adduct) and then regenerated by basic catalysis (Craig J. C. and Hamon D. P.G. 1965). The followed reaction is described in the footnotes.<sup>21</sup>

<sup>21</sup> An oven-dried 250 mL flask, fitted with a side arm and bent adaptor connected to a Hg bubbler, was charged with 9.5g of decylthioundecanoic acid (HC10SC10, see Chapter 4) and 17.5 mL of distilled  $\text{CS}_2$ . The flask was immersed in a cold bath and maintained at  $-20^\circ\text{C}$ . A pre-cooled 3 M solution of the Hexylbromoborane-Dimethyl Sulphide (q) (Cha J. S. et al. 1987a) in  $\text{CH}_2\text{Cl}_2$  (8.3 mL, 26.5 mmol) was added dropwise with stirring. After complete evolution of the  $\text{H}_2$ , the cold bath was removed, and the reaction mixture was warmed to room temperature. An additional 1.1 equivalent of q (9.2 mL, 29.2 mmol) was added and the reaction mixture was stirred for 1 h at room temperature. The reaction mixture

The obtained aldehyde was then condensed and oxidized to the corresponding nitronyl nitroxide (NitC10SC10, NIT4) as described in the general procedure with standard oxidation with  $\text{NaIO}_4$ . In scheme presented in Fig. 5.9 the complete reaction steps are sketched.

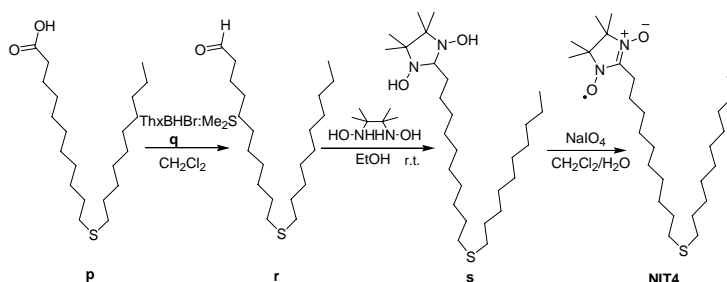


Figure 5.9 Scheme of the preparation of NIT4.

Also in this case a solution of this radical (NIT4) was characterized by ESR technique (Figure 5.10) to assess the effective purity of the compound. The spectral pattern in this case is somehow different with respect to the aromatic nitronyl nitroxide derivatives. In fact an additional hyperfine splitting due to coupling with 2 equivalent  $^1\text{H}$  ( $I=1/2$ ) nuclei in  $\alpha$  position with respect to the Nitronyl Nitroxide is observed.

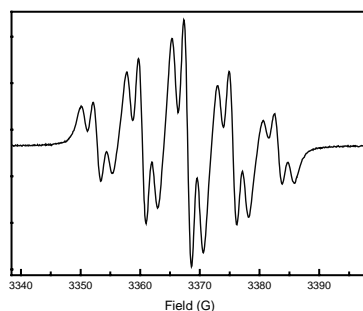


Figure 5.10. Room temperature X-band ESR spectra of NitC10SC10 in  $\text{CH}_2\text{Cl}_2$ .

was then transferred via a double-ended needle to a flask containing 25 mL of water in an ice-water bath and was hydrolyzed with vigorous stirring for 1 h at room temperature. The mixture was saturated with  $\text{NaCl}$  and separated organic layer was treated with  $\text{NaHCO}_3$  in order to neutralize the acidity. Then this solution was reversed on a 40 mL saturated solution of  $\text{NaHSO}_3$  and 85 mL of THF was added maintaining under vigorous stirring for 1h. Then the reaction mixture was cooled observing the precipitation of the adduct as expected (Brown H. C. et al. 1987). Under vigorous stirring 26 g. of this adduct was gradually added to an heated to  $90^\circ\text{C}$  mixture of an aqueous solution of 40g. of  $\text{Na}_2\text{CO}_3$  (400 mL) and heptane (400mL). When  $\text{CO}_2$  production was ceased this mixture was added to a 500mL of water and the organic layer was separated. Removing the solvent a pure 11-(decylthio)undecanal (r) was obtained. Elemental analysis (%) on a vacuum-dried sample calculated for  $\text{C}_{21}\text{H}_{42}\text{S}$  (r) C 73.62, H 12.36; found: C 73.92, H 12.86.  $^1\text{H-NMR}$  (300MHz,  $\text{CDCl}_3$ )  $\delta$  (ppm)= 9.79 (s, 1H,  $\text{CHO}$ ), 2.52 (t, 4H,  $J=2$  Hz,  $\text{CH}_2\text{S}$ ), 2.45 (t, 2H,  $J=2$  Hz,  $\text{CH}_2\text{CHO}$ ), 1.60 (m, 6H), 1.28 (m, 26H), 0.9 (q, 3H,  $\text{CH}_3$ ).

## Chapter 6

### Deposition of magnetic molecules on gold surfaces

All the synthesis of the compounds with sulphur containing linker groups described in previous Chapters have been specifically planned with the final purpose of the deposition on gold surfaces. This surface, already described in Chapter 3, is chemically inert, conductive, and easily prepared into flat, clean surfaces. It thus represents the perfect starting point for the study of single molecule properties directly from single objects.

In fact this combination is defined by our purpose to use the Self-Assembling of Monolayer technique (Ulman A. 1996; Schreiber F. 2000) as well as by the limitation due to redox stability of the complex systems that we want to deposit on the surface without effective changes in expected magnetic properties.

The next paragraphs will be devoted to the description of different methods we used to deposit these molecules and of surface characterizations that allowed us to confirm the actual deposition of these materials. We will describe first our efforts in deposition of Mn12 derivatives, the jewel of molecular nanomagnetism. Their deposition and the investigation of their magnetism represent one of the major goals of this research area also for the possible implications in quantum computation (Park H. et al. 2000; Leuenberger M. N. and Loss D. 2001).

In the second part of this chapter we decrease the complexity of the deposited molecules by investigating the deposition of simpler organic radicals. This subject seems to be less complex and less interesting compared to the previous ones, however the successful deposition of some radicals triggered many possibilities in the field of spintronics applications (Wolf S. A. et al. 2001; Tsukagoshi K. et al. 1999; Prinz G. A. 1998; Ouyang M. and Awschalom D. D. 2003; Sharma P. 2005; Rocha A. R. et al. 2005) Moreover also theoretically Nitronyl Nitroxides were suggested to be good candidates of spin  $\frac{1}{2}$  qubits for self assembled monolayer quantum devices (Rinkevicius Z. et al. 2004). For this reason strong efforts have been focused on the organization on surface as well as on the characterization on surface in order to achieve ordered monolayers of organic radicals conserving their properties on these ultrathin-film.

Finally, in the next chapter our first attempts of reading magnetism of the single layer as well as the magnetism of the single molecule will be reported, as they represent the final objective of this thesis work.

#### 1. Deposition and characterization of SMMs on surface

Different strategies have been proposed for the preparation of monolayers or sub-monolayers of SMMs on surfaces based on either covalent, electrostatic or Van der

Waals interactions (Cornia et al. 2006). In each case, the required complementarity between the molecule and the surface can be attained by properly functionalizing the cluster periphery, the surface or both as we have described in previous chapters in the specific case of direct depositions on gold surface.

Before describing our results we will provide a short overview of the different strategies for the deposition of Mn<sub>12</sub> clusters that have recently appeared in the literature.

The first-reported attempt to organize SMMs into two dimensional arrays was undertaken by Clemente-León et al. (Clemente-León M. et al. 1998; Clemente-León M. et al. 1998) using the Langmuir Blodgett (LB) technique (Roberts G. 1990) where the ability of an amphiphilic molecule to form monolayers at the air-water interface was exploited to prepare a hybrid film incorporating Mn<sub>12</sub> complexes not specifically modified for this purpose.

The previous approach permits only an indirect deposition and suffers of intrinsic problems of the LB technique. More recently, but before the start of this thesis work, our group presented the first solution for a direct deposition of functionalized Mn<sub>12</sub> molecules (Mn<sub>12</sub>LC15, 2) on gold surface through covalent S-Au bonds (Cornia A. et al. 2003). The use of these interactions has several advantages because in principle it allows the deposition of a single layer and improves the chemical stability of the resulting adsorbates and it has therefore been adopted also for this thesis.

Other research groups have explored different strategies: for instance the covalent anchoring of native SMMs can be alternatively carried out by surface pre-functionalization with carboxylate groups. Then Mn<sub>12</sub> molecules can be attached to this passivated surface via an *in-situ* ligand exchange reaction. The first attempt in this direction was reported by Condorelli et al. (Condorelli G. G. et al. 2004). These authors used hydrogen-terminated Si(100) passivated with methyl-10-undecanoate. The subsequent hydrolysis of the ester group of the grafted monolayer leads to carboxylic functions which actively bind Mn<sub>12</sub>-acetate clusters through a ligand exchange reaction.

A similar strategy has been followed by Fleury et al. to graft a mixed-ligand derivative,  $[Mn_{12}O_{12}(CHCl_2CO_2)_8(ButCH_2CO_2)_8(H_2O)_3]$  on the Si(100) surface (Fleury B. et al. 2005).

The covalent anchoring of SMMs onto pre-modified surfaces has proved to be possible also using gold substrates pre-functionalized with 11-mercaptoundecanoic acid (Nait Abdi A. et al. 2004; Steckel J. S. et al. 2004) or with 16-Mercaptohexadecanoic acid (Nait Abdi A. et al. 2005).

### 1.1 Homogeneous monolayers

The results obtained in our group for homogeneous layers of Mn<sub>12</sub>LC15 (2) on gold (Cornia A. et al. 2003) have been reproduced during this thesis in order to improve the reproducibility of the deposition procedure as well as to have the possibility to investigate in an exhaustive way the chemical and physical properties of these monolayers.

As to the original procedure, the strategy has been slightly modified in order to optimize the deposition, as described in the footnote.<sup>22</sup>

The success of the deposition procedure has been verified through STM analysis. Figures 6.1(a) and 6.1(b) show a high degree of homogeneity of this deposition; also in very large areas it is possible to observe a complete coverage and to recognize circular objects of size 5-6 nm, in reasonable agreement with the size of 2 obtained from molecular modelling studies (5.0-5.6 nm) (see Fig. 4.3 in Chapter 4). Disorder may originate from the specific arrangement of the alkyl chains of the deposited molecules that, for sterical reasons, prevents the epitaxial growth of the monolayer otherwise observed for smaller systems like simple thiols.

However, it is important to notice that the features of gold surfaces, like atomic steps and triangular dislocation, due to the misfit with the underneath mica surface, are observed also in presence of this layer of molecules. This strongly supports the effective deposition of only one layer of molecules as confirmed by the molecular ruler technique described in Chapter 6. Moreover this observation suggests that in the STM experiments we are observing a two step tunneling (Salomon A. et al. 2003): electrons coming from the tip “jump” at first to the Mn12 molecule and then tunnel to the gold surface.

This process happens only for certain applied voltages; in fact we can suppose that, for specific bias voltages, the molecular orbitals approach the Fermi level of the tip and electrons tunnel to the empty states of the molecule (Salomon A. et al. 2003). This process happens because the tip-molecule distance is much shorter than the distance that separates the tip from the gold. The electrons, shortly after, pass to the gold substrate either through the bound ligand or by tunneling.

A confirmation of this hypothesis can be obtained by applying a lower bias voltage. In this case the image of the clusters disappears (Figure 6.1c). Increasing again the bias voltage and enlarging the scanned area we can observe (Figure 6.1d) that molecules become again visible but this process is not completely reversible, in fact decreasing the bias voltage we decreased the distance between the tip and the surface thus mechanically disturbing the monolayer.

In order to corroborate the topographical indications of the presence of 2 on gold surface, different surface analysis techniques have been employed. The most significant is represented by X-ray Photoelectron Spectrometry (XPS) analysis that has been done on these samples in collaboration with Dr. Davide Barreca (Univer-

<sup>22</sup> The preparation procedure consists in dissolving the Mn12 derivative (2) (6.9 mg, 1.1  $\mu$ mol) in 4 mL of tetrahydrofuran and to add 5.4  $\mu$ L of  $\text{NH}_3$ (aq, 25% v/v) to facilitate deacylation of thioacetyl groups and to promote robust anchoring to the gold surface through Au-thiolate bonds as described in literature for simpler thioacetyl compounds (Tour J. M. et al. 2003). After 24 h, needed for the ageing of the 0.2mM solution of Mn12 derivative, a flame annealed Au(111) substrates (prepared following steps described in Chapter 3) was dropped in this solution and incubated for 24 h in order to achieve the complete coverage of the surface as confirmed via cyclic voltammetry (CV) during another work of thesis (Zobbi L. 2004) and not shown in this manuscript. The slides are carefully removed from the solution under nitrogen environment and washed subsequently with THF and  $\text{CH}_2\text{Cl}_2$  and finally dried under nitrogen flux.

sity of Padova) and supported by previous data reported in the literature both on bulk sample (Kang J. S. et al. 2002) and on deposited films (Cornia A. et al. 2003).

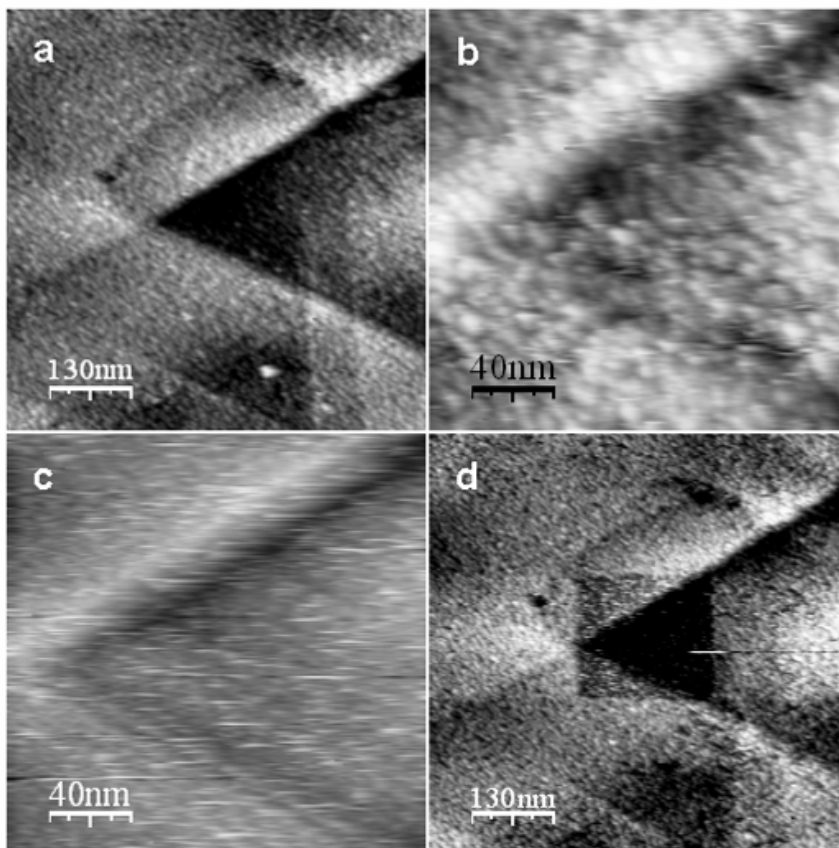


Figure 6.1. Unfiltered STM images of Mn12LC15 (2) deposited on flame annealed gold (111). In (a) is presented a  $650 \times 650 \text{ nm}^2$  scan while in (b) a zoom to a  $200 \times 200 \text{ nm}^2$  area in the same zone is shown. (a) and (b) are recorded at bias voltage of 1.8V. In (c) the same area of (b) is recorded at 0.8V while in (d) the successive scan to the same area presented in (a) and recorded again at 1.8V is presented. All the presented images have been acquired using a low current head in constant current mode with a set point of  $\sim 4.5 \text{ pA}$ .

Au(111)-adsorbates of 2 have been prepared in the best adsorption conditions, as indicated by electrochemical studies (Zobbi L. 2004), and spectral properties of the layers have been recorded for different deposition times and compared to a reference consisting of a bulk deposit obtained via drop casting on the substrate.

The spectra are shown in Figure 6.2 and reveal, already after 30' immersion, all the peaks expected from the chemical composition of 2, with binding energies (*BEs*) in agreement with the reference sample. The *BE* of Mn2p<sub>1/2</sub> peak (653.7 eV) for the grafted layer agrees closely with that observed on bulk samples of Mn12-*acetate* (Kang J. S. et al. 2002). Two different oxygen signals are supposed to contribute to

the found broadened signal. The two peaks have been assigned to the 12 oxygen atoms in the  $Mn_{12}O_{12}$  core and to the remaining 52 oxygen atoms from carboxylate and water ligands, respectively. This interpretation is consistent with that suggested in the XPS analysis of  $Mn_{12}$ -acetate (Kang J. S. et al. 2002) and is supported by a comparison with the BE's found in  $Mn_2O_3$  and  $MnO_2$  (529÷530 eV) (Strohmeier B. R. and Hercules D. M. 1984).

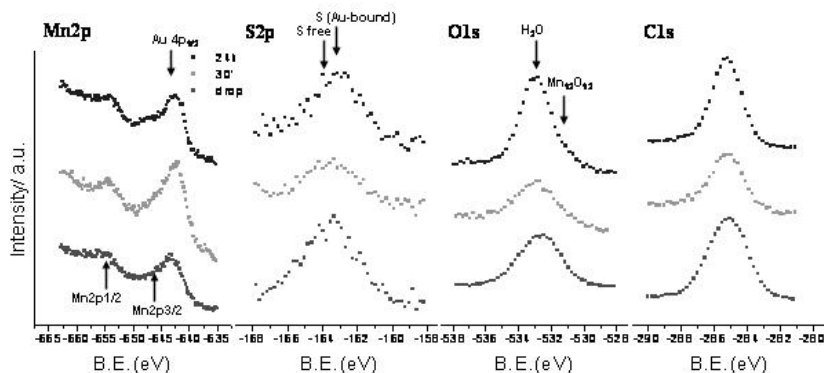


Figure 6.2. XPS core-level spectra of Au(111) films after 30' (middle, light gray) and 24h (down, dark gray) of immersion in a 24hrs old THF/ $NH_3$ (aq) solution of 2, compared to a bulk deposition obtained by drop-casting using a saturated solution of 2 in  $CH_2Cl_2$  (up, black). The spectra of each element are on the same absolute scale.

It is well known that the BEs of S(2p) electrons can be used to discriminate between free (163.4 eV) and Au-bound (161.9 eV) sulphur atoms in thiols (Takiguchi H. et al. 2000). However the experimental resolution in our experiments, as well as in the previous investigations, does not permit to resolve this small difference and assign the signals. We can thus only deduce the contemporaneous presence of both the free and the bound to gold sulphur atoms.

Semi-quantitative analysis of the chemical composition of the layer has led to atomic percentages in excellent agreement with the calculated ones (Table 6.1). These results provide clear evidence for the presence of Au-bound  $Mn_{12}$  adsorbates.

Table 6.1. Experimental XPS data and expected composition of the layer of 2. [a] Relative to Au( $4f_{7/2}$ ). O1s' and O1s'' corresponds to the oxygen near the Mn atoms and the ones of water molecules, respectively.

Peak	BE (eV) <sup>[a]</sup>	Atom% (Exptl)	Atom% (Calcd)
Mn3p	48.8	3.1	3.2
S2p	162.6	4.0	4.2
C1s	285.1	75.2	75.8
O1s'	530.3	3.2	3.2
O1s''	532.3	14.5	13.6

Another technique that has been used to characterize Mn12 functionalized surface was the Time-of-Flight Secondary Ion Mass Spectrometry (Vickerman J. C. and Briggs D. 2001). As previously discussed, this technique allows to obtain mass spectra directly from the deposited monolayer with a very high sensitivity and spatial resolution. These data have been employed also as standards in the characterization of surface patterned deposits that will be described in Paragraph 1.4 (Mannini M. et al. 2005). The ToF-SIMS data of a monolayer of 2 have been acquired in collaboration with Federica M. Piras of the Technology and University Centre of Colle di Val d'Elsa, University of Siena.

The positive ToF-SIMS spectrum<sup>23</sup> of a homogeneous SAM of 2 on gold is reported in Figure 6.3.

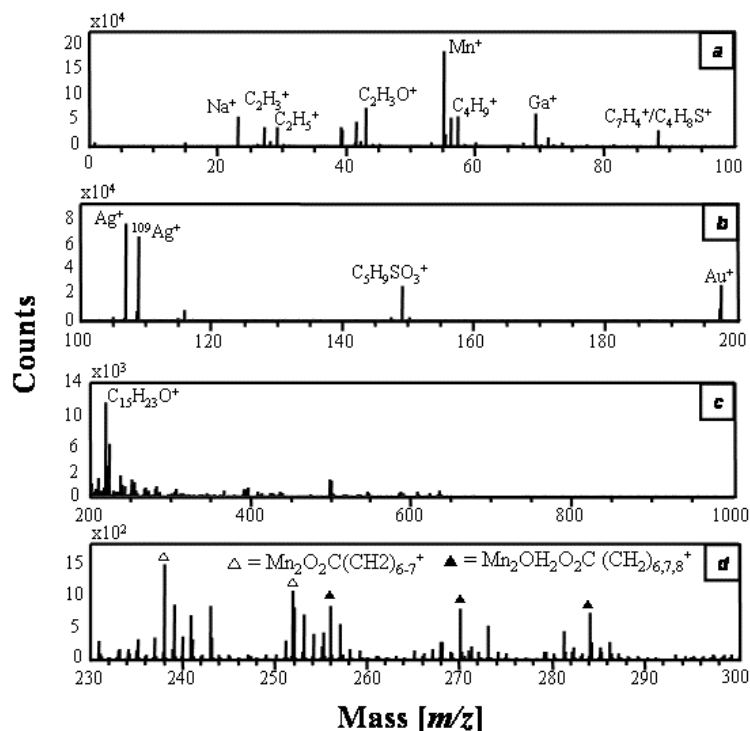


Figure 6.3. Positive ion ToF-SIMS spectrum of SAM of 2 on gold. In d, the spectral region between 230  $m/z$  and 300  $m/z$  is shown in detail. Reproduced with permission from Mannini M. et al. 2005. Copyright 2005 American Chemical Society.

<sup>23</sup> ToF-SIMS analysis was carried out with a TRIFT III time-of-flight secondary ion mass spectrometer (Physical Electronics, Chanhassen, MN, USA) equipped with a  $69\text{Ga}^+$  liquid-metal primary ion source. Positive and negative ion spectra were acquired with a pulsed, bunched 15 keV primary ion beam at 600 pA by rastering the ion beam over a  $100\ \mu\text{m} \times 100\ \mu\text{m}$  sample area. Positive data were calibrated to  $\text{CH}_3^+$  (15.023  $m/z$ ),  $\text{C}_2\text{H}_3^+$  (27.023  $m/z$ ) and  $\text{AuSCH}_2^+$  (242.954  $m/z$ ).

Characteristic peaks assigned as molecular ion fragments of **2** are observed. The most intense peak detected in the lower mass region (0-100  $m/z$ ) is the  $Mn^+$  signal at 55  $m/z$ . In the spectral region between 100 and 200  $m/z$ , the peak at 149  $m/z$  can be assigned to an oxidized ligand-fragment ( $C_5H_9SO_3^+$ ); the peaks at 197  $m/z$  ( $Au^+$ ), 107  $m/z$  ( $Ag^+$ ) and 109  $m/z$  ( $^{109}Ag^+$ ) are attributed to the gold substrate and silver contamination of gold, respectively. The spectral region between 200 and 300  $m/z$  contains the most significant signals, corresponding to molecular ion fragments of **2**. As shown in Figure 6.3d, two groups of fragments of formula  $Mn_2O_2C(CH_2)_{6-7}$  and  $Mn_2(OH_2)O_2C(CH_2)_{6-8}$ , respectively, have been detected. In Table 6.2 we list the characteristic peaks in positive ion ToF-SIMS spectrum.

Table 6.2. Characteristic peaks in the positive ion ToF-SIMS spectrum of **2** SAMs on gold.

Peak ( $m/z$ )	Molecular formula	Ion description
43	$C_2H_3O^+$	Ligand fragment
55	$Mn^+$	
88	$C_7H_4^+/C_4H_8S^+$	Ligand fragment
149	$C_5H_9SO_3^+$	Oxidized ligand fragment
197	$Au^+$	Substrate
219	$C_{15}H_{23}O^+$	Ligand fragment
238	$Mn_2O_2OC(CH_2)_6^+$	Ion fragment of ( <b>2</b> )
252	$Mn_2O_2C(CH_2)_7^+$	Ion fragment of ( <b>2</b> )
256	$Mn_2(OH_2)O_2C(CH_2)_6^+$	Ion fragment of ( <b>2</b> )
270	$Mn_2(OH_2)O_2C(CH_2)_7^+$	Ion fragment of ( <b>2</b> )
284	$Mn_2(OH_2)O_2C(CH_2)_8^+$	Ion fragment of ( <b>2</b> )

The negative spectra<sup>24</sup> appear less interesting: where the peaks at 32  $m/z$  and 80  $m/z$  are revealed and assigned to the  $S^-$  and  $SO_3^-$  ions, thus corresponding to ion fragments of the ligand and oxidized ligand, respectively.

Moreover the peaks at 35  $m/z$  ( $Cl^-$ ) and 37  $m/z$  ( $^{37}Cl^-$ ) can be attributed to the solvent used, and the bromide peaks at 79  $m/z$  ( $Br^-$ ) and 81  $m/z$  ( $^{81}Br^-$ ) are most probably due to bromide contamination of the solvent. In the high mass region (100-1000  $m/z$ ), the characteristic signal of the gold substrate at 197  $m/z$  ( $Au^-$ ) and a series of peaks, which could not be directly assigned to molecular ion fragments of cluster (**2**), have been detected. In Figure 6.4 the spectral range is shown up to 1000  $m/z$  due to the low signal-to-noise ratio above 1000  $m/z$ .

<sup>24</sup> Negative data were calibrated to  $CH^-$  (13.008  $m/z$ ),  $OH^-$  (17.003  $m/z$ ) and  $AuS^-$  (228.938  $m/z$ ).

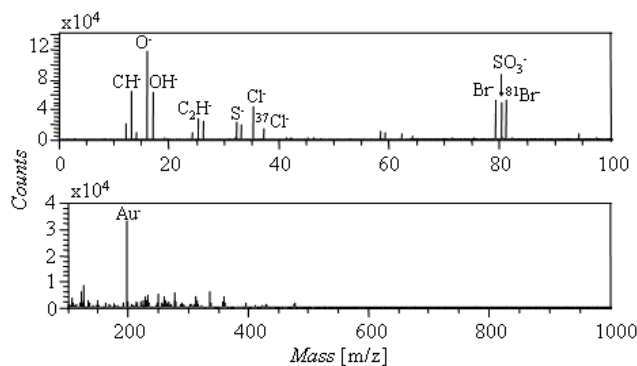


Figure 6.4. Negative ion ToF-SIMS spectrum of SAMs of 2 on gold.

A second preparation procedure has been followed in order to avoid the use of ammonia solutions. In this case grafting on gold is feasible only supposing a spontaneous deacylation of the acetylthio- group.<sup>25</sup>

As previously suggested voltammetry permitted to follow the deposition (Zobbi L. 2004), and in this case the measurements revealed a reduction of the packing of the film by observing a decreasing in the current shielding effects. Moreover XPS gave indications of a decrease of the amount of deposited material but evidenced also identical chemical characteristics of the resulting deposit. We therefore concluded that, in this case, only a smaller amount of thioacetyl groups is deacylated, spontaneously reducing in this way the amount of Au-S bond per Mn12 cluster (then reducing the passivation of the gold surface) and consequently allowing the redox processes observed in voltammetry experiments.

The deposition of one homogeneous and complete monolayer of a Mn12 derivative was achieved also using in the ligand exchange reaction an aromatic carboxylic acid instead of an aliphatic one. In fact, starting from solution of Mn12PhSAc (3), similar results in the electrochemical and in the STM analysis (see Figure 6.5) have been obtained compared to the ones achieved with deposition of 2. Due to the higher affinity of aromatic thiols to the gold surface compared to the aliphatic ones (Sabatani E. et al. 1993) the complete coverage has been achieved also for shorter time of incubation.<sup>26</sup>

<sup>25</sup> In this case Au (111) slides freshly annealed was been directly incubated for 24 h in the 0.2mM THF solution of 2. Then a similar procedure for cleaning as followed for the first deposition of 2 molecules on gold was done.

<sup>26</sup> The preparation procedure consists in dissolving the Mn12 derivative (3) (5.0 mg, 1.1  $\mu$ mol) in 4 mL of tetrahydrofuran and to add 1.8  $\mu$ L of NH<sub>3</sub>(aq, 25% v/v; without ageing of the 0.2mM solution of Mn12 derivative, a flame annealed Au(111) substrates was dropped in this solution and incubated for 30min and 24 h. Then a similar procedure used for cleaning the first deposition of 2 was followed.

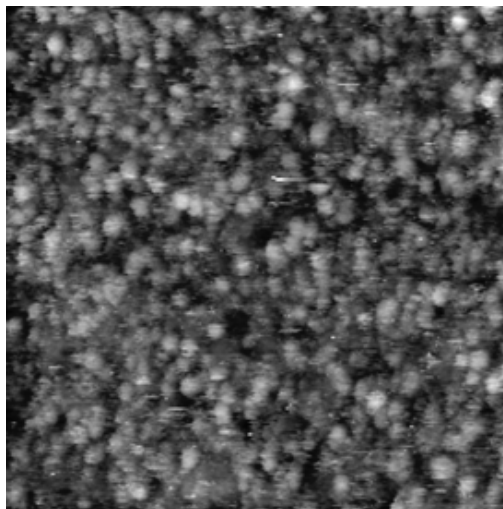


Figure 6.5. Constant-current STM images of Au(111)-films after 30' of immersion in a freshly prepared THF/NH<sub>3</sub>(aq) solution of 3 (setpoint=5 pA, bias=1.3 V).

The rigid phenyl rings surrounding the Mn<sub>12</sub> core of cluster 3, compared to the long and flexible alkyl chain of 2, are expected to promote a more controlled grafting of the molecule but no real improvement in the quality of the layers has been observed for 3. STM images provide evidence of poorly ordered particles, almost homogeneously distributed over the surface (Figure 6.5). The average size of the dots observed, appear to be between 2 and 3 nm, which is consistent with the molecular end-to-end distance of 2.8 – 3nm determined for 3. These data have been supported by XPS analysis performed examining depositions of 3 after 30' and 24 hrs immersion times. All the XPS peaks expected for 3 are just visible after 30' immersion but appear more distinctly for longer deposition times (Figure 6.6). The *C1s* spectral region shows two components that are clearly due to the presence of different bonding states (the carboxylic as well the aliphatic carbon signals) as found for Mn<sub>12</sub> anchored on Si(100) surface (Condorelli G. G. et al. 2004). The bands observed approximately at 288.2 and 285.0 eV have been assigned to the carbon atoms of coordinating carboxylate and of the remaining ligand framework, respectively. This interpretation is further confirmed by analysis of the *O1s* spectral region showing two components, centred approximately at 530.8 and 532.2 eV, respectively, and attributable to the water molecules and to the oxo-bridging atoms coordinating Mn atoms, respectively. The *S2p* signal clearly shows the presence of two bonding states allowing us to discriminate between free (163.7 eV) and Au-bound (161.6 eV) sulphur atoms.

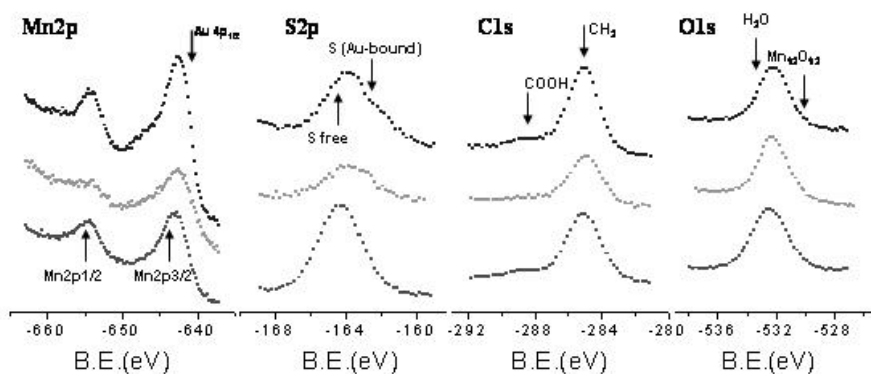


Figure 6.6. XPS core-level spectra for Au(111) films after 30' (middle, light gray) and 24h (up, dark gray) of immersion in a freshly prepared THF/NH<sub>3</sub>(aq) solution of 3, and of a bulk deposition (down, black) obtained by drop-casting using a saturated solution of 3 in CH<sub>2</sub>Cl<sub>2</sub>. The spectra of each element are on the same absolute scale.

## 1.2 Isolated (and organized?) molecules

The previous results are to be considered only the first step because they lack the possibility to address with a probe an individual SMM without interacting with a group of them. For this reason we have worked on the strength of the interaction with the surface and on tuning the incubation time in order to achieve a better control of the deposition process thus going a step forward towards the addressing of a single molecule.

In the previous sections we have shown that by using different techniques (CV, XPS, etc.) we have explored the effects of the incubation time but no effective isolation of the molecules has been observed in the topography. We have therefore investigated the deposition of other derivatives of Mn<sub>12</sub> cluster containing sulphide-functionalized ligands. It has been estimated that the interaction of sulphide derivative with the gold surfaces is approximately half than the one with thiols (Lavrich D.J. et al. 1998); this is mainly due to the different character of the interaction. In fact, while with thiols a real covalent bond is obtained, in this case we have only a smaller coordination effect due to the interaction of free pairs on the sulphur atom. Moreover neither deprotecting agents nor ageing procedures are required.<sup>27</sup>

Exploiting the weaker interaction and imposing a shorter incubation time (30 min.) of a slide of gold in solution of Mn<sub>12</sub>PhSMe (4) we obtained a smaller de-

<sup>27</sup> Deposition was then carried out by soaking flame-annealed Au(111) substrates in a 0.3 mM solution of 4 in anhydrous THF (3.2mg in 3mL) for 30' and 24 h. Then a similar procedure for cleaning as followed for the first deposition of 2 molecules on gold was done.

posit of Mn12 derivative with phenyl-methylthio linking groups characterized by the isolation of single molecule on the surface as shown by many sets of low-current STM images (Figure 6.7) (Zobbi L. et al. 2005).

The size distribution is very narrow ( $2.7 \pm 0.5$  nm) and agrees nicely with the size estimated for 4 ( $2.8$  nm x  $2.8$  nm x  $2.1$  nm) from the X-ray structure. These results are quite reproducible as they have been obtained in four different laboratories with four different STMs. They demonstrate the validity of our approach based on the incorporation of thioether groups in order to obtain a submonolayer of individually-accessible clusters. Direct attachment of the clusters to a metallic surface may now provide straightforward access to electron transport measurements using the STM tip as a second, movable electrode. The experiment has been invoked by very recent theoretical studies, which anticipate a strong interplay between quantum tunneling of the magnetization and molecular conductance (Kim G.H. and Kim T.S. 2004).

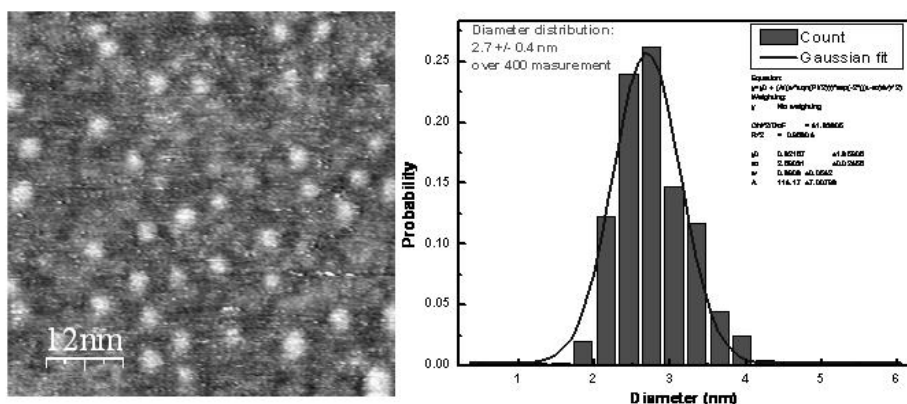


Figure 6.7. (Left) Constant-current STM image of 4 assembled on the Au(111) surface (scan area  $60 \times 60$  nm<sup>2</sup>) after 30' of immersion in a freshly prepared THF solution of 4. (Right) The distribution of diameters extracted from 400 measurements. The best-fit gaussian distribution is shown ( $R^2 = 0.97$ ,  $x_c = 2.7$  nm,  $\sigma = 0.5$  nm). Reproduced with permission from Zobbi L. et al 2005. Copyright 2005 of the Royal Society of Chemistry.

Looking at the previous images on wider scans, as the one presented in left part of Figure 6.8, it is possible to evidence that the deposited molecules appear to be arranged in a quasi-regular way. A bidimensional fast-Fourier transformation analysis evidences that this regularity is related to a hexagonal packing with regular features occurring between 6 and 8 nm.

These features suggest that Mn12 molecules in this case are adsorbed selectively in specific point of the Au(111) surfaces. In fact this surface after the flame annealing process presents, in specific cases, a “herringbone” structure (Dishner M. H. et al. 1998) in which zig-zag stripes patterning with  $\sim 7$  nm period are present, corresponding to the formation of two alternated domains. This structure (Figure 6.9) is originated by the last layer of gold packed in a *fcc*-like structure or in an *hcp*-like structure and separated by soliton walls. The Au atoms occupying the bridging sites have brighter contrast in STM. Due to the slightly lower energy of *fcc* sites, *fcc*-like domains are a

little bigger than *hcp*-like domains. Minimization of surface free energy is achieved by a secondary reconstruction manifested by a zig-zag structure in the soliton walls that contain partial dislocations at the turns (*elbows*) in the structure (Woll C. et al. 1989; Narasimhan S. and Vanderbilt D. 1992; Takiguchi H. et al. 2000).

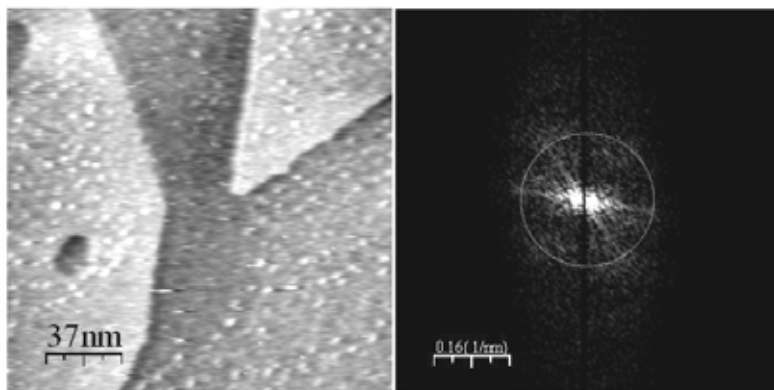


Figure 6.8 (Left) Constant-current STM image of 4 assembled on the Au(111) surface (scan area  $180 \times 180 \text{ nm}^2$ ) showing terraces and a triangular features typical of Au(111) reconstruction on mica. (Right) 2D-FFT of the image on left. Hexagonal regularity with features between 6 and 8 nm.

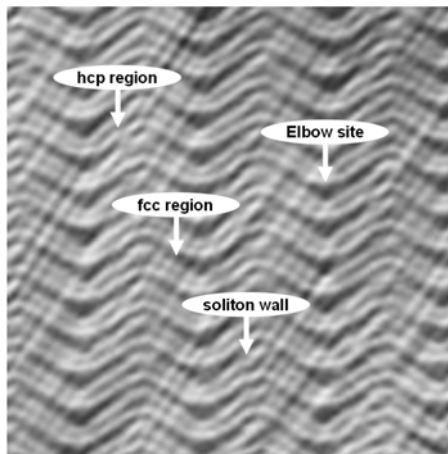


Figure 6.9. STM image ( $50 \times 50 \text{ nm}^2$ ) of “herringbone” reconstructed Au(111) surface showing periodically arranged stress domains separated by soliton walls and a secondary structure of the solitons (herringbone) with partial dislocations (elbow sites).

Normally, after the adsorption of sulphur based molecules on surface, this patterning disappears (Xie Z.-X. et al. 2002) but it has been also noted that the presence of this kind of reconstruction is enhanced by aromatic thiols (Hara M. et al. 1996). We form the hypothesis that in our case the herringbone or a slightly modified herringbone structure is still present after deposition and that Mn12 adsorbs specifically

only on *fcc* or on *hcp* regions that are separated by 6.8 nm one from each other. This is quite well consistent with previous observations on simpler mercapto-pyridine SAMs (Hara M. et al. 1996), which have been rationalized by these authors with an ordered nucleation process on top of the herringbone structure.

Further investigations will be required in the future in order to confirm this hypothesis. In any case the quantity of deposited material is decreased compared to the previous depositions. With this procedure in fact a submonolayer is achieved and we can estimate the presence of less than one molecule per 25 nm<sup>2</sup>. Nevertheless both XPS and ToF-SIMS characterizations have been at least qualitatively possible confirming the presence of the SMMs on surface.

In details, XPS measurements for depositions of 4 reveal quantifiable signals only after 24h immersion (Fig. 6.10) while for 30' depositions only a fraction of the signals overcame the detection limits. However, no remarkable decrease of the Au *4f* signal is observed for long deposition times thus suggesting that also for long immersion times low surface coverage is attained. This result is consistent with reported electrochemical studies (Zobbi L. 2004; Zobbi L. et al. 2005) and confirms the successful use of the methylthio- functionalization as weaker interacting linker group.

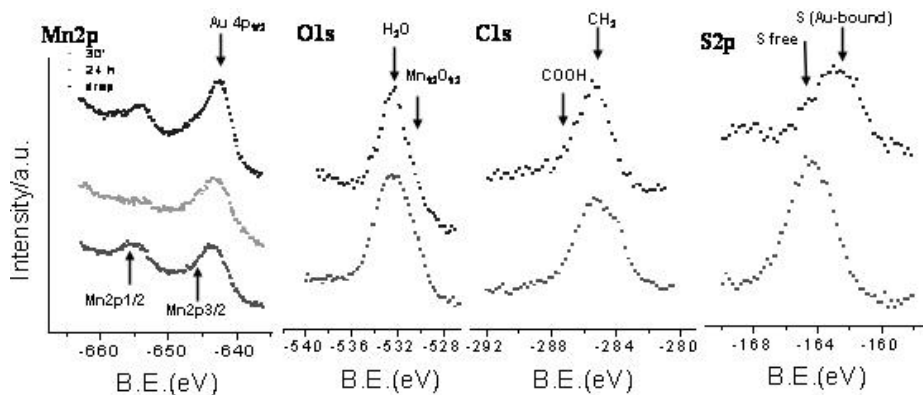


Figure 6.10. XPS core-level spectra for Au(111) films after 30' (middle, light gray, only for Mn2p) and 24h (up, dark gray) of immersion in THF solution of 4, and of a bulk deposition obtained by drop-casting (down, black) using a saturated solution of 4 in CH<sub>2</sub>Cl<sub>2</sub>. The spectra of each element are on the same absolute scale.

The Mn 2*p* signal, is just visible after 30' immersion but appears quite distinctly for longer times. The binding energy (653.7 eV for Mn 2*p*<sub>1/2</sub>) agrees well with that observed on a bulk deposit obtained by drop-casting, as well as on different Mn12 bulk samples (Kang J. S. et al. 2002; Nait Abdi A. et al. 2004). The much weaker Mn 2*p* band observed in 30' deposition is in complete agreement with an only partial surface coverage. The S2*p* signal consists of a main component at around 162eV and a low-intensity shoulder at around 164eV. However, broadening of this band prevents a detailed analysis of the spectral features.

ToF-SIMS data show characteristic peaks assigned as molecular ion fragments of 4.

Table 6.3. Characteristic peaks in the ToF-SIMS spectra of 4 SAMs on Au.

Signal (m/z)	Assignment	Description
<i>Positive ion mode</i>		
47	$\text{CH}_3\text{S}^+$	<i>Ligand fragment</i>
55	$\text{Mn}^+$	
91	$\text{C}_7\text{H}_7^+$	<i>Ligand fragment</i>
151	$\text{C}_8\text{H}_7\text{OS}^+$	$\text{CH}_3\text{SC}_6\text{H}_4\text{CO}^+$
256	$\text{C}_8\text{H}_9\text{O}_4\text{SMn}^+$	$\text{CH}_3\text{SC}_6\text{H}_4\text{COOMn}(\text{OH})_2^+$
<i>Negative ion mode</i>		
32	$\text{S}^-$	
47	$\text{CH}_3\text{S}^-$	<i>Ligand fragment</i>
87	$\text{MnO}_2^-$	
108	$\text{C}_6\text{H}_4\text{S}^-$	<i>Ligand fragment</i>
123	$\text{C}_7\text{H}_7\text{S}^-$	<i>Ligand fragment</i>
167	$\text{C}_8\text{H}_7\text{O}_2\text{S}^-$	<i>Intact ligand molecule - H</i>
269	$\text{C}_8\text{H}_6\text{O}_5\text{SMn}^-$	$\text{CH}_2\text{SC}_6\text{H}_4\text{COOMnO}_3^-$

In addition, parent molecular ion peaks representative of the intact ligand molecule and fragment peaks at lower mass values were detected.

Further developments of the deposition of this cluster are in progress and preliminary interesting results have been found by simply replacing the tetrahydrofurane incubating solution with dichloromethane. Without varying neither the incubation time (30') nor the concentration of the solution (0.3mM) a complete coverage of the gold surface has been got back as depicted in Figure 6.11.

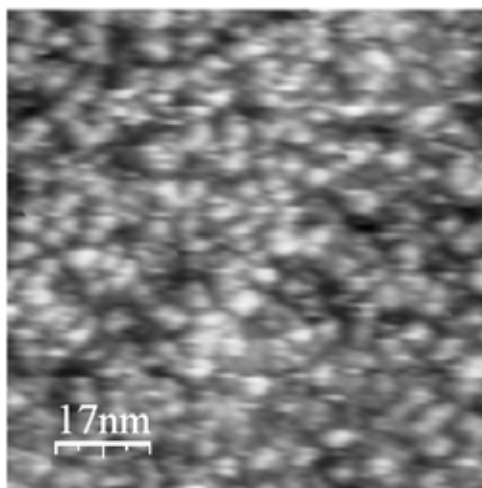


Figure 6.11. Constant-current STM images of Au(111)-films after 30' of immersion in a freshly prepared dichloromethane solution of 4.

On the other hand, another attempt to isolate of Mn12 molecules following a similar logical scheme has been employed with Mn12C10SC10 (5). We have supposed that the use of di-alkyl-sulphide ligands allows a similar deposition control obtained with 4 without deprotection or ageing of the solution and with a better organization on surfaces triggered by the use of these long chains.<sup>28</sup>

We present here only preliminary STM results on both 30' and 24h depositions. These results confirm, at least partially and for lower incubation times, that isolated molecules can be evidenced (Fig. 6.12a) while increasing the incubation time a complete coverage of the surface with some kind of order on the investigated area is achieved (Fig 6.12b). Further analysis are needed in order to confirm this very attracting evidence.

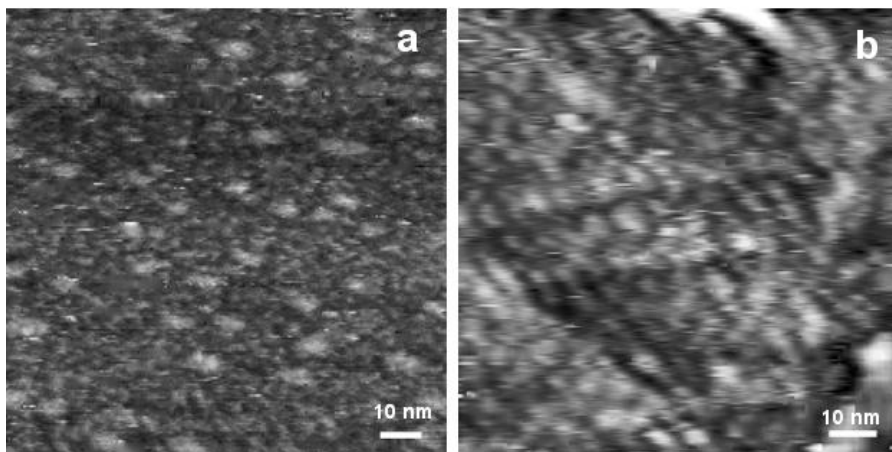


Figure 6.12. Constant-current STM images of Au(111)-films after 30' (a) and 24h (b) of immersion in a freshly prepared THF solution of 5.

Preliminary results on XPS characterization of the solution incubated for a longer time (Figure 6.13) confirm the presence of Mn12 derivative on the surface.

<sup>28</sup> Deposition was carried out by soaking flame-annealed Au(111) substrates in a 0.5 mM solution of 5 in anhydrous THF (5.5 mg in 3mL) for 30' and 24 h. Then a similar procedure for cleaning as followed for the first deposition of 2 molecules on gold was done.

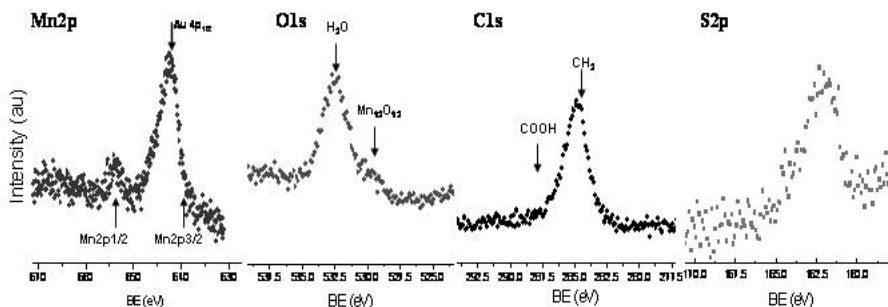
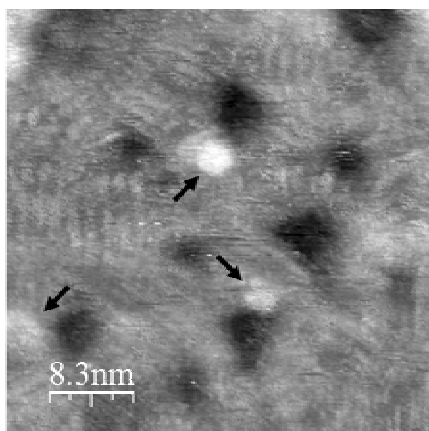


Figure 6.13. XPS core-level spectra for Au(111) films 24h of immersion in THF solution of 5.

These data are qualitatively consistent with all the previous ones but the quantitative analysis suggests also the presence of contaminants on this surface. For this reason the obtained data are considered only as a starting point for further investigations.

Recently we have investigated an alternative procedure to avoid the contamination of surfaces as well as to achieve the grafting of isolated Mn12 molecules. It consists in passivating the gold surface with an n-alkyl mercaptane with a smaller length compared to the ligand of 5 and then inserting 5 by following the described procedure for obtaining mixed SAMs (Lussem B. et al. 2006) and also already used for “large” molecule insertion (Friggeri A. et al. 2000).<sup>29</sup>

At the moment only a preliminary STM characterization of 5 included in a pre-formed SAM has been performed and the results are shown in Figure 6.14.



<sup>29</sup> Deposition was carried out first by soaking flame-annealed Au(111) substrates in a 1mM solution of heptan-mercaptane in EtOH. Subsequently the slide of gold was cleaned with fresh EtOH and CH<sub>2</sub>Cl<sub>2</sub> and soaking them in a 0.1mM solution of 5 in anhydrous THF (5.5 mg in 3 mL) for 2 h. Then a similar procedure for cleaning as followed for the first deposition of 2 molecules on gold was done.

Figure 6.14. Constant-current STM images of 5 molecules anchored on the preformed monolayer of n-dodecyl sulphide. Arrows indicates isolated molecules while also ordered monolayer are easily visible.

### 1.3 Isolated and oriented molecules

A further step toward the achievement of our goals in depositing a SMMs system on a surface is the achievement of an ordered molecular layer, with a definite lattice and the same orientation for all the molecules (i.e. the easy axis of magnetization has the same direction for all the molecules on the surface).

Mn12 clusters, with all the carboxylates replaced by sulphur carboxylate ligands, form a disordered layer of molecules probably because all the clusters have sixteen points to graft the gold, one for each ligand, and this doesn't allow the orientation of the easy axis as regards the surface, Figure 6.15a.

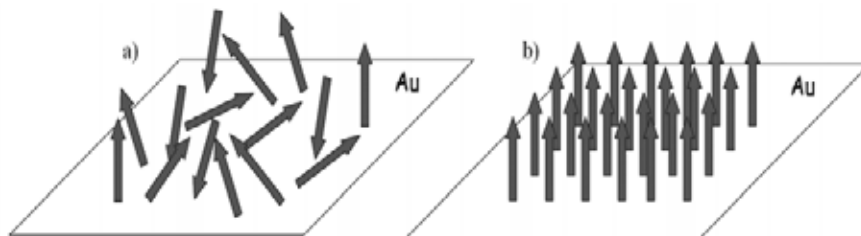


Figure 6.15. Orientation of the molecules, and so of the easy axes, on Au surface for a) generic Mn12 functionalized cluster with sulphur ligands and b) for a Mn12 functionalized cluster in a site-specific way.

An attempt to orient Mn12 on surfaces was already proposed by B. Fleury et al. (Fleury B. et al. 2005) by exploiting the selective *in situ* replacement with carboxylate prefunctionalized Si surface of the Mn12 with mixed carboxylate ligands playing on the different  $pK_a$  of the corresponding acids.

A more convincing solution to this problem could be the site-specific replacement on bulk of only few carboxylates thus leading to the spontaneous alignment of all the easy axes Figure 6.15b.

The first candidate has been Mn12ADCSMe (6) that was synthesized as described in Chapter 4. Here we report in Figure 6.16 the first evidence of its deposition.

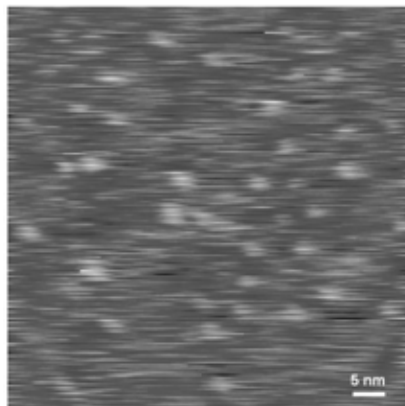


Figure 6.16. Constant-current STM images of Au(111)-films after 30' of immersion in a freshly prepared THF solution of 6.

In this very preliminary result, isolation of single molecules was achieved in analogy with deposition of 4 and 5 derivatives, but at the moment we have not enough evidences to confirm the orientation of the easy axes of the deposited molecules. Moreover a full chemical characterization of the surface to confirm the deposition of intact 6 molecules is still in progress.

#### 1.4 *Patterned molecules*

The organization of functional molecules as patterned surfaces is one of main current trends toward molecular-scale devices. Achieving the patterning of Mn12 derivative has to be considered then a breakthrough for SMMs based devices. Moreover this would allow the employment of spatially resolved surface analysis techniques even if molecular resolution is not achievable. The first attempt to prepare patterned SMMs surfaces was proposed by Cavallini et al. (Cavallini M. et al. 2003) using the lithographically-controlled wetting method (LCW) which enables to deposit SMMs on surfaces without covalent anchoring and to pattern them in specific structures. More recently the same authors suggested also that by using a dewetting procedure it is possible to grow patterned surfaces enriched in Mn12 from the demixing of a binary polymer/Mn12 mixture (Cavallini M. et al. 2005; Cavallini M. et al. 2006). In any case these techniques don't allow deposition of a real single patterned layer.

Thanks to our experience in SAMs technique as well as to the collaboration with the Prof. D. N. Reinhoudt, University of Twente (The Netherlands) we have investigated two new and alternative ways to achieve the patterning of Mn12 molecules (Mannini M. et al. 2005). This strategy can be considered as the combination of the use of SAM technique that we describe in Paragraph 1.1 of this Chapter (Cornia A. et al. 2006) and the above mentioned LCW technique (Cavallini M. et al. 2003).

In fact we exploit here for the first time the potentiality of micro-contact printing ( $\mu$ CP) technique in both direct and indirect modes to the SMMs deposition. These

procedure, already described in Chapter 3 and summarized in Figure 6.17, have been employed to achieve the Mn12 patterning by the use of Mn12LC15 (2). In both cases preparation procedure followed general indications.<sup>30</sup>

In the first procedure we suggested (Mannini M. et al. 2005) the preparation of scalable, nanopatterned monolayers of covalently-bound Mn12 SMMs by using a substrate pre-patterned with alkanethiols by  $\mu$ CP, subsequently soaked into a solution of SMMs that selectively adsorbed onto the bare gold zones. This method seems particularly well suited to evaluate the thickness of the layer of SMMs. According to the back-filling method we prepared stripes (5  $\mu$ m wide) of octadecylthiol (ODT) separated by bare gold regions (3  $\mu$ m wide). The section analysis of AFM images (Figure 6.18) clearly reveals the height of the ODT layer in the printed pattern ( $\sim$ 2.3 nm), in good agreement with the literature value (Bain C. D. et al. 1989). Next, the printed substrates were soaked in an alkaline solution of 2. The resulting pattern now consists of protruding 3- $\mu$ m wide stripes, which clearly point to selective binding of the clusters on bare gold regions in between the ODT stripes. From a comparison of the two height profiles, it follows that the thickness of the molecular layer is about 4.8 nm, which is close to that calculated in molecular modelling studies (Cornia a. et al. 2003). This result represents the first direct measurement of the thickness of a Mn12 monolayer.

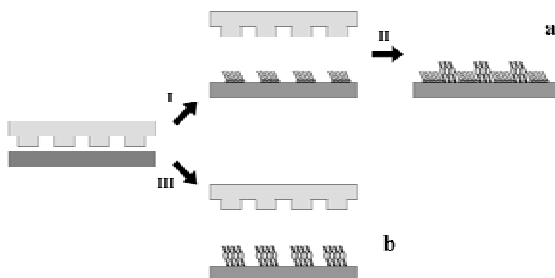


Figure 6.17. Schematic view of the process for indirect (top) and direct (bottom)  $\mu$ CP of SMMs stripes on gold surfaces: I)  $\mu$ CP of thiols, II) deposition of SMMs on a pre-printed surface, III)  $\mu$ CP of SMMs. Reproduced with permission from Mannini M. et al. 2005. Copyright 2005 American Chemical Society.

<sup>30</sup> Micro-contact printed stripes were prepared according to standard literature procedures, using a PDMS stamp replicated from a silicon master with grating of 5 to 3  $\mu$ m. Gold substrates were obtained from Ssens BV (Hengelo, The Netherlands) as a layer of 20 nm gold on titanium (2 nm) on silicon. Before use, the substrates were treated with piranha solution for 15 s (concentrated  $\text{H}_2\text{SO}_4$  and 33% aqueous  $\text{H}_2\text{O}_2$  in a 3:1 ratio). (Warning! Piranha solution should be handled with caution: it has been reported to detonate unexpectedly), rinsed with water (Millipore) and ethanol.  $5 \cdot 10^{-5}$  M solutions of 2 have been used for the direct deposition by  $\mu$ CP. Patterned films were washed with THF, ethanol and dichloromethane, dried under nitrogen flux and immediately analyzed or kept under inert atmosphere until testing.

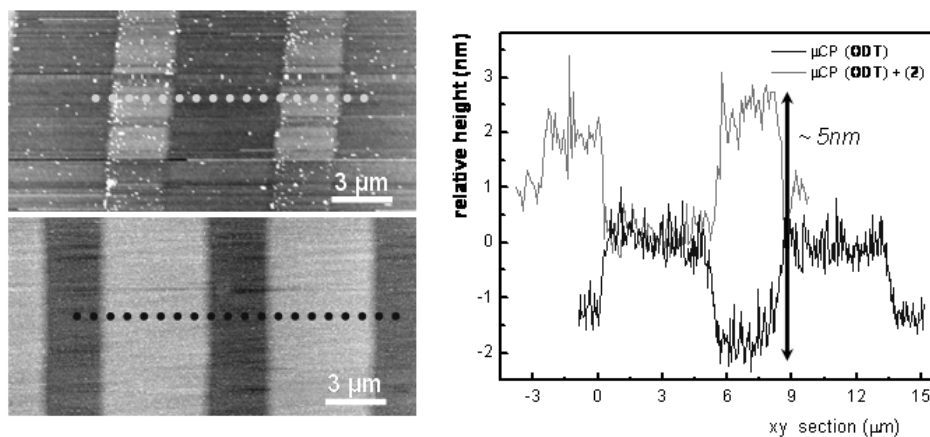


Figure 6.18. AFM images ( $20 \times 10 \mu\text{m}^2$ ) of ODT micro-contact printed in stripes on gold (down-left) and of the alternating pattern of ODT and 2 (up-left). Dotted lines indicate the sections in the xy plane presented on the right. The height of 2 has been obtained by setting the top of the ODT stripes at zero height. Reproduced with permission from Mannini M. et al. 2005. Copyright 2005 American Chemical Society.

The  $\mu\text{CP}$  technique has then been employed to demonstrate the possibility to directly pattern SMMs on a gold substrate. While  $\mu\text{CP}$  is widely employed with organic molecules, polynuclear coordination clusters have been rarely used as ink (Huang S. et al. 2004). In fact we have performed deposition (Mannini M. et al. 2005) of micro-strips of SMMs from a very dilute solution ( $[2] = 5 \times 10^{-5} \text{ M}$ ), which is directly used as the “ink” in the  $\mu\text{CP}$  procedure with a PDMS stamp (Hidber P. C. et al. 1996; Li X.-M. et al. 2003). In Figure 6.19 we present an AFM image of the direct  $\mu\text{CP}$  of 2 showing a well resolved pattern. From the section profile, the height of the printed stripes is found again compatible with that of a monolayer although clusters appear less densely packed as compared with the back-filling approach.

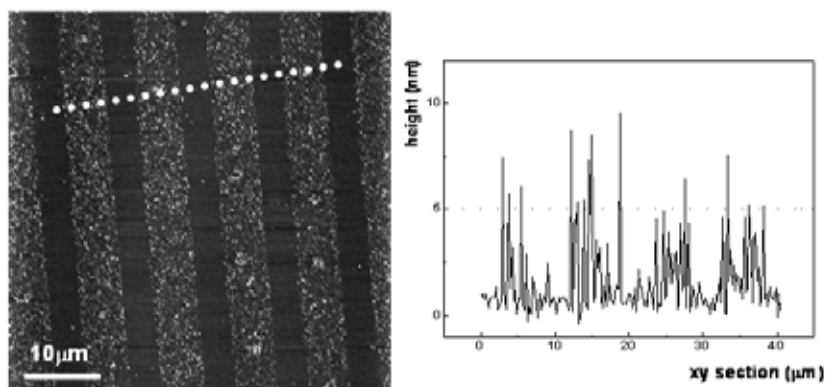


Figure 6.19. (Left) AFM image ( $50 \times 50 \mu\text{m}^2$ ) of 2 micro-contact printed in stripes on gold with a PDMS stamp ( $5 \mu\text{m}$  stripes spaced  $3 \mu\text{m}$  apart). Dotted line indicates the xy section pre-

sented on the right. Reproduced with permission from Mannini M. et al. 2005. Copyright 2005 American Chemical Society.

With respect to alternative methods reported in the literature (Cavallini M. et al. 2003), these deposited SMM stripes are covalently bound to the gold surface and are therefore chemically stable and washable with organic solvents. Careful washing is in fact essential to remove contaminants and physisorbed molecules. We have also observed that the apparent thickness of the deposited stripes slowly increases upon exposure to the air, presumably due to reversible adsorption of moisture. In fact, the original height can be recovered by introducing the sample in a chamber with a continuous flux of nitrogen.

As the spatial resolution of ToF-SIMS is high enough to resolve the micro-structure obtained with  $\mu$ CP technique, we have recorded ToF-SIMS images of patterned surface of 2 and compared with results obtained in the analysis of homogeneous deposition of 2 described in Paragraph 1.1 of this Chapter. Doing this, chemical information on the deposited stripes has been obtained by ToF-SIMS imaging applied for the first time to the investigation of a patterned film of SMMs.

The chemical composition of the micro-contact printed surface with 2 has been analyzed by ToF-SIMS imaging mode. The ToF-SIMS images of the positive total ion, the  $\text{Mn}^+$  (55 m/z), and the  $[\text{Mn}_2\text{O}_2\text{C}(\text{CH}_2)_7]^+$  ion (252 m/z) signals are shown in Figure 6.20.

In the total ion image each pixel corresponds to a total spectrum intensity. Alternate stripes of 5 and 3  $\mu\text{m}$  are clearly observed, in excellent agreement with the pattern of the starting master. In correspondence of the 5  $\mu\text{m}$  wide stripes higher intensity of the total ions,  $\text{Mn}^+$ , and  $[\text{Mn}_2\text{O}_2\text{C}(\text{CH}_2)_7]^+$  signals are observed. The higher contrast observed for  $\text{Mn}^+$  is not surprising given its dominant contribution to the ToF-SIMS spectrum (see Figure 6.3). Future work will extend the study to the use of gold liquid-metal ion gun sources, which have the advantage of significantly increasing secondary yields over  $\text{Ga}^+$  and  $\text{In}^+$  (Bryan S. R. et al. 2004; Walker A.V. and Winograd N. 2004).

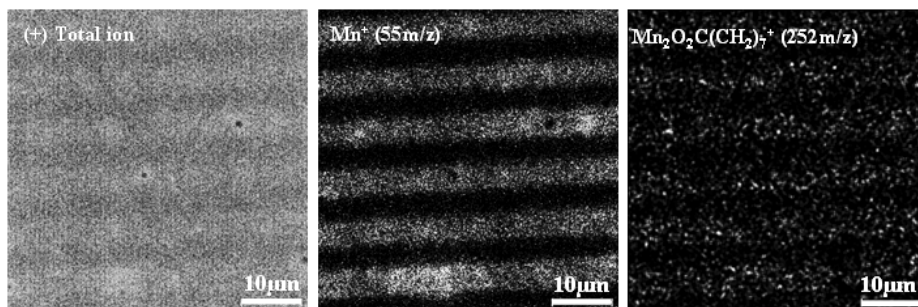


Figure 6.20. Positive ToF-SIMS image ( $50\mu\text{m} \times 50\mu\text{m}$ ) of micro-contact printed stripes of 2 on gold. Left: total ion. Middle and right:  $\text{Mn}^+$  (55m/z), and  $[\text{Mn}_2\text{O}_2\text{C}(\text{CH}_2)_7]^+$  ion (252m/z) signals, respectively. Brighter pixels correspond to a higher intensity of the signals. The image on the right has been treated with a  $[3 \times 3]$  convolution. Reproduced with permission from Mannini M. et al. 2005. Copyright 2005 American Chemical Society.

With this report we have concluded the section of this thesis dedicated to SMMs deposition, a topic still under further investigation. The efforts are at present mainly focused on preparing new SMM-based pre-functionalized systems to be grafted on surface. In particular encouraging results are coming from the deposition of propeller-like tetra-iron ( $\text{Fe}_4$ ) systems (Figure 6.21) chemically modified with specific ligands allowing grafting on gold (Mannini M. et al. 2008a) and on silicon surfaces (Condorelli G. G. et al. 2008).

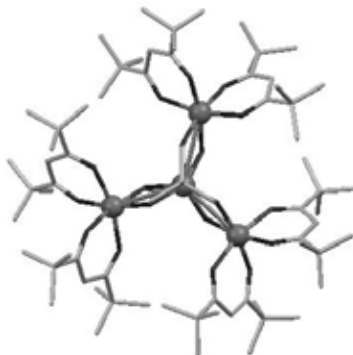


Figure 6.21. Partial view of the structure of one of the  $\text{Fe}_4$  clusters. The linking groups are omitted and can be considered as perpendicular to the presented structure coming up and down along the direction of the main symmetry axis of the molecule.

The greater stability of this kind of molecules as well as the acquired experience in functionalization and depositions of SMMs suggest that these systems will be easily organized on homogeneous and patterned surfaces.

## 2. Deposition and characterization on surface of organic radicals

In this part of the manuscript is presented our work focused on depositing Nitronyl Nitroxide sulphur derivative systems (Mannini M. et al. 2007b).

In the following a complete scheme of production of homogeneous monolayers of a series of Nitronyl Nitroxide Radicals (NITs) deposited on gold will be presented, and the results concerning deposition of patterned layers of similar systems will be reported.

### 2.1 From disordered to ordered monolayers

A previous work focused on depositing NITs with mono and multi-layer control through Langmuir-Blodgett technique (LB) has been reported by Gallani and co-workers (Gallani J. L. et al. 2001). In that work, the NITs moieties were close to the support surface and thus difficult to be accessed with a tip of an SPM. Another drawback is that LB films lack rigid bidimensional regularity. In any case an interesting averaging of the magnetic anisotropy of the deposited films was evidenced. Sugawara's group reported an attempt of deposition of NitRs through SAMs technique, but all the presented characteristics do not fit the monolayer formation suggested by

the authors (Matsushita M. M. et al. 2002). The same group presented also interesting preliminary results in functionalizing gold nanoparticles with the same molecule (Harada G. et al. 2002).

The formation of SAMs based on the use of the thiol functional group is described in literature (Troughton E. B. et al. 1988). In this case the binding energy is reduced with respect to the use of thiols by the use of methyl-thio group (Lavrich D.J. et al. 1998).

In fact in the following is described the deposition of the three methyl-thio functionalized Nitronyl Nitroxide radicals, NitPhSMe (NIT1), NitPhPhSMe (NIT2) and NitPhCH<sub>2</sub>SMe (NIT3) which syntheses are described in Chapter 5. These depositions followed the general scheme of self-assembling of monolayers<sup>31</sup> but in this case, to improve the quality of the deposition, gold slides are incubated at 60° C as suggested in literature for similar compounds (Troughton E. B. et al. 1988).

In order to check the presence of intact molecules on the layers all the samples have preliminarily been characterized by ToF-SIMS techniques. Studies on the characterization of bulk NITs by mass spectrometry techniques have recently been published. Matrix-assisted desorption/ionization time-of-flight mass spectrometry (MALDI ToF-MS) (Stroh C. et al. 2004), electron impact (EI) (Ordina J. et al. 1997), and electrospray ionization mass spectrometry (ESI-MS) (Smith C. D. et al. 2002), have been applied to the characterization of bulk NitRs. However, no ToF-SIMS studies of NITs chemisorbed on surfaces have been reported to our knowledge, even if this technique can give access to relevant pieces of information on such systems.

Positive ToF-SIMS spectra acquired on SAMs of NITs on gold are much more informative than negative ones in agreement with the results obtained on similar NITs analyzed by MALDI-ToF, EI-MS, and ESI-MS.

<sup>31</sup> All the depositions were carried out by soaking flame-annealed Au(111) substrates (a film of 150 nm evaporated on mica, annealed with a hydrogen flame) in 1-2 mM solutions in CH<sub>2</sub>Cl<sub>2</sub> of NitRs. The slides are incubated in the dark at 60°C overnight and then rinsed with anhydrous CH<sub>2</sub>Cl<sub>2</sub> and dried under nitrogen flux.

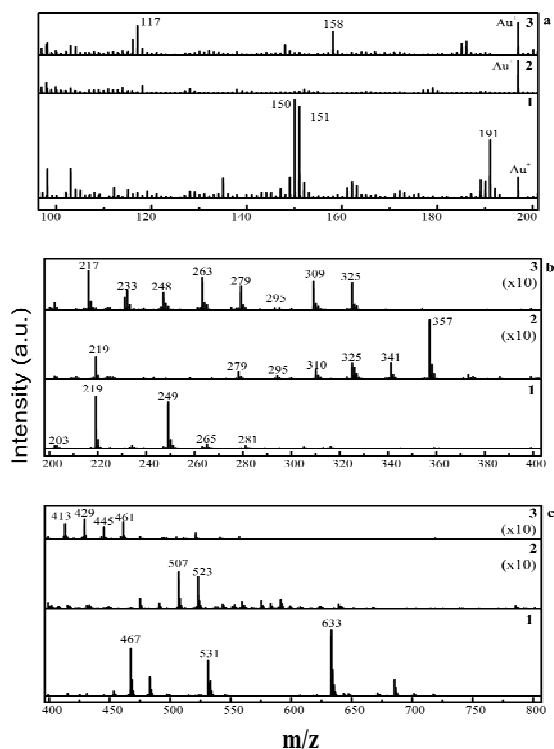


Figure 6.22. Positive ToF-SIMS spectra of SAMs of NIT1, NIT2, and NIT3 on gold. The mass regions between (a) 100  $m/z$  and 200  $m/z$ , (b) 200  $m/z$  and 400  $m/z$  (c) 400  $m/z$  and 800  $m/z$  are presented. In (a) and in (b) the intensity of the NIT2 and NIT3 spectra is amplified 10 times. Reproduced with permission from Mannini M. et al. 2007b. Copyright 2007 American Chemical Society.

In the mass region between 100 and 200  $m/z$  (Figure 6.22a), significant differences are observed in the three spectra. The spectrum of NIT2 is dominated by the Au<sup>+</sup> peak at 197  $m/z$ , while the spectrum of NIT3 shows also two intense peaks at 158  $m/z$  and 117  $m/z$  assigned to the molecular ion fragments C<sub>7</sub>H<sub>14</sub>N<sub>2</sub>O<sub>2</sub><sup>+</sup> and C<sub>7</sub>H<sub>5</sub>N<sub>2</sub><sup>+</sup>, respectively (Smith C. D. et al. 2002). In the spectrum of NIT1, intense peaks at 191  $m/z$ , 150  $m/z$ , and 151  $m/z$  attributed to C<sub>10</sub>H<sub>11</sub>N<sub>2</sub>S<sup>+</sup>, C<sub>7</sub>H<sub>6</sub>N<sub>2</sub>O<sub>2</sub><sup>+</sup>, and C<sub>7</sub>H<sub>7</sub>N<sub>2</sub>S<sup>+</sup>, respectively, are seen.

More interesting is the region at higher masses (200-800  $m/z$ , figures 6.23b and 6.23c), exhibiting similar fragmentation patterns of molecular ions and molecular ion fragments shifted by the right difference in molecular weight of the NIT analyzed. The characteristic peaks detected in the positive ToF-SIMS spectra of SAMs of NIT1, NIT2, and NIT3 on gold and their assignments are reported in Figure 6.23.

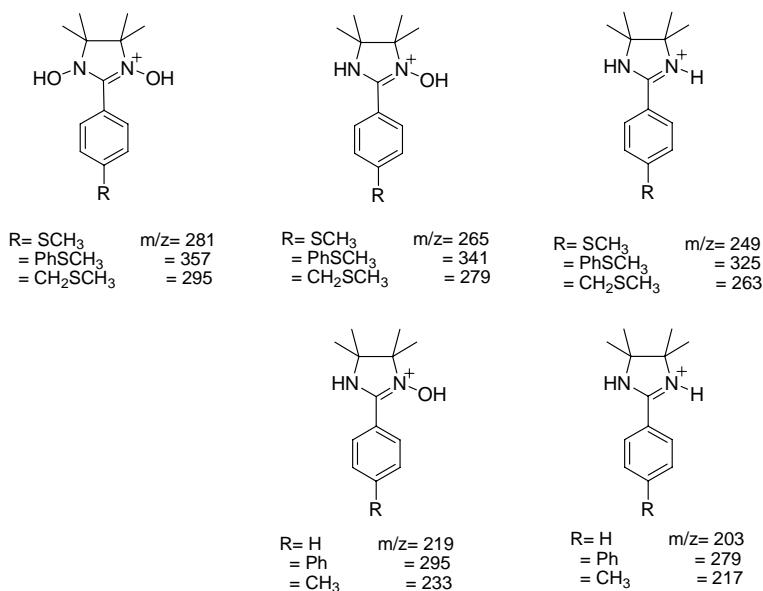


Figure 6.23. Characteristic fragments detected for all of the three NitRs in ToF-SIMS positive spectra. Reproduced with permission from Mannini M. et al. 2007b. Copyright 2005 American Chemical Society.

The detection of the bi-protonated molecular ion  $[M+2H]^+$  in all the three NitRs spectra is consistent with literature data on bulk NITs (Smith C. D. et al. 2002) and confirm the absence of a cleavage of a C-S bond during the self-assembling process (Zhong C.-J. et al. 1999). It has to be noted that in the spectra of NIT1 and NIT3 this peak is weak, while in the spectrum of NIT2 it is the most intense peak in the molecular ion mass region.

Differences are observed in the relative intensity of the peaks occurring in the high mass region ( $> 400$   $m/z$ , Figure 6.24c), the spectrum of NIT1 showing more intense peaks at higher masses. In detail, dimer fragment and Au-dimer fragment cluster ions are detected in spectrum of NIT1, indicating the formation of peroxy dimers in the SIMS experiment. The corresponding peaks are not detected in spectra of NIT2 and NIT3; however, Au-molecular fragment cluster ions and molecular cluster ions were detected for these derivatives. Details of the peak assignments are reported in Table 6.4.

Table 6.4. Characteristic peaks ( $m/z$ ) in the positive ToF-SIMS spectra of SAMs of NIT1, NIT2, and NIT3 on gold.

NIT1	NIT2	NIT3	Ion assignment
<i>Peak (m/z)</i>			
30	30	30	CH <sub>4</sub> N <sup>+</sup>
42	42	42	C <sub>2</sub> H <sub>4</sub> N <sup>+</sup>
56	56	56	C <sub>3</sub> H <sub>6</sub> N <sup>+</sup>
58	58	58	C <sub>3</sub> H <sub>8</sub> N <sup>+</sup>
70	70	70	C <sub>4</sub> H <sub>8</sub> N <sup>+</sup>

NIT1	NIT2	NIT3	Ion assignment
91	91	91	$C_7H_7^+$
103	103	103	$C_7H_5N^+$
		117	$C_7H_5N_2^+$
150			$C_7H_6N_2O_2^+$
151			$C_7H_7N_2S^+$
		158	$C_7H_{14}N_2O_2^+$
191			$C_{10}H_{11}N_2S^+$
197	197	197	$Au^+$
203	279	217	$[M-CH_3-2O-S+3H]^+$
219	295	233	$[M-CH_3-O-S+3H]^+$
249	325	263	$[M-2O+2H]^+$
265	341	279	$[M-O+2H]^+$
281	357	295	$[M+2H]^+$
		309	$[M+O]^+$ or $[(M-CH_3-O-S+2H)+Ph]^+$
		325	$[M+2O]^+$ or $[(M-CH_3-2O+2H)+Ph]^+$
		413	$[(M-CH_3-2O-S+2H)+Au]^+$
		429	$[(M-CH_3-O-S+2H)+Au]^+$
	507	445	$[(M-CH_3-2O+2H)+Au]^+$
	523	461	$[(M-CH_3-O+2H)+Au]^+$
467			$[(M-CH_3-S+2H)_2+H]^+$
531			$[(M-CH_3+2H)_2+H]^+$
633			$[(M-CH_3-O-S+3H)_2+Au]^+$

The differences observed in the three NITs spectra can be attributed to different packing density and order of the formed monolayer (as it will be evident in STM measurements). Indeed studies of ToF-SIMS spectral fragmentation patterns (Tarlov M. J. and Newman J.G. 1992; Graham D. J. and Ratner B.D. 2002; Graham D. J. et al. 2002) during the assembly of thioalkane SAMs have shown an enhancement of longer hydrocarbon fragments at short assembling times, while for longer times (i.e. fully packed, crystalline SAM) an enhancement of shorter hydrocarbon fragments is detected. In addition, long assembly times corresponds to molecular ion clusters emitted from the gold surface (Tarlov M. J. and Newman J.G. 1992; Graham D. J. and Ratner B.D. 2002; Graham D. J et al. B.D. 2002).

In agreement with this observation, the ToF-SIMS spectra of the three NITs investigated show an increase in the relative intensity of larger mass fragments as the degree of ordering of SAMs decreases (NIT1 < NIT2 < NIT3).

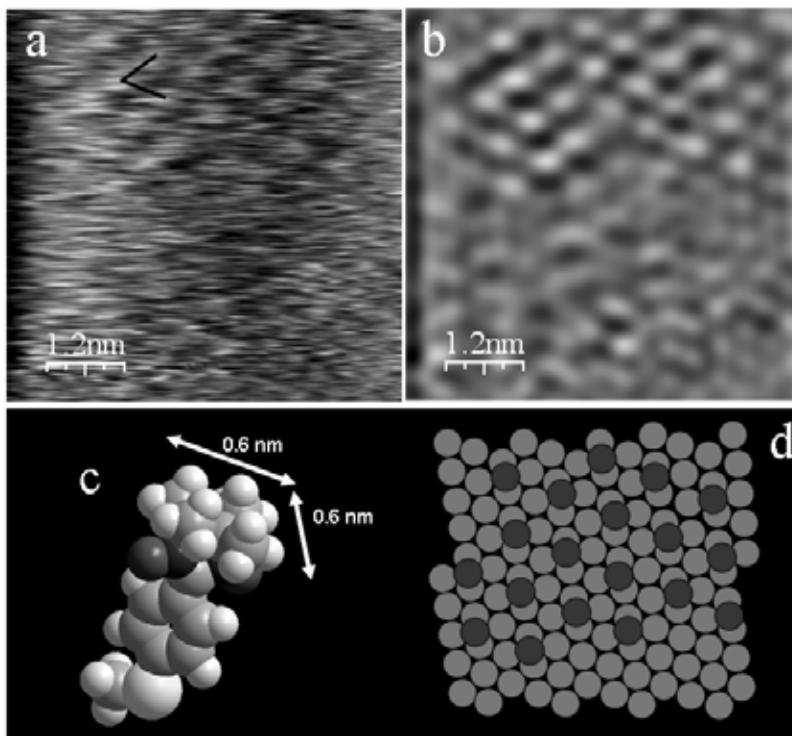


Figure 6.24. In air STM image  $5.3 \times 5.3 \text{ nm}^2$  sized of NIT1 SAM on gold surface, a) unfiltered scan, the dark lines indicate the primitive cell suggested; b) Filtered with FFT; c) 3D representation of NIT1; d) the (2x2) suggested packing model. Reproduced with permission from Mannini M. et al. 2007b. Copyright 2007 American Chemical Society.

The effective grafting of these molecules as monolayer was confirmed by the use of the Scanning Tunneling Microscopy.<sup>32</sup>

Moreover STM measurements confirmed large differences among the three deposited NitRs. SAMs obtained with NIT1 appear to be very hard to characterize by STM and in the experimental conditions we used only few small areas of the analyzed samples showed a bidimensional ordering (Figure 6.24). In one of these structured regions features with size  $0.6 \times 0.6 \text{ nm}^2$ , thus in agreement with the size of NIT1, are clearly visible. These dimensions suggest a (2 x 2) organization over the Au (111) surface as presented in the model shown in Figure 6.24c, assuming that the molecules should be linked perpendicularly to the surface.

<sup>32</sup> STM measurements were performed with a P47-Pro system (NT-MDT, Zelenograd, Moscow, Russia) equipped with a customized low-current STM head and Pt/Ir 90/10 mechanically-etched tips prepared immediately before use (positive bias voltage 600-700 mV was applied; constant current mode with a set point within 20 and 40 pA has been used). All STM measurements were carried out at room temperature, under  $\text{N}_2$  atmosphere.

STM room temperature data of the SAM obtained with NIT2 show a non-regularly organized system (Figure 6.25). The presence of biphenyl group instead of phenyl ones should enable stronger stacking interactions between neighboring NITs providing to the molecules stronger lateral interactions. We can only roughly estimate the presence of  $1.6 \times 1.0 \text{ nm}^2$  objects, in agreement with the presence of strongly tilted NIT2 molecules, but no order was observed. This may be due either to the decreased conduction through longer molecules making difficult to find the correct imaging conditions (Zhong C.-J. et al. 1999), or to an augmented rotational freedom around the long molecular axis.

Moreover NIT1 and NIT2 as reported for simpler molecules (see Figure 6.26, Tao Y.-T. et al. 1997), can bind the gold surface assuming two different orientations, with the axis of the molecule tilted of  $30^\circ$  and  $90^\circ$  with respect to the surface as evidenced in literature for this class of compounds.

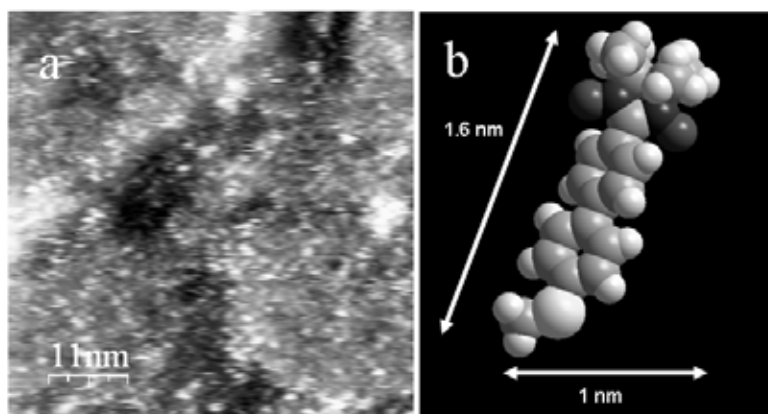


Figure 6.25. In air STM image  $50 \times 50 \text{ nm}^2$  sized of NIT2 SAM on gold surface, a) unfiltered scan,; b) 3D representation of NIT2. Reproduced with permission from Mannini M. et al. 2007b. Copyright 2007 American Chemical Society.

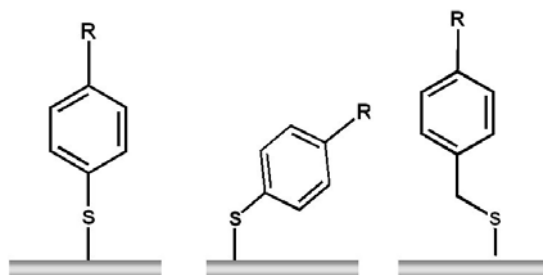


Figure 6.26. Possible orientations of monolayers of (a) thiophenol and (b) benzyl mercaptan derivatives on gold.

This fact is probably responsible for the low order we noticed in these SAMs. The methyl group, which is close to the sulphur atom in both cases, appears to hinder a regular packing as suggested by a raw calculation with a molecular modeling package.

Thanks to the CH<sub>2</sub> spacer group between the sulphur atom and the aromatic ring, NIT3 provides more ordered SAMs. In fact, this simple chemical modification reduces the degree of freedom of the molecules on the surface (Tao Y.-T. et al. 1997). Moreover, introducing the CH<sub>2</sub> spacer group, we stabilize the sterical hindrance of the methyl group. From a conformational point of view this modification stabilizes the methyl group in position close to the methylenic spacer and allows an easier link of the sulphur atom to the gold surface, as confirmed by molecular modeling calculations.<sup>33</sup>

In agreement with this hypothesis, STM images of NIT3 SAMs present a stronger bidimensional ordering on relatively large areas (Figure 6.27). The typical signature of a regular SAMs is clearly distinguishable: dark spots ~5 nm wide in the images correspond to the “pinholes” (see Chapter 3).

Moreover, also at large scan area it is possible to notice the bidimensional lattice multidomain features of the monolayer characterized by features of 0.8 x 0.7 nm<sup>2</sup>, that can be modeled assuming a (3 x 2) adlayer structure with respect to the gold surface and considering each molecule as tilted approximately by 60° with respect to the surface plane.

Concluding, STM measurements in air show different degree of ordering of SAMs of NITs and evidence how local measurement differs from averaged measurement over the entire sample.

These measurements, coupled with ToF-SIMS ones, evidenced that with no doubt one layer of molecules has been adsorbed on the surface. The confirmation that also the magnetic properties remain unchanged after deposition will be the subject of Chapter 7.

## 2.2 Patterned molecules

In analogy with the surface patterning presented above for Mn12, we have recently started to investigate also the patterning feasibility of Nitronyl Nitroxides based molecules. As discussed above, this kind of investigation allows the possibility to use specific surface techniques that would provide interesting information overcoming the needed spatial resolution to access single molecule properties. In particular the achievement of reproducible and stable patterned surfaces of these radicals would trigger an easier first test of magnetic properties detection via scanning derivative techniques as recently suggested theoretically (Rinkevicius Z. et al. 2004).

<sup>33</sup> We performed a raw molecular modeling calculation by using the commercial package Hyperchem and applying a semiempirical CNDO method with a geometrical optimization based on the Polak-Ribiere conjugate-gradient algorithm. (Hyperchem Molecular Modeling System, Release 7.5 for Windows, Hypercube Inc).

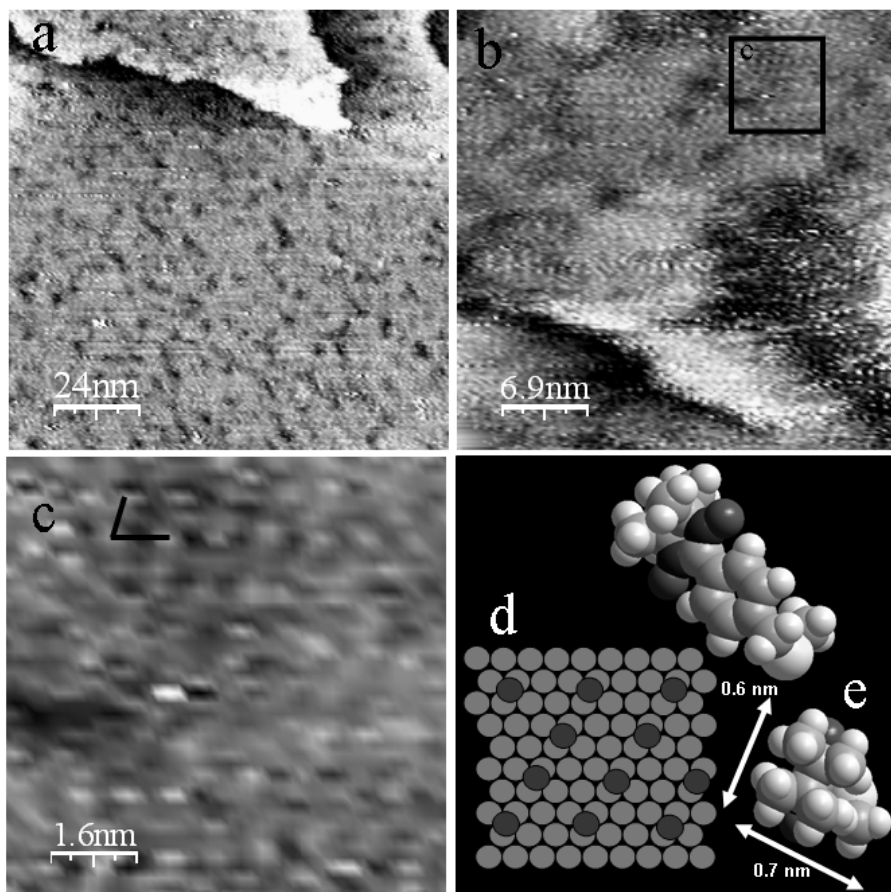


Figure 6.27. In air STM image of NIT3 SAM on gold surface, (a)  $120 \times 120 \text{ nm}^2$  sized unfiltered scan, (b)  $35 \times 35 \text{ nm}^2$  unfiltered scan, (c) digital zoom  $8 \times 8 \text{ nm}^2$  of previous image, the dark lines indicate the suggested primitive cell; (d) the  $(3 \times 2)$  suggested packing model; (e) two 3D representations of NIT3. Reproduced with permission from Mannini M. et al. 2007b. Copyright 2007 American Chemical Society.

Preliminary results (Mannini M. et al. 2008b) have been obtained starting from a PDMS stamps having the same features of the one used for Mn12 patterning (protrusion of  $5 \mu\text{m}$  stripes spaced  $3 \mu\text{m}$ ) and using as ink a new dialkyl sulphide derivative of a Nitronyl Nitroxide, the NITC10SC10 (NIT4).<sup>34</sup> These results are presented in

<sup>34</sup> Microcontact printed stripes were prepared according to an earlier described procedure, using a PDMS stamp replicated from a silicon master with grating of  $5$  to  $3 \mu\text{m}$  and  $20 \text{ nm}$  thick gold substrates evaporated on titanium ( $2 \text{ nm}$ ) on silicon and cleaned following the same cleaning procedure.  $10^{-3} \text{ M}$  solutions of NIT4 have been used in a direct deposition by  $\mu\text{CP}$ . Patterned films were washed with THF, ethanol and dichloromethane, dried under nitrogen flux and immediately analysed or kept under inert atmosphere until testing.

the following Figure and evidence a homogeneous patterning on gold surface (evaporated on Si).

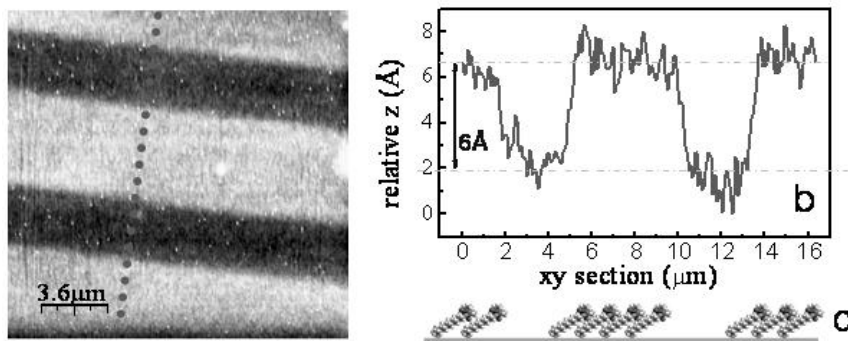


Figure 6.28. (a) AFM image ( $18 \times 18 \mu\text{m}^2$ ) of NIT4 micro-contact printed in stripes on gold with a PDMS stamp ( $5 \mu\text{m}$  stripes spaced  $3 \mu\text{m}$  apart). Dotted line indicates the xy section presented in (b). In (c) a schematic view of the expected packing of molecules on the basis of the measured profiles. Reprinted from Mannini M. et al. 2008b, Copyright 2008, with permission from Elsevier.

These data are not conclusive and do not appear to be completely convincing. In fact we extrapolate from the profiles a very strong tilting of the molecules on the surface.

Moreover, due to the small interaction within the sulphide linking group and the gold surface, a non negligible mobility of these molecule on the surfaces can be expected. Exploration of different linking group and a complete ToF-SIMS imaging characterization are necessary and represent future developments of this investigation.

We conclude here the section devoted to the preparation of magnetic molecule functionalized surfaces. The investigation of the magnetic properties of the layers will be the topic of the next chapters. It will provide also an interesting feedback concerning the presented preparation methods and suggestions for the next steps needed to improve the quality and the properties of deposited systems.



## Chapter 7

### Attempts in detecting the magnetism of one layer of molecules on surfaces

In this Chapter and in the next one we will describe our efforts in detecting magnetism of the surface functionalized materials prepared as described in the previous Chapter. These investigations represent the tip of the iceberg of our research that now is still emerging from the waters.

The main problem in investigating the magnetic properties of submonolayers of molecular material is related to the small amount of material present on surfaces and to consequent difficulties in the application of traditional magnetic characterization techniques.

#### 1. Traditional measurement of Mn12 functionalized surfaces

In order to measure magnetism of Mn12 functionalized surfaces using bulk techniques, the first problem is related to the contribution of the substrate, that in certain situation exceeds that of the deposited systems.

In fact contaminants present on the substrate can produce signals of the same relevance or with stronger intensity than the expected ones coming from the ultrathin film. Moreover, also without any effective spurious contributions, the diamagnetic component obtained from the bulk of the slide supporting the film affects the sensitivity of measurement with magnetometers.

In this sense, before any attempts of measuring these deposited materials, strong efforts were done in selection and characterization of substrates for measurements. These substrate, that for our purpose had to be based on Au(111), were obtained by evaporation on mica surface that represents the best solution for surface investigations of the STM type. However these surfaces were completely unusable for Mn12 film investigations due to the presence in the mica of contaminants like iron or manganese ions. On the contrary such supports have been successfully used for ESR investigation of monolayer of radicals due to the absence of signals in the relevant  $g = 2$  spectral region. These results will be described in Paragraph 3.

Gold evaporated on silicon with an adlayer of Ti or Al (that allows the complete and stable adhesion of gold) should represent a good alternative to mica. This has been evidenced also in SQUID experiments recently reported by Nait Abdi *et al.* (Nait Abdi A. *et al.* 2005) investigating a differently obtained deposit of Mn12 molecules. In our opinion however, the presented results must be reconsidered as they

evidence a stronger signal compared to the expected one for a theoretical monolayer calculated via sterical hindrance limitations. In any case, in these conditions, standard SQUID magnetometers appear to be really close to their detection limit. For this reason we tried to maximize surface/volume ratio by depositing these molecules on both sides of thin bulk gold foils. After the incubation and cleaning procedures obtained following the indications given in Chapter 6, these gold foils<sup>35</sup> were packed in a small volume fitting the sample space in a SQUID sample-holder.

We deposited Mn12LC15 (2) following the procedure described in Chapter 6 on these foils; considering that the use of such surfaces increases the available area (128 cm<sup>2</sup>, 27mg of gold) and supposing a similar coverage as that observed with STM, we expected to have a signal corresponding to 10<sup>14</sup> molecules on surfaces, that is sufficiently over the expected detection limit. In Figure 7.1 the resulting magnetization behaviour obtained varying the field within -6 T and +6 T is reported.

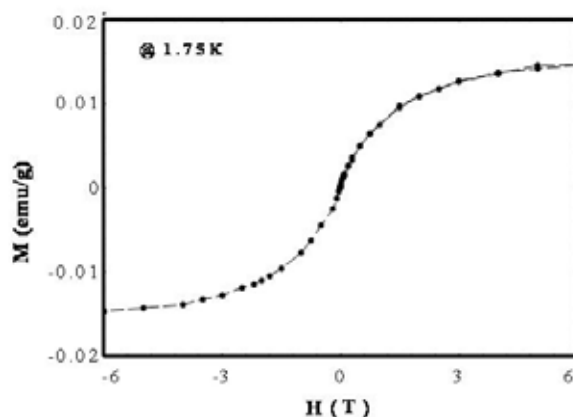


Figure. 7.1. Magnetization of gold passivated with 2 molecules at 1.8 K.

A purely paramagnetic behaviour was observed and the expected (and hoped) hysteresis loop was not found. Currently investigations are in progress based on the further increasing of the deposited material by using Mn12 functionalized gold nanoparticles.

## 2. Surface measurement of Mn12 functionalized surfaces

In order to increase the efficiency as well as the sensitivities of the magnetic measurements different techniques compared to the traditional ones have to be used. Sur-

<sup>35</sup> Foils of gold was purchased from standard producers of gold for alimental purposes. Before use it was cleaned with piranha solution (see footnote 9, in Chapter 6) and rinsed with water, ethanol and dichloromethane.

face sensitive techniques reduce the spurious sources of noise intrinsically probing only species present on the surface.

## 2.1 Magneto-optical characterization of functionalized surfaces

A first attempt to investigate magnetism of Mn12 species was done in collaboration with the European Laboratory for Non-Linear Spectroscopy in Florence by the use of a Magneto-Optical effects like Magnetic Circular Dichroism (MCD), Surface Magneto Optical Faraday (Faraday M. 1846) and Kerr Effects (Kerr J. 1877). The obtained results were described in details in another PhD thesis work (Bogani L. 2005), while here we present only a short summary of the results that now are collected in a manuscript (Bogani L. et al. 2007).

Before investigating ultrathin films, as in Chapter 6, a calibration of the instrumentation was done by investigating dispersion of Mn12 derivatives in an optically transparent elastomeric resin (Sylgard® 184 Silicone Elastomer, from Dow Corning, the same one we used for  $\mu$ CP stamp purposes). This permitted also to evaluate the sensitivity of this setup. Figure 7.2 shows hysteresis loops obtained by investigating, in transmission mode, e.g. by measuring the dichroic signal as a function of the applied magnetic field, dispersed samples with different Mn12-*pivalate* (Gerbier P. et al. 2003) concentrations indicating that the sensitivity of our apparatus allows the detection of the signal of about 5 monolayers of Mn12. No concentration effects are present, contrary to what observed in other systems (Bogani L et al. 2007).

The high sensitivity of this transmission mode has then been used to investigate the depositions of ultrathin films of Mn12 deposited on gold thin films (evaporated with a Ti adlayer on glass<sup>36</sup>). In Figure 7.2 we present results obtained from five slides passivated with Mn12 derivatives, the Mn12LC15 (2) and the Mn12PhSMe (4) with a 24h incubation time. These results are with those obtained for dispersed Mn12 samples.

No opening of the hysteresis loop is observed for monolayers of 2 and 4. Even if we are very close to the detection limit of the technique it is interesting to stress that a significative difference has been observed between deposition of 2 and 4 derivatives. In fact, even if deposited films of 2 was proved to be more dense than the films obtained with 4, a stronger magnetic contribution was observed for this last one. This evidenced an unusual behaviour, may be related to some changes in the chemical or electronic structure of the molecules. This technique is however not able to shed light on the phenomena occurring on surface. A different technique is needed to deeper investigate these samples.

<sup>36</sup> These substrates produced following our indications by SSENS inc. in the Netherlands was characterized by a 40% transmittance that allowed us to measure signals in transmission from 5 packed slides in order to be closer to the sensitivity of the used setup. A bigger amount of slides was impossible to be used because the smaller intensity of the transmitted signal.

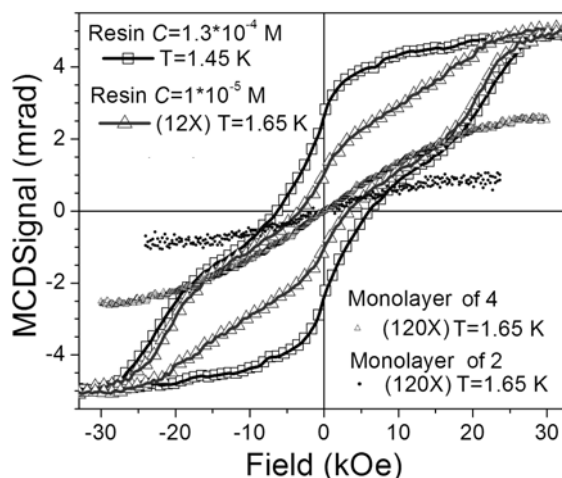


Figure 7.2. MCD signal acquired at different temperatures and concentrations. The same field-sweep rate of 12 kOe/min and the same wavelength of 632.8 nm were used for all samples. Line and squares: included sample with concentration  $C=1.3 \times 10^{-4}$  M at  $T=1.45$  K. Line and triangles: included sample with concentration  $C=1 \times 10^{-5}$  M at  $T=1.65$  K, magnified 12 times. Scatter circles: 10 superimposed plates of (2) grafted on gold, magnified 120 times. Scatter triangles: 10 superimposed plates of (4) grafted on gold, magnified 120 times. Reprinted from Bogani L. et al. 2007, Copyright 2007, with permission from Wiley-VCH.

## 2.2 XAS and XMCD characterization of functionalized surfaces

One of the most powerful technique to investigate the magnetism of nanostructure on surfaces is X-ray Magnetic Circular Dichroism (XMCD).

This technique requires synchrotron facilities and therefore is a non easily accessible technique. However its potentiality makes it a unique tool in nanomagnetism. XMCD in fact, at the same time, permits a chemical selectivity, providing information about specific atoms and their oxidation state, allows to resolve transitions involving different core orbital levels thus permitting to separate orbital and spin contributions to the magnetic moment.

Here the first results obtained with the collaboration of Dr. Philippe Saintavit and Dr. Christophe Cartier dit Moulin of the University of Pierre et Marie Curie of Paris (UPMC, France), investigating the Mn12 modified surfaces are presented (Mannini M. et al. 2008d). Just as before, we briefly describe the XMCD technique, the state of art of the theoretical and experimental investigation of bulk Mn12 using XMCD and our validation of these data by investigating bulk samples of Mn12 sulphur derivatives.

These experiments were done at BESSY II synchrotron in the UE46-PGM insertion device beamline. Here (and in all the third generation synchrotrons) an undulator modifying the trajectory of accelerated electrons inside the ring produces a packed set of x-rays. The energy of these radiations is defined by the vertical gap between the electron beam and the magnet arrays constituting the undulator. By shifting hori-

zontally the separated magnet rows as illustrated in Figure 7.3 a helical magnetic field is generated: this field brings the electron bunch on an elliptical trajectory emitting elliptically polarized light. By changing the relative arrangements of these arrays linearly as well as circularly polarized lights are produced.

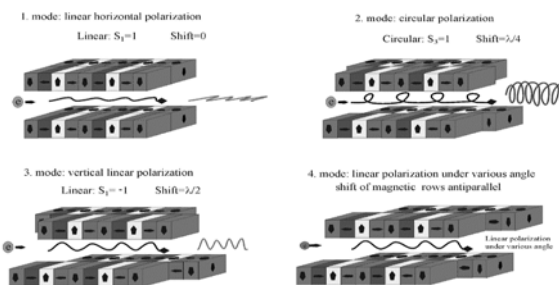


Figure 7.3. Relative arrangement of the magnet arrays achieving differently polarized lights. Courtesy of BESSY, Germany.

From the obtained polarized light, specific energy components are extracted using a plane grating monochromator. This permits the acquisition of energy dependent spectra. The beam is then shaped (increasing or decreasing the total density of photons) and focused to increase the intensity of the flux (or defocused to spread the beam) using a refocusing mirror.

The beamline end-station comprises the cryostat, which is able to reach temperatures within 1.5 K and 300 K in the  $^4\text{He}$  pumping setup and 200mK using the  $^3\text{He}$ - $^4\text{He}$  dilution refrigerator. This cryostat is also equipped with a superconducting coil ( $-7\text{ T} < B < +7\text{ T}$ ) and permits recording spectra both in absorbance (through a Total Electron Yield detector, TEY) and in fluorescence detections. In our “beamtimes” we used both cryogenic setups and the TEY detection.

The XMCD technique is based on detection of changes in the absorption cross section for circularly polarized light depending on the magnetic properties of the absorber (Schütz G. et al. 1987; Erskine J. L. and Stern E. A. 1975; Beaurepaire E. 2006). X-ray absorption comes from the excitation of electrons from deep core levels of a selected atom by the absorption of a photon (X-ray Absorption Spectroscopy, XAS) (Koningsberger D. C. and Prins R. 1988).

Historically, “dichroism” was referred to the change of colour of some material when absorbing light along two different directions but, more generally in terms of absorption, is used to characterize the dependence of the measured spectra on the polarization of the incident light (Faraday M. 1846; Kerr J. 1877).

In the XMCD/XAS experiment the photon energies are typically of the order of few hundred eV involving excitation of electrons from core levels to unoccupied valence states in the sample. The absorption in the exchange split valence states is different for the two orientations of the circularly polarized light according to a dipolar selection rule:

$$\Delta j = 0, \pm 1; \Delta s = 0; \Delta m = +1 \text{ (left circular)} -1 \text{ (right circular)} \quad (\text{Eq. 7.1})$$

Schematically, as described in Figure 7.4, in a simplified one electron vision, considering the  $L_{2,3}$  edges (the transition within 2p and 3d levels that we are interested in studying in 3d transition metals) the XMCD experiment can be described in a two-step picture (Stöhr J. et al. 1994).

In the first step, the absorption of left (right) circularly polarized light leads to spin-up (spin-down) polarization of the photoelectrons at the  $L_3$  edge via spin orbit coupling in the core level ( $j = 1 + s$ ). In the second step, the d-valence band acts as a spin detector. Due to spin-conservation the left-circularly polarized light probes mainly the larger number of unoccupied spin-up states with respect to the direction of the magnetization. Hence, the adsorption cross sections for the two helicities differ due to the imbalance of the spin-up and spin-down d-valence band. The effect reverses at the  $L_2$  edge due to the opposite spin-orbit coupling in the core level ( $j = 1 - s$ ).

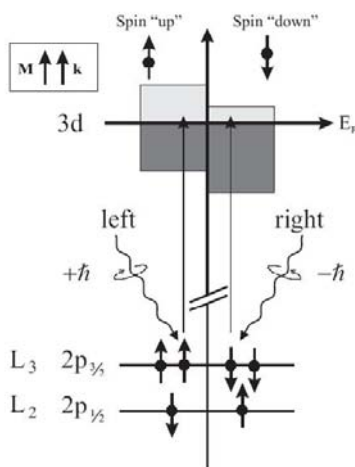


Figure. 7.4. Scheme of the physical origin of the L-edges XMCD in the two-step model.

The strong dichroism at the  $L_{2,3}$  edges of transition-metal ions and  $M_{4,5}$  edges of rare-earth ions provides information about their ground-state magnetic properties. Moreover, by exploiting the chemical sensitivity of X-ray absorption edges, contributions from different transition-metal and rare-earth ions within the molecule can be easily separated.

The previous model is a very simplified one and in most cases (and also in our specific case) supports only a qualitative analysis. In fact to describe quantitatively these systems a more complex multi-electron description, the 'crystal-field multiplet approach' including Coulomb and exchange integrals has to be used (Yamaguchi T. et al. 1982; Thole B.T. et al. 1988; van der Laan G. et al. 1988).

First attempts to investigate bulk samples of Mn12 exploiting XMCD was done by our group, before the starting of this thesis work, in collaboration with the UPMC group (Moroni R. et al. 2003; Ghigna P. et al. 2001). In these works the ferrimagnetic structure of Mn12-*acetate* was confirmed, and the individual magnetic moments of MnIII and MnIV ions were found to be in good agreement with the values

obtained by means of first-principles calculations and polarized neutron diffraction experiments (Robinson R.A et al. 2000). The orbital and spin contributions to the magnetic moment have been evaluated for each manganese ion, providing the evidence of negligible orbital magnetic moments for both MnIII and MnIV ions.

Usually, XMCD spectra can be powerfully analyzed by means of *sum rules* technique (Thole B.T. et al. 1992) that allows the determination of the orbital and spin magnetic moments of the constituent atoms. However, in this case, due to the co-presence of Mn ions in different oxidation states with overlap of the bands coming from the  $2p^63d^n \rightarrow 2p^53d^{n+1}$  transitions, this treatment is not applicable.

A *crystal-field multiplet* calculation has been applied simulating independently reference spectra for MnIII and MnIV in the same coordination geometry present in the Mn12 structure (elongated octahedral and octahedral respectively) by extrapolating the characteristic parameters from standard samples with the same geometry. Crystal-field multiplet calculations provide the atomic and crystal-field parameters used as a starting point to simulate the XMCD spectra of Mn12-*acetate*.

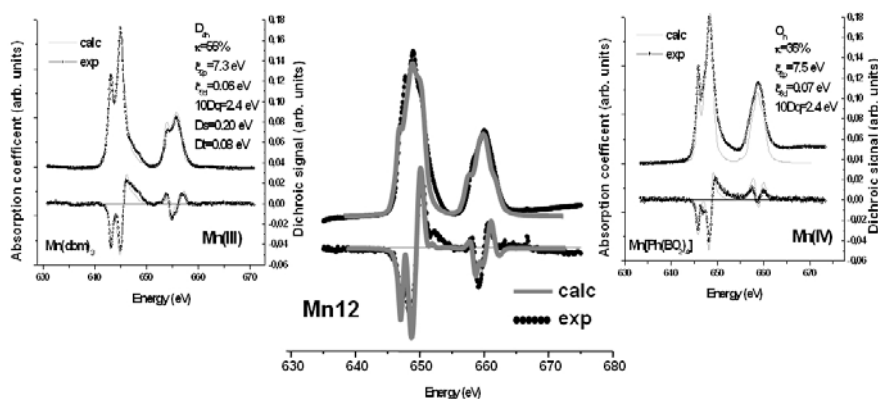


Figure 7.5 (Left) Mn(III), (right) Mn(IV), and (middle) Mn12-*acetate* XAS and XMCD. Courtesy of Dr. Philippe Saintavitt. Original data published in Moroni R. et al. 2003.

This approach, where the synthesis of model molecular compounds is combined with crystal-field multiplet calculations, allowed the separation of the contributions from MnIII and MnIV ions and the extraction of information about their respective ground-state electronic and magnetic properties. For our purposes these spectra are considered as a starting point and a reference for Mn12 a XMCD fingerprint.

In fact our first experiments focused on confirming that the procedures for sulphur based ligand functionalization of Mn12 don't affect the oxidation states of MnIII and MnIV atoms contained in Mn12 molecules as well as their antiferromagnetic coupling. This was done merely by measuring bulk samples of Mn12 derivatives Mn12LC15 (2) and Mn12PhSMe (4). XAS spectra gave indications of the unaltered oxidation state while XMCD spectra provided the confirmation that coupling is unchanged as it can be seen in Figure 7.6 showing spectra obtained by measuring a sample of powder of Mn12PhSMe (4) pressed over a copper plate as sample holder. These experiments evidenced spectra similar to those obtained with Mn12-*acetate*.

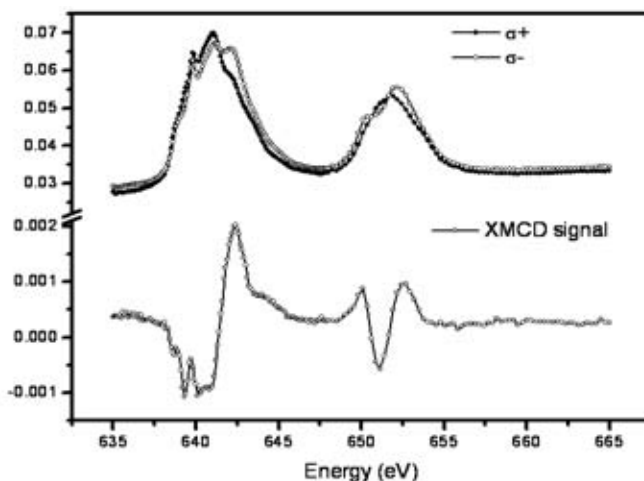


Figure 7.6 XAS spectra and XMCD signal at Mn  $L_{2,3}$  edges in bulk 4.

XAS and XMCD characterizations obtained at 4.2 K and in an induction of 4 T showed the persistence of the ferrimagnetic spin structure. Similar results were obtained also with Mn12LC15 (2) as also confirmed by independent room temperature XAS measurements reported in the literature (Del Pennino U. et al. 2006).

The second step was to confirm that a procedure of drop casting generating a thick film of molecules on gold doesn't introduce any degradation of the clusters. The spectra obtained at 2.5K depositing 4 using this procedure is shown in Figure 7.7.

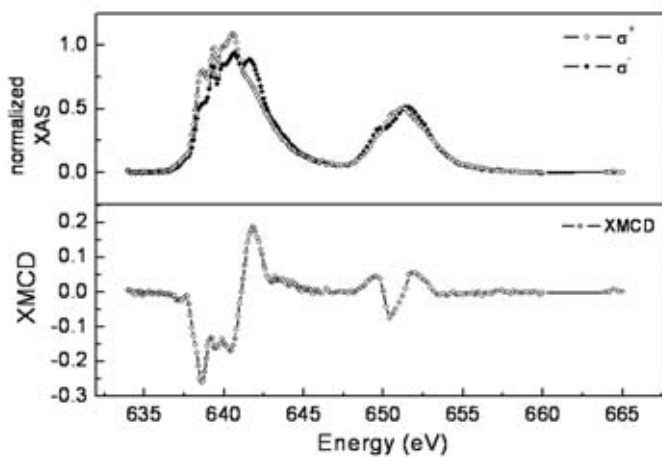


Figure. 7.7. XAS spectra and XMCD signal at Mn  $L_{2,3}$  edges of drop cast 4 on gold.

With this procedure, samples with similar characteristics to the bulk sample are obtained, even with some minor differences that can be attributed to the use of the gold substrate. Charging problems, easily observable with insulating powders, are here avoided thanks to the proximity of the conducting surface. In any case, by exploiting the absorption detection through the TEY detection mode, we are essentially sensitive to the region most distant from the conductive substrate excluding any effect of the conductive substrate.

In these conditions we observed that, also with some small effects of reduction of the Mn12 (evidence by the feature on the left of the  $L_3$  edge, as we will describe in the following), the sampled region of the spectrum conserves the feature observed in powders of Mn12 clusters.

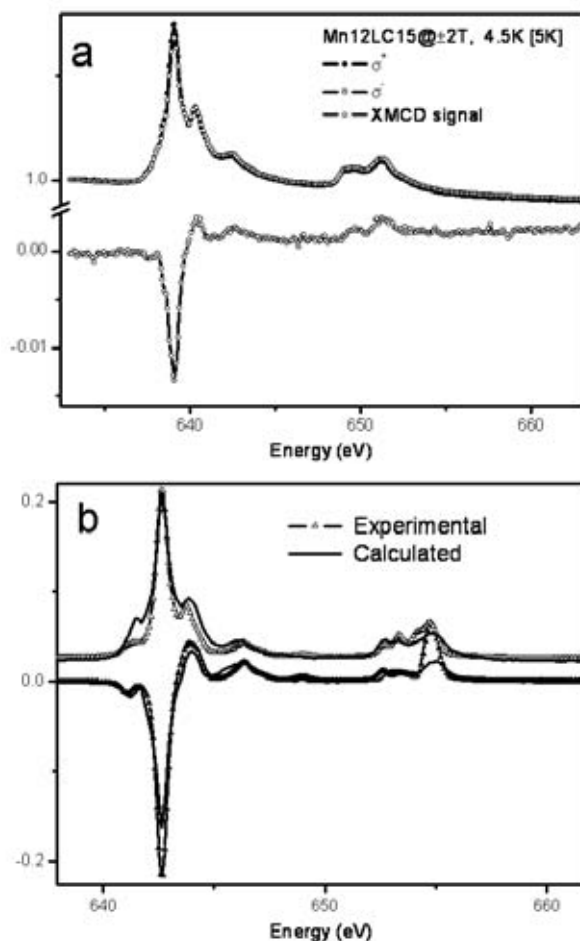


Figure 7.8. (a) XAS spectra and XMCD signal at Mn L<sub>2,3</sub> edges of a monolayer of 2 on gold deposited after the treatment of the solution with ammonia. (b) Simulated and recorded spectra obtained for a MnII based compound in an octahedral geometry. Experimental data are obtained from the investigation of  $[\text{Mn}(\text{Me}_6[14]\text{jane-N}_4)\text{Cu}(\text{oxpn})](\text{CF}_3\text{SO}_3)_2$ .

These attractive results were obtained by hard work on optimizing the experimental setup, which should pave the way to the investigation of monolayer deposits. Thanks to this optimized setup in fact we were able to avoid damaging of the samples by the beam. Photo-reduction is likely to be encountered due to the high photon flux, as observed in previous attempts. In order to cope with that, UE46-PGM beamline was ideal since it permitted to reduce the number of photons on the sample by a factor of 500 by maintaining the cooled aperture closed to  $0.2 \times 0.2 \text{ mm}^2$ , the exit slit equal to  $20 \mu\text{m}$ , and it permitted also to decrease the photon density (gaining an extra factor of 400) thanks to a toroidal mirror that provided a parallel beam.

On the basis of such experiments and maintaining this low damaging setup we started to characterize monolayer deposit of Mn12 derivatives described in Chapter 6. The first sample we investigated was the Mn12LC15 (2) deposited after the addition of ammonia as deprotecting agent of the thio-acetyl group, as discussed in Section 6.1.1. This kind of samples was preliminary investigated by room temperature XAS spectrometry at Elettra synchrotron facility in Trieste (Del Pennino U. et al. 2006).

It is clear from Figure 7.8a that the spectra, recorded at 4.5K, present features completely different from the expected ones. These features appear to correspond to the observed one with a simpler MnII based compound (Figure 7.8b).

This result has to be confirmed and carefully analyzed; in fact, if we confirm that such a significant reduction is not due to the beam, we will have to reconsider the results obtained with this material (Cornia A. et al. 2003; Mannini M. et al. 2005).

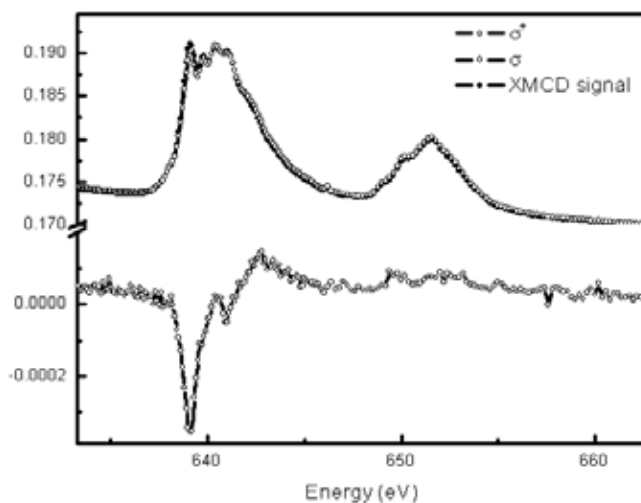


Figure 7.9. XAS spectra and XMCD signal at Mn  $L_{2,3}$  edges of a monolayer of 2 on gold.

For the moment we noticed that this effect is reproducible and that this reduced species signal appears to be constant in time during successive analysis. Moreover, we have to keep in mind that STM and AFM provide reproducible features corresponding to the size of Mn12 clusters. For this reason we started to think about

sponding to the size of Mn12 clusters. For this reason we started to think about a possible chemical origin of this reduction and we found that ammonia used in deprotection step can act as reducing agent, as a  $g=2$  signal is observed when measuring frozen solution of Mn12 cluster with ammonia. We tried then to use the modified deposition procedure consisting in directly grafting (2) without ageing and deprotection passage, as described in Chapter 6. Figure 7.9 presents results obtained examining at 2.5 K samples prepared under these conditions.

Focusing on the XAS spectra we observe that similar features as observed in the bulk analysis, and therefore corresponding to the expected features, are found. On the contrary we noticed that the XMCD signal is strongly reduced compared to the bulk and that again the highest signals origin from MnII even if a second negative assignable to Mn12 is now observed.

In order to justify this surface damaging an origin can be found in the grafting mechanism of thiols also when kept protected with acetylthio- groups. The grafting of thiols induces the production of molecular hydrogen in a redox reaction obtaining the formation of S-Au bond. In this case however it is also possible that instead of hydrogen, MnIII or MnIV inside Mn12 were reduced.

With the purpose of verifying this hypothesis we exploited the deposition of (4), the grafting of which doesn't involve any redox reaction. These samples prepared ex situ form a submonolayer of isolated molecules as described in Chapter 6. With respect to the deposition of (2) the amount of material present on surface is decreased down to one molecule per  $25 \text{ nm}^2$  however the detected signals are significant and no evidence of appreciable photo-reduction was noticed after one day of measurements.

Figure 7.10a shows that even if XAS spectra of the molecular submonolayer recorded at 2.5K strongly resemble those of the bulk sample, some spurious MnII contributions still remain in the XMCD signal. In any case we noticed (see Figure 7.10b) that by removing the MnII contribution (by normalizing the experimental spectra of 4 in respect to the component of MnII and subtracting the normalized spectra of a MnII compound) we can isolate components of the XMCD spectra that nicely agree with the expected ones for Mn12.

These results allow us to suppose that two phases are present on the surface and that at least partially the grafting procedure do not modify the magnetic properties of the cluster and the antiparallel alignment of the MnIII and MnIV spins is conserved. The fact that the dichroic signal is substantially modified after the deposition on the Au surface can be justified because also a slight presence of a MnII phase on the surface strongly affects the shape of the signal. In fact the antiparallel aligned MnIII and MnIV components partially cancel each other thus providing a resultant signal less intense than the one coming from MnII visible at lower energy.

Considering these traces of MnII as a separated spurious phase present together with Mn12 on the surface, recently we have started new experiments by exploiting an increased coverage of surface by the use of the deposition of Mn12PhSMe (4) from a 0.1 M dichloromethane solution (as described in Chapter 6). By doing so we supposed to increase the contribution of the unaltered component maintaining constant the spurious contamination of MnII. In order to better evidence the contribution of Mn12 very low temperature measurements using the  $^3\text{He}$ - $^4\text{He}$  dilution set-up have been performed.

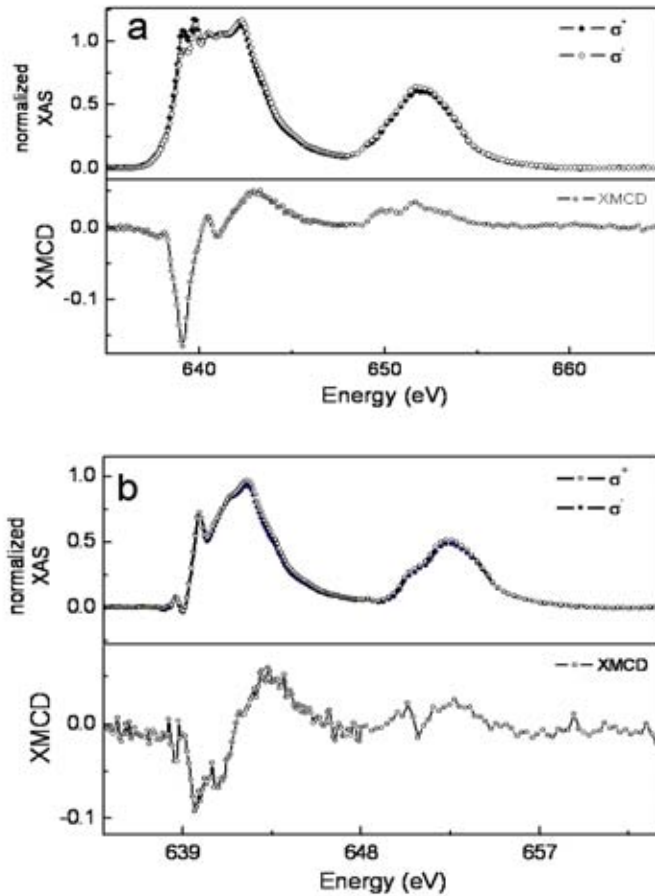


Figure 7.10. (a) Untreated XAS spectra and XMCD signal at Mn  $L_{2,3}$  edges of a monolayer of 4 on gold. (b) Elaborated XAS spectra and XMCD signal at Mn  $L_{2,3}$  edges of a monolayer of 4 on gold after the removal of MnII contribution.

Results obtained at 400 mK by applying 4T (Figure 7.11a) confirmed our suppositions, in fact, also if a small MnII component is still observed, at this time a strong dichroic component coming from unaltered Mn12 is observed. Here in fact are easily recognisable both the dichroic effect on the end of the  $L_3$  edge and on the  $L_2$  edge. In this configuration we investigate also different samples. Interestingly the investigation of monolayer depositions of Mn12 derivative deposited on Silicon functionalized surface, prepared by the group of Talal Mallah, Université de Paris Sud (Fleury B. et al. 2005) provides in the same of measurement condition, a signal very similar to the one observed for Mn12LC15, corresponding to a dominant paramagnetic MnII signal (Figure 7.11c).

We are not able to identify in this case the origin of the damaging of the originally deposited cluster as in this case also an ageing of the investigated sample due to transportation problem can be supposed. However for our purpose this sample has

been used to emulate the spurious MnII contribution of the damaged phase present in the previous one in order to isolate the Mn12 contribution again by normalizing both the spectra and subtracting the last one to the original spectra obtained for Mn12PhSMe (4). The resulting spectra are reported in Figure 7.11c and present features expected for a Mn12 derivative even if the approximation induced by the subtraction procedure have to be kept in mind.

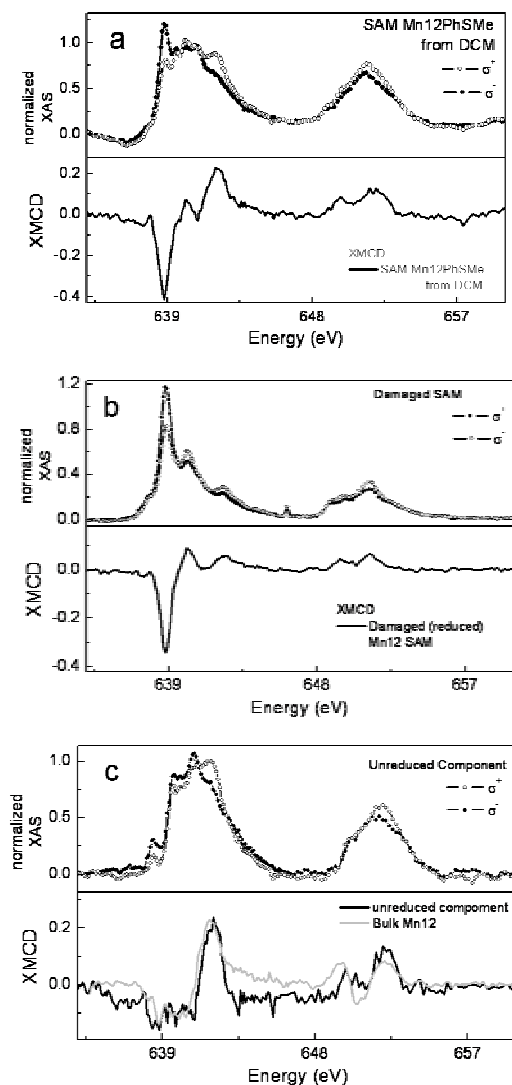


Figure 7.11. (a) Untreated XAS spectra and XMCD signal at Mn  $L_{2,3}$  edges of a monolayer of 4 on gold deposited from dichloromethane. (b) Untreated XAS spectra and XMCD signal at Mn  $L_{2,3}$  edges of a monolayer of the damaged sample which preparation is described in (Fleury B. et al. 2005). (c) Elaborated XAS spectra and XMCD signal at Mn  $L_{2,3}$  edges of a monolayer of 4 on gold after the removal of the supposed MnII contribution derived from (b).

In order to clarify these qualitative observations we studied the dependences of these XMCD signals varying the magnetic field. This allowed us to evidence a different magnetic behaviour of the two detected phases.

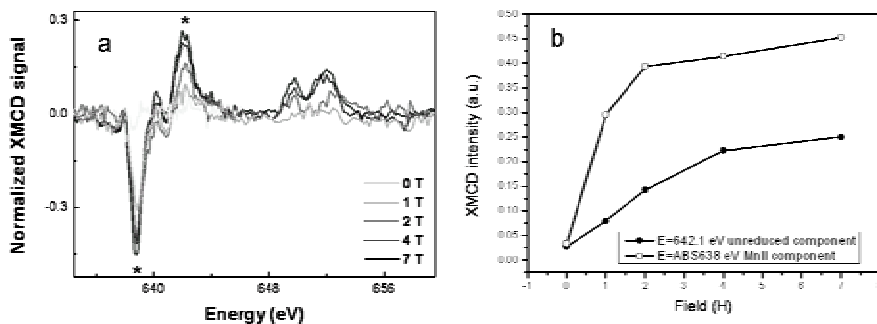


Figure 7.12. (a) XMCD signal at Mn  $L_{2,3}$  edges of a monolayer of 4 on gold deposited from dichloromethane varying the external magnetic field. (b) Dependences with the magnetic field of the most significant peaks (marked with asterisks) observed in (a).

In Figure 7.12a, where the intensity of XMCD spectra at the peak relative to the “MnII phase” (638 eV) and at the peak of “MnIII&MnIV phase” (642 eV) are reported as a function of the magnetic field. In fact, by plotting the intensity of these signals vs. the magnetic field we construct a sort of magnetization curves. We observe that the “MnII phase” saturate faster than the “MnIII&MnIV phase”. We can therefore conclude that these two phases are really independent in agreement with our hypothesis that the “MnIII&MnIV phase” corresponds reasonably to the undecomposed Mn12PhSMe and that partially decomposed clusters are also present on the surface in the form of MnII species. Obviously all these suppositions have to be confirmed by Ligand Field Multiplet calculations that are still in progress.

These XMCD experiments on monolayers of Mn12 have to be considered as a preliminary investigation. However this represents the best in this field. In fact only a few of experiments has been done in similar condition of small amount of material (Gambardella P et al. 2002) and never it has been done with similarly delicate systems like Mn12.

XMCD allowed us to evidence for the first time what really happens depositing Mn12 derivatives on surfaces (Mannini M. et al. 2008d). Actually it permitted to have feedback in the deposition due to their unique capability of evidence (also for this small amount of material) differences in the oxidation states of the Mn atoms present on surface.

At the moment we are not able to define precisely the origin of reduced species observed as well as we are no able to exclude some effect of the beam in this process. However we used the apparatus in unusual condition of very low damaging in order to exclude (or at least to minimize) this degradation process.

Surely XMCD would provide also information about the dynamic of the magnetization of the monolayer of Mn12 but, up to now, any successful attempt in this direction has been done neither in the bulk phase. This kind of experiments will be the subject of further studies that will be focused also on the investigation of newer

SMMs on bulk phases as well as on surface (Mannini M. et al. 2008a, Mannini M. et al. 2008c, Mannini M. et al. 2008d).

### 3. Measurement of Nitronyl Nitroxide functionalized surfaces

The investigation of the magnetism of Nitronyl Nitroxide functionalized surfaces is, at least in a qualitative viewpoint, less problematic than in the Mn12 case. In fact ESR spectrometers equipped with high sensitivity cavities are able to detect the signal coming from a single layer of deposited molecules (Mannini M. et al. 2007b). As anticipated earlier in the text (Chapter 6), with ESR we are able to investigate directly the same kind of samples we characterized with STM and ToF-SIMS. In this way we exclude any difference due to a different substrate in the induced morphology of the film.

In the following ESR characterization of the Nitronyl Nitroxides NIT1, NIT2, NIT3 is described.<sup>37</sup> X-Band ESR spectroscopy has been used to verify the effect of the deposition procedure on the magnetic properties of different NITRs and to get information about the dynamics and the degree of organization of the deposited molecules, in order to complement the information obtained by STM and ToF-SIMS techniques (Mannini M. et al. 2007b). Indeed, ESR acts as a local probe and it is in principle an ideal technique to obtain such kind of information on organized monolayers, which can be derived from the *g*- and *A*- tensor anisotropy as well as from the analysis of the temperature dependence of the spectrum. However the main problem which strongly limits the number of studies published in literature (Gallani J. L. et al. 2001; Ruthsteinet S. al. 2005) up to date is the very small amount of material that is probed when a single monolayer is investigated, which is often close to the sensitivity limit of ESR.

A typical ESR spectrum of a SAM of NIT1 obtained at room temperature is reported in Figure 7.13.

The detection of an ESR signal indicates the presence of a paramagnetic species on the gold surface. We note here that the spectral appearance is not appreciably changing with time thus indicating that the organization of the SAM is stable with time.

Analysis of more subtle peculiarities could in principle give access to important pieces of information on differences among motional properties and spin–spin interactions in different radicals. However, a suitable simulation program for quantitatively reproducing the dynamic effects in species containing more than one nuclei coupled to one unpaired electron has been reported in literature only recently (Polimeno A. et al. 2006) and has been applied to NIT1 molecules up to now only on so-

<sup>37</sup> ESR measurements were carried out on an X-band Bruker Elexsys E500 spectrometer equipped with a ER 4131VT liquid nitrogen cryostat for variable temperature studies and a ER4122SHQE cavity to enhance the sensitivity of the instruments (with a nominal weak pitch sensitivity of 3000:1). The sample was mounted on a sample holder for single crystals connected to a goniometre for orientation dependent studies. Samples were prepared according to the procedure described above.

lutions (Barone V. et al. 2006) with the future purpose to describe the behaviour of deposition. Here we restricted investigation to a qualitative analysis of the systems.<sup>38</sup>

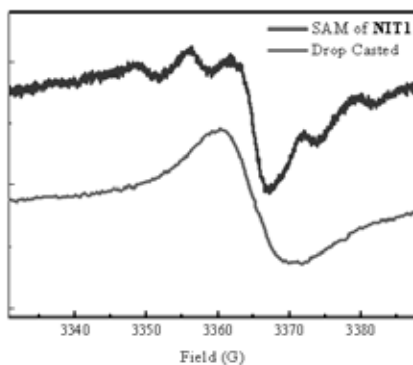


Figure 7.13. Comparison of a frozen solution ESR spectrum of NIT1 with that of a drop cast sample.

The hyperfine structure of the signals, structured in five lines with approximate spacing of 7.5 G and centred around  $g=2.009$ , indicates without any doubt that the deposited species are NITRs with the unpaired electron being delocalized on the two equivalent  $^{14}\text{N}$  ( $I=1$ ) nuclei. The spectra are similar to those recorded in solution of the same radical and reported in Figure 5.3.

A first piece of information can be gained by comparing the SAM spectrum with that obtained on samples prepared by drop casting and successive evaporation of the solvent: in this case the hyperfine structure is lost due to the strong intermolecular exchange interactions, typical for a concentrated spin system (see Figure 7.11). This indicates that the intermolecular interactions in the radical SAMs are reduced with respect to the sample obtained by drop-casting, suggesting that the distance between each radical is increased and the coverage is reduced in the former case. Furthermore it rules out the possibility that the ESR spectra observed for SAMs are due to a simple evaporation of the solution on the surface with solid radical precipitation. Instead, these data clearly indicate that a real chemisorption process occurs. The comparison of the SAM spectrum to that of a NITR solution containing a known and comparable number of spins, allowed us to obtain a rough estimate of the number of paramagnetic centres on the surface ( $\sim 5 \times 10^{13}$  spin). By assuming a surface occupation for each radical of  $6 \times 6 \text{ \AA}^2$  and considering a surface of the gold slide of about  $20 \text{ mm}^2$  one can estimate an approximately complete coverage of the surface. Notwithstanding the inherent limitations of quantitative EPR measurements and the approximations involved (neglecting of the roughness of gold surface, neglecting of possible

<sup>38</sup> The obtained S/N ratio was quite low and this, coupled with the presence of a relevant instrumental background signal that had to be subtracted from the raw ESR signals made the analysis of the spectra difficult.

SAM defects), this result suggests a quite homogeneous coverage of the surface and confirms the presence of only one molecular layer. Further it might be considered as an independent confirmation of the intermolecular distances estimated by STM. On this respect it has to be considered that with these distances the calculated dipolar contribution would be large enough to hamper the detection of a resolved hyperfine structure. Indeed, for a pair of Nitronyl Nitroxide radicals at a distance of  $6\text{\AA}$ , setting half a spin on the mid-point of each N-O bond (Benelli C. et al. 1989), would result in a dipolar field of about 40 G. However, this value refers to a fixed configuration of neighbouring molecules and does not take into account the dynamic of the paramagnetic groups which is expected to produce an averaging of anisotropic interactions.

Indeed, the global spectral appearance suggests a quite large mobility of the radical on surface. This is not completely unexpected because the methyl-thio linking group provides a weaker interaction with gold than that of thiol (Troughton E. B. et al. 1988; Lavrich D.J. et al. 1998). A comparison of the SAM of NIT1 room temperature spectrum with the temperature dependence of the solution spectra (Figure 7.14) suggests that the motion of the radicals on gold surface occurs on a timescale which is comparable to that of a viscous solution (around 180 K, just above the melting point of  $\text{CH}_2\text{Cl}_2$ ). This indicates a slow dynamic of the radical molecules on the surface, occurring on a time-scale comparable to that of the viscous solution; it further suggests that molecular motion occurs through large oscillations which result in quasi-isotropic spectra.

This interpretation is strengthened by the analysis of the temperature dependence of the SAMs spectra of the three deposited radicals, reported in Figure 7.14, where is evident that general features of the ESR spectra are essentially the same for the three radicals.

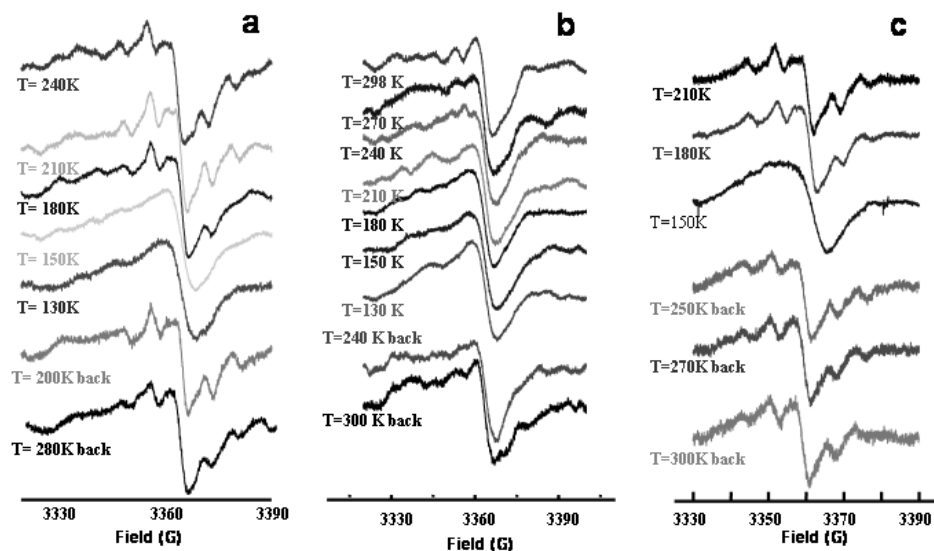


Figure 7.14. Temperature and time evolution of the ESR spectrum of a SAM of NIT1(a), NIT2 (b) and NIT3 (c) deposited on gold. Magnetic field oriented along the normal to the gold slide.

Within 180 and 150 K lines broaden so much that the spectrum collapses to a single broad transition centred at  $g = 2.009$ . On heating back to room temperature the original spectra are restored. This behaviour is a signature of the freezing of the radical motion below 160 K, resulting in a non-averaging of the anisotropic interactions and then in a broadening of the lines, which leads to the appearance of a single broad transition. The reversibility of the phenomenon indicates the stability of the SAMs with respect to thermal cycling and thus rules out that the spectral changes were due to a disruption of the SAMs with consequent formation of a powder-like phase.

Finally, in Figure 7.15 the variation of the spectra as a function of the angle of the applied field with the gold surface of the three different deposited radicals are reported.

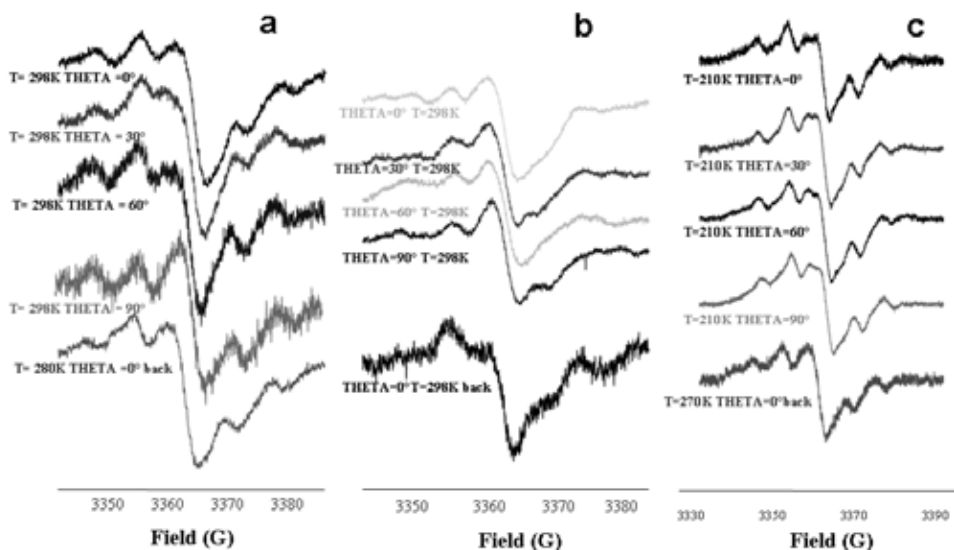


Figure 7.15. Angle dependencies of the ESR spectrum of a SAM of NIT1(a), NIT2 (b) and NIT3 (c) deposited on gold. Theta is the angle within the magnetic field and the normal to the gold slide.

The virtually complete absence of orientation dependence of the spectra is evident. At first glance this result might appear in contradiction with STM observation, which indicated the presence of ordering within the monolayer. However this is not unexpected if we consider that the qualitative analysis of the spectra suggested a quasi-isotropic motion of the radicals and that this motion occurs on a timescale which is slow for ESR spectroscopy, but is fast and thus undetectable for STM. We suggest that this spectral behaviour might result from the sum of the contribution of regions with slow, quasi-isotropic dynamics of the radicals and with different relative orientations. These can easily form as a consequence of differently oriented domains of the gold substrate and to the roughness of polycrystalline surface (Ulman A. 1991).

We can then conclude that the ESR analysis prove unambiguously that the paramagnetic character of the molecules is retained after deposition on gold and the SAMs are really made up of NITs. ESR spectra confirm the formation of a single layer of paramagnetic molecules with approximately complete coverage of the surface. The spectra show an intermediate behaviour between that of fluid solution and the one observed in the solid state thus suggesting a quite large rotational degree of freedom of the radical on surface. Finally, the presence of differently oriented domains on gold surfaces results in regions of differently oriented SAM and thus to the absence of orientation dependence of the spectrum.

We conclude here this chapter focused on investigating the magnetism obtained from at the most one layer of molecules. This objective has been partially attained for both the investigated series of systems. Concerning the Mn12 monolayers and sub-monolayers the magnetical characterization via XMCD appear to be the state of the art for this kind of samples. These experiments permitted to evidence failures in the employed procedures and to find some indication to improve the deposition in addition to the first series of real measurements of magnetism of one layer of single molecule magnets deposited on surfaces.

ESR characterization of self-assembled organic radicals allows us to evidence the permanence of the magnetism on surfaces of these molecules and provide, coupled with STM and ToF-SIMS techniques, an effective protocol for achieving appropriate samples for the ESN-STM experiments that will be described in the following chapter. As discussed in the next chapter, these experiments represent one of the possible solution for the ultimate level of magnetism measurements, the addressing and the reading of the spin in one single molecule.



## Chapter 8

### Magnetism of single molecules

In previous chapters a pathway for preparation of derivatives of single molecule magnets and organic radicals, their bulk characterization, their deposition and the following surface characterization as well as the study of magnetism of these systems on surface was described. The last part of the pathway, described in the previous chapter, resulted close to the limits of standard characterization techniques and in some cases required very sophisticated experiments like XMCD. Here we describe our first attempts focused on continuing this itinerary and trying to extrapolate new destinations. Our purpose is in fact the achievement of local investigation of the magnetism of single molecules. This result would imply a tremendous scaling down of existing memory devices and molecules are exciting candidates (Gatteschi D. et al. 2006; Miller J. S. and Drillon M. 2001-2005). Further interest is in exploring the possibilities related to the use of a single spin as a qubit for quantum computation, information and spintronics (Rugar D. et al. 2004; Elzerman J. M. et al. 2004; Xiao M. et al. 2004; Heinrich A. J. et al. 2004). All such issues are central goals in nano-scale science and technology and different solutions devoted to the access to single molecule magnetism have been proposed.

In this chapter we summarize different solutions for single molecule reading, describing a technique that have been evoked as good candidates for this single molecule magnetism investigation. We report some of the first attempts presented in the literature describing this kind of experiments. Finally we conclude this thesis work with our preliminary results about the use of a technique for detecting a single spin by a modified STM setup that detect the “noise” in radiofrequencies range induced by a single electron spin in the AC component of the tunneling current in the presence of a magnetic field. The presented measurements are not conclusive, in fact only preliminary results have been obtained at the moment. Moreover positive results have been obtained only for simple molecules like nitronyl nitroxides and not with SMMs. Nevertheless this reflects the state of the art of the detection of the magnetism of single molecules that is growing in interest but is still a young research area, far from having developed standard characterization procedures.

#### 1. Magnetism of a single molecule magnet

For historical reasons and for the great appealing in the community due to their incomparable SMM features, Mn12 has been considered the first candidate for single molecule magnetic investigations and in fact also before any experimental verifica-

tion, many theoretical papers have been presented (see for instance Park H. et al. 2000; Leuenger M. N. and Loss D. 2001). These theoretical studies describes the wide potentiality of measuring electronic transport properties through these molecules in presence of a magnetic field as a way to obtain information strictly related to the single molecule magnetism but also as a way toward an application of these systems in quantum and spintronics devices.

Experimentally, one of the most intriguing solution to investigate the Mn12 magnetism is based on the study of the electronic transport of these molecules when inserted within two nano-electrodes prepared via the break-junction or the electromigration techniques (Heersche H. B. et al. 2006; Jo M.-H. et al. 2006). With this technique, the electronic transport through a single Mn12 molecule weakly coupled to gold electrodes has been measured. Current suppression and negative differential conductance on the energy scale of the anisotropy barrier have been observed suggesting some insight toward an electronic control of nano-magnets.

Another suggestion for measuring single molecule magnetism has been proposed very recently by J.-P. Cleuziou et al. They describe the build up of a nanoSQUID assembled from single carbon nanotubes (Cleuziou J.-P. et al. 2006). In this case a Mn12 molecule is expected to be deposited inside a nanotube or on the external surface of the nanotube constituting the nano-SQUID and of course this is not a trivial task. No results have been reported at the moment but this very attracting solution seems to be a feasible way to characterize a single molecule magnet.

In any case direct probe of magnetism of SMM magnetism is expected to be achievable using scanning probe derivative techniques. STM and AFM techniques, as evidenced in Chapter 2, have pushed the resolution limit to atomic size, but detection of single spins and single molecule magnetism is still a hard challenge. Derivative SPM techniques allowing to access to magnetic information are sketched in Figure 8.1 and classified as AFM and STM based techniques. The description of the techniques is beyond the scope of this thesis and will be omitted. All these techniques must be considered as young techniques, with a strong potential of further developments. However, at least for the moment, only some of them possess the resolution needed to image single molecule and, in particular, the spatial resolution to detect the magnetic image of a single molecule.

For instance, Magnetic Force Microscopy, MFM, that is one of the oldest derivative techniques, fails in measuring single molecules, as we have verified during this thesis work thanks to the collaboration with the group of H.-J. Hug of the University of Basel (Switzerland). In fact, even if AFM mode at low temperature (8K) was able to detect single molecules, MFM analysis at these temperature in presence of strong magnetic field has not provided a magnetic contrast coming either from a single molecule or averaged over many molecule.

Other problems affect this SPM based technique. For instance special imaging conditions commonly employed for these experiments, like for instance strong tunneling currents, do not coincide with the best experimental conditions to investigate Mn12 on surfaces. Reducing the complexity of the molecule to be investigated on the surface, for instance employing the organic radicals described in the previous chapters instead of polynuclear clusters, has significantly reduced the difficulties, making the detection of a single molecule paramagnetism feasible, as described in the next section.

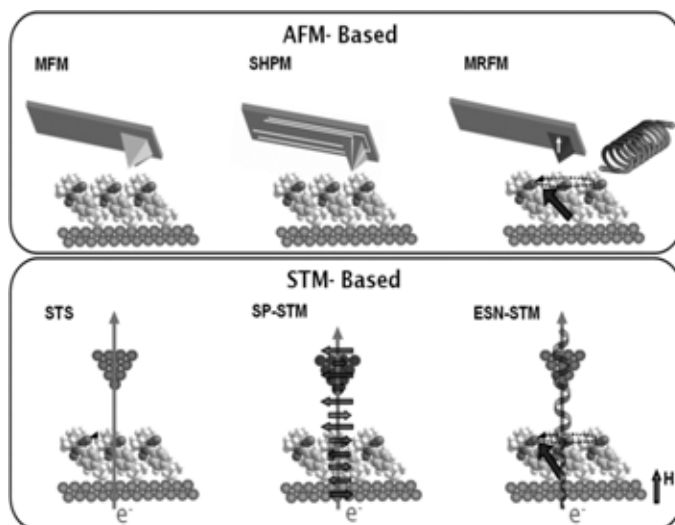


Figure 8.1. AFM based magnetic measurements (Up, from left) Magnetic Force Microscopy (Martin Y. and Wickramasinghe H. K. 1987), Magnetic Resonance Force Microscopy (Rugar D. et al. 2004), Scanning Hall Probe Microscopy (Oral A. et al. 1996). STM based magnetic measurements (Down, from left) Scanning Tunneling Microscopy (Zhao A. et al. 2005; Wiesendanger R. 1994), Spin Polarized STM (Wiesendanger R. et al 1990), Electron Spin Noise STM (Manassen Y. et al. 1989).

## 2. Detection of a single spin of organic radicals through the ESN-STM

A promising technique for single spin detection is the ESN-STM technique, which is based on the detection of noise in the tunneling current of the STM experiment at the Larmor frequency of the spin. This technique (Manassen Y. et al. 1989) has been first described and proved to be effective more than a decade ago by Y. Manassen, of the Ben Gurion University of the Negev, Be'er Sheva (Israel). These measurements exploit the unparalleled spatial resolution of the Scanning Tunneling Microscope (STM) to image the individual spin centres on a surface. In order to explore the magnetic properties of the molecules, ESN-STM introduces a sensitive RF recovery system for detecting very low RF power in the tunnelling current, a permanent magnet in order to introduce a DC field of several hundreds Gauss, coils for phase sensitive detection and RF filters.

ESN-STM is also known as Electron Spin Resonance (ESR)-STM (Manassen Y. et al. 1989) but it is indeed a noise spectroscopy.<sup>39</sup> In fact what is detected is the spectral density of the noise in the tunnelling current, which appear to be not completely white

<sup>39</sup> We terms noise spectroscopy the observation in frequency, without any external excitation, of the natural response of a system to the “thermal” noise.

but to have a detectable component at the Larmor frequency of the spin of the paramagnetic molecule in the external applied field. This is why this technique is termed “noise spectroscopy” (Manassen Y. 1997, Manassen Y. et al. 2000; Balatsky A.V. et al. 2002): the fluctuation of the single spin is basically detected as an incoherent phenomenon, like in *nuclear spin noise* spectroscopy (Sleator T. et al. 1985).

Physical systems are often studied by measuring their response to an external perturbation. Measuring the intrinsic noise of a physical system can provide the same information as measuring its response to a perturbation, but noise spectroscopy measurements often disturb the physical system less strongly and scale more favourably with system size reduction. For quantum systems at very low temperature, noise from quantum fluctuations in the ground state of an observable that does not commute with the Hamiltonian, can be used as a probe of the system properties. Indeed even if there is no effective resonance (as no energy is pumped into the system), ESN-STM locally exploits the same observable recovered as average value in standard ESR measurement, i.e. the precession frequency of the electron spin under the action of a static magnetic field. Moreover, due to their local resolution, this technique can provide additional information that are lost in averaging with macroscopic ESR like, for instance, differences in spectra obtained above different parts of molecules.

## 2.1 ESN-STM instrumentation description

At the same time of the beginning of this thesis our group started a strong collaboration with Y. Manassen giving me the opportunity to participate in the construction and the testing phases of one of these type of instrumental facilities (Messina P. et al. 2007; Mannini M. et al. 2007a) actually operative and on further development in the INSTM laboratory in Trieste in collaboration with the APE Research company. In Figure 8.2 some photos of this apparatus are presented.

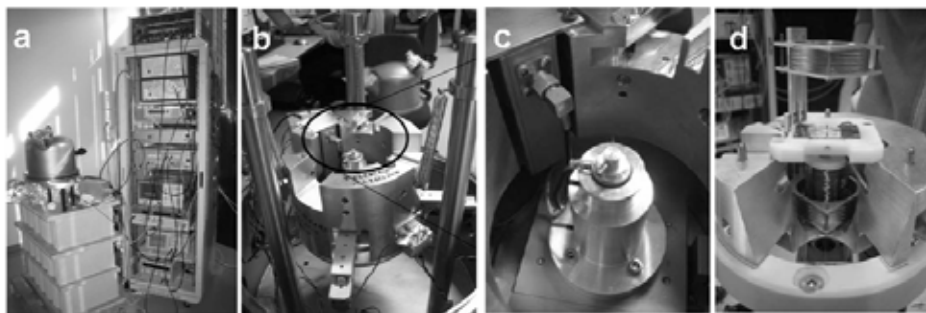


Figure. 8.2. ESN-STM apparatus. (a) Complete setup. (b) STM head and zoom of the tip (c) with damping system and first stage of amplification. (d) Sample holder with permanent magnets and coils for the application of the magnetic field. Images courtesy of Veronica Mugnaini and Mauro Fabrizioli.

Essentially our ESN-STM set-up is a room temperature STM with standard electronics. It differs from standard STMs for the higher shielding of external noise, for the possibility of applying an external (DC and AC) magnetic field and for the pres-

ence of an RF detection system. The tunnelling current coming out from the usual tunnelling junction formed between the sample and the metallic tip of the microscope is divided into two channels. The first acquires the DC component with a conventional current-voltage converter for the STM imaging through the distance control feedback circuit, while the second one collects the AC component to be analysed by a RF amplifier. In order to enhance the sensitivity to weak signals this amplifier is inserted inside the STM head.

We have used a general protocol presented earlier to detect the low level RF signal from the STM tip (Manassen Y. 1997, Manassen Y. et al. 2000). The scheme of this apparatus is illustrated in Figure 8.3.

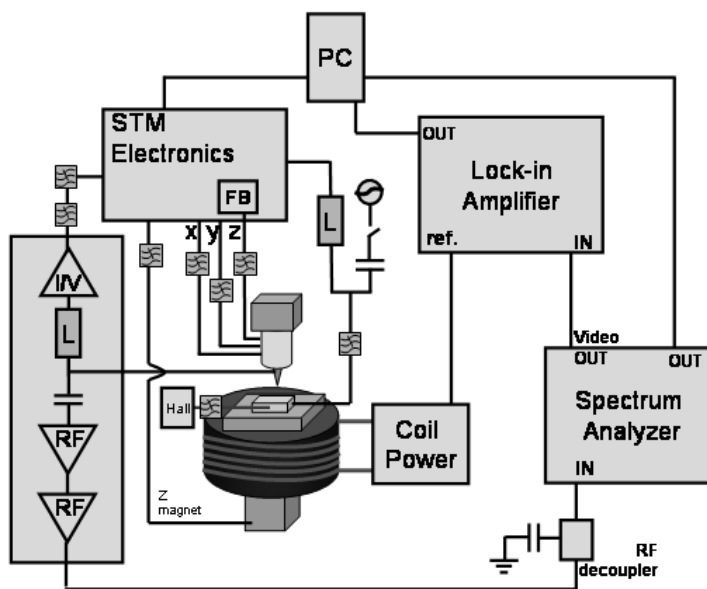


Figure. 8.3. Detection scheme for ESN-STM. The signal (which occurs as a result of a magnetic field) is recovered from the STM tunnelling current and is split into the DC and AC part. The AC part is then amplified and detected by a spectrum analyzer and evidenced through a PSD by the Lock-in Amplifier (if the magnetic field is modulated). Reprinted from Mannini M. et al. 2007a, Copyright 2007, with permission from Elsevier.

A small oscillating magnetic field is added to a static magnetic field so that, close to the sample, the magnetic field, modulated along the direction of the static field, is  $B = B_0 + \Delta B \cos(\omega_m t)$ . Here  $\omega_m$  is the modulation frequency and  $2\Delta B$  is the peak-to-peak intensity of the modulation. The signal is extracted from the tunnelling current as a peak occurring at the Larmor frequency  $\nu_L = \omega/2\pi = g\mu_B B/h$  (where  $\mu_B$  is the Bohr magneton and  $h$  the Planck's constant) which is modulated at  $\omega_m$ . The frequency at which the signal is observed depends on the  $g$  factor of the spin centre, on the hyperfine coupling, on the applied field  $B$  and on other parameters. It can be expressed as:

$$\Omega(t) = \omega_0(t, T_1) + \Delta\omega \cos(\omega_m t + \phi(t, T_2)) \quad (\text{Eq. 8.1})$$

where  $\omega_0$  is the unmodulated frequency,  $\omega_m$  is the modulation frequency of the oscillating field,  $\phi$  is the phase and  $\Delta\omega = g\mu_B\Delta B/\hbar$  is the frequency modulation intensity, with both  $\omega_0$  and  $\phi$  unknown functions of the time. The former depends on the hyperfine interaction, the  $g$ -anisotropy and the longitudinal relaxation time  $T_1$ , while the latter is determined by the transverse relaxation time  $T_2$  (Manassen Y. 1997, Manassen Y. et al. 2000).

The Fourier transform of such a signal, obtained by a spectrum analyser through a super-heterodyne detector, will give a typical sideband spectrum structure constituted by a set of equally spaced sidebands with frequencies  $(\omega_0 \pm n \omega_m)$  and with intensities of  $J_n(m_\omega)$  where  $J_n$  is the  $n^{\text{th}}$ -order Bessel function of the first kind and  $m_\omega = \Delta\omega/\omega_m$  is the modulation index corresponding roughly to the maximum value of  $n$ , so that the total width of the spectrum equals to  $2\Delta\omega$ .

Due to the small size of the expected signal blurred into background noise, a better sensitivity in its detection is obtained by setting the modulation index equal to 2, so to maximize the  $J_1$  component of the Fourier spectrum, and making use of a lock-in amplifier referenced to  $\omega_m$  to exploit PSD: all the signal goes into the first harmonic component, which is the only ones detected by the lock in amplifier.

The complete mechanism of ESN-STM is unclear yet. The three most plausible explanations of this phenomenon are the following:

1) *Rotating magnetic fields:*

If we do some calculations on electron tunnelling environment, we can estimate that the precessing spin generates a field of ca 1T at a distance of 0.3 nm. This means that the Lorentz force applied on a tunneling electron through a paramagnetic molecule is not negligible compared to the electric field and then can induce some effect in the tunneling.

2) *Temporary polarization of the tunneling electrons:*

If the tunneling current is paramagnetic (supposing a long time correlation) exchange interaction with the precessing spin should occur leading to a signal.

3) *Spin flip processes:*

If we assume an Anderson model, namely that we have a double barrier and a Zeeman level in between, it is possible to show that electrons tunneling into the barrier, which involves spin flips (namely excitation terms) are involving off diagonal elements in the time evolution of the tunneling current and therefore causes a peak (or a dip) in the Larmor frequency.

More experimental work is necessary to prove (or disprove) these suggestions. At the moment it has been noted that the frequency of the signal depends on the magnetic field while the intensity of the signal increases linearly with the tunneling current and is supposed to increase as the temperature is decreased. Then, if we consider the third proposed model, it follows that a single spin needs energy in order to flip in respect to the direction of the static magnetic field. This energy is obtained from tunneling process that transmits thermal noise. Examining AC white noise in the tunneling current we detect coloured noise due to interactions between coherently precessing tunneling electrons and the electron in the paramagnetic molecule. Concluding, when we do a noise spectroscopy with this modified STM apparatus, we explore the noise searching for the absorbed/emitted frequencies corresponding to the required energy to do this kind of process.

## 2.2 Testing of the ESN-STM with standards

ESN-STM signal can be detected not only in dangling bonds at silicon surfaces as originally demonstrated (Manassen Y. et al. 1989) but also looking at organic radicals deposited on surfaces as reported recently by Durkan and co-workers (Durkan C. and Welland M. E. 2002). In their work Durkan *et al.* drop cast samples of a stable radical, the BDPA ( $\alpha,\gamma$ -Bisdiphenylene- $\beta$ -phenylallyl) molecule have been investigated. No control of the deposition procedure has been used by the authors that nevertheless showed very nice spectra corresponding to clusters of molecules deposited on HOPG surfaces.

In order to test the functioning of our instrumentation we decided to start by investigating the same molecule but improving the control of deposition achieving monolayer and single molecule depositions. This has been achieved by selecting an appropriate surface that is incubated in very diluted solutions as well as by exploiting cleaning of the deposited surface by pure solvent after the incubation.

In addition to BDPA molecules also the DPPH (2,2'-diphenyl-1-picrylhydrazyl radical) molecule deposited in a similar way is used for these first tests of our ESN-STM apparatus. In both cases, gold slides have been pre-characterized by acquiring ESR spectra from ultrathin films of DPPH and BDPA grown on Au(111). In this way we proved that the paramagnetic molecules preserve their magnetism on the surface. Later, STM local investigation have confirmed from a topographical viewpoint the source of this magnetism. More in details, continuous wave ESR (CW-ESR) measurements on ultrathin films of BDPA and DPPH radicals, that we employed in similar condition optimized for Nitronyl Nitroxide Radical monolayers (Chapter 7), have been used here as a preliminary characterization tool to get information about the amount of deposited radicals, the level of aggregation of the samples and the effect of deposition procedure on the magnetic properties of the deposited material. A single ESR signal is observed at  $g=2.005(5)$  for BDPA and at  $g=2.003(6)$  for DPPH, with no evidences for hyperfine structure (see Figure 8.4).

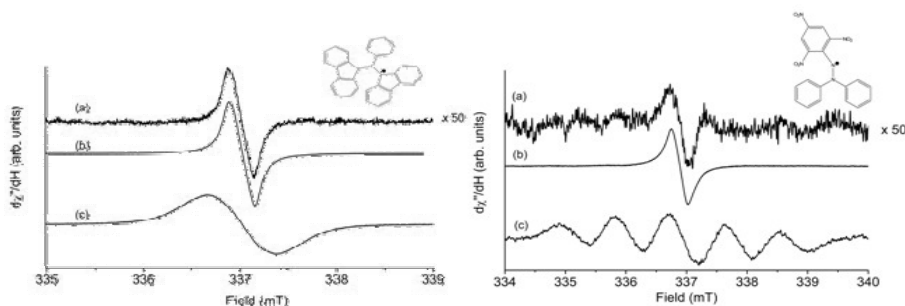


Figure 8.4. Left: Room temperature CW-ESR spectra of BDPA (molecule sketched in the upper right inset) as ultrathin film sample (a), drop cast sample from a solution  $100\mu\text{M}$  (b), and dichloromethane  $100\mu\text{M}$  solution (c). Right: Room temperature CW-ESR spectra of DPPH (molecule sketched in the upper right inset) as ultrathin film sample (a), drop cast sample from a solution  $100\mu\text{M}$  (b), and dichloromethane  $10\mu\text{M}$  solution (c). For both molecules the intensity of ESR spectrum of ultrathin film is multiplied by a factor 50 to be compared with that of drop cast sample, acquired in the same conditions. Reprinted from Messina P. et al. 2007, Copyright 2007, with permission from the American Institute of Physics.

A single line is observed also for solution spectra of BDPA in  $\text{CH}_2\text{Cl}_2$  with 7 G linewidth, as reported in literature (Koksharov Y. A. et al. 2002). On the contrary, solution spectra of DPPH show a five lines pattern (Kikuchi C. and Cohen V. N. (954) due to the hyperfine coupling with two almost equivalent  $^{14}\text{N}$   $I=1$  nuclei (coupling with  $^1\text{H}$  being unresolved).

Accurate information about the degree of molecular aggregation could in principle be provided by comparison of the spectral lineshape and/or linewidth with those of solution and solid state spectra. Unfortunately, due to the low intensity of the signal we had to overmodulate (modulation amplitude of 3 G) the spectra to obtain a reasonable signal to noise ratio. This, coupled with the relatively large baseline correction, induces a sizeable lineshape distortion and makes impossible a detailed analysis. It is however interesting to note that for both radicals the observed peak to peak linewidths, even if overmodulated, are smaller than those observed for dilute solutions with low modulation (0.3 G), but broader than the corresponding solid state spectra. If one also considers the absence of hyperfine structure, it can be concluded that the spectra are dominated by contribution of small molecular aggregates for which exchange narrowing processes are active (Abragam A. and Bleaney B. 1986; Goldsborough J. P. et al. 1960; Lloyd J. P. and Pake G. E. 1953).

On this respect, a comparison of the doubly integrated signal with standards containing known amount of spins, suggests that within the inherent limitations of quantitative ESR spectroscopy (Weil J. A. et al. 1994) the number of spins on each gold slide is of the order of  $10^{12}$ . If one considers an optimal packing (i.e. a surface occupation for each molecule of BDPA and DPPH of 130 and 140  $\text{\AA}^2$  respectively) this yields for both molecules a surface coverage of about  $15 \pm 3\%$ . The relatively low coverage suggests that the presence of a sizeable amount of isolated molecules, which by STM images have been shown to coexist on surfaces with molecular aggregates, can be considered as probable. We stress here that the spectrum of ultrathin films is far less intense than that obtained by drop casting method (see Fig. 8.4), with an approximate ratio of 1:50. This implies that for the latter method, used e. g. by Durkan for preparing ESN-STM samples (Durkan C. and Welland M. E. 2002), the formation of multilayer and aggregates is much more probable.

A final observation concerns the effect of incubation time over the number of spins, as determined via ESR, deposited on gold. For DPPH it is clearly seen that this number increase with increasing time deposition (30 min - 4 h). It is probable that this will result in an easier formation of aggregates for longer time of exposure. This is an important point to be considered, as samples for ESN-STM have been incubated for a much shorter time than those for CW-ESR; it is then conceivable to assume that the number of molecular aggregates will be reduced in those samples.

Concluding this pre-characterization, CW-ESR spectra were used to prove that the paramagnetic character of a large number of BDPA and DPPH molecules is retained after deposition on gold. Further they suggest that the obtained coverage is limited to about 15%. As a consequence, the presence of large aggregates is less probable in samples prepared with the deposition method here described than in those obtained by drop casting (Durkan C. and Welland M. E. 2002), thus making the former better candidates for observation of ESN-STM on single molecules.

The samples characterized with ESR spectroscopy was considered as ready to be investigated with our ESN-STM setup but, in order to rule out the presence of spurious noise signals in the ESN-STM experiment, the first necessary test implied the collection of a series of spectra without approaching the STM tip to the surface. Later the RF detection was checked by introducing an external RF signal of intensity comparable to the expected one. This step permitted to build up a statistical criterion to discriminate signal to noise that is fundamental due to the very small intensity of the detecting signals.

After having successfully accomplished these tests, real measurements were performed in tunnelling conditions.

Obviously the first step consisted of a standard STM characterization of the sample aimed at finding the best imaging conditions and checking the quality of the molecular film.

Figures 8.5a and 8.5b show typical images observed for DPPH and BDPA molecules deposited on Au(111) surfaces. As the geometrical size of the smallest white spots corresponds to DPPH and BDPA molecular size within experimental error, we attribute them to DPPH and BDPA single molecules. Larger white spots indicate the formation of agglomerates of two or few molecules. ESN-STM signal reported herein were always obtained from spots that correspond in our analysis to single molecules.

Molecules deposited by spontaneous adsorption from diluted solutions did not form agglomerates with a large vertical size as found in samples prepared by drop casting (Durkan C. and Welland M. E. 2002). STM imaging was achieved only for tunnel currents below 30 pA. The obtained STM images for BDPA molecules are distorted and we attribute this effect to an internal reorientation of the molecule caused by the tunnelling currents as well as to molecular diffusion processes on Au(111).

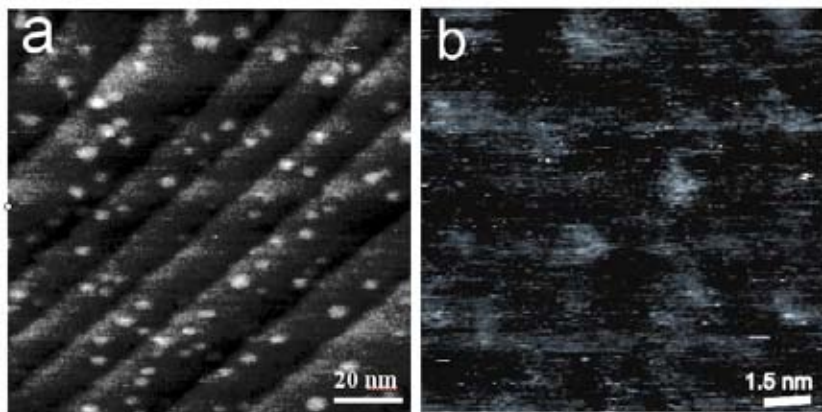


Figure 8.5. (a) STM image ( $100 \times 100 \text{ nm}^2$ ) of DPPH molecules deposited on Au(111). Tunneling current  $I_t = 10 \text{ pA}$ , Bias Voltage  $BV = 0.1 \text{ V}$ . (b) STM image ( $15 \times 15 \text{ nm}^2$ ) of BDPA molecules deposited on Au(111).  $I_t = 50 \text{ pA}$ ,  $BV = 0.1 \text{ V}$ . Reprinted from Messina P. et al. 2007, Copyright 2007, with permission from the American Institute of Physics.

After the spatial localization of a single molecule we finally reproduced Durkan results on ESN-STM investigation on BDPA.

Spin noise measurements were performed on ultrathin films where we identified by STM imaging isolated molecules or at least small cluster of molecules. ESN-STM signals reported were obtained by collecting noise spectra during scanning. Only 0.5% of the sampling gave a real signal with respect to the noise, a behaviour which we attribute to the elusive characteristics of the signal (Messina P. et al. 2007). Indeed, to detect a signal it is necessary that it persists at a given frequency for the entire duration of the sweep of the spectrum analyzer; this condition might be difficult to achieve for molecules with largely spreading hyperfine sublevels. Notwithstanding these inherent limitations, signals coming from single molecule can be detected as shown below and in previous papers (Durkan C. and Welland M. E. 2002).

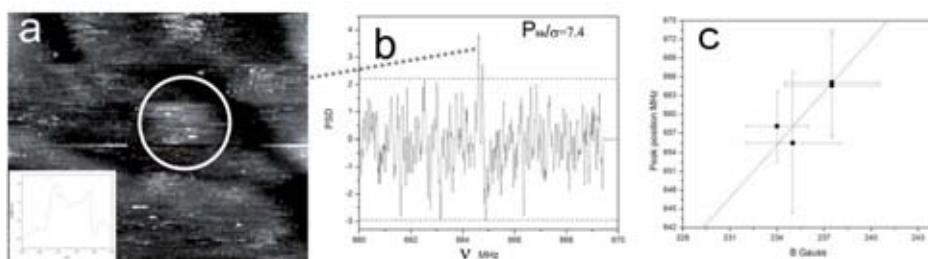


Figure 8.6. (a) STM image ( $7 \times 7 \text{ nm}^2$ ) of a BDPA molecule on which the ESN-STM spectrum reported in b) is measured. It= 30 pA, BV= 0.3 V during STM imaging. (b) ESN-STM spectrum showing a peak at 664.8 MHz (237.4 G). SPAN= 660-670 MHz, BW=VBW=30 KHz. SWT=6 sec. Tunneling current during spectroscopy 0.3 nA. Bias voltage during spectroscopy 0.3 V. AC field modulation 15 KHz, 10 mG. Lock in sensitivity 200  $\mu\text{V}$ , time constant 10 ms. (c) ESN-STM peaks were detected at the expected frequency. The horizontal error bar represents the magnetic field range measured over the sample surface. The vertical error bar indicates the frequency range in which the ESN-STM signal was searched. The frequency range was divided in two or three sub-range that were investigated separately. Reprinted from Messina P. et al. 2007, Copyright 2007, with permission from the American Institute of Physics.

Figure 8.6b reports the ESN-STM spectrum detected on the BDPA molecule highlighted in Figure 8.6a. The tunnelling current during ESN-STM spectroscopy is always confined in the range 0.3 to 0.6 nA, less than half the value reported in Durkan's experiments (Durkan C. and Welland M. E. 2002). This spectrum was measured with a lock-in amplifier sensitivity of 200 $\mu\text{V}$  and the frequency of the peaks measured is consistent with the measured magnetic field as illustrated in Figure 8.6c. The uncertainty of this measurements comes from the fact that the sample position on the plane is varied, while the magnet  $z$  position is always constant (effect of  $B$  inhomogeneity in the sample).

As anticipated earlier a similar investigation has been obtained on a new organic radical, quite similar to the BDPA in order to advance the know-how in this technique that, up to now, has been employed to characterize only a few of molecules.

The ESN-STM investigation on DPPH molecules evidenced, also in this case, a peak whose frequency varied with the applied magnetic field. The signal presented in Figure 8.7b has been observed when the STM tip has been localized on the molecule of Figure 8.7a indicated by the arrow, at a frequency of 254 MHz which for  $g=2.0$  corresponds, within the error bar, to the measured applied DC magnetic field of  $91 \pm 1.5$  G, while in Figure 8.7d a peak at higher field is reported. The tunnel current during spectroscopies was raised to 1 nA and a bias voltage of 50 mV while scanning was achieved at 30 pA. When a peak appeared in the spectrum the position of the tip was always localized on a single molecule.

We note that in both cases peaks do not show the expected derivative lineshape; we suppose that this signal distortion might be induced by a value of the modulation amplitude higher than the optimal one (Manassen Y. 1997). To clarify this point further experiments are planned in the next future.

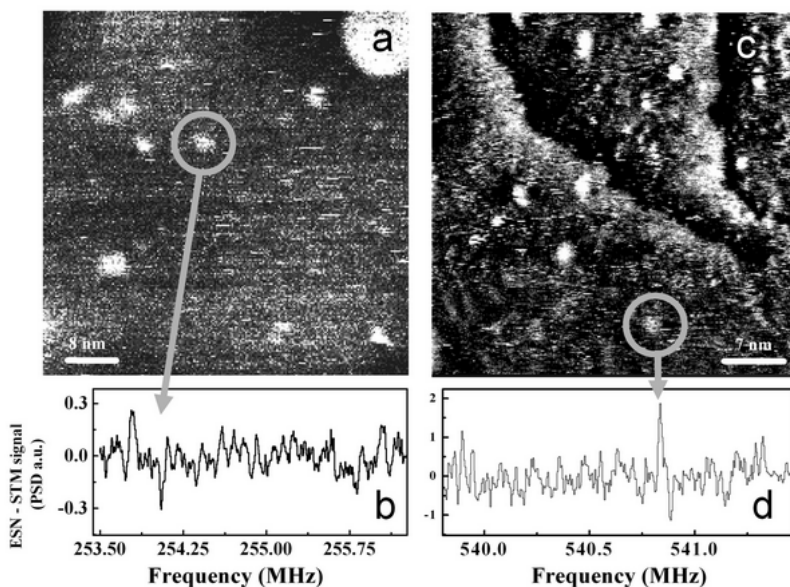


Figure 8.7. (a) STM image of DPPH molecules and aggregates during ESN-STM measurement. (b) ESN-STM spectrum of a DPPH molecule deposited on Au(111), indicated by the arrow in (a). (c) STM image of DPPH molecules on Au(111) observed in a different region of the sample and (d) ESN-STM spectrum of a single DPPH molecule, evidenced by the arrow in (c), with increased S/N ratio. The ESN-STM spectra were acquired with AC modulation frequency and intensity of 16 KHz and 13 mG respectively. Reprinted from Mannini M. et al. 2007a, Copyright 2007, with permission from Elsevier.

In order to confirm the physical origin of these signals, we performed spin noise measurements at further different DC magnetic field values and in this way the theoretical linear dependence of the Larmor frequency with the magnetic field has been verified as shown in Figure 8.8.

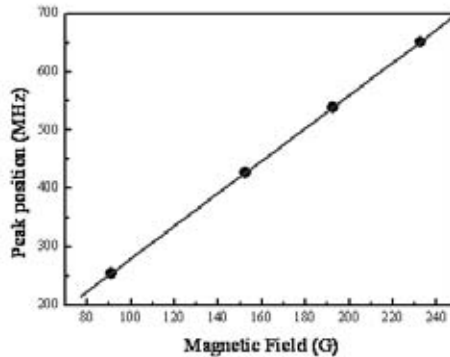


Figure 8.8. Position of ESN-STM peak measured at different values of applied magnetic field. The slope of the best fit line is  $g\mu_B/h$ ; the obtained value for  $g$  is equal, within experimental error, to 2.0. Reprinted from Mannini M. et al. 2007a, Copyright 2007, with permission from Elsevier.

It has to be noted that we explored only the central region of the expected five lines hyperfine structure of DPPH due to present limitations of our instrumental setup. Further investigation and upgrading of the experimental setup are currently in progress.

Our main effort is directed to improve the sensitivity by matching and tuning procedures and, in parallel, by improving the characteristics of investigated samples.

The first procedure of optimization is related to the fact that the AC current we are looking for in this frequency is like a wave and if the impedance of the source differs from the impedance of the detector ( $50 \Omega$ ) the signal is reflected to the source (and it can be reflected again into the detector etc.). These reflections increase the noise and attenuate the signal. In order to prevent them and to improve the SNR it is important to match the impedance of the source to  $50 \Omega$ .

Another possible improvement is related to a tuning procedure. The idea behind tuning is to create a parallel resonance circuit, where the parasitic capacitance of the tip - sample junction and of the other contacts in the microscope is cancelled by a parallel inductor. In this way losses of signals into this capacitance will be avoided.

Further improvement can be also reached by the use of a real time analysis of radio frequencies by rebuilding up a new detection setup that in analogy to Fourier transformed spectroscopies will acquire signal coming from different frequencies at the same time.

Finally we have exploited the know-how acquired during this thesis work in the preparation of self assembled monolayer of Nitronyl Nitroxide radicals and their characterization with STM, ToF-SIMS and ESR on surface in order to build-up an effective protocol for achieving appropriate samples for the ESN-STM experiments. Indeed we feel that a deeper knowledge of the characteristics of the sample to be investigated by ESN-STM might increase the probability of a successful measurement. This work results in the successful spin noise experiments briefly described in next paragraph.

### 2.3 ESN-STM investigation of Nitronyl Nitroxide molecules.

In the Chapter 5 we have described our efforts in deposition of a class of sulphur modified Nitronyl Nitroxides. The result of these studies evidenced the best modification and some optimized condition to achieve ordered monolayer of these stable organic radicals on gold surfaces (Mannini M. et al. 2007b). ESR characterization of these surfaces described in Chapter 7 confirms that these molecules keep intact their paramagnetic behaviour. An important achievement of this thesis work has been the possibility to show, even if in a preliminary way, that is possible to use ESN-STM to locally characterize these surface thus starting the exploration of local magnetism.

Preliminary observations suggest that these samples give a signal above the noise level, with a seemingly increased reproducibility and detectability of the signal due to the increased quality of the samples. However, many more experiments are necessary in order to reach a definite conclusion. In figure 8.9b the first observation of a signal originated from a NitPhCH<sub>2</sub>SMe (NIT3) molecule is presented. Obviously, we selected this molecule due to the higher quality level obtained in the pre-characterization described in previous chapters.

We note here that the resolution quality of the topography presented in figure 8.9a, and obtained with our home-made ESN-STM is lower than the commercial standard STM used for STM analysis described in Chapter 6, and only reveals the presence of features typical of monolayers like pinholes (the darker spots in the figure 8.9a). This instrumental limitation can however be overcome through the above described physico-chemical characterization, which provides convincing evidences that ESN-STM measurements are performed on monolayers, and thus of the single molecular character of the reported spectra.

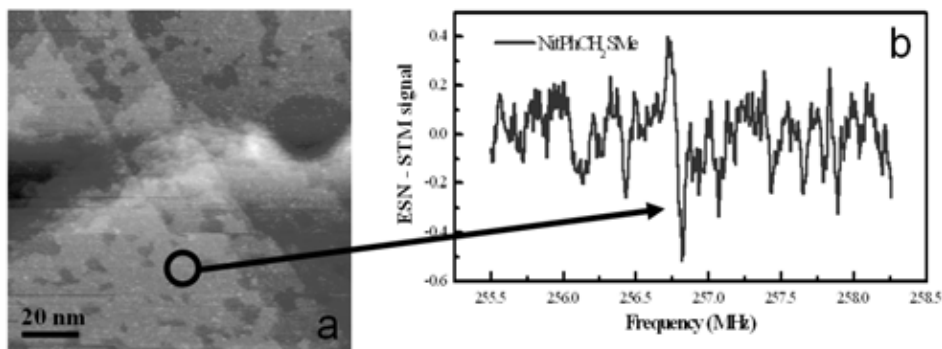


Figure 8.9. STM image (a) and ESN-STM spectrum (b) of the self-assembled monolayers of NIT3 radical presented in (a). The spectrum was taken in the zone marked with the circle. Experimental conditions during STM imaging:  $I_t = 30$  pA,  $BV = 0.1$  V (b) ESN-STM spectrum showing a peak at 257 MHz. The parameters during ESN-STM measurement were: tunnelling current: 1 nA, bias voltage 50 mV. AC field modulation frequency and intensity: 16 KHz, 13 mG. Reprinted from Mannini M. et al. 2007a, Copyright 2007, with permission from Elsevier.

The results of Figure 8.9, as anticipated, have to be reproduced and extended. In fact first of all we have to consider that the deposited radical presents a hyperfine coupling that should be visible also using this technique, as indeed showed by Durkan for the TEMPO (2,2,6,6-Tetramethylpiperidine 1-oxyl) molecule in a very discussed paper (Durkan C. 2004). The reproduction of this observation with a different molecule like a Nitronyl Nitroxyde will represent for this reason a real advance for the ESN-STM technique as well as for spintronic purposes (Balatsky A.V. et al. 2006).

## Chapter 9

### Conclusions

During this thesis we explored the feasibility of the deposition of magnetic molecules (including Single Molecule Magnets as well as purely organic radicals) by the use of Self-Assembling of Monolayer and Micro-Contact Printing techniques. Both these techniques allowed to control the deposition of single layer of molecules by exploiting chemical anchoring of them to the surface. This has been achieved by introducing in the external shell of these molecules some suitable linker groups for the selected surface to be functionalized, the gold surface.

Concerning the specific SMM we focused our work on the dodecamanganese cluster (Mn<sub>12</sub>), we introduced by a ligand exchange reaction some carboxylic acids initially functionalized with some acetyl protected thiols, then by sulphide groups. The use of sulphide groups was needed in order to improve the quality of the deposition and to avoid problems related to the deprotection phase. It allowed further to simplify the procedure of monolayer assembly in order to reduce uncontrollable phenomena like spurious contamination. Almost unexpectedly we observed that the sulphide functionalization permitted the isolation of single molecules on the surfaces, allowing their real identification by Scanning Probe Microscopy and suggesting the feasibility of a single molecule magnetic reading. We noticed also that in these conditions of deposition some ordering effects are present, providing a real improvement in the purpose of the preparation of ordered arrays of SMMs.

Exploiting micro-contact printing technique we obtained some structured deposition also in a larger scale. These patterned depositions allowed us to employ different surface sensitive technique providing incomparable information but lacking the spatial resolution needed to observe single molecules.

The biggest problem we have had to face in these three years of research has been to correlate nice imaging evidence with magnetic properties. Actually traditional magnetic techniques lack the necessary sensitivity to detect the signal coming from one layer of molecules and therefore we have spent a lot of energy to try to overcome this problem. Finally with XMCD experiments we have been able to collect first evidences of the magnetism of one layer of SMMs. These investigations, due to the incomparable sensitivity and specificity of the technique, have provided us an invaluable feedback for the sample preparation that allowed us to identify and to solve some bugs in our deposition procedure.

These results represent the achievement of some of the initial objectives of this thesis. Nevertheless, during these three years, the long term purposes of this research area has been slightly modified. Originally the general purpose was to provide some

prototype of SMM-based device for single molecule data-storage applications. However the limitation on the blocking temperatures remains a great drawback. Recently some theoretical works have suggested a new possibility: the use of SMMs and more in general magnetic molecules for Spintronics purposes. In fact in the last year quite a few theoretical articles and the first experimental results have been presented to the scientific community. These have shown the hidden potentiality of magnetic molecules for electron transport and in quantum computing applications.

For these Molelectronics purposes also simpler molecules, like organic radicals, have become attractive and this has amplified the interest in the second topic of this thesis, i.e. the deposition of the series of Nitronyl Nitroxides radicals.

In this last case, once the problems related to the compatibility of the paramagnetic unit and the linker group have been solved, it has been much easier to organize the entire process of deposition and characterization of these radicals. We investigated in parallel thin film deposits with STM, ToF-SIMS and ESR, obtaining evidence of the presence of these molecules as ordered monolayers maintaining their paramagnetic behaviour.

The use of the simpler molecules expanded the potentiality of scanning probe based techniques to detect magnetic properties of single molecules. In this sense our efforts in applying the ESN-STM technique to paramagnetic molecules has represented a real success for our strategy and the obtained results suggest the future direction for our studies in deposition of molecular magnetic materials on solid surfaces.

## Bibliographic references

- Abraham A. and Bleaney B. (1986) *Electron paramagnetic resonance of transition ions*. New York: Dover Publications.
- Allara D.L. and Nuzzo R. G. (1985) Spontaneously organized molecular assemblies. 1. Formation, dynamics, and physical properties of n-alkanoic acids adsorbed from solution on an oxidized aluminum surface. *Langmuir* 1, 45-51.
- An J. et al. (2000) Influence of the ligands and solvents on the magnetic properties of the single molecule magnets:  $[\text{Mn}_{12}\text{O}_{12}(\text{O}_2\text{CR})_{16}(\text{L})_4] \cdot n \text{ S}$  (R=3-Cl-C<sub>6</sub>H<sub>4</sub>, L=3-Cl-C<sub>6</sub>H<sub>4</sub>CO<sub>2</sub>H and water, n=1, S=3-Cl-C<sub>6</sub>H<sub>4</sub>CO<sub>2</sub>H (1); R=CH<sub>2</sub>Cl, L=water, n=0 (2)). *Inorg. Chim. Acta* 299, 28-34.
- Arduengo A. J. et al. (1990) Molecular control of self-assembled monolayer films of imidazole-2-thiones: Adsorption and reactivity. *J. Am. Chem. Soc.* 112, 6153-6154.
- Arndt Th. et al. (1989) Self-assembled and Langmuir-Blodgett films of thiocarbinates: A comparative study. *Thin Solid Films* 178 319-326.
- Aromi G. et al. (1998) Manganese carboxylate clusters: from structural aesthetics to single-molecule magnets. *Polyhedron* 17, 3005-3020.
- Artus P. et al. (2001) Single-Molecule Magnets: Site-Specific Ligand Abstraction from  $[\text{Mn}_{12}\text{O}_{12}(\text{O}_2\text{CR})_{16}(\text{H}_2\text{O})_4]$  and the Preparation and Properties of  $[\text{Mn}_{12}\text{O}_{12}(\text{NO}_3)_4(\text{O}_2\text{CCH}_2\text{But})_{12}(\text{H}_2\text{O})_4]$ . *Inorg. Chem.* 40, 4199-4210.
- Aubin S. M. J. et al. (1999) Reduced Anionic Mn<sub>12</sub> Molecules with Half-Integer Ground States as Single-Molecule Magnets. *Inorg. Chem.* 38, 5329-5340.
- Aubin S. M. J. et al. (2001) Single-Molecule Magnets: Jahn-Teller Isomerism and the Origin of Two Magnetization Relaxation Processes in Mn<sub>12</sub> Complexes. *Inorg. Chem.* 40, 2127-2146.
- Aue W. A. and Hastings C. R. (1969) Preparation and chromatographic uses of surface-bonded silicones. *J. Chromatogr.* 42 319-335.
- Aviram A. and Ratner M. A. (1974) Molecular rectifiers. *Chem. Phys. Lett.* 29, 277-283.
- Bae S.-S. et al. (2004) Selectively Assembled Co Nanoparticle Stripes Prepared by Covalent Linkage and Microcontact Printing. *J. Phys. Chem. B* 108, 2575-2579.
- Bain C. D. et al. (1989) Formation of monolayers by the coadsorption of thiols on gold: variation in the head group, tail group, and solvent. *J. Am. Chem. Soc.* 111, 7155-7164.
- Balatsky A.V. et al. (2002) Exchange Based Noise Spectroscopy of a Single Precessing Spin with Scanning Tunneling Microscopy. *Phil. Mag. B* 82, 1291-1298.
- Balatsky A.V. et al. (2006) STM NMR and nuclear spin noise. *Phys. Rev. B* 73, 184429.
- Barone V. et al. (2006) Development and Validation of an Integrated Computational Approach for the Modeling of cw-ESR Spectra of Free Radicals in Solution: p-(Methylthio)phenyl Nitronyl Nitroxide in Toluene as a Case Study. *J. Am. Chem. Soc.* 128, 15865-15873.
- Barra, A.-L. et al. (1997) Electronic Structure of Manganese(III) Compounds from High Frequency EPR Spectra. *Angew. Chemie Int. Ed. Engl.* 36, 2329-2331.

- Barth J. V. et al. (1990) Scanning tunneling microscopy observations on the reconstructed Au(111) surface: Atomic structure, long-range superstructure, rotational domains, and surface defects *Phys. Rev. B* 42 9307-9318.
- Basetti B. et al. (1990) The Role of Conformational Defects in Solid- Solid Phase Transitions. *J. Phys. France* 51 (1990) 259-275.
- Beaurepaire E. (2006) *Magnetism: A Synchrotron Radiation Approach*. Berlin: Springer.
- Belu A. M. et al. (2003) ToF-SIMS: Techniques and Applications for the Characterization of Biomaterial Surfaces. *Biomaterials* 24 3635-3653.
- Benelli C., et al. (1989) One Dimensional Magnetism of a Linear Chain Compound Containing Yttrium(III) and a Nitronyl Nitroxide Radical. *Inorg. Chem.* 28, 3230-3234.
- Benninghoven A. (1973) Surface investigation of solids by the statical method of secondary ion mass spectroscopy (SIMS). *Surf. Sci.* 35, 427-457.
- Bertram H.N. and Williams M. (2000) SNR and density limit estimates: A comparison of longitudinal and perpendicular recording. *IEEE Trans. Mag.* 36 4-9.
- Bian G. Q. (2004) A Mn<sub>12</sub> Single-Molecule Magnet [Mn<sub>12</sub>O<sub>12</sub>(OAc)<sub>12</sub>(dpp)<sub>4</sub>] (dppH = Diphenyl Phosphate) with No Coordinating Water Molecules. *Inorg. Chem.* 43, 4790-4792.
- Bigelow W. C. (1946) Oleophobic monolayers. Films adsorbed from solution in non-polar liquids. *J. Colloid Sci.* 1 (1946) 513-538.
- Binnig G. and Rohrer H. (1982) Scanning tunneling microscopy. *Helvetica Phys. Acta* 55, 726-735.
- Binnig G. et al. (1982) Surface studies by scanning tunneling microscopy. *Phys. Rev. Lett.* 49, 57-61.
- Binnig G. and Rohrer H. (1986) Scanning tunneling microscopy. *IBM J. Res. Develop.* 30, 355-369.
- Binnig G. et al. (1986) Atomic Force Microscope. *Phys. Rev. Lett.* 56, 930-933.
- Bogani L. (2005) *Magnetic and Optical properties of Molecular Magnets*. PhD Thesis Università di Firenze.
- Bogani L. et al. (2007) Magneto-Optical Investigations of Nanostructured Materials Based on Single-Molecule Magnets Monitor Strong Environmental Effects. *Adv. Mater.* 19, 3906-3911.
- Boskovic C. et al. (2001) Single-Molecule Magnets: Ligand-Induced Core Distortion and Multiple Jahn-Teller Isomerism in [Mn<sub>12</sub>O<sub>12</sub>(O<sub>2</sub>CMe<sub>8</sub>(O<sub>2</sub>PPh<sub>2</sub>)<sub>8</sub>(H<sub>2</sub>O)<sub>4</sub>]. *J. Am. Chem. Soc.* 123, 9914-9915.
- Bourg M.-C. et al. (2000) Gold-Sulfur Bonding in 2D and 3D Self-Assembled Monolayers: XPS Characterization. *J. Phys. Chem. B* 104, 6562 - 6567.
- Boyd P. D. et al. (1988) Potential building blocks for molecular ferromagnets: [Mn<sub>12</sub>O<sub>12</sub>(O<sub>2</sub>CPh)<sub>16</sub>(H<sub>2</sub>O)<sub>4</sub>] with a S = 14 ground state. *J. Am. Chem. Soc.* 110 8537-8539.
- Brechin E. K. (2005) Using tripodal alcohols to build high-spin molecules and single-molecule magnets. *Chem. Commun.* 5141-5153.
- Brown H. C. et al. (1987) Selective reductions. 39. Partial reduction of carboxylic acids with tetrachloroborane-methyl sulfide. A direct and simple aldehyde synthesis. *J. Org. Chem.* 52, 5400-5406.
- Bryan S. R. et al. (2004) Evaluation of a gold LMIG for detecting small molecules in a polymer matrix by ToF-SIMS. *Appl. Surf. Sci.* 231-232, 201-206.
- Bryant M. A. et al. (1992) Raman scattering from monolayer films of thiophenol and 4-mercaptopyridine at platinum surfaces. *Langmuir* 9, 753-756.
- Bucher J. P. et al. (1994) Thermal Healing of Self-Assembled Organic Monolayers: Hexane- and Octadecanethiol on Au(111) and Ag(111). *Langmuir* 10, 979-983.
- Bush J. B. Jr. et al. (1968) Oxidation reactions of manganese(III) acetate. II. Formation of gamma-lactones from olefins and acetic acid. *J. Am. Chem. Soc.* 90, 5903-5905.

- Caneschi A. et al. (1991) Alternating Current Susceptibility, High Field Magnetization, and Millimeter Band EPR Evidence for a Ground  $S = 10$  State in  $[\text{Mn}_{12}\text{O}_{12}(\text{CH}_3\text{COO})_{16}(\text{H}_2\text{O})_4]_2 \cdot \text{CH}_3\text{COOH} \cdot 4\text{H}_2\text{O}$ . *J. Am. Chem. Soc.* 113, 5873-5874.
- Caneschi A. et al. (1995) Ferromagnetic intermolecular coupling in the nitronyl nitroxide radical 2-(4-thiomethylphenyl)-4,4,5,5-tetramethylimidazoline-1-oxyl-3-oxide, NIT(Sme)Ph. *Inorg. Chim. Acta* 235, 159-164.
- Caneschi A. et al. (2001) Cobalt(II)-Nitronyl Nitroxide Chains as Molecular Magnetic Nanowires. *Angew. Chem. Int. Ed. Engl.* 40, 1760-1763.
- Caneschi A. et al. (1989) Toward molecular magnets: the metal-radical approach. *Acc. Chem. Res.* 22, 392-398.
- Cavallini M. et al. (2003) Multiple Length Scale Patterning of Single-Molecule Magnets. *Nano Lett.* 3, 1527-1530.
- Cha J. S. et al. (1987a) Direct conversion of saturated and unsaturated carboxylic acids into aldehydes by the xlylbromoborane-dimethyl sulphide. *Tetr. Lett.* 28, 2389-2392.
- Cha J. S. et al. (1987b) Facile reduction of saturated and unsaturated carboxylic acids and their salts to aldehydes by the xlylbromoborane-dimethyl sulphide. *J. Org. Chem.* 52, 5030-5032.
- Chakov N. E. et al. (2003) Single-molecule magnets. A  $\text{Mn}_{12}$  complex with mixed carboxylate-sulfonate ligation:  $[\text{Mn}_{12}\text{O}_{12}(\text{O}_2\text{CMe})_8(\text{O}_3\text{SPh})_8(\text{H}_2\text{O})_4]$ . *Dalton Trans.* 2243-2248.
- Cheesman M. R. et al. (1997) Magnetically induced optical bi-stability of the molecular nanomagnet  $\text{Mn}_{12}\text{O}_{12}(\text{OOCMe})_{16}(\text{H}_2\text{O})_4$  in an organic glass. *Chem. Commun.* 1677-1678.
- Chen C.J. (1993) *Introduction to Scanning Tunneling Microscopy*. New York: Oxford University Press.
- Chiarelli R. et al. (1993) A ferromagnetic transition at 1.48 K in an organic nitroxide. *Nature* 363, 147-149.
- Ciszek J. W. et al. (2004) Spontaneous Assembly of Organic Thiocyanates on Gold Surfaces. Alternative Precursors for Gold Thiolate Assemblies. *J. Am. Chem. Soc.* 126, 13172-13173.
- Clemente-León M. et al. (1998) Langmuir-Blodgett films of single-molecule nanomagnets. *Angew. Chem. Int. Ed. Engl.* 37, 2842-2845.
- Clemente-León M. et al. (2003) Organized assemblies of magnetic clusters. *C.R. Chimie* 6, 683-688.
- Clemente-Leon M. et al. (2003) Incorporation of  $\text{Mn}_{12}$  single molecule magnets into mesoporous silica. *J Mater Chem.* 13, 3089-3095.
- Cleuziou J.-P. et al. (2006) Carbon nanotube superconducting quantum interference device. *Nature Nanotech.* 1, 53-59.
- Colchero J. et al. (1992) Scanning Force and Friction Microscopy. *Phys. Stat. Sol.* 131, 73-75.
- Condorelli G. G. et al. (2004) Anchoring molecular magnets on the Si(100) surface", *Ang. Chem.-Int. Ed. Angew. Chem, Int. Ed. Engl.* 43, 4081-4084.
- Condorelli G. G. et al. (2008) Site-Specific Anchoring of Tetrairon(III) Single Molecule Magnets on Functionalized Si(100) Surfaces. *Chem. Mater.* 20, 2405-2411.
- Cornia A. et al. (2002a) Disorder Effects in  $\text{Mn}_{12}$  acetate at 83 K. *Acta Crystallogr. C-Cryst. Str.* 58, M371-M373.
- Cornia A. et al. (2002b) Origin of second order transverse magnetic anisotropy in  $\text{Mn}_{12}$  acetate. *Phys. Rev. Lett.* 89, 257201.
- Cornia A. et al. (2003) Direct Observation of Single-Molecule Magnets Organized on Gold Surfaces. *Angew. Chem. Int. Ed. Engl.* 42, 1645-1648.
- Cornia A. et al. (2006) Preparation of Novel Materials Using SMMs. *Structure & Bonding.* 122, 133-161.

- Coronado E. et al. (2001) Toward Multifunctional Single-Molecule Magnets: Characterization of Dodecanuclear Manganese Complexes by Electrospray Ionization Mass Spectrometry. *Inorg. Chem.* 40, 6084-6085.
- Craig J. C. and Hamon D. P.G. (1965) Studies Directed toward the Synthesis of Plasmalogens. II. ( $\pm$ )-cis- and -trans-3-(n-Hexadec-1'-enyloxy)-1,2-propanediol. *J. Org Chem.* 30, 4168-4175.
- Davies N. et al. (2003) Development and experimental application of a gold liquid metal ion source. *Appl. Surf. Sci.* 203-204, 223.
- Del Pennino U. et al. (2006) Valence band resonant photoemission of Mn<sub>12</sub> single molecules grafted on Au(1 1 1) surface. *Surf Sci.* 18, 4185-4189.
- Dicke C. et al. (2002) Surface Inorganic Chemistry: The Reaction of Hydroxyl-Terminated Thiols on Gold with a Zirconium Coordination Compound. *Langmuir* 18, 336-344.
- Dishner M. H. et al. (1998) Preparation of gold thin films by epitaxial growth on mica and the effect of flame annealing. *J. Vac. Sci. Technol. A* 16, 3295-3300.
- Domingo N. et al. (2004) Magnetism of isolated Mn<sub>12</sub> single-molecule magnets detected by magnetic circular dichroism: Observation of spin tunneling with a magneto-optical technique. *Phys. Rev. B* 69, 052405-524054.
- Durkan C. and Welland M. E. (2002) Electronic spin detection in molecules using scanning-tunneling- microscopy-assisted electron-spin resonance. *Appl. Phys. Lett.* 80, 458-460.
- Durkan C. (2004) Detection of single electronic spins by scanning tunnelling microscopy. *Contemp. Phys.* 45, 1-10.
- Edinger K. et al. (1997) Corrosion of gold by alkane thiols. *Phys. Chem.* 101, 1811-1815
- Edwards T. R. G. et al. (1989) Construction of a stable flavin-gold electrode displaying very fast electron transfer kinetics. *J. Chem. Soc. Chem. Commun.* 15, 1041-1043.
- Einstein A. (1905) Über einen die Erzeugung und Verwandlung des Lichtes betreffenden heuristischen Gesichtspunkt. *Ann. Phys.* 17, 132-148.
- Elzerman J. M. et al. (2004) Single-shot read-out of an individual electron spin in a quantum dot. *Nature* 430, 431-435.
- Eppley H. J. et al. (1995) High-spin molecules: Unusual magnetic susceptibility relaxation effects in [Mn<sub>12</sub>O<sub>12</sub>(O<sub>2</sub>CET)<sub>16</sub>(H<sub>2</sub>O)<sub>3</sub>] (S = 9) and the one-electron reduction product (PPh<sub>4</sub>)[Mn<sub>12</sub>O<sub>12</sub>(O<sub>2</sub>CET)<sub>16</sub>(H<sub>2</sub>O)<sub>4</sub>] (S = 19/2). *J. Am. Chem. Soc.* 117, 301-317.
- Eppley H. J. et al. (1997) Single-molecule magnets: Characterization of complexes exhibiting out-of-phase AC susceptibility signals. *Mol. Cryst. Liq. Cryst.* 305, 167-179.
- Erskine J. L. and Stern E. A. (1975) Calculation of the M<sub>2,3</sub> magneto-optical absorption spectrum of ferromagnetic nickel. *Phys. Rev. B* 12, 5016-5024.
- Faraday M. (1846) Experimental Researches in Electricity. *Philosoph. Trans. Royal Soc. London* 136, 1-20.
- Feynman R. P. (1959) There's Plenty of Room at the Bottom. *Annual meeting of the American Physical Society at the California Institute of Technology*, December 29th.
- Fléury B. et al. (2005) A new approach to grafting a monolayer of oriented Mn<sub>12</sub> nanomagnets on silicon. *Chem. Commun.* 15, 2020-2022.
- Friedman J. R. et al. (1996) Macroscopic measurement of resonant magnetization tunneling in high-spin molecules. *Phys. Rev. Lett.* 76, 3830-3833.
- Friggeri A. et al. (2000) Insertion of Individual Dendrimer Molecules into Self-Assembled Monolayers on Gold: A Mechanistic Study. *Langmuir* 16, 7757-7763.
- Gallani J. L. et al. (2001) Induced Ferromagnetic Interactions in Langmuir-Blodgett Films of an Organic Radical. *Langmuir* 17, 1104-1109.

- Gambardella P. et al. (2002) Ferromagnetism in one-dimensional monatomic metal chains. *Nature* 416, 301-304.
- Garcia R. and Perez R. (2002) Dynamic atomic force microscopy methods. *Surf. Sci. Rep.* 47, 197-301.
- Gatteschi D. and Sessoli R. (2003) Quantum Tunneling of Magnetization and Related Phenomena in Molecular Materials. *Angew. Chem. Int. Ed.* 42, 268-297.
- Gatteschi D. et al. (2006) *J. Molecular Nanomagnets*. Oxford: Oxford University Press.
- Gerbier P. et al. (2003) Synthesis and Characterization of a  $[\text{Mn}_{12}\text{O}_{12}(\text{O}_2\text{CR})_{16}(\text{H}_2\text{O})_4]$  Complex Bearing Paramagnetic Carboxylate Ligands. Use of a Modified Acid Replacement Synthetic Approach. *Monatsh. Chem.* 134, 265-276.
- Ghigna P. et al. (2001) X-ray magnetic-circular-dichroism spectra on the superparamagnetic transition-metal ion clusters  $\text{Mn}_{12}$  and  $\text{Fe}_8$ . *Phys. Rev. B* 64, 132413.
- Giessibl F. J. (2003) Advances in atomic force microscopy. *Rev. Mod. Phys.* 75, 949-983.
- Gimzewski J. K. et al. (1987) Scanning Tunneling Microscopy of Individual Molecules of Copper Phthalocyanine Adsorbed on Polycrystalline Silver Surfaces. *Surf. Sci.* 81 267-277.
- Goldsborough J. P. et al. (1960) Influence of Exchange Interaction on Paramagnetic Relaxation Times Phys. Rev. Lett. 4, 13-15.
- Gómez-Romero P. and Sanchez C. (2004) *Functional Hybrid Materials*. Weinheim: Wiley.
- Gomez-Segura J. et al. (2005) Trihaloacetic acids: an investigation of steric and inductive ligand effects on the synthesis of  $[\text{Mn}_{12}\text{O}_{12}(\text{O}_2\text{CCX}_3)_{16}(\text{H}_2\text{O})_4]$  single-molecule magnets. *New. J. Chem.* 29, 499-503.
- Gorini L. et al. (2006) TPAP/NMO System as a Novel Method for the Synthesis of Nitronyl Nitroxide Radicals. *Synlett.* 6, 948-950.
- Gorini L. (2008) *Produzione e studio di monostrati di paramagneti e magneti a singola molecola*. PhD thesis, Università di Firenze
- Gorini L. et al.(2008) Addressing Single Molecules of a Thin Magnetic Film. *Inorg. Chim. Acta* 361, 4089-4093
- Gottlieb A. D. and Wesoloski L. (2006) Bardeen's tunnelling theory as applied to scanning tunnelling microscopy: a technical guide to the traditional interpretation. *Nanotechnology*, 17, R57-R65.
- Graham D. J. and Ratner B.D. (2002) Multivariate Analysis of TOF-SIMS Spectra from Dodecanethiol SAM Assembly on Gold: Spectral Interpretation and TOF-SIMS Fragmentation Processes. *Langmuir* 18, 5861-5868.
- Graham D. J. et al. (2002) Solution Assembled and Microcontact Printed Monolayers of Dodecanethiol on Gold: A Multivariate Exploration of Chemistry and Contamination. *Langmuir* 18, 1518-1527.
- Grant J. T. and Briggs D. (2003) *Surface Analysis by Auger and X-ray Photoelectron Spectroscopy*. West Chester (UK): IM Publications.
- Grobis M. et al. (2002) Local electronic properties of a molecular monolayer: C60 on Ag(001). *Phys. Rev. B* 66, 161408.
- Guisseppi-Elise A. (2000) *Cleaning and Surface Activation of Microfabricated Interdigitated Microsensor Electrodes (IMEs), Planar Metal Electrodes (PMEs), Independently Addressable Microband Electrodes (IAMEs), and E'Chem "Cell-On-A-Chip"*. *Abtech Application Note* (from <http://www.abtechsci.com>) Abtech Scientific, inc. Last check 03/10/2008.
- Hara M. et al. (1996) Ordered nucleation of a self-assembled monolayer on Au(111) studied by scanning tunneling microscopy. *Thin Solid Films* 273, 66-69.
- Harada G. et al. (2002) Preparation and Characterization of Gold Nano-Particles Chemisorbed by  $\pi$ -Radical Thiols. *Chem. Lett.* 1030-1031.

- Heersche H. B. et al. (2006) Electron Transport through Single Mn<sub>12</sub> Molecular Magnets. *Phys. Rev. Lett.* 96, 206801.
- Heinrich A. J. et al. (2004) Single-Atom Spin-Flip Spectroscopy. *Science* 306, 466-469.
- Hembacher S. et al. (2003) Revealing the hidden atom in graphite by low-temperature atomic force microscopy. *PNAS* 100, 12539-12542.
- Hidber P. C. et al. (1996) Microcontact Printing of Palladium Colloids: Micron-Scale Patterning by Electroless Deposition of Copper. *Langmuir* 12, 1375-1380.
- Hill W. and Wehling B (1993) Potential- and pH-Dependent Surface-Enhanced Raman Scattering of pMercaptoaniline on Silver and Gold Substrates. *J. Phys. Chem.* 97, 9451-9455.
- Howland R. and Benatar L. (2000) *A practical guide to scanning probe microscopy*. ThermoMicroscopes Ed.
- Huang S. et al. (2004) Growth of aligned SWNT arrays from water-soluble molecular clusters for nanotube device fabrication. *J. Phys. Chem. Chem. Phys.* 6, 1077-1079.
- Jin Q. et al. (1999) Self-assembly of aromatic thiols on Au(111). *Surf Sci.* 425, 101-111.
- Jo M.-H. et al. (2006) Signatures of Molecular Magnetism in Single-Molecule Transport. Spectroscopy *Nano Lett.* 6, 2014-2020.
- Kang J. S. et al. (2002) Photoemission Spectroscopy of a Mn<sub>12</sub> Molecular Magnet. *J. Korean Phys. Soc.* 37, L402-L405.
- Kappler J. -P. and Bucher J.-P. (2006) *private communication*.
- Katz E. et al. (1992) Effects of monolayer packing on the electrochemical activity of chemisorbed thioderivatized N,N'-dialkyl-4,4'-bipyridinium. *J. Electroanal. Chem.* 336, 357-362.
- Kerr J. (1877) On rotation of the plane of polarization by reflection from the pole of a magnet. *Lond. Edinb. Dublin Philos. Mag.* 3, 321-343.
- Kikuchi C. and Cohen V. N. (1954) Paramagnetic Resonance Absorption of Carbazyl and Hydrazyl. *Phys. Rev.* 93, 394-399.
- Kim J. et al. (2003) Tip-height-controlled removal of alkanethiol self-assembled monolayer on Au(111) surface. *Jpn. J. Appl. Phys.* 42, 4770-4772.
- Kim G.H. and Kim T.S. (2004) Electronic Transport in Single-Molecule Magnets on Metallic Surfaces. *Phys. Rev. Lett.* 92, 137203.
- Knapp H. F. and Guckenberger R. (1998) *Procedures in Scanning Probe Microscopies* pag. 67 ed. by Colton R. et al. Chichester (UK): John Wiley & Sons Ltd.
- Koksharov Y. A. et al. (2002) Radicals as EPR probes of magnetization of gadolinium stearate Langmuir-Blodgett film. *Mat. Sci. Eng. C* 22, 201-207.
- Koningsberger D. C. and Prins R. (1988) *X-ray absorption. Principles and applications: techniques of EXAFS, SEXAFS and XANES Chemical Analysis*, Wiley 92.
- Kumar A. and Whitesides G.M. (1993) Features of gold having micrometer to centimeter dimensions can be formed through a combination of stamping with an elastomeric stamp and an alkanethiol "ink" followed by chemical etching. *Appl. Phys. Lett.* 63, 2002-2004.
- Kuroda-Sowa T. et al. (2001) Effects of Paramagnetic Ferrocenium Cations on the Magnetic Properties of the Anionic Single-Molecule Magnet [Mn<sub>12</sub>O<sub>12</sub>(O<sub>2</sub>CC<sub>6</sub>F<sub>5</sub>)<sub>16</sub>(H<sub>2</sub>O)<sub>4</sub>]<sup>-</sup>. *Inorg. Chem.* 40, 6469-6480.
- Kuroda-Sowa T. et al. (2004) A novel Mn<sub>12</sub> single-molecule magnet with a μ<sub>3</sub>-methanesulfonate bridge. *Chem. Lett.* 33 540-541.
- Laibinis P.E. et al. (1991) Comparisons of Self-Assembled Monolayers on Silver and Gold: Mixed Monolayers Derived from HS(CH<sub>2</sub>)<sub>2</sub>1X and HS(CH<sub>2</sub>)<sub>10</sub>Y (X, Y = CH<sub>3</sub>, CH<sub>2</sub>OH) Have Similar Properties. *Langmuir* 7, 3167-3173.

- Larsen N. B. et al. (1997) Order in Microcontact Printed Self-Assembled Monolayers. *J. Am. Chem. Soc.* 119, 3017-3026.
- Lavrich D.J. et al. (1998) Physisorption and Chemisorption of Alkanethiols and Alkyl Sulfides on Au(111). *J. Phys. Chem. B* 102, 3456-3465.
- Leuenberger M. N. and Loss D. (2001) Quantum computing in molecular magnets. *Nature* 410, 789-793.
- Levi S. A. et al. (2001) Direct observation of surface-controlled self-assembly of coordination cages by using AFM as a molecular ruler. *Angew. Chem. Int. Ed.* 40, 1892-1896.
- Li T. T.-T. et al. (1984) Intramolecular Electron Transfer at Metal Surfaces. 3. Influence of Bond Conjugation on Reduction Kinetics of Cobalt(111) Anchored to Electrodes via Thiophenecarboxylate Ligands. *J. Am. Chem. Soc.* 106, 1233-1239.
- Li Y. et al. (1992) Characterization of thiol self-assembled films by laser desorption fourier transform mass spectrometry. *J. Am. Chem. Soc.* 114, 2428-2432.
- Li X.-M. et al. (2003) Sulfonic Acid-Functionalized Gold Nanoparticles: A Colloid-Bound Catalyst for Soft Lithographic Application on Self-Assembled Monolayers. *J. Am. Chem. Soc.* 125, 4279-4184.
- Liebau M. et al. (2002) Preparation of dendritic polysulfides and their assembly on air/water interfaces and gold surfaces. *Langmuir* 18, 674-682.
- Linford M. R. and Chidsey C. E. D. (1993) Alkyl Monolayers Covalently Bonded to Silicon Surfaces. *J. Am. Chem. Soc.* 115, 12631-12632.
- Lis T. (1980) Preparation, structure, and magnetic properties of a dodecanuclear mixed-valence manganese carboxylate. *Acta Cryst.* B36, 2042-2046.
- Lloyd J. P. and Pake G. E. (1953) Spin-Lattice Relaxation and the Residual Width of Highly Exchange-Narrowed Paramagnetic Resonances. *Phys. Rev.* 92, 1576-1576.
- Lu X. et al. (2003) Spatially Mapping the Spectral Density of a Single C<sub>60</sub> Molecule. *Phys. Rev. Lett.* 90, 96802.
- Lussem B. et al. (2006) STM Study of Mixed Alkanethiol/Biphenylthiol Self-Assembled Monolayers on Au(111). *Langmuir* 22, 3021-3027.
- Maivald P. et al. (1991) Using force modulation to image surface elasticities with the atomic force microscope. *Nanotechnology* 2, 103-106.
- Manassen Y. et al. (2000) Electron-spin-resonance STM on iron atoms in silicon. *Phys. Rev. B.* 61 16223-16228.
- Manassen Y. et al. (1989) Direct observation of the precession of individual paramagnetic spins on oxidized silicon surfaces. *Phys. Rev. Lett.* 62, 2531-2534.
- Manassen Y. (1997) Real Time Response and Phase - Sensitive Detection to Demonstrate the Validity of ESR - STM Results. *J. Magn. Reson.* 126, 133-137.
- Mannini M. et al. (2005) Advances in single-molecule magnet surface patterning through microcontact printing. *Nano Lett.* 5, 1435-1438.
- Mannini M. et al. (2007a) Addressing individual paramagnetic molecules through ESN-STM. *Inorg. Chim. Acta* 360, 3837-3842.
- Mannini M. et al. (2007b) Self-Assembled Organic Radicals on Au(111) Surfaces: A Combined ToF-SIMS, STM, and ESR Study. *Langmuir* 23, 2389 - 2397.
- Mannini M. et al. (2008a) Magnetic Memory of a Single-Molecule Quantum Magnet wired to a Gold Surface. *submitted*
- Mannini M. et al. (2008b) Patterned monolayers of nitronyl nitroxide radicals. *Inorg. Chim. Acta* 361, 3525-3528.
- Mannini M. et al. (2008c) X-ray Magnetic Circular Dichroism Picks out Single-Molecule Magnets Suitable for Nanodevices. *Adv. Mater.* in press (doi: 10.1002/adma.200801883)
- Mannini M. et al. (2008d) XAS and XMCD Investigation of Mn<sub>12</sub> Monolayers on Gold. *J. Eur. Chem.* 14, 7530-7535.

- Martin Y. et al. (1987) Atomic force microscope-force mapping and profiling on a sub 100-Å scale. *J. Appl. Phys.* 61, 4723-4729.
- Martin Y. and Wickramasinghe H. K. (1987) Magnetic imaging by "force microscopy" with 1000 Å resolution. *Appl. Phys. Lett.* 50, 1455-1457.
- Matsushita M. M. et al. (2002) Formation of self-assembled monolayer of phenylthiol carrying nitronyl nitroxide on gold surface. *Chem. Lett.* 596-597.
- McInnes E. J. L. et al. (2002) Optical detection of spin polarization in single molecule magnets [Mn<sub>12</sub>O<sub>12</sub>(O<sub>2</sub>CR)<sub>16</sub>(H<sub>2</sub>O)<sub>4</sub>]. *J. Am. Chem. Soc.* 124, 9219-9228.
- Messina P. et al. (2007) Spin noise fluctuations from paramagnetic molecular adsorbates on surfaces. *J. Appl. Phys.* 101, 053916.
- Michel B. et al. (2001) Printing Meets Lithography: Soft Approaches to High Resolution Patterning. *IBM J. Res. Dev.* 45, 697-719.
- Mielczarski J. A. and Yoon R. H. (1991) Spectroscopic Studies of the Structure of the Adsorption Layer of Thionocarbamate. 2. On Cuprous Sulfide. *Langmuir* 7, 101-108.
- Miller J. S. and Drillon M. (2001-2005) *Series: Magnetism: Molecules to Materials*. Vol. I-V Weinheim Wiley-VCH.
- Mina B.K. et al. (2005) Reaction of Au(111) with Sulfur and Oxygen: Scanning Tunneling Microscopic Study *Top. Catal.* 36, 77-90.
- Mironov V.L. (2004) *Fundamental of Scanning Probe Microscopy*, Nizhny Novgorod: NT-MDT, Zelenograd, Moscow, Russia (www.ntmdt.com).
- Moore G. E. (1965) Cramming More Components onto Integrated Circuits. *Electronics* 38, 114-117.
- Moroni R. et al. (2003) X-ray magnetic circular dichroism investigation of magnetic contributions from Mn(III) and Mn(IV) ions in Mn<sub>12</sub>-ac. *Phys. Rev. B* 68, 064401.
- Morrish A. H. (1966) *The physical principles of magnetism*. New York: John Wiley & Sons, Inc..
- Nait Abdi A. et al. (2004) Magnetic Properties of Bulk Mn<sub>12</sub>Pivalate<sub>16</sub> Single Molecule Magnets and their Self-Assembly on Gold Surface. *J. Appl. Phys.* 95, 7345-7347.
- Nait Abdi A. et al. (2005) Self-assembling and magnetism of Mn<sub>12</sub> nanomagnets on native and functionalized gold surfaces. *Adv. Mater.* 17, 1612-1617.
- Narasimhan S. and Vanderbilt D. (1992) Elastic stress domains and the herringbone reconstruction on Au(111). *Phys. Rev. Lett.* 69, 1564-1567.
- Néel L. (1949) Theorie du Trainage magnetique des ferro- magnetiques en grains fins avec applications aux Terres Cuites. *Ann. Geophys.* 5, 99-136..
- Ni C. et al. (2006) Enhanced differential conductance through light induced current switching in Mn<sub>12</sub> acetate molecular junctions. *Appl. Phys. Lett.* 89, 212104.
- Nomura K. (2002) *Intermediate Temperature Solid Conductors - Crystal Structure Gallery* (<http://staff.aist.go.jp/nomura-k/english/itscgallery-e.htm>). Last check 03/10/2008.
- Nonnenmacheri M. et al. (1991) Kelvin probe force microscopy. *Appl. Phys. Lett.* 58, 2921-2923.
- Nuzzo R. G. and Allara D. L. (1983) Adsorption of Bifunctional Organic Disulfides on Gold Surfaces. *J. Am. Chem. Soc.* 105, 4481-4483.
- Nuzzo R. G. et al. (1987) Fundamental Studies of the Chemisorption of Organosulfur Compounds on Au(111). Implications for Molecular Self-Assembly on Gold Surfaces. *J. Am. Chem. Soc.* 109, 733-740.
- Odom T.W. et al. (2002) Generation of 30-50 nm structures using easily fabricated, composite PDMS masks. *J. Am. Chem. Soc.* 124, 12112-12113.

- Okuno H. et al. (1990) Synthesis of tetranuclear iron–sulphur protein analogues with tetrathiol ligands attached to macrocycles which provide intramolecular hydrophobic domains. *J. Chem. Soc. Dalton Trans.* 3375-3381.
- Oral A. et al. (1996) Real-time scanning Hall probe microscopy. *Appl. Phys. Lett.* 69 1324-1326.
- Ordina J. et al. (1997) Mass Spectrometric Study of alpha-Nitronyl Nitroxides. A Class of Stable Organic Radicals. *Rapid Commun. Mass Sp.* 2, 1103-1106.
- Osiecki J. H. and Ullman E. F. (1968) Studies of free radicals. I. alpha.-Nitronyl nitroxides, a new class of stable radicals. *J. Am. Chem. Soc.* 90, 1078-1080.
- Ouyang M. and Awschalom D. D. (2003) Coherent Spin Transfer Between Molecularly Bridged Quantum Dots. *Science* 301, 1074-1078.
- Pacchioni M. (2005) Studio d Sistemi Molecolari con rilassamento lento della magnetizzazione. PhD thesis, Università di Firenze.
- Pacchioni M. et al. (2004) Site-specific ligation of anthracene-1,8-dicarboxylates to an Mn<sub>12</sub> core: a route to the controlled functionalisation of single-molecule magnets. *Chem. Commun.* 22, 2604-2605.
- Pankhurst Q. A. et al. (2003) Applications of magnetic nanoparticles in biomedicine. *J. Phys. D: Appl. Phys.* 36, R167-R181.
- Park H. et al. (2000) Nanomechanical oscillations in a single-C60 transistor. *Nature* 407, 57-60.
- PI (Physik Instrumente) Tutorial (2005):  
[http://www.physikinstrumente.com/en/pdf\\_extra/PI\\_designing\\_with%20piezo\\_actuators\\_tutorial\\_2005c.pdf](http://www.physikinstrumente.com/en/pdf_extra/PI_designing_with%20piezo_actuators_tutorial_2005c.pdf). Last check: 6/10/2008.
- Pohl D. W. et al. (1984) Optical stethoscopy: Image recording with resolution  $\lambda/20$ . *Appl. Phys. Lett.* 44, 651-653.
- Poirier G.E. (1997) Characterization of organosulfur molecular monolayers on Au(111) using scanning tunneling microscopy. *Chem. Rev.* 97, 1117-1127.
- Poirier G. E. (1999) Coverage-Dependent Phases and Phase Stability of Decanethiol on Au(111). *Langmuir* 15, 1167-1175.
- Polimeno A. et al. (2006) Stochastic Modeling of CW-ESR Spectroscopy of [60]Fulleropyrrolidine Bisadducts with Nitroxide Probes. *J. Am. Chem. Soc.* 128, 4734-4741.
- Pontillon Y. et al. (1999) Spin density in a ferromagnetic nitronyl nitroxide free radical *Physica B* 267-268, 51-55.
- Porter M. D. (1987) Spontaneously organized molecular assemblies. 4. Structural characterization of n-alkyl thiol monolayers on gold by optical ellipsometry, infrared spectroscopy, and electrochemistry. *J. Am. Chem. Soc.* 109, 3559-3568.
- Prinz G. A. (1998) Magnetoelectronics. *Science* 282 1660-1663.
- Reed N.M. and Vickerman J. C. (1993) The application of static secondary ion mass spectrometry (SIMS) to the surface analysis of polymer materials. Sabbatini L, Zambonin P.G., editors. In Surface characterization of advanced polymers. Weinheim, (D): VCH.
- Rinkevicius Z. et al. (2004) Characteristic parameters and dynamics of two-qubit system in self-assembled monolayers. <http://arxiv.org/abs/quant-ph/0411202>.
- Riviere J. C. (1990) *Surface Analytical Techniques*. Oxford (UK): Oxford University Press.
- Roberts G. (1990) *Langmuir-Blodgett Films*. New York: Plenum Press.
- Robinson R.A et al. (2000) Internal magnetic structure of Mn<sub>12</sub> acetate by polarized neutron diffraction. *J. Phys.: Condens. Matter* 12, 2805-2810.
- Rocha A. R. et al. (2005) Towards molecular spintronics. *Nature Mater.* 4, 335-339.

- Romeike C. et al. (2006) Kondo-Transport Spectroscopy of Single Molecule Magnets. *Phys. Rev. Lett.* 97, 206601.
- Rugar D. et al. (2004) Single spin detection by magnetic resonance force microscopy. *Nature* 430, 329-332.
- Ruiz D. (1998) Single-Molecule Magnets: Different Rates of Resonant Magnetization Tunneling in  $Mn_{12}$  Complexes. *Angew. Chem. Int. Ed. Engl.* 37, 300-302.
- Ruiz-Molina D. et al. (2002) Characterisation of nanoscopic  $[Mn_{12}O_{12}(O_2CR)_{16}(H_2O)_4]$  single-molecule magnets: physicochemical properties and LDI- and MALDI-TOF mass spectrometry. *J. Mater. Chem.* 12, 1152-1161.
- Ruthsteinet S. al. (2005) EPR studies on the organization of self-assembled spin-labeled organic monolayers adsorbed on GaAs. *Phys. Chem. Chem. Phys.* 7, 524-530.
- Sabatani E. et al. (1993) Thioaromatic monolayers on gold: a new family of self-assembling monolayers. *Langmuir* 9, 2974-2981.
- Sagiv J. (1980) Organized monolayers by adsorption. 1. Formation and structure of oleophobic mixed monolayers on solid surfaces. *J. Am. Chem. Soc.* 102, 92-98.
- Salomon A. et al. (2003) Comparison of Electronic Transport Measurements on Organic Molecules. *Adv. Mater.* 15, 1881-1890.
- Schmid H. and Michel B. (2000) Siloxane Polymers for High-Resolution, High-Accuracy Soft Lithography. *Macromolecules* 33, 3042-3049.
- Schreiber F. (2000) Structure and growth of self-assembling monolayers. *Prog. Surf. Sci.* 65, 151-257.
- Schubert U. and Hüsing N. (2005) *Synthesis of Inorganic Materials*. Weinheim: Wiley.
- Schütz G. et al. (1987) Absorption of circularly polarized x rays in iron. *Phys. Rev. Lett.* 58, 737 - 740.
- Semaltianos N. G. and Wilson E. G. (2000) Investigation of the surface morphology of thermally evaporated thin gold films on mica, glass, silicon and calcium fluoride substrates by scanning tunneling microscopy. *Thin Solid Films* 366, 111-116.
- Sessoli R. et al. (1993a) Magnetic bistability in a metal-ion cluster. *Nature* 365, 141-143.
- Sessoli R. et al. (1993b) High-spin molecules:  $[Mn_{12}O_{12}(O_2CR)_{16}(H_2O)_4]$ . *J. Am. Chem. Soc.* 115, 1804-1816.
- Sharma P. (2005) How to Create a Spin Current. *Science* 307, 531-533.
- Shimazu K. et al. (1994) Packing State and Stability of Self-Assembled Monolayers of 11-Ferrocenyl-1-undecanethiol on Platinum Electrodes. *Bull. Chem. Soc. Jpn.* 67, 863-866.
- Sleator T. et al. (1985) Nuclear-spin noise. *Phys. Rev Lett.* 55, 1742-1745.
- Smith C. D. et al. (2002) Electrospray mass spectrometry of stable iminyl nitroxide and nitronyl nitroxide free radicals. *J. Mass Spectrom.* 37, 897-902.
- Smith R.K. et al. (2004) Patterning Self-Assembled Monolayers. *Prog. Surf. Sci.* 75 1-68.
- Soler M. et al. (2000) A third isolated oxidation state for the  $Mn_{12}$  family of single-molecule magnets. *Chem. Commun.* 2417-2418.
- Soler M. et al. (2001) Single-Molecule Magnets: Preparation and Properties of Mixed-Carboxylate Complexes  $[Mn_{12}O_{12}(O_2CR)_8(O_2CR')_8(H_2O)_4]$ . *Inorg. Chem.* 40, 4902-4912.
- Soler M. et al. (2003) New example of Jahn-Teller isomerism in  $[Mn_{12}O_{12}(O_2CR)_{16}(H_2O)_4]$  complexes. *Polyhedron* 22, 1783-1788.
- Steckel J. S. et al. (2004) Monolayer and Multilayer Films of  $[Mn_{12}O_{12}(O_2CMe)_{16}]$ . *Nano Lett.* 4, 399-402.
- Stöhr J. et al. (1994) *New Directions in Research with Third-Generation Soft X-Ray Synchrotron Radiation Sources*. Amsterdam: Kluwer p. 221.
- Stroh C. et al. (2004) Rigid nitronyl-nitroxide-labelled anchoring molecules: syntheses, structural and magnetic investigations. *Tetrahedron Letters* 45, 9623-9626.

- Strohmeier B. R. and Hercules D. M. (1984) Surface spectroscopic characterization of manganese/aluminum oxide catalysts. *J. Phys. Chem.* 88, 4922-4929.
- Strong L. and Whitesides G. M. (1988) Structures of Self-Assembled Monolayer Films of Organosulfur Compounds Adsorbed on Gold Single Crystals: Electron Diffraction Studies. *Langmuir* 4, 546-558.
- Sun Z. M. et al. (1998) Isomeric Forms of  $[\text{Mn}_{12}\text{O}_{12}(\text{O}_2\text{CR})_{16}(\text{H}_2\text{O})_4]$  Single-Molecule Magnets. *Inorg. Chem.* 37, 4758-4759.
- Sun Z. M. et al. (1999) The origin of the second relaxation process in the  $[\text{Mn}_{12}\text{O}_{12}(\text{O}_2\text{CR})_{16}(\text{H}_2\text{O})_4]$  single-molecule magnets: Jahn-Teller isomerism in the  $[\text{Mn}_{12}\text{O}_{12}]$  core. *Chem. Comm* 1973-1974.
- Takahashi S. et al. (2004) Discrete easy-axis tilting in  $\text{Mn}_{12}$ -acetate, as determined by EPR: Implications for the magnetic quantum tunneling mechanism. *Phys. Rev. B* 70, 094429.
- Takeda K. and Awaga K. (1997) Magnetic properties of (mMPYNN+) $[\text{Mn}_{12}\text{O}_{12}(\text{O}_2\text{CPh})_{16}(\text{H}_2\text{O})_4]$ :- Enhancement of magnetic relaxation in the  $\text{Mn}_{12}$  cluster caused by the organic radical. *Phys. Rev. B* 56, 14560-14565.
- Takeda K. et al. (1998) Crystal structure and magnetic properties of  $[\text{Mn}_{12}\text{O}_{12}(\text{O}_2\text{CPh})_{16}(\text{H}_2\text{O})_4]_2(\text{PhCO}_2\text{H})$ : Evidence of domain formation with different blocking temperatures. *Phys. Rev. B* 57, R11062- R11064.
- Takiguchi H. et al. (2000) Delicate Surface Reaction of Dialkyl Sulfide Self-Assembled Monolayers on Au(111). *Langmuir* 16, 1703-1710.
- Tamura M. et al. (1991) Bulk ferromagnetism in the  $\beta$ -phase crystal of the p-nitrophenyl nitronyl nitroxide radical. *Chem. Phys. Lett.* 186, 401-404.
- Tao Y.-T. et al. (1997) Structure evolution of aromatic-derivatized thiol monolayers on evaporated gold. *Langmuir* 13, 4018-4023.
- Tarlov M. J. and Newman J.G. (1992) Static Secondary Ion Mass Spectrometry of self-assembled alkanethiol monolayers on gold. *Langmuir* 8, 1398-1405.
- Tengvall P. (2000) *Biomaterial Group Linköpings universitet website*. [www.ifm.liu.se/appphys/biomaterial/research/sam.html](http://www.ifm.liu.se/appphys/biomaterial/research/sam.html). Last check 03/11/2008.
- Tersoff J. and Hamann D. R. (1985) Theory of the scanning tunneling microscope. *Phys. Rev. B* 31, 805-813.
- Thibault C. et al. (2005) Direct microcontact printing of oligonucleotides for biochip applications. *J. Nanobiotech* 3, 7.
- Thole B.T. et al. (1988) Spin-mixed ground state of Fe phthalocyanine and the temperature-dependent branching ratio in X-ray absorption spectroscopy. *Chem. Phys. Lett.* 149, 295-299.
- Thole B.T. et al. (1992) X-ray circular dichroism as a probe of orbital magnetization. *Phys. Rev. Lett.* 68, 1943-1946.
- Thomas L. et al. (1996) Macroscopic quantum tunnelling of magnetization in a single crystal of nanomagnets. *Nature* 383, 145-147.
- Tour J. M. et al. (1995) Self-Assembled Monolayers and Multilayers of Conjugated Thiols, .alpha.,.omega.-Dithiols, and Thioacetyl-Containing Adsorbates. Understanding Attachments between Potential Molecular Wires and Gold Surfaces. *J. Am. Chem. Soc.* 117, 9529-9534.
- Tour J. M. et al. (1998) Molecular scale electronics: A synthetic/computational approach to digital computing. *J. Am. Chem. Soc.* 120, 8486-8493.
- Tour J. M. et al. (2003) NanoCell Electronic Memories. *J. Am. Chem. Soc.* 125,13279-13283.
- Tripp C. P. and Hair M. L. (1995) Reaction of methylsilanols with hydrated silica surfaces: The hydrolysis of trichloro-, dichloro-, and monochloromethylsilanes and the effects of curing. *Langmuir* 11, 149-155.

- Troughton E. B. et al. (1988) Monolayer films prepared by the spontaneous self-assembly of symmetrical and unsymmetrical dialkyl sulfides from solution onto gold substrates: Structure, properties, and reactivity of constituent functional groups. *Langmuir* 4, 365-385.
- Tsai H. et al. (2001) A single-molecular magnet:  $[\text{Mn}_{12}\text{O}_{12}(\text{O}_2\text{CCH}_2\text{Br})_{16}(\text{H}_2\text{O})_4]$ . *Inorg. Chem. Commun.* 4, 511-514.
- Tsukagoshi K. et al. (1999) Coherent transport of electron spin in a ferromagnetically contacted carbon nanotube. *Nature* 401, 572-574.
- Ullman E. F. et al. (1970) Stable free radicals. VIII. New imino, amidino, and carbamoyl nitroxides. *J. Org. Chem.* 35, 3623-3631.
- Ullman E. F. et al. (1972) Studies of stable free radicals. X. Nitronyl nitroxide monoradicals and biradicals as possible small molecule spin labels. *J. Am. Chem. Soc.* 94, 7049-7059.
- Ulman A. (1989) Ultrathin Organic Films: From Langmuir-Blodgett to Self-Assembly. *J. Mater. Educ.* 11 205-280.
- Ulman A. (1991) *An introduction to Ultrathin Organic Films*; Boston: Academic Press.
- Ulman A. (1996) Formation and structure of self-assembled monolayers. *Chem. Rev.* 96, 1533-1554.
- Ulman A. (2001) Self-assembled monolayers of 4-mercaptobiphenyls. *Acc. Chem. Res.* 34, 855-863.
- Ihs A. et al. (1993) Infrared and photoelectron spectroscopic studies of ethyl and octyl xanthate ions adsorbed on metallic and sulfidized gold surfaces: Glycine, l-alanine and  $\beta$ -alanine *Langmuir* 9, 733-739.
- Van der Laan G. et al. (1988) Multiplet structure in the  $L_{2,3}$  x-ray-absorption spectra: A fingerprint for high- and low-spin  $\text{Ni}^{2+}$  compounds. *Phys. Rev. B* 37, 6587-6589.
- Vickerman J. C. and Briggs D. (2001) *ToF-SIMS: Surface Analysis by Mass Spectrometry, Surface Spectra* Manchester (UK): IMPublications.
- Villain J. et al. (1994) Magnetic Relaxation in Big Magnetic Molecules. *Europhys. Lett.* 27, 159-164.
- Walczak M. W. et al. (1991) Structure and interfacial properties of spontaneously adsorbed n-alkanethiolate monolayers on evaporated silver surfaces. *J. Am. Chem. Soc.* 113, 2370-2378.
- Walker A.V. and Winograd N. (2004) Prospects for Imaging with TOF-SIMS Using Gold Liquid Metal Ion Sources. *Appl. Surf. Sci.* 203-204, 198-200.
- Wei Y.-G. et al. (1997) A mesoscopic molecular superparamagnet: preparation, crystal structure and magnetic properties of  $[\text{Mn}_{12}\text{O}_{12}(\text{O}_2\text{CMe})_4(\text{O}_2\text{CEt})_{12}(\text{H}_2\text{O})_4] \cdot 2\text{H}_2\text{O} \cdot 4\text{EtCO}_2\text{H}$  with an  $S = 9$  ground state. *Polyhedron* 16, 1471-1475.
- Weil J. A. et al. (1994) *Electron Paramagnetic Resonance, Elementary Theory and Practical Applications*; New York: Wiley p. 462.
- Wernsdorfer W. (2001) Classical and Quantum Magnetization Reversal Studied in Nanometer-Sized Particles and Clusters. *Adv. Chem. Phys.* 118, 99-190.
- Widrig C. A. et al. (1991) The electrochemical desorption of n-alkanethiol monolayers from polycrystalline Au and Ag electrodes. *J. Electroanal. Chem.* 310, 335-359.
- Wiesendanger R. (1994) *Scanning Probe Microscopy and Spectroscopy*, Cambridge(UK): Cambridge University Press.
- Wiesendanger R. et al. (1990). Observation of Vacuum Tunneling of Spin-Polarized Electrons With the Scanning Tunneling Microscope. *Phys. Rev. Lett.* 65, 247-250.
- Williams and C. C. and Wickramasinghe H. K. (1987) Scanning thermal profiler. *Appl. Phys. Lett.* 49, 1587-1589.

- Wolf S. A. et al. (2001) Spintronics: A Spin-Based Electronics Vision for the Future *Science* 294, 1488-1495.
- Woll C. et al. (1989) Determination of atom positions at stacking-fault dislocations on Au(111) by scanning tunneling microscopy. *Phys. Rev. B* 39, 7988-7991.
- Wong S. C. C. (2003) Development of a  $C_{60}^+$  ion gun for static SIMS and chemical imaging. *Appl. Surf. Sci.* 203–204 219-222.
- Wu X. C. et al. (2004) Microcontact Printing of CDS/Dendrimer Nanocomposite Patterns on Silicon Wafers. *Adv. Mater.* 16, 413-417.
- Xia Y. and Whitesides G. M. (1998) Soft Lithography. *Annu. Rev. Mater. Sci* 28, 153-184.
- Xiao M. et al. (2004) Electrical detection of the spin resonance of a single electron in a silicon field-effect transistor. *Nature* 430, 435-439.
- Xie Z.-X. et al. (2002) Influence of reconstruction on the structure of self-assembled normal-alkane monolayers on Au(111) surfaces. *Chem. Chem. Phys.* 4, 1486-1489.
- Yamaguchi T. et al. (1982) Inner-core excitation spectra of transition-metal compounds: II. p-d absorption spectra. *J. Phys. C* 15, 2641-2650.
- Young R. et al. (1972) The topografiner: An instrument for measuring surface microtopography. *Rev. Sci. Instr.* 43, 999-1011.
- Zangwill A. (1988) *Physics at surfaces*. Cambridge (UK): Cambridge University Press.
- Zhao H. H. et al. (2004) Structural Characterization, Magnetic Properties, and Electrospray Mass Spectrometry of Two Jahn-Teller Isomers of the Single-Molecule Magnet  $[Mn_{12}O_{12}(CF_3COO)_{16}(H_2O)_4]$ . *Inorg. Chem.* 43, 1359-1369.
- Zhao A. et al. (2005) Controlling the Kondo Effect of an Adsorbed Magnetic Ion Through Its Chemical Bonding. *Science* 309, 1542-1544.
- Zhong C.-J. et al. (1999) Organosulfur Monolayers at Gold Surfaces: Reexamination of the Case for Sulfide Adsorption and Implications to the Formation of Monolayers from Thiols and Disulfides. *Langmuir* 15, 518-525.
- Zobbi L. (2004) *Organization of single-molecule magnets at surfaces*. PhD Thesis Università di Modena e Reggio Emilia.
- Zobbi L. et al. (2005) Isolated single-molecule magnets on native gold. *Chem. Commun.* 12, 1640-1642.



## Ringraziamenti

Niente ringraziamenti in inglese. Non ne posso più e ci sarebbe il rischio di conservare la freddezza della lingua scientifica nel ringraziare delle persone a cui tengo...

Le persone che devo ringraziare le saluto in italiano, anche se per ringraziarle tutte ci vorrebbe una tabella, un mappamondo... Cominciamo da vicino.

Cominciamo da chi ha corretto tutto il manoscritto. Ringrazio per questo il Prof. Dante Gatteschi e la Prof. Roberta Sessoli che hanno reso questo lavoro leggibile ma soprattutto perché mi hanno guidato durante questi *anni di ricerca*.

Ringrazio il mentore delle mie divagazioni scientifiche Prof. Andrea Caneschi che primo tra tutti mi ha ascoltato, appoggiato e sopportato. E ringrazio i miei maestri del LAMM, il Professore e maestro Andrea Dei, il Dr. Claudio Sangregorio, il Dr. Lorenzo Sorace, il Prof. Cristiano Benelli e la Dott.ssa Donella Rovai, amici e unici istruttori indispensabili, ad essi devo ovviamente aggiungere il Prof. Andrea Cornia e il Dr. Giovanni Aloisi. Non posso dimenticarmi di chi mi ha trasmesso molte delle conoscenze che ho utilizzato durante la tesi e che per una ragione o per l'altra non sono più sotto l'ala protettrice del fiorentino Mn12... ovvero, Lapo Bogani, Daniele Bonacchi, Laura Zobbi, Mirco Pacchioni e Guillaume Chastanet che abbraccio e ringrazio di tutto. E poi ringrazio chi ancora patisce per i corridoi di questo dipartimento e che in qualche modo ha contribuito a questo lavoro. Primo tra tutti Francesco *Pine* Pineider amico di sofferenze di giorno e di notte (a Berlino, non fraintendiamo), e poi Kevin (nonostante sia francese), Lapo (nonostante sia a Manchester perché tira più...ah lo sport...), Patrizio (nonostante sia portoghese), Giordano (nonostante sia del Piscetto), Mario (nonostante sia Mario), Federico (nonostante sia il Totti), Alessandra (brava Alesandra), Claudia (nonostante ora sia in Nuova Zelanda o in Australia) e tutti quelli che solo per la fretta di andare a stampare mi sono scordato (nonostante siano stati dimenticati).

Poi devo ringraziare tutte le persone che ho trovato in giro per l'Europa (a volte anche senza vederli mai) e che mi hanno insegnato qualcosa, tra tutti mi piace ricordare: Philippe e Christophe a Parigi/Berlino, Christian, Mircea, Laurent, J.P. Kappler e soprattutto il prof. J.P. Bucher a Strasburgo, Tim, Nicolas e il prof. H. Hug a Basilea, Paolo Imperia a Berlino, il prof. Y.Manassen a Trieste/Be'er Sheva, Mauro, Paolo Singalotti e Paolo Pittana a Trieste, Paolo Messina a Firenze/Trieste, Davide Barreca a Padova, Andras Perl, B. J. Ravoo e il prof. D. Reinhardt a Eschede, e poi tutti quelli che se mi sono di nuovo dimenticato...

Adesso mi manca da ringraziare le persone care, gli amici che mi sono stati vicini senza capire (beati loro che sono giustificati) a cosa servano i magneti molecolari... Prima di tutto ringrazio mamma Maura e babbo Varesco che hanno continuato a camparmi e incoraggiarmi a continuare a coltivare la mia passione, grazie davvero tutto questo è merito vostro, dei vostri sacrifici e della vostra pazienza.

Un pensiero va anche ai miei nonni Giuliano, Rosalba e Brunetta e alla memoria di Corrado che hanno creato dal niente le fondamenta di quei sacrifici che mi hanno portato fin qua.

E poi ringrazio la persona che mi ha supportato, ascoltato e sopportato di più. Mio fratello Andrea.

Non mi dimentico certo di chi mi ha fortunatamente allontanato dalla scienza avvicinandomi alla musica, alla poesia e all'amicizia, e che nonostante questo ha pure saputo darmi la spinta a continuare quando la voglia diminuiva, i miei amici Marco, Guido e Andrea, preparatevi per le prossime zingarate...

Grazie anche agli amici veri che magari non si salutano da anni ma che restano lì, pronti alla prima telefonata.

Infine ringrazio la mia dolce Tania perché la serenità che è rimasta in me nonostante il consueto stress da tesi. È solo merito tuo, del tuo amore e del tuo starmi vicino, sempre.

PREMIO FIRENZE UNIVERSITY PRESS  
TESI DI DOTTORATO

Coppi E., *Purines as Transmitter Molecules. Electrophysiological Studies on Purinergic Signalling in Different Cell Systems*, 2007

Natali I., *The Ur-Portrait. Stephen Hero ed il processo di creazione artistica in A Portrait of the Artist as a Young Man*, 2007

Petretto L., *Imprenditore ed Università nello start-up di impresa. Ruoli e relazioni critiche*, 2007

Mannini M., *Molecular Magnetic Materials on Solid Surfaces*, 2007

Bracardi M., *La Materia e lo Spirito. Mario Ridolfi nel paesaggio umbro*, 2007

Finito di stampare presso  
la tipografia editrice Polistampa